RESPONSIVE TEMPERATURE AND PRESSURE SENSOR DESIGN FOR IN-SITU PROSTHESIS MONITORING APPLICATIONS BASED ON THE PIEZOELECTRIC AND PYROELECTRIC EFFECTS IN LEAD ZIRCONATE TITANATE

ALAN DAVIDSON

Registration No: 201367275

Department of Electronic and Electrical Engineering

University of Strathclyde

April 2020

Declaration of authenticity

This thesis is the result of the author's original research. It has been composed by the author and has not been previously submitted for examination, which has led to the award of a degree.

Alan Davidson

April 2020

This thesis is submitted to the University of Strathclyde in partial fulfilment of the requirements for the degree of Doctor of Philosophy.

This doctoral work has been performed at the Department of Electronic and Electrical Engineering, Centre for Intelligent Dynamic Communications (CIDCOM), with Professor Ivan Glesk and Dr Arjan Buis as main supervisors, and Dr Anthony McGarry as co-supervisor.

Dedicated to my Mother, Brother, family,

and to the memory of my Father

Acknowledgements

I would like to express my gratitude to my first supervisor, Professor Ivan Glesk for the tremendous opportunity to commence this PhD and for his subsequent guidance, advice and unstinting support throughout that made it possible for me to complete this thesis. I am grateful to Dr Aryan Buis for his advice and support, and to Dr Helena Gleskova for her advice and for providing generous access to additional specialised laboratory equipment critical to the experimental investigations.

I would like to thank my Mother, Brother, Aunt and Sister-in-law for their support and advice, particularly during the stressful times. I also thank my friends and office colleagues, particularly Stuart, Mohamed, Shakil, Umair, Ama and Mohsin for the great discussions, and most of all for the laughs.

Abstract

This thesis presents the development of a sensor based on the pyroelectric and piezoelectric effects that can be used to measure both temperature and/or axial stress for specific use within a prosthetic socket, and more generally as a responsive temperature sensor capable of detecting high frequency skin temperature oscillations in medical diagnostic applications.

Knowledge of an amputees' residual limb skin temperature is considered to be of particular importance as an indicator of tissue health. With this in mind, a prototype wearable sensor for real-time temperature measurement at the skin/ prosthetic socket/liner interface was developed and measurements that provide a proof of concept are presented. The sensor exploits the large pyroelectric effect present in ferroelectric lead zirconate titanate $PbZr_x\left(Ti_{(1-x)}O_3\right)$ (PZT) and has several inherent advantages over other methods of temperature sensing.

The sensor element chosen is a low cost commercially available diaphragm PZT-5H element with a brass substrate. While the development of the sensor concentrates on the specific application of surface temperature measurement, the mathematical models developed also describe the sensor response to an applied axial stress that can be used as a measure of the pressure applied to the residual limb by the confinement of a prosthetic socket. Using the mathematical models, substrate clamping was found to significantly increase the effective pyroelectric coefficient. A subsequent experimentally obtained value for the effective pyroelectric coefficient was found to be very close to the value predicted by the mathematical models, confirming the effect of substrate clamping.

Immittance models are developed to investigate the temperature dependence of the sensor elementimmittance. mechanical and constant strain electrical capacitances over the temperature range $20°C$ to $40°C$. Both capacitances were found to be significantly temperature dependent and therefore charge-mode signal conditioning was chosen to mitigate temperature effects on the signal-conditioning response. Subsequent response measurements were found to yield a linear response over the temperature range of interest.

Bipolar and unipolar charge amplifier designs are developed and built to provide signal-conditioning for use in sensor response measurements. The unipolar type is a single supply $5V$ prototype with low power consumption and is also designed for use with an e-Health platform in a wearable sensor configuration. In addition, a single supply enhanced open loop gain design that mitigates the effect of reduced dielectric resistance in the sensor element is presented.

Using the developed mathematical models, the sensor is predicted to be capable of measuring frequencies from DC up to $6.8rads^{-1}$ with a rise time to the 98% peak of $0.12s$ and $0.18s$ for a DC and $6.8rads^{-1}$ step, respectively. However, the use of a polymer liner between the sensor element and measurement surface is found to severely limit the usable frequency response of the sensor due to severe amplitude and phase distortion, precluding direct use of the sensor to measure skin surface temperature.

Being relevant to the safety of remote e-Health monitoring, the challenges ICT networks must face to maintain quality of service are discussed and it is shown that an increasing amount of traffic, increasing power consumption and electronic bottlenecks are three main challenges that require a solution. The ability of ICT

networks to satisfy the growing global demand for data is under threat due to the speed limitations of current CMOS based electronic technologies, leading to electronic bottlenecks and threats to the sustainability of the quality of service critically required for e-Health monitoring.

Table of contents

List of figures

List of tables

List of symbols and abbreviations

x_3	Longitudinal poling axis	m
x_1, x_2	Transverse axes	m
T	Stress vector	Nm^{-2}
S	Strain vector	m/m
E	Electric field vector	Vm^{-1}
D	Electric displacement field vector	Cm^{-2}
ε^S	Permittivity matrix at constant strain (clamped)	Fm^{-1}
ε^T	Permittivity matrix at constant stress	Fm^{-1}
c^E	Stiffness matrix at constant electric field	Nm^{-2}
c^D	Stiffness matrix at constant displacement field	Nm^{-2}
s^E	Compliance matrix at constant electric field	m^2N^{-1}
s^D	Compliance matrix at constant displacement field	m^2N^{-1}
β^S	Inverse permittivity matrix at constant strain	mF^{-1}
β^T	Inverse permittivity matrix at constant stress	mF^{-1}
d	Strain charge piezoelectric coefficient matrix	CN^{-1}
h	Stress voltage piezoelectric coefficient matrix	NC^{-1}
g	Strain voltage piezoelectric coefficient matrix	m^2C^{-1}
e	Stress charge piezoelectric coefficient matrix	Cm^{-2}
e_{31}	Stress charge coefficient – ratio of x_3 effect to x_1 cause	Cm^{-2}
e_{33}	Stress charge coefficient – ratio of x_3 effect to x_3 cause	Cm^{-2}
P_s	Spontaneous polarisation	Cm^{-2}
P_r	Remanent polarisation	Cm^{-2}
S_r	Remanent strain	m/m
G_e	Electric Gibbs thermodynamic potential	Jm^{-3}
u	Internal energy	J
q	Heat	J
w	Work	J
σ	Entropy	JK^{-1}
W	Work density	Jm^{-3}
U	Internal energy density	Jm^{-3}
Q	Heat density	Jm^{-3}
Σ	Entropy density	$Jm^{-3}K^{-1}$
$\Sigma_{thermal}$	Entropy density at constant S and E	$Jm^{-3}K^{-1}$
ρ	Piezoelectric density	kgm^{-3}
ρ_b	Substrate density	kgm^{-3}
C_{spb}^S	Specific heat capacity of substrate at constant S	$Jkg^{-1}K^{-1}$

$C_{sp}^{S,E}$	Specific heat capacity of piezoelectric at constant S and E	$Jkg^{-1}K^{-1}$
$C_{spv}^{S,E}$	Volume specific heat capacity at constant S and E	$Jkg^{-1}K^{-1}$
γ^{E}	Thermal stress/piezo-caloric vector at constant E	$Nm^{-2}K^{-1}$
p^{S}	Primary pyroelectric/electro-caloric vector at constant S	$Cm^{-2}K^{-1}$
p^{S}	Primary pyroelectric coefficient in the x_3 axis at constant S_3	$Cm^{-2}K^{-1}$
P^{T}	Primary pyroelectric/electro-caloric vector at constant T	$Cm^{-2}K^{-1}$
P^{T}	Primary pyroelectric coefficient in the x_3 axis at constant T_3	$Cm^{-2}K^{-1}$
φ_{p}^{E}	Thermal expansion vector in the piezoelectric at constant E	$m(mK)^{-1}$
φ_{p1}^{E}	Thermal expansion coefficient in the x_1 and x_2 axes	$m(mK)^{-1}$
φ_{p3}^{E}	Thermal expansion coefficient in the x_3 axis	$m(mK)^{-1}$
φ_{b}	Thermal expansion vector in the substrate	$m(mK)^{-1}$
φ_{b}	Substrate thermal expansion coefficient	$m(mK)^{-1}$
φ_{a}	Adhesive thermal expansion coefficient	$m(mK)^{-1}$
c_{b}	Stiffness matrix of substrate	Nm^{-2}
$\Delta\theta$	Temperature change in the piezoelectric	K
$\Delta\theta_{b}$	Temperature change in the substrate	K
$\Delta\theta_{e}$	Temperature change in the elastomer liner	K
$\Delta\bar{\theta}$	Spatial mean temperature change – piezoelectric medium	K
$\Delta\bar{\theta}_{b}$	Spatial mean temperature change – substrate medium	K
$\Delta\theta_{tr}$	Common boundary temperature change – substrate / piezo	K
$\Delta\theta'_{tr}$	Common boundary temperature change – substrate / liner	K
$\Delta\theta_{s}$	Substrate external surface temperature	K
$\Delta\theta_{skin}$	Skin surface temperature	K
θ_{c}	Curie temperature	K
θ	Absolute temperature	K
θ_{o}	Initial system temperature	K
θ_{g}	Glass transition temperature	K
T_{b}	Substrate stress vector	Cm^{-2}
S_{b}	Substrate strain vector	m/m
γ_{b}	Substrate thermal stress/elasto-caloric vector	$Nm^{-2}K^{-1}$
Ψ_3	Rate of heat flow per unit area along the x_3 axis	Wm^{-2}
k_{p}	Thermal conductivity of piezoelectric	$Wm^{-1}K^{-1}$
k_{b}	Thermal conductivity of substrate	$Wm^{-1}K^{-1}$
k_{e}	Thermal conductivity of elastomer liner	$Wm^{-1}K^{-1}$
K_{b}^{S}	Diffusion coefficient of substrate at constant strain	m^2s^{-1}
$K^{S,E}$	Diffusion coefficient at constant S and E	m^2s^{-1}
K_{e}	Diffusion coefficient of elastomer liner	m^2s^{-1}
K_{effb}^{S}	Effective diffusion coefficient of substrate at constant S	m^2s^{-1}

$K_{eff}^{S,E}$	Effective diffusion coeff at constant S and E	$m^2 s^{-1}$
η	Piezoelectric diffusion equation coupling term	K
ξ	Substrate equation coupling term	K
η'	Piezoelectric diffusion equation coupling term	$Nm^{-2}K^{-1}$
ξ'	Substrate equation coupling term	No units
T_s	Sampling period	s
τ_q	Thermal relaxation time – piezoelectric medium	s
τ_{qb}	Thermal relaxation time – substrate medium	s
T	Stress in the x_1 and x_2 axes	Nm^{-2}
T_3	Stress in the x_3 axis	Nm^{-2}
S	Strain in the x_1 and x_2 axes	mm^{-1}
S_3	Strain in the x_3 axis	mm^{-1}
E_3	Electric field in the x_3 axis	Vm^{-1}
D_3	Displacement field in the x_3 axis	Cm^{-2}
c_{11}^E	Stiffness coefficient – ratio of x_1 effect to x_1 cause	Nm^{-2}
c_{12}^E	Stiffness coefficient – ratio of x_1 effect to x_2 cause axis	Nm^{-2}
c_{31}^E	Stiffness coefficient – ratio of x_3 effect to x_1 cause	Nm^{-2}
c_{33}^E	Stiffness coefficient – ratio of x_3 effect to x_3 cause	Nm^{-2}
ε_{33}^S	Constant strain permittivity in x_3 axis at constant S	Fm^{-1}
ε_{33}^T	Constant stress permittivity in x_3 axis at constant S	Fm^{-1}
ε_o	Permittivity of free space	Fm^{-1}
χ_{33}^S	Susceptibility at constant S	No units
p^S	Primary pyroelectric/electro-caloric coefficient in the x_3 axis	Cm^{-2}
T_b	Substrate stress in the x_1 and x_2 axes	Nm^{-2}
T_{b3}	Substrate stress in the x_3 axis	Nm^{-2}
S_b	Substrate strain in the x_1 and x_2 axes	mm^{-1}
S_{b3}	Substrate strain in the x_3 axis	mm^{-1}
E_b	Substrate Young's modulus	Nm^{-2}
μ_b	Substrate Poisson's ratio	No units
K	Curvature	m^{-1}
A_b	Diametric cross-sectional area of the substrate	m^2
A_p	Diametric cross-sectional area of the piezoelectric	m^2
A_a	Diametric cross-sectional area of the adhesive	m^2
l_b	Thickness of the substrate	m
l_p	Thickness of the piezoelectric	m
l_e	Thickness of the elastomer liner	m
F	Force	N
$\bar{T}$	Spatial mean lateral stress	Nm^{-2}
$\bar{S}_3$	Spatial mean axial strain	mm^{-1}

$\bar{E}_3$	Spatial mean axial electric field	Vm^{-1}
A_{bs}	Surface area of the substrate	m^2
A_{ps}	Surface area of the piezoelectric	m^2
A_s	Surface area of the piezoelectric electrodes	m^2
α_b	Mechanical constant: $E_b/(1-\mu_b)$	Nm^{-2}
α	Mechanical constant: $c_{11}^E + c_{12}^E - 2\,(c_{31}^E)^2/c_{33}^E = E_{p1}^E/(1-\mu_{p1}^E)$	Nm^{-2}
β	Electrical constant: $2(e_{31} - e_{33}\,c_{31}^E/c_{33}^E) = 2(e_{31} - e_{33}\,\mu_{p3}^E/(1-\mu_{p1}^E))$	Cm^{-2}
V_o	Sensor element voltage	V
I_o	Sensor element external current	A
V_{out}	Signal conditioning output voltage	V
E_{p1}^E	Young's modulus, piezoelectric, 1-2 axes – at constant E	Nm^{-2}
μ_{p1}^E	Poisson's ratio, piezoelectric, 1-2, 2-1 axes – at constant E	No units
μ_{p3}^E	Poisson's ratio, piezoelectric, 3-1,2 axes – at constant E	No units
δ_{33}	Internal conductivity of the piezoelectric medium	Sm^{-1}
R_p	Equivalent resistance of the piezoelectric element	Ω
C_p	Low frequency capacitance	F
C_o	Clamped or constant strain capacitance	F
C_m	Mechanical capacitance	F
R_s	BVD resonance loss resistance at resonance – damping	Ω
C_s	BVD mechanical capacitance at resonance – stiffness	F
L_s	BVD mechanical inductance – inertial mass	H
ω_s	Series resonance frequency	$rads^{-1}$
ω_a	Anti-resonance frequency – maximum impedance	$rads^{-1}$
ω_c	Cut-off/cut-on $-3dB$ frequency	$rads^{-1}$
B	Susceptance	S
δ_s	External equivalent conductivity	Sm^{-1}
$\bar{\sigma}_t$	Spatial mean total volume charge density	Cm^{-3}
$\bar{\sigma}_b$	Spatial mean bound volume charge density	Cm^{-3}
$\bar{\sigma}_f$	Spatial mean free volume charge density	Cm^{-3}
$\overline{\mathrm{Q}}_\mathrm{t}$	Spatial mean total surface charge	C
$\overline{\mathrm{Q}}_\mathrm{b}$	Spatial mean bound surface charge	C
$\overline{\mathrm{Q}}_\mathrm{f}$	Spatial mean free surface charge	C
Q	Negative piezoelectric bound surface charge, $\mathrm{Q} = -\overline{\mathrm{Q}}_\mathrm{b}$	C
J_3	Current density in the x_3 axis	$Cm^{-2}s^{-1}$
$\bar{J}_3$	Spatial mean current density in the x_3 axis	$Cm^{-2}s^{-1}$
i_b^-	Bias current at the inverting input of OA1	A
i_b^+	Bias current at the inverting input of OA2	A
i_{b-os}	Input offset bias current	A
V_{os}	Input offset voltage	V

$\hat{A}_v$	DC open loop gain	No units
$\hat{A}_{ve}$	Enhanced open loop gain	No units
A_v	Frequency dependent open loop gain	No units
$\pm V_{cc}$	Op-amp supply rail voltage	V
G	Forward difference gain	No units
G_g	Enhancement gain $= \hat{A}_{ve}/\hat{A}_v$	No units
A_r	Attenuation factor	No units
τ_r	Rise time constant	s
τ_d	Decay time constant	s
a	Voltage divider fraction – fine adjust	No units
b	Voltage divider fraction – fine adjust	No units
a'	Voltage divider fraction	No units
b'	Voltage divider fraction	No units
$G.n$	Dot product of a general vector G and the unit normal n	N/A
$\nabla.G$	Divergence of a general vector G	N/A
p	Spatial Laplace variable	m^{-1}
s	Temporal Laplace variable	s^{-1}
z	Z-transform variable	s^{-1}
T_s	Sampling period	s
$*$	Complex conjugation (superscript)	N/A
$*$	Time domain convolution	N/A

PZT-5H	Doped Lead Zirconate Titanate
PZT	Lead Zirconate Titanate
MPB	Morphotropic phase boundary
LF	Low frequency regime
CF	Voltage – temperature conversion factor
NIRS	Near infrared spectroscopy
HbO_2	Oxyhaemoglobin
Hb	De-oxyhaemoglobin
PPG	Photoplethysmography
SpO_2	Pulse oxygenation
SaO_2	Arterial oxygenation
LTI	Linear time invariant
StO_2	Tissue oxygenation
RFID	Radio frequency identification
ECG	Electrocardiogram
GPML	Gaussian process machine learning
FSR	Force sensitive resistor
MEMS	Micro electrical mechanical systems
RTD	Resistive temperature device

ESD	Electrostatic discharge
GBP	Gain bandwidth product = closed loop unity gain frequency, $\hat{A}_v\omega_c$
ADC	Analogue to digital converter
MPB	Morphotropic phase boundary
RMS	Root mean square
CMOS	Complementary metal oxide semiconductor
PVDF	Polyvinylidene fluoride
OA	Op-amp
GPRS	General packet radio switching
DFT	Discrete Fourier transform
PSD	Power spectral density
DTI	Deep tissue injury
PID	Proportional integrator differentiator controller
DWDM	Dense wave division multiplexing
OEO	Optical electronic optical
CPU	Central processing unit

List of publications

Journal publications

1. Davidson, A, Buis, A & Glesk, I 2017, 'Toward novel wearable pyroelectric temperature sensor for medical applications', *IEEE Sensors Journal*, vol. 17, no. 20, pp. 6682-6689.
   The paper was wholly researched and written by the lead author, A.Davidson.

2. Davidson, A, Glesk, I & Buis, A 2016, 'The rising role of photonics in today's data centres', *Cuban Journal of Physics (Revista Cubana de Física)*, vol. 33, no. 1E, pp. E17-E25.
   The paper was wholly researched and written by the lead author, A.Davidson.

3. Davidson, A, Mathur, N, Glesk, I & Buis, A 2015, 'Power supply issues in e-health monitoring applications', *Renewable Energies and Power Quality Journal.* vol. 1, no. 13, pp. 733-737.
   The paper was mainly researched and written by the lead author, A. Davidson, whose contributions were the research and writing of sections 1,3 and 4.

4. Davidson, A, Glesk, I & Buis, A 2014, 'Has silicon reached its limit?', *Advances in Electrical and Electronic Engineering*, vol. 12, no. 6, pp. 590-598.
   The paper was wholly researched and written by the lead author, A.Davidson.

5. Kepak, S, Cubik, J, Zavodny, P, Siska, P, Davidson, A, Glesk, I & Vasinek, V 2016, 'Fibre optic track vibration monitoring system' *Optical and Quantum Electronics*, vol. 48, no. 7, 354.
   The paper was partly researched and written by the co-author, A. Davidson, whose contributions were the taking of preliminary measurements and carrying out a full review and rewrite of the content.

6. Hannah, S, Davidson, A, Glesk, I, Uttamchandani, D, Dahiya, R & Gleskova, H 2018, 'Multifunctional sensor based on organic field-effect transistor and ferroelectric poly(vinylidene fluoride trifluoroethylene)' *Organic Electronics*, vol. 56, pp. 170-177.
   The paper was partly researched and written by the co-author, A. Davidson. whose contributions were the force measurements described in section 3.

Conference publications

1. Davidson, A, Glesk, I, Buis, A, Wang, J & Chen, L 2014, Recent advancements towards green optical networks. in A Popiolek-Masajada & W Urbanczyk (eds), *Proc. SPIE 9441: 19th Polish-Slovak-Czech Optical Conference on Wave and Quantum Aspects of Contemporary Optics.* vol. 9441, 944117, 19th Polish-Slovak-Czech Optical Conference on Wave and Quantum Aspects of Contemporary Optics, Jelenia Gora, United Kingdom, 8/09/14.
   The paper was mainly researched and written by the lead author, A. Davidson, whose contributions were the research and writing of the sections entitled 'Introduction', 'The electronic bottleneck', 'Optical networks and bottlenecks', 'III-Nitride photonics for datacenters' and 'Conclusions'.

2. Mathur, N, Davidson, A, Buis, A & Glesk, I 2016, Tissue viability monitoring - a multi-sensor wearable platform approach. in J Müllerová, D Senderáková, L Ladányi & Ľ Scholtz (eds), *20th Slovak-Czech-Polish Optical Conference on Wave and Quantum Aspects of Contemporary Optics.* vol. 10142, 1014205, Bellingham WA, 20th Slovak-Czech-Polish on Wave and Quantum Aspects of Contemporary Optics, Jasna, Slovakia, 5/09/16.
   The paper was partly researched and written by the co-author, A. Davidson, whose contributions were the research and writing of sections 1,3 and the force measurement, methodology, and results described in section 4.

3. Mathur, N, Glesk, I, Davidson, A, Paul, G, Banford, J, Irvine, J & Buis, A 2016, Wearable mobile sensor and communication platform for the in-situ monitoring of lower limb health in amputees. in *2016 IEEE International Symposium on Circuits and Systems (ISCAS).* IEEE, Piscataway, NJ, pp. 1336-1339, IEEE International symposium on circuits and systems, Montreal, Canada, 22/05/16.

   The paper was partly researched and written by the co-author, A. Davidson, whose contributions were the research and writing of sections I and II.

4. Glesk, I & Davidson, A 2015, Terabit communications – tasks, challenges, and the impact of disruptive technologies. A Dzubinska & M Reiffers (eds), *21. konferencia slovenskych fyzikov.* Košice, pp. 1-6, 21. konferencia slovenskych fyzikov, Nitra, Slovakia, 7/09/15.

   The paper was mainly researched and written by the co-author, A. Davidson, whose contributions were the research and writing of the sections entitled ‘Introduction’, ‘IP demand’ and ‘Conclusions’.

5. Glesk, I, Buis, A & Davidson, A 2014, How photonic networking can help data centres. in M Jaworski & M Marciniak (eds), *16th International Conference on Transparent Optical Networks (ICTON), 2014.* IEEE, IEEE Explorer, ICTON 2014, Graz, Austria, 6/07/14.

   The paper was mainly researched and written by the co-author, A. Davidson, whose contributions were the research and writing of sections 1,2 and 4.

Chapter 1

Introduction

1.1 Motivation for research

The incidence of limb amputation is increasing worldwide particularly in the wealthier western nations [1]. Limb amputations result from not only trauma but also increasingly from the complications of disease. In particular, trends toward poor diet and lifestyle choices, and an ageing population in the western nations have led to an increase in the prevalence of many diseases including type-2 diabetes and ischaemic heart disease [2]. In particular, poorly managed diabetes can lead to devastating medical complications such as poor circulation leading to the amputation of digits or limbs. Diabetes has become the single biggest cause of amputation in the UK and in the US more than 90% of amputations performed are as a direct result of the circulatory complications of diabetes with up to 80% of those operations involving the lower limbs and digits [3]. While prosthetic limbs and in particular leg prostheses can restore a considerable level of freedom and improve the quality of life of the amputee, residual lower limbs are load bearing and are therefore particularly prone to injury by even a well-fitting prosthetic socket.

The use of even a well-fitting prosthesis by a healthy person and in particular by a health impaired person with a lower limb amputation can cause the development of serious tissue injuries such as pressure ulcers (decubitus ulcers, also called pressure sores) and tissue breakdown if not regularly monitored by the amputee and health authority. Injuries can start deep inside the residual limb near the bone (deep tissue injury) and/or at the surface of the skin and can affect all types of tissue including the bone [4].

Of particular concern is deep tissue injury (DTI) where the ulcer becomes apparent only when it reaches the surface of the skin and severe injury has therefore already occurred. DTI is caused when the volume of tissue in the residual limb reduces during wear, resulting in downward bone movement i.e. pistoning [5]. The downward movement of the residual limb bone may lead to boundary shear at the bone/tissue interface which may result in deep tissue injury (DTI) and the formation of ulcers that progress from the bone to the skin. Specifically, this type of injury may be caused by restricted perfusion (pressure induced ischaemia) and physical trauma caused by mechanical overload of the deep tissues [6]. In addition, forces on the skin can result in surface pressure ulcers caused by the constriction of blood flow resulting in reduced perfusion and ultimately tissue necrosis while excess temperature can cause sweating that leads to tissue maceration, friction blistering and breakdown. Pressure ulcers at the skin surface can progress from the skin surface down to the bone and are apparent by the breakdown of the skin [7]. Infection will accelerate the progression of ulcers which in extreme cases can be life threatening. Long-term hospital admission is often necessary which is both disruptive for the patient and costly to the health authority. In addition, diabetics are at increased risk due to the additional medical complications of compromised circulation, a deficit in feeling sensation at the extremities and increased risk of infection and morbidity due to infection [8]. Diabetic patients may therefore develop a pressure ulcer sooner, suffer faster progression of the ulcer and be less likely to feel the characteristic symptoms of tissue injury than a patient considered healthy.

An additional and equally important consideration is that of patient comfort while wearing a prosthesis. In particular, it is well known that the body's temperature control mechanisms are interrupted while wearing a prosthetic socket due to the

confinement of the residual limb and the low thermal conductivity of the socket and liner. The socket materials act as heat insulating barriers, leading to thermal discomfort and a reduction in the use of the prosthesis, and as a consequence a reduction in quality of life. It is well known that the temperature of the prosthetic socket environment has a significant bearing on the quality of life of amputees, both from residual limb health and comfort perspectives [9],[10]. In particular, it is suggested that raised temperature is associated with the risk of tissue maceration and infection through a combination of confined environment and perspiration. In [11] it is demonstrated that after donning a prosthesis, the residual limb/prosthesis interface temperature rises significantly during resting due to the thermal insulating effect of the prosthetic socket and liner, and rises further over a period of approximately 5 minutes when walking, the increase being dependent on anatomical location within the prosthetic socket. In [12] and [13] prosthesis wearers also report discomfort due to perceived increases in temperature while in [14], 72% of the subjects reported loss of quality of life due to excessive heat and sweating. It is perhaps surprising then that the research and development of sensor systems that allow the real time measurement of interface temperature; and in-situ systems that mitigate temperature extremes is to date sparse.

It would be of great benefit to amputees, particularly lower limb diabetics to reduce the risk of residual limb injury while wearing a prosthetic limb. Temperature and pressure measurement data obtained from monitoring at the prosthetic socket/residual limb interface can provide an early warning of an increased risk of injury and allow remedial action to be taken before actual tissue injury and potentially serious complications occur. A reliable continuous monitoring system based on skin temperature and interface pressure sensors within the prosthetic socket that can alert both the user and health authority could reduce admissions to hospital by allowing early intervention. In addition, since residual limb volume changes while wearing a prosthetic socket, the interface pressure data can be used to infer the quality of fit of the prosthesis as a function of the residual limb pressure. Other advantages are a reduction in the associated costs of treatment; improved patient quality of life and perhaps a significant reduction in the frequency of outpatient check-up appointments. In addition, the information provided by a monitoring

system on areas prone to injury can be used to inform prosthetists and contribute toward better design for an improved socket fit. Important considerations are that such a sensor and platform be unobtrusive to the wearer and be low cost to allow affordability to financially constrained health services.

As a mature technology, the extremely low cost, robustness and wide availability of commercially available acoustic transmitter devices based on piezoelectric ceramic PZT present an interesting proposition as an effective solution to the problem of identifying a suitable sensor technology. In addition, since this technology has the unique property of being able to measure both temperature and pressure changes, then using the appropriate signal conditioning configurations, the same sensor technology can be used to measure both temperature and pressure changes at the measuring site.

However, many issues arise in the design and implementation of such a sensing and data transmission system which must be both reliable and robust, not least of which is the continuing ability of ICT (information and communication technology) networks to provide the quality of service required to ensure that patient monitoring data is reliably conveyed to the relevant health authority.

1.2 Thesis objectives

The main objectives of this thesis are to investigate the use of a low cost and widely available PZT-5H piezoelectric diaphragm for use as the sensing element in a responsive sensor system for installation within a prosthetic socket to measure temperature and pressure, and to develop the necessary signal conditioning electronics to enable prolonged use over an $8\ hour$ continuous measurement period. Additional objectives are wearability, overall low cost, low power consumption, low drift and low signal decay over the measurement period. The fast response indicates that it may also be used more generally as a diagnostic support tool to measure the fast temperature changes that are symptomatic of some diseases [15],[16].

This thesis addresses the following additional objectives:

- To derive the specific governing small signal linear elastic-dielectric-thermal constitutive state equations from the starting point of the first and second laws of thermodynamics that allow a subsequent characterisation of the piezoelectric element surface temperature and applied axial pressure responses from a linear time invariant system perspective.

- To develop mathematical models for the electric field response by solving the developed state equations for a heat source/sink applied at the piezoelectric element substrate surface and applied axial stress.

- To use the sensor mathematical models to develop a Matlab based set of scripts for the thermal transient time-frequency analysis of the sensor response that may be applied more generally to any sensor design where the sensing element is configured from a transverse isotropic piezoelectric patch and isotropic/transverse isotropic substrate. The Matlab scripts allow estimation of the time dependent frequency response, phase delay and frequency dependent time-domain response.

- To develop a wearable, low voltage single supply unipolar charge-mode signal conditioning design(s) for use with the piezoelectric element. The necessary specification requires a very long time constant to allow a continuous use of several hours, low drift, low power consumption and the ability to be powered by an Arduino platform $+5V$ on-board regulated power supply.

- To investigate problems with the quality of service of remote e-Health monitoring due to pressures placed on ICT systems caused by unsustainably increasing power consumption, rapidly increasing data throughput demand and fundamental physical limitations on the processing speed possible using the ubiquitous CMOS technology.

1.3 Thesis outline

This thesis presents research into the application of commercially available and inexpensive PZT elements as highly responsive temperature and pressure sensors specifically for application as wearable sensors mounted within the environment of a prosthetic socket, and for medical applications in general. While this research concentrates specifically on temperature sensing, a theoretical treatment that presents solutions for the measurement of an applied normal stress at the skin/prosthetic socket boundary is also completed, the ultimate aim being the application of piezoelectric technology to the measurement of both temperature and stress.

Chapter 2 introduces the main background and principles of piezoelectricity and specifically the PZT piezoelectric material used in this thesis. Chapter 3 describes the development of the governing small signal linear coupled elastic-dielectric-thermal equations in stress-charge form, which are derived from the starting point of the first and second laws of thermodynamics and the electric Gibbs free energy thermodynamic potential. From the developed constitutive state equations, the coupled elastic-dielectric-thermal heat diffusion equations are derived for both the piezoelectric and substrate media. The resulting state equations allow the subsequent characterisation of the piezoelectric element surface temperature and applied axial pressure responses in terms of a linear time invariant perspective.

Chapter 4 describes the frequency and Laplace domain solutions of the governing Equations for the relevant specific boundary conditions that allow the investigation of the response characteristics for the PZT-5H sensor element. The solutions form a set of general elastic-dielectric-thermal mathematical models that are later used to investigate the sensor response to a temperature change and/or applied axial stress. The mathematical models developed are general such that they may be applied as a design tool for general application to other transverse isotropic piezoelectric and isotropic substrate material combinations. Chapter 5 describes the investigation of the piezoelectric device via immittance measurements that indicate the dependency of the piezoelectric material constants over the temperature range of interest. This investigation yields the identification of the most appropriate method of signal conditioning. In Chapter 6, the design of three and construction of two signal-conditioning amplifier circuits is presented. The designs realise the time constant,

very low drift and low power consumption specifications required for both the experimental analysis and as part of a portable battery operated wearable sensor system. The amplifier output is interfaced with an Arduino based platform to allow transmission of the sensor signal data to an external database and smartphone. Chapter 7 describes the time-frequency response at the signal-conditioning output to a surface temperature measurand applied at the sensor element substrate and via a polymer liner. The time-frequency analysis allows the thermal effects of the sensor element and signal-conditioning decay on the temperature measurand to be predicted. Finally, in Chapter 8 potential threats to data transmission through ICT systems are discussed to identify possible serious limitations to e-Health data transmission and processing in the near future.

1.4 Approaches to reading the thesis

The thesis may be read in order of chapter 1 through chapter 9 for a comprehensive description of all aspects of the research undertaken. Chapter 8 is self-contained and may be read in isolation for readers interested only in the treatment of future threats to the quality of service in e-health delivery. On the other hand, readers interested only in the central application of PZT for temperature and pressure sensing can omit chapter 8 together with the introductory chapters 1 and 2. Chapter 3 is also self-contained and may be read in isolation for readers interested only in the derivation of the constitutive state equations.

Chapters 4 and 5 are mostly self-contained and may be read in isolation for readers interested only in the PZT sensor element response models and effect of temperature on the response, respectively. However, the constitutive equations derived in chapter 3 are applied in both chapters and it is therefore recommended that the results of chapter 3 are familiar before reading chapters 4 and 5. Chapter 6 can be read in isolation for readers interested only in the method and design of the signal conditioning circuits. On the other hand, chapter 7, which details the experimental and theoretical pyroelectric responses of the PZT sensor and signal conditioning system, is a natural progression of chapters 4, 5 and 6. It is therefore recommended

that these chapters be read together before reading chapter 7. A roadmap describing the main content and findings of each chapter is given in Table 1.1.

Chapter	Content and main findings
1. Introduction	States the motivation and contributions of the research, gives a thesis outline and defines the thesis objectives.
2. Research background	Derives from first principles the set of small signal constitutive state equations and heat diffusion equations necessary to describe the PZT diaphragm response to an applied surface temperature and axial stress.
3. Equations of state	Derives from first principles the set of small signal constitutive state equations and heat diffusion equations necessary to describe the PZT diaphragm response to an applied surface temperature and axial stress.
4. Sensor response modelling	Discusses the PZT diaphragm and proposed mounting configuration, derives models describing the electric field response, and the piezoelectric & substrate spatial mean temperature responses to both an applied substrate surface temperature and via an elastomer liner of various thicknesses. Defines the equivalent circuit model and the physical nature of the measured charge. The substrate is found to increase the pyroelectric response by 180%. The effect of the PZT/brass substrate adhesive on the sensor element response is found to be negligible.
5. Temperature dependence of Clamped and LF immittances	Investigates experimentally the effect of temperature on the equivalent capacitances of the PZT sensor diaphragm. Both the electrically and mechanically derived capacitances are found to be strongly temperature dependent over the $20°C$ to $40°C$ measurement range.
6. Signal conditioning and e-Health platform	Presents charge-mode signal conditioning designs and identifies these as mitigating the effect of the temperature dependence by greatly reducing the influence of the capacitances on the response. Unipolar and bipolar designs are presented and it is found that a reduction in the resistivity of the PZT diaphragm can reduce the time constant of the amplifiers. Presents a rigourous noise analysis of the bipolar design. The forward gain stage is found to contribute by far the greatest noise to the total noise at the output. The e-Health platform is presented and it's operation described.
7. Sensor pyroelectric response	Introduces decay compensation and Padé approximant methods and applies these to investigate experimentally and theoretically the sensor response to a temperature change using charge mode signal conditioning. The response is found to be linear over the $20°C$ to $40°C$ measurement range and the measured pyroelectric response is found to agree well with the theoretical response discussed in Chapter 4. The transient time-frequncy response simulations predict a flat amplitude and phase response over wide time and frequency ranges when temperature is measured directly via the substrate surface.
8. ICT limitations to e-Health	Discusses possible future threats to e-health quality of service due to ICT limitations in the face of increasing demand, limitations to CMOS scaling, interconnect scaling and increasing power consumption that have lead to latency and electronic bottlenecks. Discusses possible short term and long term solutions via the latest developments in CMOS technology and all-optical computing, respectively.
9. Conclusions and future work	Discusses and juxtaposes the individual chapter conclusions and discusses future work.

Table 1.1 Roadmap of thesis chapters

1.5 Thesis contributions

- Rigorous development of temperature and axial pressure sensor models of piezoelectric with substrate devices from a dielectric-thermal-elastic coupled thermodynamics perspective. The models developed allow the description and simulation of the sensor frequency-response behaviour. The models indicate that both temperature and pressure changes can be measured using the same sensor technology. This investigation also demonstrated a non-negligible reduction in the heat diffusion coefficients or diffusivity of the piezoelectric and substrate media due to the dielectric-thermal-elastic coupling.

- Development of Matlab analysis scripts based on the Padé approximant method that are used to determine the time-frequency amplitude, phase and phase delay response to an applied surface temperature. These scripts may also be used more generally in the design of piezoelectric pressure and temperature sensor devices with a piezoelectric and substrate media design configuration for time-frequency analysis to estimate the time dependent frequency response, range of phase linearity and time-domain response.

- Development of a wearable, portable, and low voltage single supply unipolar charge mode signal conditioning designs for use with piezoelectric sensing devices, having the features of long time constant, low drift, enhanced open loop gain, fast rise time, low power consumption and the ability to be powered from an Arduino platform $+5V$ on-board regulated power supply.

- Investigation into the electrical field response of a piezoelectric element to a surface temperature change demonstrates a fast response to a change in temperature and linearity in the response over the temperature range of interest using charge-mode signal conditioning. In addition it is demonstrated theoretically and confirmed experimentally that the response observed is greatly enhanced by the presence of the metallic substrate through which the temperature is measured.

- The demonstration of possible future problems with the quality of service of remote e-Health monitoring due to pressures placed on ICT systems caused by unsustainably increasing power consumption, rapidly increasing data throughput demand and fundamental physical limitations on the processing speed possible using the current CMOS technology.

Chapter 2

Research background

2.1 Introduction

The discussion in Section 1.1 clearly indicates that there is a growing need for in-situ prosthetic socket e-health monitoring sensor systems. This chapter starts with a literature review of the current state of the art of both e-health sensors in general and prosthetic socket sensors in particular. Section 2.2 describes the state of the art developments in commercial and experimental e-Health technology in general, while Section 2.3 describes more specifically the currently available commercial and the experimental sensor technologies designed for application within a prosthetic socket to improve the fit and ultimately the quality of life for the wearer. The selection of the appropriate sensor technology against specific requirements is discussed in Section 2.4, while the required specification of the sensor is discussed in Section 2.5. The underlying background theory and basic constitutive state equations of the selected technology, and the principles applied in the development of the sensor are discussed in Section 2.6 and Section 2.7.

2.2 E-Health sensors – state of the art

With the advent of demand for commercially available devices for monitoring health and fitness, companies like Apple, Asus, Fitbit, Garmin and Huawei among others have been marketing wearable 'fitness tracker' devices that allow some parameters to be automatically and continuously recorded.

The most common parameters measured are heart rate, steps taken, calories burned, body core temperature, arterial oxygenation and the tracking of sleep patterns. Recent developments have been the introduction of a fitness tracker by Asus that can also measure blood pressure by touching a sensor on front of the device, and an ECG (electro-cardiogram) waveform-measuring device by Moov that monitors heart health and that can detect atrial fibrillation and send the measured data to the user's doctor. The 'Heartguide' smart watch device by Omron released in 2019 allows continuous monitoring of blood pressure using an oscillometric technique that uses a cuff to measure arterial wall vibrations when a skin-cuff interface pressure of between the systolic and diastolic blood pressure values is applied by the cuff over an artery. Retrieval of the values of diastolic and systolic pressures is achieved by analysis of the measured vibrations. This device also records daily activity measurements such as steps taken, calories burned and distance travelled. However, discomfort caused by the cuff may preclude continuous use over extended periods.

The use of wearable medical e-health devices allows the remote monitoring of vital signs and the health status of patients over a suitable period of days or weeks without the requirement of routine attendance at healthcare facilities. By allowing the appropriate vital sign monitoring over an extended period during daily activity, rare cardiac or other events can be observed that could otherwise be missed, and a richer body of data can be collected than with a single visit to a healthcare facility. Such a monitoring system thus facilitates improved disease diagnosis, adjustment of medication, reduced recovery rates after treatment, and a general improvement in patient care and quality of life. There is presently intense interest in the development of wearable medical e-health devices that allow continuous monitoring of a wide range of vital signs for assessment by health professionals. In the literature, transmission of the measured data to the health facility is commonly achieved by

interfacing the sensor data streams to a smartphone app using Wi-Fi, Bluetooth, ZigBee, which uses the IEEE 802.15.4 communication standard, or other wireless technology. The measurement data is streamed in real-time via GPRS (general packet radio switching) or Wi-Fi to the health facility or is stored on-board for later transmission.

The core vital signs that give an indication of clinical deterioration and that are the most important to continuously monitor are suggested in [17]. These are body temperature, heart rate, blood pressure, arterial oxygenation and respiration rate. Other desirable vital signs highlighted are ECG used to indicate cardiac health, blood glucose level used to determine metabolic rate and monitor diabetic patients, and perspiration rate. Additional vital signs that are identified to be of immediate importance when the patient is considered to be in danger are capnography (CO_2 in exhaled respiration gases) and stroke volume [18].

Heart rate monitoring using a miniature accelerometer and signal conditioning package is described in [19], however the measured heart rate data is found to be prone to motion artefacts and the method is therefore less reliable than the more easily accomplished extraction of the heart rate using photoplethysmography (PPG) or ECG data [20]. In contrast to the 'Heartguide' smart watch device by Omron described above that requires the use of a cuff, a cuff-less blood pressure monitoring method using a modified oscillometric technique is demonstrated in [21] where a PPG signal, which is related to volumetric changes in blood, is measured over an artery. The volumetric changes extracted from the PPG signal are in turn related to the arterial blood pressure by a non-linear relationship [22] allowing an unobtrusive and continuous measurement of arterial blood pressure. Respiratory rate is often neglected but is never the less considered an extremely important vital sign for the detection of serious respiratory problems [23], [24], [25]. In [26] a prototype wearable respiratory rate sensor has been developed that uses a garment made of a piezo-resistive fabric to measure volume changes in the abdomen and chest. It is demonstrated that the sensor produces good accuracy when compared to a standard piezoelectric respiratory belt. A piezoelectric respiratory belt operates on the well-established principle of elastomeric plethysmography where an elastic belt applies a force to piezoelectric sensing elements producing an output voltage in

response to changes in volume. In [27] a vest for use by soldiers was developed to measure respiratory rate, providing some insight into the mental state of combatants. The vest uses the principle of impedance plethysmography where the electrical impedance of the body changes due to breathing induced expansion and contraction of the chest and abdomen.

Arterial blood oxygenation measurement using PPG has been commonplace in clinical environments for many years. PPG is an optical technique using for example near infrared spectrometry (NIRS) to measure blood oxygen saturation, heart rate blood volume and that, as described above, can also be used to measure changes in blood pressure. The application of NIRS to the human body was first developed in the 1970's for the invasive monitoring of cerebral and cardiac oxygenation, and for chemical analysis of blood taken from the patient [28]. NIRS is an optical method of illuminating blood borne compounds that absorb, reflect, and scatter light. For arterial oxygen saturation and heart rate measurements, the targeted blood factors are oxyhaemoglobin (HbO_2) and deoxyhaemoglobin (Hb). Since oxyhaemoglobin carries nearly all the oxygen in the blood stream, measurement of these factors allows the estimation of blood oxygen saturation by a non-invasive, low-cost and intrinsically safe method. The PPG waveform is comprised of a pulsatile AC waveform produced in response to changes in blood volume with each heartbeat and super-imposed on a slowly varying DC baseline produced by the absorption of light in veinous blood and tissues. PPG is used in pulse oximeters where the pulsatile AC part of the PPG waveform is used to give the SpO_2 (pulse oxygen) saturation and also the heart rate. The SpO_2 measurement closely approximates the arterial blood oxygen saturation denoted by SaO_2 and gives an indication of how well the heart and lungs are functioning. The most common method of SpO_2 measurement is by using a finger-probe pulse oximeter that measures the PPG waveforms by alternately transmitting two frequencies of NIR light using two LEDs at frequencies of $660nm$ and $940nm$ through a finger or earlobe to a photodiode. At $940nm$, HbO_2 absorbs more light than H_b and conversely at $660nm$, H_b absorbs more light than HbO_2. The two PPG waveforms received by the photodiode are then used to infer the blood oxygen saturation. In [29] a finger ring pulse oximeter is presented that it is claimed can be comfortably worn

for extended periods and is suitable for the diagnosis of sleep apnoea disorders. A multi-channel chest mounted reflectance mode pulse oximeter is demonstrated in [30] that measures the light reflected from the body rather than the light transmitted through a finger or earlobe, allowing greater flexibility in the choice of site and improvement in comfort while wearing the device. The wearability of the device over extended periods is demonstrated to facilitate its use in the diagnosis of sleep apnoea disorders. In [31] the development of a reflectance mode oximeter allows the measurement of local tissue oxygenation (StO_2) that can be used to diagnose tissue ischaemia, which is more common in diabetic patients. Under controlled conditions the measurement of StO_2 is found to correlate well with the gold standard method but is shown to be susceptible to error due to corruption by motion artefacts.

In [32] two skin temperature sensors, one based on arrays of pin diodes on a flexible substrate and the other based on arrays of serpentine with traces made of gold each $50nm$ thick by $20\mu m$ that rely on the temperature coefficient of resistance of the material are presented. It is demonstrated that the serpentine sensor response correlates well with the response of a high quality infrared temperature sensor, while the frequency responses show coincidental temperature peaks at $0.01Hz$ and $0.04Hz$ but with significant differences around $0.07Hz$. Low frequency skin temperature oscillations are identified as correlating with tissue blood flow and as such the monitoring of skin temperature is suggested as having value in the diagnosis of diseases such as congestive heart disease and tissue hypoxia in addition to serving as a marker for other disease processes [33]. In [34] a wearable and battery-less epidermal thermometer for continuous core body temperature measurement that uses a radio frequency identification (RFID) module and reader with Bluetooth connectivity suitable for skin contact is presented. It is reported that by placing the sensor under the arms or on the chest, an accurate measurement of body core temperature with a constant error of $0.6°C$ is achieved.

The use of ECG measurements is of vital importance in the diagnosis of cardiovascular diseases such as angina, artherosclerosis and atrial fibrillation among others. Many wearable ECG devices that include sensors integrated into textiles have been described [35],[36],[37],[38],[39]. A wearable device for continuous measurement over extended periods allows the early detection and treatment of such

diseases. A prototype wearable ECG sensor based on a capacitive technique that avoids direct contact with the skin is proposed in [39]. The capacitive electrodes and associated signal conditioning and transmission printed circuit board are integrated into a conventional cotton T-shirt. The system is reported to include signal processing to mitigate motion artefact, to be thin, of small size and have low power consumption. It is demonstrated that the measurement traces correlate well with those produced by a conventional wet electrode device.

Blood glucose monitoring is critical to the health of diabetics. The joint development of an eye contact lens by Novartis and Google that has an integrated sensor for analysing tears to give a measurement of blood glucose levels was announced in 2014 [40]. However, to date no commercially available device has been announced from this joint development. A wearable and commercially available blood glucose measurement system developed by EyeSense (FibreSense) is appraised in [41]. The EyeSense device operates using the principle of fluorescence. The glucose concentration of tissue fluid, which correlates to blood glucose concentration, is measured using an optical fibre with a biosensor embedded in hydrogel which is attached to the fibre tip. The biosensor reacts specifically to glucose but must be implanted at a depth of $2mm$ into the skin to operate. The device was tested by being worn on the upper arm over a 14 day period and is reported to provide consistently reliable measurements of subcutaneous glucose levels over the test period. While consistent performance and reliability is reported, a disadvantage of this system is that it is mildly invasive, requiring that the sensor be implanted under the skin. A wearable glucose monitoring system developed by Nemaura medical is currently due for release in 2019 [42]. The SugarBEAT® device operates by passing a low current through the skin, the action of which draws a small amount of glucose from tissue fluids just under the skin. The glucose is then deposited on a patch within a chamber for measurement. The patch is disposable and is replaced on a daily basis. The glucose measurement device transmits the measured glucose level to a smartphone app via Bluetooth every $5\,minutes$ for continuous blood glucose monitoring. The principle of operation is not disclosed but unlike the EyeSense device and other similar devices by Abbott Libre and Dexcom that require needles or sensors to be implanted, the SugarBEAT device is truly non-invasive. The

device has achieved CE (European Conformity) approval in the European community with further clinical trials planned to gain approval for use in critical care settings and for Federal Drug Administration approval in the United States.

2.3 Prosthetic socket sensors - state of the art

Although research into the development of sensor technologies for monitoring within the prosthetic socket have been under investigation since the 1960's [43],[44], there are currently no commercially available prosthetic socket mounted sensor systems for continuous and real time monitoring of patients during daily activities. It is well known that knowledge of residual limb skin temperature and skin-socket interface pressures are important in determining residual limb health and assessing the risk of injury [45],[46],[47]. However, prosthetic socket/residual limb interface pressure sensing research to date has mainly concentrated on providing prosthetists with a measure of the pressure distribution at the socket/residual limb interface during the assessment and fitting stages to improve socket fit and comfort.

In [48] a prediction method based on a Gaussian processes for machine learning (GPML) approach is used to predict the residual limb skin temperature by measuring the temperature at the liner-prosthetic socket interface. The machine learning process is accomplished by measuring the temperature at both the liner/socket interface and skin surface using thermocouples. In [49] a prototype temperature regulation system has been developed based on a diode temperature sensor array and a heat pump. This system uses a thermoelectric Peltier device, fan and heatsink for thermoregulation that allows both heating and cooling within the prosthetic socket with the aims of reduced sweating and the maintenance of a comfortable environmental temperature within the prosthetic socket. However the system that has been developed is bulky and has not undergone clinical trials to date. The most common technologies reported in the literature for measuring socket/residual limb interface pressures are FSR (force sensing resistor using the piezo-resistive effect), piston type SG (strain guage), capacitive, and optical fibre based systems. Utilising the principle of piezo-resistivity, force sensing resistor

(FSR) technology is commonly used for assessing socket fit with the Tekscan F-socket and Rincoe SLS systems that measure pressure at the residual limb/socket interface using a flexible multi-sensor FSR strip technology being the most widely used systems [50]. However these systems are not wearable and therefore cannot provide real time information of interface pressures in everyday use. Furthermore, in [51] and [52] large accuracy errors have been reported with these systems due to significant signal drift, hysteresis and problems associated with calibration. Additionally, both systems exhibited significant deterioration in the FSR sensor strips over a 3-month period. In [53] a fibre Bragg grating prosthetic socket pressure sensor is described as durable with sufficient sensitivity and low hysteresis error, while a piezo-resistive bubble sensor based on MEMS technology is demonstrated in [54]. The bubble sensor is found to have good drift characteristics compared to the authors capacitive and strain sensor comparisons but to suffer from poor hysteresis characteristics that are suggested by the authors as attributable to the sensor silicone encapsulation material.

In [55], a comparison of pressure sensor types under conditions of cyclic loading is reported: two FSR sensors by Tekscan (Flexiforce) and Interlink, a capacitive sensor by Pressure Profiles Systems, a bubble liquid pressure sensor by Sandia (as described above), and an optical sensor that measures reflected light intensity through a transparent elastomer, also by Sandia. The Sandia optical and bubble sensors have integrated signal conditioning electronics while the Pressure Profiles System sensor is supplied with the necessary signal conditioning electronics and the Tekscan and Interlink sensors were used with signal conditioning amplifiers recommended by the manufacturer.

The capacitive sensor was found to exhibit adequate sensitivity, linearity and hysteresis performance but to have the poorest drift characteristics, while the Interlink FSR exhibited substantial nonlinearity, drift and hysteresis under dynamic loading. The Flexiforce FSR suffered from a severe reduction in sensitivity over the trial period, reducing to almost zero after several tests while the Sandia optical sensor exhibited some hysteresis and substantial drift. The bubble sensor was found to have the best overall performance with the lowest drift and hysteresis characteristics

compared to the other sensor types, but with the disadvantages compared to the others of having a greater thickness profile and not being commercially available.

2.4 Choice of sensing technology

2.4.1 Initial observations

The discussion of Section 2.3 highlights the need for, and the lack of commercially available in-situ prosthetic socket mounted sensor systems, and describes some of the shortcomings of the technologies discussed. These shortcomings present a potential barrier to the development of a reliable, robust, and commercially available solution. This undesirable status quo is therefore at least in part due to the unsuitability of currently available methods of measurement to the application of in-situ temperature and pressure monitoring within a prosthetic socket. The following discussion defines the desired characteristics for a prosthetic mounted sensor technology, compares the various currently available technologies, and discusses the disruptive application of a well known mature technology as a solution.

2.4.2 Required characteristics

To identify suitable sensor technologies for temperature and pressure measurement within the confines of a prosthetic socket, consideration was given to several commercially available candidate sensor technologies by comparing them against a checklist of the constraints listed below.

- For temperature sensing, to exhibit no or very low self-heating at the sensor site.
- Require no temperature reference.
- Exhibit a response fast enough to faithfully track temperature changes.
- Present a low thickness profile at the sensor site.
- Be portable and operate from a $5V$ low current rating power supply.

- Have low power consumption and require minimal wiring.
- Be low cost, rugged and exhibit linearity, low hysteresis, low drift and repeatability.

2.4.3 Candidate sensor technologies

Thermocouples are rugged, inexpensive and are self-powered, however the requirement of a stable reference temperature is problematic for a wearable sensor that will be exposed to a constantly changing environment. The cold junction compensation method requires the measurement of temperature by another method, increasing cost, weight and complexity. Resistive temperature detectors (RTD) are more stable than thermocouples and provide a high degree of accuracy and linearity. In addition, RTDs are also available with a low thickness profile where the device construction consists of a thin film of conductor deposited on a ceramic substrate. However, RTDs are expensive, fragile and have relatively high power consumption. In addition, they require a current source and are prone to inaccuracy due to self-heating. Thermistors are relatively inexpensive in comparison to RTDs but are prone to the same disadvantages, in addition to exhibiting a non-linear response and having a thicker profile. As discussed in Section 2.3, commercially available pressure sensors used for interface pressure measurements are mainly based on the FSR principle of piezo-resistance where the resistance of the sensor material varies with an applied stress [56]. While this method is used in practice to measure pressure at the residual limb/prosthetic socket interface, FSR sensors exhibit nonlinearity, drift, self-heating and hysteresis under dynamic loading and in addition have high power consumption. While capacitive sensing offers the linearity and low hysteresis characteristics required, it exhibits poor drift characteristics.

2.4.4 PZT sensors

In light of the shortcomings of the sensor technologies discussed in Section 2.4.3, detailed consideration was given to the utilisation of the pyroelectric effect inherent in Lead Zirconate Titanate (PZT). The pyroelectric effect is already widely

used in pyrometry for remote temperature sensing, infrared imaging and motion detection [57], [58] and [59]. When operated within their linear response regime, that is where signals are small enough such that the response is directly proportional to an applied stimulus, PZT devices provide an interesting proposition as they satisfy all of the requirements discussed in Section 2.4.2. PZT devices are widely used for sensor, resonator and actuator applications and have, among their advantages, relatively large piezoelectric and pyroelectric constants, high Curie temperature and low cost.

In particular, as a sensor the PZT devices are self-powered, do not self-heat, are inexpensive, are rugged and have a low thickness profile. In common with all pyroelectric and piezoelectric devices they exhibit dielectric loss which at low frequency and DC is due to dielectric leakage currents [60]. These leakage currents mean that piezoelectric devices cannot strictly speaking be used for true DC temperature measurements. The DC and low frequency signal response voltage decays exponentially with a time constant equal to RC where R and C are the equivalent leakage resistance and low frequency capacitance of the device respectively. However, in tandem with the appropriate signal conditioning design, it is possible to realise very long time constants, making it possible to measure pseudo-static and continuous low frequency temperature variations about a mean.

The ultimate aim is to find a very low cost solution that in tandem with the appropriate signal conditioning will serve the dual purpose of measuring both residual limb temperature and interface pressure using the same technology. A crucial advantage of using ferroelectric materials such as PZT is that in addition to temperature, this technology is equally suitable for measuring interface pressure via the direct piezoelectric effect where an electric field and/or electric displacement charge are generated in response to an applied stress. This is of particular interest as in common with temperature, interface pressure is also clinically accepted as affecting tissue health and is implicated in the development of decubitus ulcers [61]. A low cost prototype temperature sensor based on the pyroelectric effect has been designed to provide continuous measurement of temperature within a prosthetic socket. In operation, it is envisaged that the sensor would be recessed into the socket wall using a compliant adhesive to allow free thermal expansion and to avoid erroneous responses due to strains induced by socket flexing. An extension to

simultaneous measurement of temperature and pressure at the same site is possible by modification of the PZT sensor element and signal conditioning system and this will be discussed further in Section 4.3.

2.5 Basic sensor specification

A preliminary specification set at the beginning of this research is that the sensor must operate over an $8\ hour$ period with no more than a 2% signal amplitude decay over this period. The period of $8\ hour$s was chosen based on a reasonable estimate for the length of time a prosthetic socket may be used, while a 2% signal decay specification over this period was chosen to limit phase distortion such that the sensor response adequately represents the actual temperature signal. The 2% signal decay specification also ensures that no amplitude error occurs when using an $8-bit$ digital to analogue converter (ADC) such as that used on the sensor platform.

2.6 Piezoelectricity

2.6.1 Background

The term ‘piezoelectricity’ derives from the Greek language and means ‘electricity from pressure’. This definition describes the direct effect where an applied stress produces an electric charge on the surface of solid materials such as tourmaline, quartz, some ceramics, and even bone and some proteins. The Greeks are believed to have first observed the phenomenon of piezoelectricity over 2000 years ago, however the discovery of the direct piezoelectric effect is attributed to the French physicists Jacques and Pierre Curie who first demonstrated in 1880 that the direct piezoelectric effect is present in several materials including Rochelle salt, tourmaline, quartz, topaz and cane sugar. The Curie brothers demonstrated that among the materials they studied, Rochelle salt exhibited the greatest response.

While the Curie brothers used their discovery to invent the piezoelectric quartz electrometer, piezoelectricity did not come into widespread use until the invention of sonar based on piezoelectric quartz transducers during the First World

War. Quartz remains an important piezoelectric material today and is widely used in accelerometers and timing oscillators. Further research and development led to the discovery of ferroelectric materials, in particular Barium Titanate that was used to develop sonar transducers during the Second World War. Further research subsequently lead to the development of the Lead Zirconate Titanate (PZT) materials, which exhibit relatively high piezoelectric and pyroelectric coefficients and are widely used and important materials today. Modern devices that use PZT include in-ear headphones, mobile phone ringers, and ultrasound scanners for medical and non-destructive structural testing applications.

All materials that exhibit the piezoelectric effect such as quartz, or that can be made to exhibit the piezoelectric effect such as the ferroelectric materials Barium Titanate and Lead Zirconate Titanate are subsets of the general set of dielectric materials. Figure 2.1 illustrates the material relationship hierarchy.

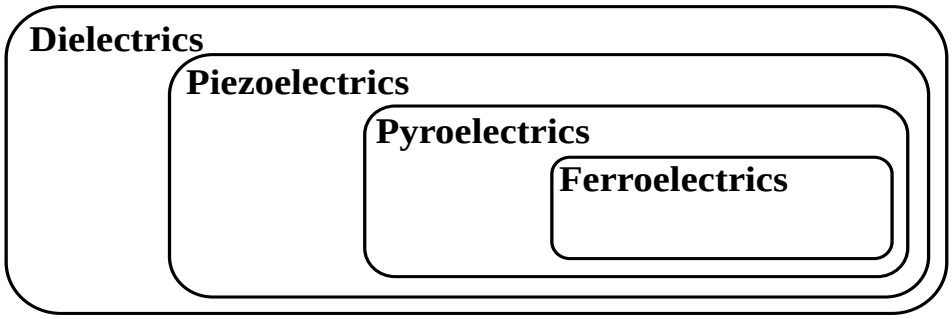

Figure 2.1 Venn diagram of the material class set hierarchy

Figure 2.1 shows that within the proper superset of dielectric materials there exist proper subsets of materials that have the following relationships: All ferroelectric materials exhibit pyroelectric, piezoelectric and dielectric behaviour; all pyroelectric materials exhibit piezoelectric and dielectric behaviour, but are not necessarily ferroelectric; and all piezoelectric materials exhibit dielectric behaviour, but are not necessarily ferroelectric, and do not necessarily exhibit pyroelectric behaviour.

The piezoelectric effect occurs in 20 out of the 32 crystal classes and is associated with a non-centrosymmetric crystal structure such that a spontaneous polarisation exists in the unit cell crystal. For materials such as quartz that occur naturally, the inherent piezoelectric effect exhibited is due to the crystalline

structure of the material. However, for manufactured materials like ferroelectric PZT, while there is a spontaneous polarisation in the unit cell, there is no net polarisation due to the random alignment of domains. The piezoelectric effect is imparted by 'poling' the ferroelectric material using an applied electric field that is sufficiently high to align the domains, producing a net remanent polarisation that remains after the electric field is removed. The effect of poling is discussed further in Section 2.7.

2.6.2 Basic isothermal constitutive equations

Under small signal conditions, the linear theory of piezoelectricity for the independent variables of stress and electric displacement is described by the well-known coupled set of matrix constitutive equations given by Equation 2.1 and Equation 2.2 using matrix-vector notation and assuming isothermal conditions such that no temperature change or flow of heat takes place.

$$\boldsymbol{T} = \boldsymbol{c}^{E,\Delta\theta}\boldsymbol{S} - \boldsymbol{e}^{t,\Delta\theta}\boldsymbol{E} \tag{2.1}$$

$$\boldsymbol{D} = \boldsymbol{e}^{\Delta\theta}\boldsymbol{S} + \boldsymbol{\varepsilon}^{S,\Delta\theta}\boldsymbol{E} \tag{2.2}$$

where all terms in Equations 2.1 and 2.2 are matrices or column vectors as described in [62], $\boldsymbol{T}$ is the stress vector (Nm^{-2}), $\boldsymbol{c}^{E,\Delta\theta}$ is the stiffness matrix, S is the strain vector (m/m), $\boldsymbol{e}^{\Delta\theta}$ is the piezoelectric stress-charge coefficient matrix (Cm^{-2}), $\boldsymbol{E}$ is the electric field vector (Vm^{-1}), $\boldsymbol{D}$ is the electric displacement vector (Cm^{-2}) and $\boldsymbol{\varepsilon}^{S,\Delta\theta}$ is the constant strain permittivity matrix (Fm^{-1}). The superscripts $\Delta\theta$, E and S indicate measurement under isothermal conditions, measurement at constant electric field, and measurement at constant strain respectively while the superscript t indicates transpose matrix. To reduce notation, it is customary to omit the superscript $\Delta\theta$ in the literature and this will be applied henceforth in this thesis, it being understood that all constants are measured under isothermal conditions such that the temperature change $\Delta\theta$ is constant.

With matrix transformation and substitution, Equations 2.1 and 2.2 can be described in a further three alternative and entirely equivalent forms, each pair

derivable from the other using matrix manipulation and each having different dependent and independent variables. The set of four formulations are given by Equations 2.3 to 2.10.

$$\boldsymbol{T} = \boldsymbol{c}^{E}\boldsymbol{S} - \boldsymbol{e}^{t}\boldsymbol{E} \qquad (2.3)$$

$$\boldsymbol{D} = \boldsymbol{e}\boldsymbol{S} + \boldsymbol{\varepsilon}^{S}\boldsymbol{E} \qquad (2.4)$$

$$\boldsymbol{S} = \boldsymbol{s}^{E}\boldsymbol{T} + \boldsymbol{d}^{t}\boldsymbol{E} \qquad (2.5)$$

$$\boldsymbol{D} = \boldsymbol{d}\boldsymbol{T} + \boldsymbol{\varepsilon}^{T}\boldsymbol{E} \qquad (2.6)$$

$$\boldsymbol{T} = \boldsymbol{c}^{D}\boldsymbol{S} - \boldsymbol{h}^{t}\boldsymbol{D} \qquad (2.7)$$

$$\boldsymbol{E} = -\boldsymbol{h}\boldsymbol{S} + \boldsymbol{\beta}^{S}\boldsymbol{D} \qquad (2.8)$$

$$\boldsymbol{S} = \boldsymbol{s}^{D}\boldsymbol{T} + \boldsymbol{g}^{t}\boldsymbol{D} \qquad (2.9)$$

$$\boldsymbol{E} = -\boldsymbol{g}\boldsymbol{T} + \boldsymbol{\beta}^{T}\boldsymbol{D} \qquad (2.10)$$

where $\boldsymbol{s}$ is the mechanical compliance which is the matrix reciprocal of the stiffness $\boldsymbol{c}$, $\boldsymbol{d}$ is the strain-charge constant, $\boldsymbol{h}$ is the stress-voltage constant, $\boldsymbol{g}$ is the strain-voltage constant and $\boldsymbol{\beta}$ is the matrix reciprocal of the permittivity. For harmonic excitation, all constants are in general complex and the most appropriate choice of independent variables is specific to the problem under consideration. The superscripts E, D, S and T indicate a term that is evaluated at constant electric field, electric displacement, constant strain or constant stress respectively.

The existence of the electro-caloric and piezo-caloric effects infer that under isothermal conditions the application of an electrical or mechanical stimulus must induce a flow of heat into or out of the piezoelectric medium such that there is a net increase or decrease in the entropy of the piezoelectric medium respectively. For all four forms of the piezoelectric constitutive equations given by Equations 2.3 to 2.10, a third constitutive equation exists that describes this effect. Adiabatic conditions can be assumed when the piezo-caloric and electro-caloric effects are small enough such that any heat flow can be neglected. The Heckmann diagram that describes the full piezoelectric thermal-elastic-dielectric interactions for the stress-charge-entropy dependent variables form of the constitutive equations is shown in Figure 2.2 where Σ and $\Delta\theta$ denote a change in entropy density and temperature respectively. The arrows on the diagram indicate the direction of cause to effect of the variables connected while keeping all other constitutive equation variables constant.

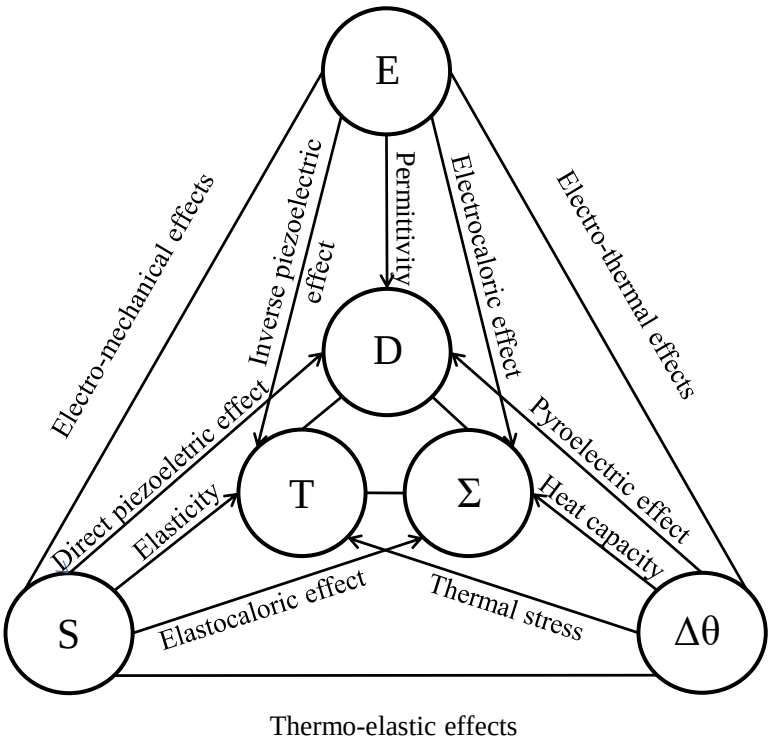

Figure 2.2 Heckmann diagram for the stress-charge-entropy constitutive form adapted from [63]

2.6.3 Validity of the constitutive equations

Equations 2.3 to 2.10 are valid under isothermal conditions and for small signal excitation where the piezoelectric material operates within the linear regime. The linear regime requires that the material can be considered to obey Hooke's law and behave as a linear dielectric where the strain, stress, electric field and electric displacement have a mutually linear relationship such that the elastic and electric coefficients in addition to the piezoelectric coefficients are considered constant over the small signal range. This small signal approximation is assumed throughout this thesis. In addition, the assumptions of 'quasi-static' and 'electrostatic' conditions are applied unless otherwise stated. The assumption of 'quasi-static' conditions is valid for the DC and low frequency mechanical or electrical excitation and requires that the acoustic wavelength of the mechanical disturbance in the piezoelectric medium and substrate are very much greater than the dimensions of the piezoelectric medium. The validity of assuming 'electrostatic' conditions requires that the frequency of the

electric field in the piezoelectric medium due to a mechanical disturbance is sufficiently low such that the effect of the rate of change of the magnetic field due to the rate of change of currents can be neglected. The condition of 'quasi-static' validity is assumed where appropriate and 'electrostatic' validity is assumed throughout.

2.7 PZT materials

2.7.1 PZT crystalline structure

The crystalline structure of PZT for all proportions $(1 - \mathrm{x}) \times 100\%$ of Lead titanate above the Curie temperature, which is denoted by θ_c, is shown in Figure 2.3.

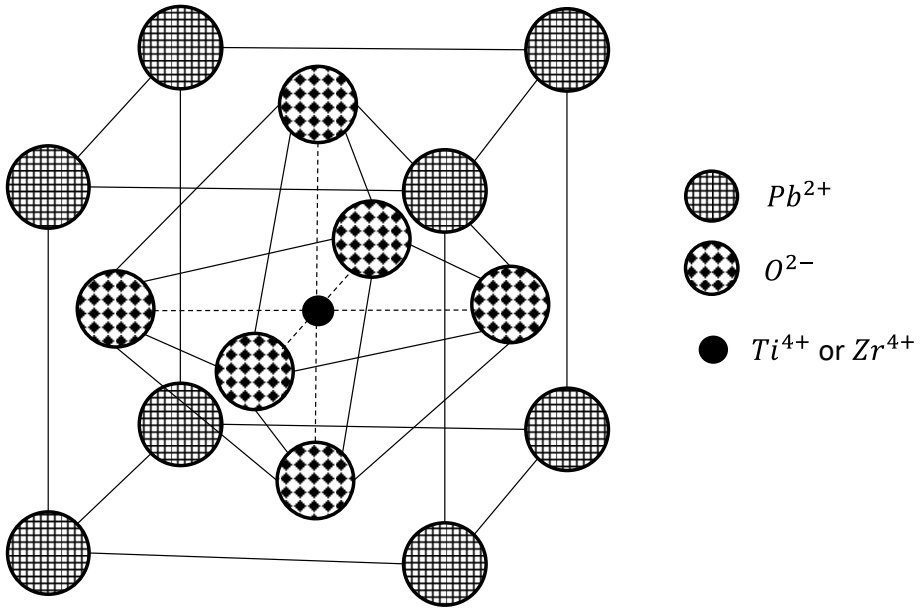

Figure 2.3 Cubic phase perovskite structure of $\mathrm{Pb(Zr_xTi_{(1-x)})O_3}$ $(\theta > \theta_c)$

The crystalline structure is cubic and symmetric such that the central titanium or zirconium atom is centred. There is therefore no spontaneous polarisation in the unit crystal and the material exhibits paraelectric behaviour. However, below θ_c and for a proportion of lead titanate approximately $(1 - \mathrm{x}) \times 100\% > 48\%$, the crystalline structure of PZT is tetragonal as shown in Figure 2.4. The crystalline

structure now exhibits a spontaneous polarisation denoted by P_s that is responsible for the ferroelectric behaviour.

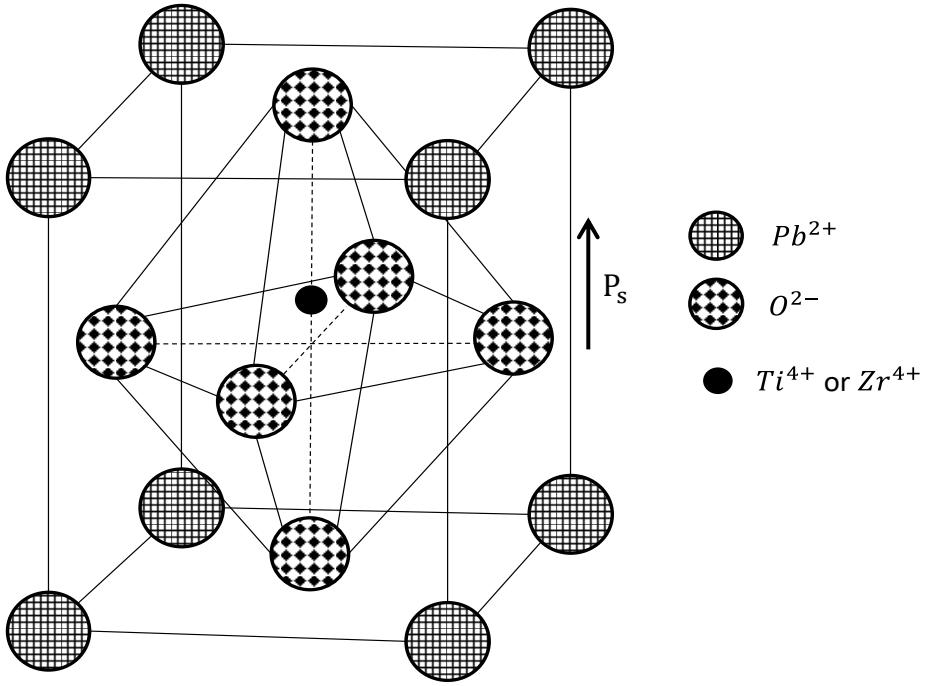

Figure 2.4 Tetragonal phase Perovskite structure of $Pb(Zr_xTi_{(1-x)})O_3$ $(\theta < \theta_c)$

With large piezoelectric and coupling coefficients, devices based on $Pb(Zr_xTi_{(1-x)})O_3$ (PZT) have found widespread use in both sensors and actuators in recent years. These desirable properties were first recognised by Berlincourt et al. [64] in 1960.

2.7.2 PZT phase diagram

Figure 2.5 shows the phase diagram of PZT as a function of the molar percentage of lead titanate and the temperature. It can be seen that the morphotropic phase boundary (MPB) between rhombohedral and tetragonal phases, where the concentrations of Zr^{4+} and Ti^{4+} ions are approximately equal, is largely independent of temperature from zero Celsius up to the Curie temperature, providing a stable material phase composition for sensing at room and body temperature ranges. It is well known that the piezoelectric constants peak near the MPB boundary and that these are strongly dependent on the proportions of $PbZrO_3$ and $PbTiO_3$,

although the mechanisms for this phenomenon are not fully understood. Although the sharp transition of MPB suggests the material has either a tetragonal phase or a rhombohedral phase, there is in fact evidence to suggest that both phases may coexist at room temperature near the MPB [65]. Other research suggests that there also exists a monoclinic phase at the MPB boundary between the rhombohedral and tetragonal phases, and that this phenomenon contributes to the large piezoelectric and dielectric constant of PZT at approximately equal Zr^{4+} and Ti^{4+} concentrations by allowing continuous rotation of the polarization direction in a plane. This phenomenon is discussed for $Pb(Zr_{0.52}Ti_{0.48})O_3$ in [66]. PZT materials with compositions around the MPB are also easier to pole than purely tetragonal or rhombohedral PZT compositions.

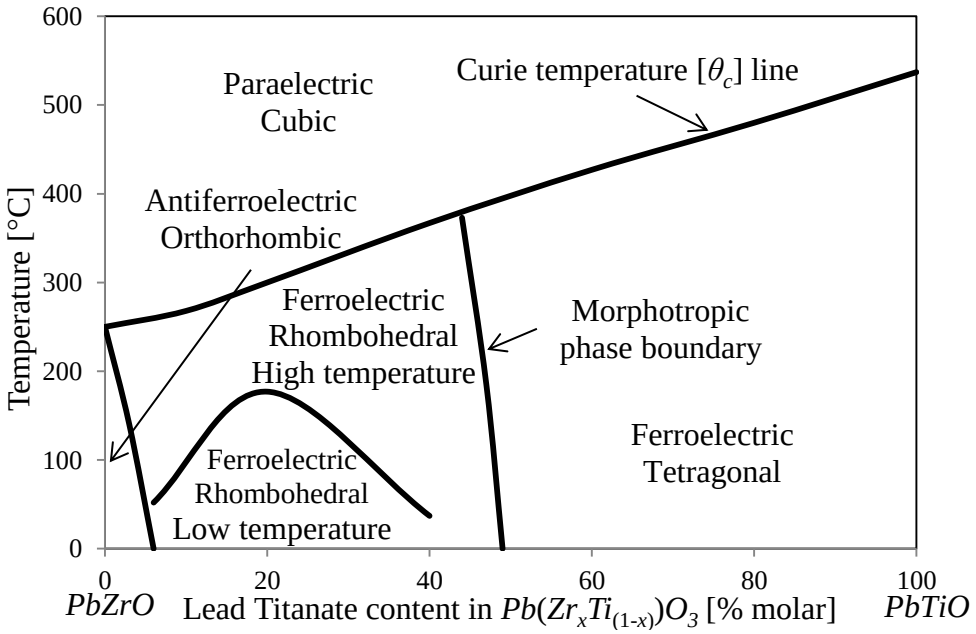

Figure 2.5 Phase diagram of $Pb(Zr_xTi_{(1-x)})O_3$ adapted from [67]

While the manufacturer of the PZT devices used in this thesis, Murata declines to disclose the PZT composition, it is strongly believed to be manufactured using PZT-5H which is commonly used for this type of device, and which has a composition of 53% zirconium and 47% titanium $(Pb(Zr_{0.53}Ti_{0.47})O_3)$ [68]. By inspection of the phase diagram of Figure 2.5, this composition indicates that PZT-5H lies 3% to the left of the MPB. It is therefore expected to contain a mixture of tetragonal and rhombohedral phases at the temperatures of interest $(20°C\ to\ 40°C)$,

and exhibit enhanced piezoelectric and dielectric properties relative to formulations further from the MPB. An additional contribution to the piezoelectric properties is achieved using donor dopants. While the dopant used is not disclosed and varies by manufacturer, PZT-5 types are generally doped with Niobium Nb^{+}, which produces negative ion vacancies in the PZT structure, enhancing domain reorientation during poling and leading to an improvement in the piezoelectric coefficients realised. Published data for the piezoelectric constants of PZT-5H are given in Appendix A.1.

2.7.3 Domain structure

Figure 2.6 illustrates the ferroelectric domain structure of polycrystalline ceramics such as PZT below the Curie temperature in both the unpoled and poled state.

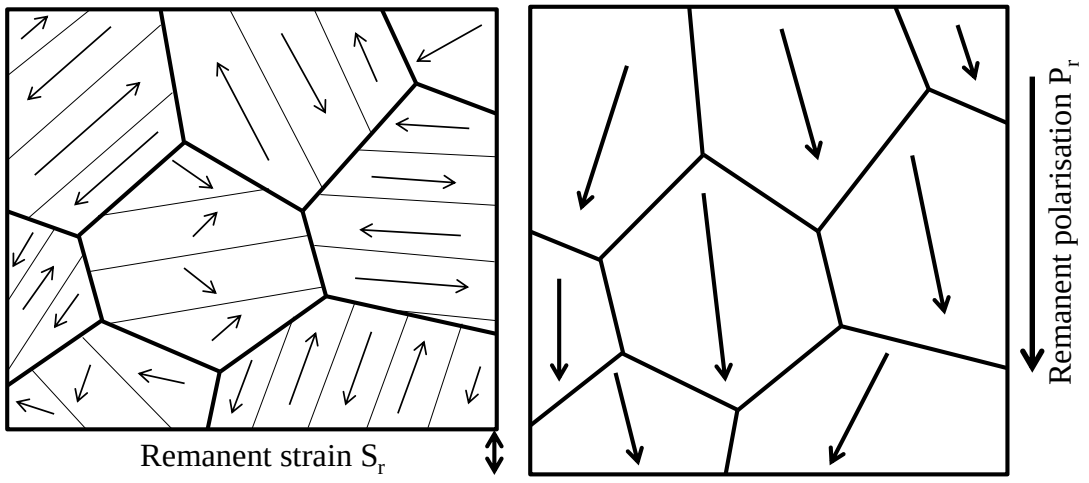

Figure 2.6 Illustrative ferroelectric ceramic domain structures before poling illustrating 90° and 180° adjacent domain orientations (left) and after poling (right)

A typical ferroelectric ceramic is polycrystalline with each crystal containing many domains that are separated by domain walls within each crystal. In the unpoled ferroelectric the electric dipoles, each of which is equal to the spontaneous polarisation P_s described above, are aligned in each domain resulting in a uniform polarisation that is also equal to P_s. The orientation of P_s in adjacent domains within

a crystal may be orientated at either 90° or 180° to each other giving rise to so-called 90° and 180° domain wall boundaries. In the unpoled state as shown in Figure 2.6 left, the ferroelectric ceramic exhibits no piezoelectric properties due to the random orientation of the domains that result in a macroscopic spatial average polarisation of zero before poling. However, piezoelectric properties can be imparted to the ferroelectric ceramic by applying a large enough electric field in the 'poling' direction such that the electric dipoles in each domain within each crystal are forced to align close to the applied electric field direction such that a single domain exists within each crystal. The crystal boundary is therefore also the domain boundary. As shown in Figure 2.6 right, the poling process results in a built-in remanent polarisation, denoted by P_r, and remanent strain, denoted by S_r, in the ferroelectric ceramic when the applied electric field is removed. It can be seen that P_s is not aligned parallel to the applied electric 'poling' field everywhere within the ferroelectric ceramic due to the relative orientations of each crystal within the crystalline structure and therefore in general the remanent polarisation is less than the spontaneous polarisation such that $P_r < P_s$.

2.7.4 Conductivity in PZT materials

In doped PZT materials such as PZT-5H, hole conduction typical of p-type semiconductors is thought to be the dominant conduction mechanism with defects and contaminants that act as donors and acceptors also contributing to the conduction [69]. On the other hand, in un-doped PZT, where contaminants are much less likely, it was first proposed in [70] that the dominant electrical conduction mechanism is also p-type hole conduction, but in this case due to lead vacancies caused by the high volatility of lead and resulting loss during the high temperature sintering process required during manufacture. Despite these conduction mechanisms, the conductivity of PZT materials is low at approximately $10^{-11} Sm^{-1}$. However, the measured voltage developed by a PZT element in response to an applied surface temperature or axial pressure cannot be used directly as a measure of DC and low frequency temperatures or pressures. This is due to the low native time constant of the sensor, which is equal to the product of the low frequency capacitance specified and the

equivalent resistance of the piezoelectric medium, or alternatively the ratio of the permittivity to the conductivity of the piezoelectric medium. The actual time constant observed is further reduced by the finite input resistance of any follow-on voltage measuring circuit, leading to severe DC signal decay and attenuation at low frequencies. The effect of conductivity on the sensor response is discussed further in Chapter 4 and Chapter 5, with the mitigation of signal decay and low frequency attenuation by the use of an appropriate signal-conditioning scheme being discussed in Chapter 6.

2.8 Conclusions

There has been a rapid expansion and availability of commercially available wearable e-health monitoring devices. However, there are currently no commercially available wearable sensor technologies designed for the real time monitoring of temperature and pressure within the environment of a prosthetic socket despite the desirability of such a system for monitoring amputee patients during daily activity, and despite ongoing prosthetic socket mounted sensors research since the 1960's.

Commercially available PZT elements are identified as promising candidates for use as wearable prosthetic socket mounted sensors. PZT devices exhibit both piezoelectric and pyroelectric effects and are therefore interesting candidates for both temperature and pressure sensing applications. They also fulfil the requirements of robustness, a low thickness profile and low cost. A major disadvantage not exhibited by other sensor technologies is response voltage decay due to the finite input impedance of the necessary signal conditioning amplifier and dielectric leakage. It is however possible to mitigate these problems by the application of an appropriate signal conditioning design. A solution to this problem is discussed in Chapter 6.

Chapter 3

Equations of state

3.1 Introduction

In this chapter, the elastic-dielectric-thermal constitutive equations in stress-charge-entropy dependent variable form and the associated heat diffusion equation is derived for the piezoelectric medium. The elastic-dielectric-thermal constitutive equations are an extension of the piezoelectric constitutive equations discussed in Section 2.6.2. From this analysis, the elastic-thermal constitutive and diffusion equations for the substrate medium are stated.

The elastic-dielectric-thermal constitutive equations, together with the elastic-thermal constitutive and associated heat diffusion equations are required to develop the desired mathematical models of the PZT sensor element. The models developed are generally applicable to other piezoelectric and substrate media combinations. While there are several alternative and equivalent constitutive equation forms, the use of the stress-charge-entropy dependent variable form allows the effect of the mechanical and electrical constants on the sensor response to be delineated for analysis in a computationally efficient way. The required constitutive equations have independent variables of strain, electric field and temperature, and are derived using

the electric Gibbs thermodynamic potential, denoted by G_e and the first and second laws of thermodynamics.

While analyses of the general type discussed in the following sections are mostly described in the non-engineering literature using a tensor formulation [71],[72],[73] a vector-matrix formulation of the linear piezoelectric equations is used by convention in the engineering literature and therefore an approach with consistent notation using vector and matrix calculus has been developed for use throughout the analysis to follow [74],[75],[76]. The method devised for use in this thesis is similar to the numerator convention where vectors are of the column type by default. The introduction of the superscript t indicates a transpose or row vector.

3.2 Analytical assumptions

All analyses pertaining to the piezoelectric and substrate media in this thesis are valid for a small temperature change and for small signal excitation where the piezoelectric material operates within the linear regime. The linear regime requires that the material be considered to obey Hooke's law from a mechanical standpoint and to behave as a linear dielectric where the strain, stress, electric field and electric displacement have a mutually linear relationship such that the elastic and electric coefficients, in addition to the piezoelectric coefficients, are considered constant over the small signal range. In addition, the assumptions of 'quasi-static' and 'electrostatic' conditions are applied unless otherwise stated. The assumption of 'quasi-static' conditions is valid for the DC and low frequency mechanical or electrical excitation and requires that the acoustic wavelength of the mechanical disturbance in the piezoelectric medium and substrate are very much greater than the dimensions of the piezoelectric medium. The validity of 'electrostatic' conditions requires that the frequency of the electric field in the piezoelectric medium due to a mechanical disturbance is sufficiently low such that the effect of the rate of change of the magnetic field due to the rate of change of currents is negligible. 'Quasi-static' validity is assumed where appropriate and 'electrostatic' validity is always assumed. Additional assumptions with regard to the thermodynamic processes described are stated in the body text as necessary.

3.3 Constitutive state Equations – piezoelectric medium

3.3.1 Analysis

The derivation of the piezoelectric constitutive equations in $\boldsymbol{S}$, $\boldsymbol{E}$ and $\Delta\theta$ independent variable form required to describe the thermal-elastic-dielectric behaviour of the sensor element are discussed in this section.

The first law of thermodynamics, which is given by Equation 3.1, states that an infinitesimal change in the total internal energy du of a system is the sum of an infinitesimal amount of heat dq transferred into or out of a system and an infinitesimal amount of work dw done by or on the system.

$$du = dq + dw \tag{3.1}$$

A positive value of dw is defined as an infinitesimal amount of work done on the system while a negative value of dw is an incremental work done by the system. If the system is thermodynamically 'closed' such that there is no mass transfer into or out of the system, then from the second law of thermodynamics, dq can be substituted using $dq = \theta d\sigma$. The term $d\sigma\ (JK^{-1})$ is the infinitesimal change in entropy of the system due to an infinitesimal amount of heat dq transferred to the system, and $\theta(K)$ is the absolute temperature of the system. Although strictly speaking valid only for reversible processes, setting $dq = \theta d\sigma$ is valid for both the ideal reversible thermodynamic process demonstrated for example by the well-known Carnot thermodynamic cycle, and in general for quasi-static irreversible thermodynamic processes [77].

The entropy $\sigma\ (JK^{-1})$ is defined as the change in entropy from an equilibrium state and does not represent the absolute entropy. On the other hand, the absolute entropy is defined as a change in entropy over the temperature range of absolute zero to the current absolute temperature. With the exception of θ that represents the absolute temperature (K), this is also true of all other variables that are considered to be a change from the resting state. In the case of a solid material, for which mass transfer is naturally zero, Equation 3.1 is written as Equation 3.2, which

is always true whether it is used to describe ideal reversible or irreversible thermodynamic processes since it is described in terms of all the state variables. As such, the use of Equation 3.2 to describe any thermal-elastic-dielectric process is dependent only on the initial and final states, and not on the path taken between the states. The use of higher case script for the internal energy U and Σ indicates that the terms in Equation 3.2 are now measured as volume energy densities ($Jm^{-3}K^{-1}$).

$$dU = \theta d\Sigma + \boldsymbol{T}^t d\boldsymbol{S} + \boldsymbol{E}^t d\boldsymbol{D} \tag{3.2}$$

In common with all real thermodynamic systems, heat transfer and work in the overall system (piezoelectric medium, substrate and external environment) is always strictly thermodynamically irreversible. However, if the temperature change is sufficiently small compared to the initial absolute temperature when considering heat transfer to and within the PZT-5H sensor element then the initial absolute temperature can be considered approximately constant such that $\theta \cong \theta_o$. It can therefore be considered that in the absence of significant losses due to heat transfer to the external environment, Joule heating or viscous friction, that the approximation of a thermodynamically reversible process is valid. It is therefore considered that the application and removal of the same amount of heat or work returns the piezoelectric medium and external environment system to its original thermodynamic steady state with no resultant change in entropy either in the piezoelectric medium or external environment over the heat cycle.

In general all variables will be a function of both dimension and time and therefore Σ is defined as the volume entropy density, the total entropy of the solid (in this case the piezoelectric body and substrate) being the volume integral of Σ. By convention, compressive stress, $\boldsymbol{T}$ and strain, $\boldsymbol{S}$ are considered negative quantities, while tensile stress, $\boldsymbol{T}$ and strain, $\boldsymbol{S}$ are considered positive quantities.

The superscript t indicates a transpose matrix and in the case of a vector using the denominator convention, $\boldsymbol{T}^t$ and $\boldsymbol{E}^t$ are therefore defined as row vectors. The electric Gibbs potential also known as the electric enthalpy is defined by Equation 3.3 [78] written in matrix form. The use of the electric Gibbs potential allows the constitutive state equations to be derived in S, E and $\Delta\theta$ independent variable form. Alternative thermodynamic potentials that allow derivation of the

other independent variable forms of the constitutive state Equations are described in Appendix A.2.

$$G_e = U - \theta\Sigma - \boldsymbol{E}^t\boldsymbol{D} \tag{3.3}$$

In differential form, Equation 3.3 is written as Equation 3.4.

$$dG_e = dU - \theta d\Sigma - \Sigma d\theta - \boldsymbol{E}^t d\boldsymbol{D} - \boldsymbol{D}^t d\boldsymbol{E} \tag{3.4}$$

Substituting Equation 3.2 into Equation 3.4 yields Equation 3.5.

$$dG_e = \boldsymbol{T}^t d\boldsymbol{S} - \boldsymbol{D}^t d\boldsymbol{E} - \Sigma d\theta \tag{3.5}$$

Equation 3.5 implies that $G_e = G_e(\boldsymbol{S}, \boldsymbol{E}, \theta)$ and therefore the independent variables for the electric Gibbs potential are $\boldsymbol{S}$, $\boldsymbol{E}$ and θ. Total differentiation of $G_e = G_e(\boldsymbol{S}, \boldsymbol{E}, \theta)$, such that partial derivatives are taken with respect to each independent variable while keeping the others constant, yields Equation 3.6 using the vector differentiation numerator layout convention. The subscripts outside the brackets indicate variables that are held constant during the partial differentiation.

$$dG_e = \left(\frac{\partial G_e}{\partial \boldsymbol{S}^t}\right)_{\boldsymbol{E},\theta} d\boldsymbol{S} + \left(\frac{\partial G_e}{\partial \boldsymbol{E}^t}\right)_{\boldsymbol{S},\theta} d\boldsymbol{E} + \left(\frac{\partial G_e}{\partial \theta}\right)_{\boldsymbol{E},\boldsymbol{S}} d\theta \tag{3.6}$$

Comparing Equation 3.5 with Equation 3.6 yields Equations 3.7

$$\left(\frac{\partial G_e}{\partial \boldsymbol{S}^t}\right)_{\boldsymbol{E},\theta} = \boldsymbol{T}^t \qquad \left(\frac{\partial G_e}{\partial \boldsymbol{E}^t}\right)_{\boldsymbol{S},\theta} = -\boldsymbol{D}^t \qquad \left(\frac{\partial G_e}{\partial \theta}\right)_{\boldsymbol{E},\boldsymbol{S}} = -\Sigma \tag{3.7}$$

The implication of Equation 3.6 and Equation 3.7 is that since $G_e = G_e(\boldsymbol{S}, \boldsymbol{E}, \theta)$, then the dependent variables $\boldsymbol{T}$, $\boldsymbol{D}$ and Σ must also be linear functions of the dependent variables such that $\boldsymbol{T} = \boldsymbol{T}(\boldsymbol{S}, \boldsymbol{E}, \theta)$, $\boldsymbol{D} = \boldsymbol{D}(\boldsymbol{S}, \boldsymbol{E}, \theta)$ and $\Sigma = \Sigma(\boldsymbol{S}, \boldsymbol{E}, \theta)$. By applying total differentiation, these relationships are written in differential form to yield Equations 3.8 to 3.10.

$$d\boldsymbol{T} = \left(\frac{\partial \boldsymbol{T}}{\partial \boldsymbol{S}^t}\right)_{\boldsymbol{E},\theta} d\boldsymbol{S} + \left(\frac{\partial \boldsymbol{T}}{\partial \boldsymbol{E}^t}\right)_{\boldsymbol{S},\theta} d\boldsymbol{E} + \left(\frac{\partial T}{\partial \theta}\right)_{\boldsymbol{E},\boldsymbol{S}} d\theta \tag{3.8}$$

$$d\boldsymbol{D} = \left(\frac{\partial \boldsymbol{D}}{\partial \boldsymbol{S}^t}\right)_{\boldsymbol{E},\theta} d\boldsymbol{S} + \left(\frac{\partial \boldsymbol{D}}{\partial \boldsymbol{E}^t}\right)_{\boldsymbol{S},\theta} d\boldsymbol{E} + \left(\frac{\partial \boldsymbol{D}}{\partial \theta}\right)_{\boldsymbol{E},\boldsymbol{S}} d\theta \tag{3.9}$$

$$d\Sigma = \left(\frac{\partial \Sigma}{\partial \boldsymbol{S}^t}\right)_{\boldsymbol{E},\theta} d\boldsymbol{S} + \left(\frac{\partial \Sigma}{\partial \boldsymbol{E}^t}\right)_{\boldsymbol{S},\theta} d\boldsymbol{E} + \left(\frac{\partial \Sigma}{\partial \theta}\right)_{\boldsymbol{E},\boldsymbol{S}} d\theta \tag{3.10}$$

The partial derivative terms in Equations 3.8 to 3.10 can be considered constant for sufficiently small changes in their respective variables and therefore Equations 3.8 to 3.10 may be integrated over a small change in each variable to give Equations 3.11 to 3.13 where $\Delta\theta$ is a small temperature change relative to the initial temperature θ_o such that $\Delta\theta = (\theta - \theta_o)$. This result assumes that changes in both the dependent and independent variables are small enough such that the linear relationship is valid.

$$\boldsymbol{T} = \left(\frac{\partial \boldsymbol{T}}{\partial \boldsymbol{S}^t}\right)_{\boldsymbol{E},\theta} \boldsymbol{S} + \left(\frac{\partial \boldsymbol{T}}{\partial \boldsymbol{E}^t}\right)_{\boldsymbol{S},\theta} \boldsymbol{E} + \left(\frac{\partial \boldsymbol{T}}{\partial \theta}\right)_{\boldsymbol{E},\boldsymbol{S}} \Delta\theta \tag{3.11}$$

$$\boldsymbol{D} = \left(\frac{\partial \boldsymbol{D}}{\partial \boldsymbol{S}^t}\right)_{\boldsymbol{E},\theta} \boldsymbol{S} + \left(\frac{\partial \boldsymbol{D}}{\partial \boldsymbol{E}^t}\right)_{\boldsymbol{S},\theta} \boldsymbol{E} + \left(\frac{\partial \boldsymbol{D}}{\partial \theta}\right)_{\boldsymbol{E},\boldsymbol{S}} \Delta\theta \tag{3.12}$$

$$\Sigma = \left(\frac{\partial \Sigma}{\partial \boldsymbol{S}^t}\right)_{\boldsymbol{E},\theta} \boldsymbol{S} + \left(\frac{\partial \Sigma}{\partial \boldsymbol{E}^t}\right)_{\boldsymbol{S},\theta} \boldsymbol{E} + \left(\frac{\partial \Sigma}{\partial \theta}\right)_{\boldsymbol{E},\boldsymbol{S}} \Delta\theta \tag{3.13}$$

Five of the partial differential constant terms can be defined immediately from Hooke's law, the dielectric equation for polarised media and the definitions of the piezoelectric constant, stress coefficient and primary pyroelectric coefficient as the definitions given by Equations 3.14.

$$\left(\frac{\partial \boldsymbol{T}}{\partial \boldsymbol{S}^t}\right)_{\boldsymbol{E},\theta} \triangleq \boldsymbol{c}^E \qquad \left(\frac{\partial \boldsymbol{D}}{\partial \boldsymbol{E}^t}\right)_{\boldsymbol{S},\theta} \triangleq \boldsymbol{\varepsilon}^S \qquad \left(\frac{\partial \boldsymbol{D}}{\partial \boldsymbol{S}^t}\right)_{\boldsymbol{E},\theta} \triangleq \mathbf{e}$$

$$\left(\frac{\partial \boldsymbol{T}}{\partial \theta}\right)_{\boldsymbol{E},\boldsymbol{S}} \triangleq -\boldsymbol{\gamma}^E \qquad \left(\frac{\partial \boldsymbol{D}}{\partial \theta}\right)_{\boldsymbol{E},\boldsymbol{S}} \triangleq \boldsymbol{p}^S \tag{3.14}$$

The remaining four partial differential constant terms are determined by application of the well-known Maxwell relations for partial differentiation and the internal energy U. In the absence of shear stress and strain components, $\boldsymbol{c}^E$, $\boldsymbol{\varepsilon}^S$ and $\mathbf{e}$ are 3×3 matrices while $\boldsymbol{\gamma}^E$ and $\boldsymbol{p}^S$ are 3×1 column vectors. Applying partial differentiation to each of the Equations 3.7 yields the pairs of Equations 3.15 to 3.17.

$$\left(\frac{\partial \boldsymbol{T}^t}{\partial \boldsymbol{E}}\right)_{\boldsymbol{S},\theta} = \left(\frac{\partial \left(\frac{\partial G_e}{\partial \boldsymbol{S}^t}\right)_{\boldsymbol{E},\theta}}{\partial \boldsymbol{E}}\right)_{\boldsymbol{S},\theta}; \qquad -\left(\frac{\partial \boldsymbol{D}^t}{\partial \boldsymbol{S}}\right)_{\boldsymbol{E},\theta} = \left(\frac{\partial \left(\frac{\partial G_e}{\partial \boldsymbol{E}^t}\right)_{\boldsymbol{S},\theta}}{\partial \boldsymbol{S}}\right)_{\boldsymbol{E},\theta} \tag{3.15}$$

$$\left(\frac{\partial \boldsymbol{T}^t}{\partial \theta}\right)_{\boldsymbol{E},\boldsymbol{S}} = \left(\frac{\partial\left(\frac{\partial G_e}{\partial \boldsymbol{S}^t}\right)_{\boldsymbol{E},\theta}}{\partial \theta}\right)_{\boldsymbol{E},\boldsymbol{S}} ; \quad -\left(\frac{\partial \Sigma}{\partial \boldsymbol{S}^t}\right)_{\boldsymbol{E},\theta} = \left(\frac{\partial\left(\frac{\partial G_e}{\partial \theta}\right)_{\boldsymbol{E},\boldsymbol{S}}}{\partial \boldsymbol{S}^t}\right)_{\boldsymbol{E},\theta} \tag{3.16}$$

$$-\left(\frac{\partial \boldsymbol{D}^t}{\partial \theta}\right)_{\boldsymbol{E},\boldsymbol{S}} = \left(\frac{\partial\left(\frac{\partial G_e}{\partial \boldsymbol{E}^t}\right)_{\boldsymbol{S},\theta}}{\partial \theta}\right)_{\boldsymbol{E},\boldsymbol{S}} ; \quad -\left(\frac{\partial \Sigma}{\partial \boldsymbol{E}^t}\right)_{\boldsymbol{S},\theta} = \left(\frac{\partial\left(\frac{\partial G_e}{\partial \theta}\right)_{\boldsymbol{E},\boldsymbol{S}}}{\partial \boldsymbol{E}^t}\right)_{\boldsymbol{S},\theta} \tag{3.17}$$

Noting that the pair of Equations 3.15 have a matrix transpose relationship to each other and that the order of differentiation on the right hand side of Equations 3.15 to 3.17 is arbitrary, then comparing each of the pairs of Equations 3.15 to 3.17 yields the Maxwell relations given by Equations 3.18 to 3.20.

$$\left(\frac{\partial \boldsymbol{T}}{\partial \boldsymbol{E}^t}\right)_{\boldsymbol{S},\theta} = \left(\frac{\partial \boldsymbol{T}^t}{\partial \boldsymbol{E}}\right)^t_{\boldsymbol{S},\theta} = -\left(\frac{\partial \boldsymbol{D}}{\partial \boldsymbol{S}^t}\right)^t_{\boldsymbol{E},\theta} \triangleq -\boldsymbol{e}^t \tag{3.18}$$

$$-\left(\frac{\partial \boldsymbol{T}^t}{\partial \theta}\right)_{\boldsymbol{E},\boldsymbol{S}} = \left(\frac{\partial \Sigma}{\partial \boldsymbol{S}^t}\right)_{\boldsymbol{E},\theta} = \boldsymbol{\gamma}^{E,t} \tag{3.19}$$

$$\left(\frac{\partial \boldsymbol{D}^t}{\partial \theta}\right)_{\boldsymbol{E},\boldsymbol{S}} = \left(\frac{\partial \Sigma}{\partial \boldsymbol{E}^t}\right)_{\boldsymbol{S},\theta} = \boldsymbol{P}^{S,t} \tag{3.20}$$

For a thermodynamically reversible process, a change in the volume heat density dQ (Jm^{-3}) due to the addition of a quantity of heat dq to an infinitesimal volume dv is given by the second law of thermodynamics as $dQ = \theta d\Sigma$. If the temperature change is sufficiently small compared to the absolute temperature θ such that $\theta \cong \theta_o$, then the process can be considered thermodynamically reversible such that θ can be considered constant and be directly replaced by the initial absolute temperature θ_o. Therefore, using the well-known specific heat formula relationship between heat and temperature at constant strain and electric field given by $dQ = dU \cong \theta_o d\Sigma = \rho C_{sp}^{S,E} d\theta$ yields Equation 3.21a and Equation 3.21b where ρ is the density of the medium (kgm^{-3}) and $C_{spv}^{S,E}$ and $C_{sp}^{S,E}$ are the volume specific heat capacity $(Jm^{-3}K^{-1})$ and specific heat capacity $(Jkg^{-1}K^{-1})$ respectively at constant strain and electric field.

$$\left(\frac{\partial U}{\partial \theta}\right)_{\boldsymbol{E},\boldsymbol{S}} = \rho C_{sp}^{S,E} = C_{spv}^{S,E} \tag{3.21a}$$

$$\left(\frac{\partial \Sigma}{\partial \theta}\right)_{\boldsymbol{E},\boldsymbol{S}} = \frac{\rho C_{sp}^{S,E}}{\theta} \cong \frac{\rho C_{sp}^{S,E}}{\theta_o} \tag{3.21b}$$

The full set of material constant relationships in terms of their associated partial derivatives is now complete and these are summarised in Table 3.1.

$\left(\frac{\partial \boldsymbol{T}}{\partial \boldsymbol{S}^t}\right)_{\boldsymbol{E},\theta} \triangleq \boldsymbol{c}^E$	$\left(\frac{\partial \boldsymbol{T}}{\partial \boldsymbol{E}^t}\right)_{\boldsymbol{S},\theta} = -\boldsymbol{e}^t$	$\left(\frac{\partial \boldsymbol{T}}{\partial \theta}\right)_{\boldsymbol{E},\boldsymbol{S}} \triangleq -\boldsymbol{\gamma}^E$
$\left(\frac{\partial \boldsymbol{D}}{\partial \boldsymbol{S}^t}\right)_{\boldsymbol{E},\theta} \triangleq \boldsymbol{e}$	$\left(\frac{\partial \boldsymbol{D}}{\partial \boldsymbol{E}^t}\right)_{\boldsymbol{S},\theta} \triangleq \boldsymbol{\varepsilon}^S$	$\left(\frac{\partial \boldsymbol{D}}{\partial \theta}\right)_{\boldsymbol{E},\boldsymbol{S}} \triangleq \boldsymbol{p}^S$
$\left(\frac{\partial \Sigma}{\partial \boldsymbol{S}^t}\right)_{\boldsymbol{E},\theta} = \boldsymbol{\gamma}^{E,t}$	$\left(\frac{\partial \Sigma}{\partial \boldsymbol{E}^t}\right)_{\boldsymbol{S},\theta} = \boldsymbol{p}^{S,t}$	$\left(\frac{\partial \Sigma}{\partial \theta}\right)_{\boldsymbol{E},\boldsymbol{S}} = \frac{\rho C_{sp}^{E,S}}{\theta_o}$

Table 3.1 Material constants in stress-charge-entropy form

Substituting the material coefficients given in Table 3.1 into Equations 3.11 to 3.13 yields the required stress-charge-entropy form of the small signal linear constitutive state equations given by Equations 3.22 to 3.24.

$$\boldsymbol{T} = \boldsymbol{c}^E\boldsymbol{S} - \boldsymbol{e}^t\boldsymbol{E} - \boldsymbol{\gamma}^E\Delta\theta \tag{3.22}$$

$$\boldsymbol{D} = \boldsymbol{e}\boldsymbol{S} + \boldsymbol{\varepsilon}^S\boldsymbol{E} + \boldsymbol{p}^S\Delta\theta \tag{3.23}$$

$$\Sigma = \boldsymbol{\gamma}^{E,t}\boldsymbol{S} + \boldsymbol{p}^{S,t}\boldsymbol{E} + \frac{\rho C_{sp}^{S,E}\Delta\theta}{\theta_o} \tag{3.24}$$

Equation 3.25 gives a compact matrix representation of the stress-charge-entropy constitutive equations where the left hand side is the dependent variable vector and the right hand side is the product of the material constant matrix and the independent variable vector.

$$\begin{bmatrix} \boldsymbol{T} \\ \boldsymbol{D} \\ \Sigma \end{bmatrix} = \begin{bmatrix} \boldsymbol{c}^E & -\boldsymbol{e}^t & -\boldsymbol{\gamma}^E \\ \boldsymbol{e} & \boldsymbol{\varepsilon}^S & \boldsymbol{p}^S \\ \boldsymbol{\gamma}^{E,t} & \boldsymbol{p}^{S,t} & \rho C_{sp}^{E,S}/\theta_o \end{bmatrix} \begin{bmatrix} \boldsymbol{S} \\ \boldsymbol{E} \\ \Delta\theta \end{bmatrix} \tag{3.25}$$

In Equation 3.25, Σ is a change in entropy density ($Jm^{-3}K^{-1}$), $\boldsymbol{p}^S$ is the constant strain pyroelectric coefficient vector ($Cm^{-2}K^{-1}$) and $\boldsymbol{\gamma}^E$ is the thermal stress coefficient vector ($Nm^{-2}K^{-1}$) equal to $\boldsymbol{c}^E\boldsymbol{\varphi}_p^E$ where $\boldsymbol{\varphi}_p^E$ is the coefficient of thermal expansion (m/mK) vector at constant electric field. With the exception of superscripts, terms in light font are non-matrix scalar quantities.

3.3.2 Discussion

It can be seen from Equation 3.24 that the entropy density Σ at any point within the piezoelectric material is dependent on the strain and electric field in addition to the change in temperature. The amount of heat required to achieve a change in the temperature, $\Delta\theta$ is increased under positive (tensile) strain and applied electric field, and conversely is reduced under negative (compressive) strain and negative applied electric field.

The terms $\boldsymbol{\gamma}^{E,t}\boldsymbol{S}$ and $\boldsymbol{p}^{S,t}\boldsymbol{E}$ respectively are scalars and reflect the mechanical and electrical contributions to the total volume entropy density within the body of the piezoelectric material. The material constant vectors $\boldsymbol{\gamma}^E$ and $\boldsymbol{p}^S$ measured at constant temperature are also defined as the piezo-caloric (or elasto-caloric) coefficient at constant electric field and the electro-caloric coefficient at constant strain (mechanically clamped) respectively. Here the electro-caloric coefficient is defined as the ratio of the change in entropy of a material to an applied electric field under isothermal and constant strain conditions, and the piezo-caloric coefficient is defined as the ratio of the change in entropy to an applied strain under isothermal and constant electric field conditions. Under adiabatic conditions such that the change in entropy of the system is zero and no heat enters, leaves or flows in the piezoelectric medium, the electro-caloric effect can be described as producing a reversible temperature change due to an applied spatially uniform electric field at constant strain. Similarly, the piezo-caloric effect can be described as producing a reversible temperature change due to an applied spatially uniform strain at constant electric field.

3.4 Electric Gibbs potential G_e

The Electric Gibbs potential can be derived by taking the vector transpose throughout of Equations 3.11 and 3.12, and substituting the vector transposed Equations 3.11 and 3.12 together with Equation 3.13 into Equation 3.5 which yields the differential form of the electric Gibbs potential given by Equation 3.26.

$$dG_e = \left(\boldsymbol{S}^t\left(\frac{\partial \boldsymbol{T}^t}{\partial \boldsymbol{S}}\right)_{\boldsymbol{E},\theta} + \boldsymbol{E}^t\left(\frac{\partial \boldsymbol{T}^t}{\partial \boldsymbol{E}}\right)_{\boldsymbol{S},\theta} + \left(\frac{\partial \boldsymbol{T}^t}{\partial \theta}\right)_{\boldsymbol{E},\boldsymbol{S}} \Delta\theta\right) d\boldsymbol{S}$$

$$-\left(\boldsymbol{S}^t\left(\frac{\partial \boldsymbol{D}^t}{\partial \boldsymbol{S}}\right)_{\boldsymbol{E},\theta} + \boldsymbol{E}^t\left(\frac{\partial \boldsymbol{D}^t}{\partial \boldsymbol{E}}\right)_{\boldsymbol{S},\theta} + \left(\frac{\partial \boldsymbol{D}^t}{\partial \theta}\right)_{\boldsymbol{E},\boldsymbol{S}} \Delta\theta\right) d\boldsymbol{E}$$

$$-\left(\left(\frac{\partial \Sigma}{\partial \boldsymbol{S}^t}\right)_{\boldsymbol{E},\theta} \boldsymbol{S} + \left(\frac{\partial \Sigma}{\partial \boldsymbol{E}^t}\right)_{\boldsymbol{S},\theta} \boldsymbol{E} + \left(\frac{\partial \Sigma}{\partial \theta}\right)_{\boldsymbol{E},\boldsymbol{S}} \Delta\theta\right) d\theta \qquad (3.26)$$

Substituting the partial differential constants given in Table 3.1 into Equation 3.26 yields Equation 3.27 where for isotropic and transverse isotropic materials, $\boldsymbol{c}^E = \boldsymbol{c}^{E,t}$ and that it is always true that $\boldsymbol{\varepsilon}^{S,t} = \boldsymbol{\varepsilon}^S$ since only the main diagonal or trace terms are non-zero in $\boldsymbol{\varepsilon}^S$.

$$dG_e = (\boldsymbol{S}^t\boldsymbol{c}^E - \boldsymbol{E}^t\boldsymbol{e} - \boldsymbol{\gamma}^{\boldsymbol{E},t}\Delta\theta)d\boldsymbol{S}$$

$$-(\boldsymbol{S}^t\boldsymbol{e}^t + \boldsymbol{E}^t\boldsymbol{\varepsilon}^S + \boldsymbol{P}^{S,t}\Delta\theta)d\boldsymbol{E} - \left(\boldsymbol{\gamma}^{E,t}\boldsymbol{S} + \boldsymbol{P}^{\boldsymbol{S},t}\boldsymbol{E} + \frac{\rho C_{sp}^{E,S}}{\theta_o}\Delta\theta\right) d\theta \qquad (3.27)$$

Collecting and rearranging the terms in Equation 3.27 yields Equation 3.28.

$$dG_e = \boldsymbol{S}^t\boldsymbol{c}^E d\boldsymbol{S} - \boldsymbol{E}^t\boldsymbol{\varepsilon}^S d\boldsymbol{E} - \frac{\rho C_{sp}^{S,E}}{\theta_o}\Delta\theta d\theta - (\boldsymbol{\gamma}^{E,t}\Delta\theta d\boldsymbol{S} + \boldsymbol{\gamma}^{E,t}\boldsymbol{S}d\theta)$$

$$-(\boldsymbol{p}^{S,t}\Delta\theta d\boldsymbol{E} + \boldsymbol{p}^{S,t}\,\boldsymbol{E}d\theta) - (\boldsymbol{E}^t\boldsymbol{e}d\boldsymbol{S} + \boldsymbol{S}^t\boldsymbol{e}^t d\boldsymbol{E}) \qquad (3.28)$$

Assuming $\boldsymbol{e}$, $\boldsymbol{c}^E$, $\boldsymbol{\gamma}^{E,t}$, $\boldsymbol{\varepsilon}^S$, $\boldsymbol{p}^{S,t}$ and $\rho C_{sp}^{S,E}/\theta_o$ are constant, then integrating the $d\theta$ terms over the appropriate range $\theta = \theta_o$ to $\theta = \theta_o + \Delta\theta$, and integrating the $\boldsymbol{S}$ and $\boldsymbol{E}$ terms over the range 0 to $\boldsymbol{S}$ and 0 to $\boldsymbol{E}$ to indicate a change in each variable respectively yields Equation 3.29, where all variables are considered to be changes from the resting state.

$$G_e = \frac{1}{2}\left(\boldsymbol{S}^t\boldsymbol{c}^E\boldsymbol{S} - \boldsymbol{E}^t\boldsymbol{\varepsilon}^S\boldsymbol{E} - \frac{\rho C_{sp}^{S,E}(\Delta\theta)^2}{\theta_o}\right) - (\boldsymbol{\gamma}^{E,t}\boldsymbol{S} + \boldsymbol{p}^{S,t}\boldsymbol{E})\Delta\theta - \boldsymbol{E}^t\boldsymbol{e}\boldsymbol{S} \qquad (3.29)$$

Equation 3.29 is the electric Gibbs potential, $G_e\ (J/m^3)$ in matrix-vector form. The truncated MacLaurin series expansion approximation given by $\ln(1 + \Delta\theta/\theta_o) \cong \Delta\theta/\theta_o - 0.5(\Delta\theta/\theta_o)^2$ has been used in the derivation of Equation 3.29. This approximation ignores terms in $(\Delta\theta/\theta_o)^3$ and higher and is valid under the assumption of small $\Delta\theta$ such that $\Delta\theta \ll \theta_o$. This approximation is in keeping with the derivations of Section 3.2, which for the piezoelectric medium is equivalent to calculating the thermal entropy density contribution to the total entropy density, denoted by $\Sigma_{thermal}$, and given by the $\Sigma_{thermal} = \rho C_{sp}^{S,E}\Delta\theta/\theta_o$ term in Equation 3.24 using the well-known second law of thermodynamics entropy equation given by $\Sigma_{thermal} = \int_{\theta_o}^{\theta_o+\Delta\theta}\left(\rho C_{sp}^{S,E}/\theta\right)d\theta$. By invoking the argument that θ in the denominator changes very little during heat transfer, such that heat transfer is considered to occur in an equilibrium state, then θ can be replaced by θ_o and taken outside of the integral. In practice linearity in response to temperature has been demonstrated for relatively large temperature changes under electrical short circuit conditions [79] and therefore the piezoelectric constitutive equations derived in Section 3.3 are considered applicable for use in the development of the sensor where the maximum $\Delta\theta$ is of the order $20K$ compared to values of θ_o of approximately $300K$. In the case of ferroelectric materials such as PZT, where in certain applications hysteresis phenomena may be important, these equations are valid for small changes in electric field and strain such that the $\boldsymbol{D} - \boldsymbol{E}$ and $\boldsymbol{S} - \boldsymbol{E}$ rate-independent hysteresis characteristics of the material can be considered linear and free of rate-independent hysteresis over the required measurement ranges. Equation 3.29 is equivalent to the commonly used tensor notation form and simplifies the derivation of the constitutive equations in their matrix form.

The $\boldsymbol{T}$, $\boldsymbol{D}$, and Σ dependent variable form of the constitutive equations are given by the partial derivatives of the scalar electric Gibbs potential with respect to the dependent vector variables as stated by Equations 3.7. Using Equations 3.7 and 3.29, and performing partial differentiation of the Gibbs electric potential function with respect to the independent variables $\boldsymbol{S}$, $\boldsymbol{E}$ and $\Delta\theta$ in turn, noting that $\partial\theta \equiv \partial\Delta\theta$,

using vector differentiation and taking the vector transpose of each throughout yields the linear constitutive equations 3.22 to 3.24 given in Section 3.3 that describe the coupled dielectric-elastic-thermal behaviour of piezoelectric materials.

Further verification of the Gibbs electric potential function can be made by taking the total derivative of Equation 3.29 with respect to an arbitrary variable denoted here by z where the vector differential relationships given by Equations 3.30 have been performed on the electric Gibbs potential terms $\boldsymbol{S}^t\boldsymbol{c}^E\boldsymbol{S}$, $\boldsymbol{E}^t\boldsymbol{\varepsilon}^S\boldsymbol{E}$ and $\boldsymbol{E}^t\boldsymbol{e}\boldsymbol{S}$. The term $v = \boldsymbol{X}^t\boldsymbol{a}\boldsymbol{Y} = \boldsymbol{Y}^t\boldsymbol{a}^t\boldsymbol{X}$ is a scalar quantity, $\boldsymbol{X}$ and $\boldsymbol{Y}$ are column vectors, $\boldsymbol{a}$ is a square matrix (number of rows equals number of columns), and z is an arbitrary dummy variable.

$$\frac{dv}{dz} = \left(\frac{\partial v}{\partial \boldsymbol{X}^t}\right)_{\boldsymbol{Y}} \frac{d\boldsymbol{X}}{dz} + \left(\frac{\partial v}{\partial \boldsymbol{Y}^t}\right)_{\boldsymbol{X}} \frac{d\boldsymbol{Y}}{dz} \qquad \frac{dv}{dz} = \boldsymbol{Y}^t\boldsymbol{a}^t \frac{d\boldsymbol{X}}{dz} + \boldsymbol{X}^t\boldsymbol{a}\frac{d\boldsymbol{Y}}{dz} \tag{3.30}$$

Performing total differentiation with respect to z on the terms $\rho C_{sp}^{S,E}(\Delta\theta)^2/\theta_o$, $\Delta\theta\boldsymbol{\gamma}^{E,t}\boldsymbol{S}$ and $\Delta\theta\boldsymbol{p}^{S,t}\boldsymbol{E}$, and by setting v to each of the terms $\boldsymbol{S}^t\boldsymbol{c}^E\boldsymbol{S}$, $\boldsymbol{E}^t\boldsymbol{\varepsilon}^S\boldsymbol{E}$ and $\boldsymbol{E}^t\boldsymbol{e}\boldsymbol{S}$ in Equations 3.30 recovers the differential form dG_e given by Equation 3.28 as expected.

3.5 Internal energy in $\boldsymbol{S}-\boldsymbol{E}$ form

An expression for the internal energy U in $\boldsymbol{S}-\boldsymbol{E}$ form can be found by writing Equations 3.23 and 3.24 in differential form and substituting these along with the differential form of the vector transpose of Equation 3.22 into Equation 3.2, yielding Equation 3.31. The substitution $\theta \cong \theta_o$ for small $\Delta\theta$ used in Equation 3.24 cannot be introduced until the end of the analysis and θ_o is therefore properly replaced by θ in Equation 3.31.

$$dU = \theta\left(\boldsymbol{\gamma}^{E,t}d\boldsymbol{S} + \boldsymbol{p}^{S,t}d\boldsymbol{E} + \frac{\rho C_{sp}^{S,E}d\theta}{\theta}\right) + (\boldsymbol{S}^t\boldsymbol{c}^E - \boldsymbol{E}^t\boldsymbol{e} - \boldsymbol{\gamma}^{E,t}\Delta\theta)d\boldsymbol{S} + \boldsymbol{E}^t(\boldsymbol{e}d\boldsymbol{S} + \boldsymbol{\varepsilon}^S d\boldsymbol{E} + \boldsymbol{p}^S d\theta) \tag{3.31}$$

Collecting terms and rearranging Equation 3.31 yields Equation 3.32 where the relationship $\theta = \theta_o + \Delta\theta$ has been substituted.

$$dU = \theta_o \boldsymbol{\gamma}^{E,t} d\boldsymbol{S} + \theta \boldsymbol{p}^{S,t} d\boldsymbol{E} + \boldsymbol{E}^t \boldsymbol{p}^S d\theta + \rho C_{sp}^{S,E} d\theta + \boldsymbol{S}^t \boldsymbol{c}^E d\boldsymbol{S} + \boldsymbol{E}^t \boldsymbol{\varepsilon}^S d\boldsymbol{E} \tag{3.32}$$

Integrating Equation 3.32 yields Equation 3.33 for the internal energy with strain and electric field as the independent variables.

$$U = \theta_o \boldsymbol{\gamma}^{E,t} \boldsymbol{S} + \theta \boldsymbol{p}^{S,t} \boldsymbol{E} + \rho C_{sp}^{S,E} \Delta\theta + \frac{1}{2}(\boldsymbol{S}^t \boldsymbol{c}^E \boldsymbol{S} + \boldsymbol{E}^t \boldsymbol{\varepsilon}^S \boldsymbol{E}) \tag{3.33}$$

For a reversible process and a small temperature change such that $\theta \cong \theta_o$, Equation 3.33 can be written as Equation 3.34 that describes an idealised reversible thermodynamic process.

$$U = \theta_o(\boldsymbol{\gamma}^{E,t} \boldsymbol{S} + \boldsymbol{p}^{S,t} \boldsymbol{E}) + \rho C_{sp}^{S,E} \Delta\theta + \frac{1}{2}(\boldsymbol{S}^t \boldsymbol{c}^E \boldsymbol{S} + \boldsymbol{E}^t \boldsymbol{\varepsilon}^S \boldsymbol{E}) \tag{3.34}$$

For reversible processes and the assumption of $\theta \cong \theta_o$ only, the work density is therefore given by $W = \frac{1}{2}(\boldsymbol{S}^t \boldsymbol{c}^E \boldsymbol{S} + \boldsymbol{E}^t \boldsymbol{\varepsilon}^S \boldsymbol{E})$ while the heat density is given by $Q = \theta_o(\boldsymbol{\gamma}^{E,t} \boldsymbol{S} + \boldsymbol{p}^{S,t} \boldsymbol{E}) + \rho C_{sp}^{S,E} \Delta\theta$. For reversible thermodynamic processes it can also be seen that $Q = \theta_o \Sigma$, which is used in Section 3.6 for the derivation of the coupled heat diffusion equation for the piezoelectric medium. Equation 3.34 describing the internal energy U in the piezoelectric medium is valid only where loss terms are not considered. Losses and associated internal heating are discussed further in Appendix A.3. The internal energy in $\boldsymbol{T} - \boldsymbol{E}$ form is discussed in Appendix A.4.

3.6 Constitutive state Equations – substrate medium

By a similar procedure and under the same assumptions applied to the piezoelectric medium described in Section 3.3, the coupled elastic-thermal Equations for the substrate are stated immediately as Equations 3.35 and 3.36 where the subscript b refers to a variable that applies to the substrate. Equation 3.35 is the well-known Hooke's law and is valid for small changes is stress, strain and temperature.

$$\boldsymbol{T}_b = \boldsymbol{c}_b \boldsymbol{S}_b - \boldsymbol{\gamma}_b \Delta\theta_b \tag{3.35}$$

$$\Sigma_b = \boldsymbol{\gamma}_b^t \boldsymbol{S}_b + \frac{\rho_b C_{spb}^S \Delta\theta_b}{\theta_o} \tag{3.36}$$

Σ_b is a small change in entropy density ($Jm^{-3}K^{-1}$), $\boldsymbol{\gamma}_b$ is the thermal stress coefficient (Nm^2K^{-1}) equal to $\boldsymbol{c}_b\boldsymbol{\varphi}_b$ where $\boldsymbol{c}_b$ is the isotropic stiffness matrix of the substrate (Nm^{-2}), $\boldsymbol{\varphi}_b$ is the coefficient of thermal expansion (m/mK) vector in the substrate, $\boldsymbol{T}_b$and $\boldsymbol{S}_b$ are the stress strain respectively and C_{spb}^{S} is the specific heat capacity of the substrate at constant strain and ρ_b is the density of the piezoelectric material (kgm^{-3}). A description of the isotropic substrate stiffness matrix c_b is discussed in further detail in Appendix A.5.

In the following sections, Equations 3.24 and 3.36 are used to solve for the diffusion equation and Equations 3.22, 3.23 and 3.35 are used in addition to the diffusion equations for both the piezoelectric film and substrate to solve for the sensor response to temperature and axial stress stimuli.

3.7 Heat diffusion equation – piezoelectric medium

3.7.1 1-D Heat flow

As discussed in Section 3.3, by using the second law of thermodynamics and assuming a small temperature change and reversible process, the volume heat density Q is related to the volume density change in entropy Σ in the piezoelectric medium by Equation 3.37. The assumption of $\theta \cong \theta_o$ indicates that the heat cycle is approximated as a thermodynamically reversible heat transfer process such that the total entropy change of the system in a cycle is zero. A change in the volume entropy density at any point in a medium is therefore dependent only a change in the volume heat density at that point in the medium.

$$Q = \theta_o \Sigma \tag{3.37}$$

One dimensional (1-D) heat flow in the x_3 direction (this is the direction perpendicular to the piezoelectric electrode surfaces) is considered where it is assumed that there is negligible heat flow along the transverse x_1 and x_2 axes such that the temperature along x_1 and x_2 can be considered constant. Taking a small segment of volume $A\Delta x_3$ of cross sectional area A in the x_1 - x_2 plane and thickness Δx_3, the change of heat in the segment in time Δt is equal to the difference between

the heat into the segment and the heat out of the segment in a time Δt. The change of heat in the segment in time Δt is therefore given by $\Delta q = A\Delta x_3\big(Q(t+\Delta t) - Q(t)\big)$. Substituting Equation 3.24 into Equation 3.37 yields Equation 3.38 for Δq.

$$\Delta q = A\Delta x_3 \begin{Bmatrix} \big[\theta_o\big(\boldsymbol{\gamma}^{E,t}\boldsymbol{S}(x_3, t+\Delta t) + \boldsymbol{p}^{S,t}\boldsymbol{E}(x_3, t+\Delta t)\big) + \rho C_{sp}^{S,E}\Delta\theta(x_3, t+\Delta t)\big] \\ -\big[\theta_o(\boldsymbol{\gamma}^{E,t}\boldsymbol{S}(x_3, t) + \boldsymbol{p}^{S,t}\boldsymbol{E}(x_3, t)) + \rho C_{sp}^{S,E}\Delta\theta(x_3, t)\big] \end{Bmatrix}$$

(3.38)

The Maxwell – Cattaneo generalised one-dimensional Fourier heat law is given by Equation 3.39 [80] where Ψ_3 is the one-dimensional rate of heat flow per unit area (W/m^2) along the x_3 polar direction and k_p is the thermal conductivity of the piezoelectric medium. The heat flow relaxation time denoted by τ_q implies that an imposed temperature gradient will not induce an instantaneous flow of heat along a negative temperature gradient, but will rather approach a steady state dictated by the heat flow relaxation time τ_q thus avoiding the well-known paradox of instantaneous heat propagation as predicted by the Fourier heat law of Equation 3.40. However, a problem with the Maxwell-Cattaneo law is that it predicts negative temperatures during transient heat propagation that are dependent on the value of τ_q [81]. Furthermore, values of τ_q for specific materials are not generally available and determining a meaningful value of τ_q for specific materials is not a trivial process [82], [83].

$$\Psi_3 + \tau_q \frac{\partial \Psi_3}{\partial t} = -k_p \frac{\partial \Delta\theta(x_3,t)}{\partial x_3} \tag{3.39}$$

At the very low frequencies considered, the effect of τ_q is considered to be negligible such that at low frequency, $\tau_q \partial \Psi_3 / \partial t \ll \Psi_3$. The Fourier heat in the familiar form of Equation 3.40 is therefore used.

$$\Psi_3(x_3, t) = -k_p \frac{\partial \Delta\theta(x_3,t)}{\partial x_3} \tag{3.40}$$

The difference between the heat into the segment and the heat out of the segment in time Δt is the instantaneous amount of heat (J) in the segment, Δq and is therefore given by Equation 3.41.

$$\Delta q = -k_p A \Delta t \left(\frac{\partial \Delta\theta(x_3,t)}{\partial x_3}\Big|_{x_3} - \frac{\partial \Delta\theta(x_3,t)}{\partial x_3}\Big|_{x_3+\Delta x_3} \right) \tag{3.41}$$

Equating 3.38 and 3.41, dividing both sides by $\Delta x_3 \Delta t$, rearranging and letting $\Delta t \to 0$ and $\Delta x_3 \to 0$ yields Equation 3.42 which is the one-dimensional heat diffusion equation with electro-mechanical source or sink terms dependent on whether work is done on or by the piezoelectric medium respectively. Equation 3.43 includes the effect of the heat flow relaxation time τ_q. The term $K^{S,E}$ is the diffusion coefficient or diffusivity at constant strain and electric field given by $K^{S,E} = k_p/\rho C_{sp}^{S,E}$.

$$\frac{\partial \Delta\theta}{\partial t} = K^{S,E} \frac{\partial^2 \Delta\theta}{\partial x_3^2} - \frac{\theta_o}{\rho C_{sp}^{S,E}} \left(\boldsymbol{\gamma}^{E,t} \frac{\partial \boldsymbol{S}}{\partial t} + \boldsymbol{p}^{S,t} \frac{\partial \boldsymbol{E}}{\partial t} \right) \tag{3.42}$$

$$\frac{\partial \Delta\theta}{\partial t} + \tau_q \frac{\partial^2 \Delta\theta}{\partial t^2} = K^{S,E} \frac{\partial^2 \Delta\theta}{\partial x_3^2} - \frac{\theta_o}{\rho C_{sp}^{S,E}} \left(\boldsymbol{\gamma}^{E,t} \left(\frac{\partial \boldsymbol{S}}{\partial t} + \tau_q \frac{\partial^2 \boldsymbol{S}}{\partial t^2} \right) + \boldsymbol{p}^{S,t} \left(\frac{\partial \boldsymbol{E}}{\partial t} + \tau_q \frac{\partial^2 \boldsymbol{E}}{\partial t^2} \right) \right) \tag{3.43}$$

As described above, the terms in τ_q can be considered negligible by noting that the frequencies of the temperature change and applied axial stress measurands are low. The terms containing the relaxation time τ_q are therefore dropped from further analysis. However, in applications where the frequencies of the applied stimuli are high, it may become necessary to include the effect of τ_q by using Equation 3.43 rather than Equation 3.42. Three alternative and equivalent forms of Equation 3.42 in other independent variable forms are given in Appendix A.6.

Equations 3.37, 3.40 and 3.41 imply the relationships given by Equation 3.44 for the assumptions of an approximately thermodynamically reversible process and a small temperature change.

$$\frac{\partial Q}{\partial t} = \theta_o \frac{\partial \Sigma}{\partial t} = -\frac{\partial \Psi_3}{\partial x_3} = k_p \frac{\partial^2 \Delta\theta}{\partial x_3^2} \tag{3.44}$$

The relationships of Equation 3.44 are valid for heat flow in the piezoelectric medium in response to a small temperature change. The instantaneous rate of change of entropy at any location within the piezoelectric medium is therefore proportional to the instantaneous negative gradient of the heat flow in the x_3 direction for small temperature changes. Internal Joule or viscous friction heating can also add heat to

the piezoelectric medium without the requirement of an external heat source. In the case of an adiabatic and closed medium, heat can be added internally without a temperature gradient (for low frequency excitation) by the application of mechanical or electrical work. In this case, a spatially uniform increase in temperature and entropy takes place, both of which rise monotonically with time and for which the process is thermodynamically irreversible. Joule and viscous friction heating are discussed in Appendix A.3.

3.7.2 Extension to 3-D Heat flow

For applications where heat flow along the x_1 and x_2 axes cannot be ignored, the heat diffusion equation may be derived by considering a small volume $\Delta x_1 \Delta x_2 \Delta x_3$ rather than a segment $A\Delta x_3$ and adding the heat flows in the x_1 and x_2 dimensions to Equation 3.41. Equation 3.45 now gives the 3-dimensional heat diffusion equation.

$$\frac{\partial \Delta\theta}{\partial t} = K^{S,E}\nabla^2 \Delta\theta - \frac{\theta_o}{\rho C_{sp}^{S,E}}\left(\boldsymbol{\gamma}^{E,t}\frac{\partial \boldsymbol{S}}{\partial t} + \boldsymbol{p}^{S,t}\frac{\partial \boldsymbol{E}}{\partial t}\right) \tag{3.45}$$

Where ∇^2 is equal to the divergence of the gradient applied to a scalar variable and is the Laplacian operator for which $\nabla^2 \Delta\theta$ is given by Equation 3.46.

$$\nabla^2 \Delta\theta = \frac{\partial^2 \Delta\theta}{\partial x_1^2} + \frac{\partial^2 \Delta\theta}{\partial x_2^2} + \frac{\partial^2 \Delta\theta}{\partial x_3^2} \tag{3.46}$$

3.7.3 Definition of the heat source / sink term

The term given by $-\theta_o\left(\boldsymbol{\gamma}^{E,t}\frac{\partial \boldsymbol{S}}{\partial t} + \boldsymbol{P}^{S,t}\frac{\partial \boldsymbol{E}}{\partial t}\right)$ describes thermal-dielectric-elastic coupling in the piezoelectric medium due to the piezo-caloric and electro-caloric effects and can be considered as a heat source or heat sink. The effect of this term under compressive strain or negative electric field is equivalent to an additional volume power density heat source, and under tensile strain or positive electric field is equivalent to a heat sink (W/m^3). The description of the terms $\boldsymbol{\gamma}^{E,t}$ and $\boldsymbol{P}^{S,t}$

discussed in Section 3.3 as the piezo-caloric and electro-caloric coefficients is therefore clear in the context of the diffusion equation.

3.8 Heat diffusion equation - substrate

By a similar analysis to the development of the piezoelectric heat diffusion equation in Section 3.7, Equation 3.36 is used to yield the diffusion equation for the substrate given by Equation 3.47, where there is naturally no electric field term. The subscript b indicates a quantity that applies to the substrate material and the terms K_b^S, $\boldsymbol{\gamma}_b^t$, C_{spb}^S and ρ_b are the diffusion coefficient, transpose thermal stress coefficient matrix, specific heat capacity at constant strain and density of the substrate respectively. The thermal stress coefficient matrix can be written $\boldsymbol{\gamma}_b = \boldsymbol{c}_b\, \boldsymbol{\varphi}_b$ such that $\boldsymbol{\gamma}_b^t = \boldsymbol{\varphi}_b^t \boldsymbol{c}_b$ and the diffusion coefficient is given by $K_b^S = k_b/\rho_b\, C_{spb}^S$ where k_b is the thermal conductivity of the substrate. Equation 3.48 includes the heat flow relaxation time, which is denoted by τ_{qb}. In high frequency applications where the relaxation times cannot be ignored and where the assumption of large wavelength compared to the physical dimensions of the piezoelectric device is invalid, Equations 3.43 and 3.48 can in principle be used and solved together with the respective associated set of acoustic wave equations. The acoustic wave equations can be derived by applying Newton's second law of motion to the stress constitutive state equation of the piezoelectric media in $\boldsymbol{T} - \boldsymbol{E}$ (stress-voltage) form, and to Hooke's law for the substrate given by Equation 3.35.

$$\frac{\partial \Delta\theta_b}{\partial t} = K_b^S \frac{\partial^2 \Delta\theta_b}{\partial x_3^2} - \frac{\theta_o}{\rho_b C_{spb}^S} \boldsymbol{\gamma}_b^t \frac{\partial \boldsymbol{S}_b}{\partial t} \tag{3.47}$$

$$\frac{\partial \Delta\theta_b}{\partial t} + \tau_{qb} \frac{\partial^2 \Delta\theta_b}{\partial t^2} = K_b^S \frac{\partial^2 \Delta\theta_b}{\partial x_3^2} - \frac{\theta_o}{\rho_b C_{spb}^S} \boldsymbol{\gamma}_b^t \left(\frac{\partial \boldsymbol{S}_b}{\partial t} + \tau_{qb} \frac{\partial^2 \boldsymbol{S}_b}{\partial t^2} \right) \tag{3.48}$$

In common with the piezoelectric medium, low frequency operation infers that the effect of the heat flow relaxation time τ_{qb} will be negligible and it is henceforth dropped from further analysis.

3.9 Conclusions

The piezoelectric and substrate constitutive state equations and associated low frequency diffusion equations required to find an LTI model of the sensor response to external thermal and elastic stimuli have been derived. Equations 3.22, 3.23, 3.35, 3.42 and 3.47 are the equations required to yield low frequency mathematical models of the electric field response due to a surface temperature and applied axial stress. These models are developed in Chapter 4 by applying the quasi-static conditions appropriate for low frequency operation and setting the boundary conditions appropriate to the PZT-5H sensor design configuration to find the required solutions of Equations 3.42 and 3.47.

Chapter 4

Sensor response modelling

4.1 Introduction

In this chapter, a proposed prosthetic socket mounting design for the PZT-5H sensor element is presented. The diffusion Equation 3.42 and Equation 3.47, together with the linear constitutive Equations 3.22, 3.23 and 3.35 are expanded to solve for the one-dimensional heat flow within the piezoelectric device that leads to the development of a low frequency mathematical model of the sensor. This model yields the sensor output voltage response to the application of an interface temperature and/or applied axial stress. While all practical measurements presented in this thesis pertain to the measurement of an interface temperature change, the theoretical research presented yields solutions for the sensor response to both temperature and applied normal stress (or pressure) measurands for application to the future practical investigation of the sensor for the combined measurement of both a temperature change and normal stress.

Section 4.2 describes the PZT-5H sensor element construction and specification, while Section 4.3 describes the prototype sensor prosthetic socket (or elastomer liner) mounting configuration for both temperature and/or pressure

measurement. In Section 4.4, the spatial mean and spatially dependent electric field response models are derived. The spatial mean electric field model is derived in terms of an applied axial stress and mean applied temperature changes in the substrate and piezoelectric media. Section 4.5 discusses the effect of the adhesive used to affix the piezoelectric medium to the substrate while Section 4.6 discusses the effect of the substrate on the pyroelectric coefficients. Section 4.7 describes the low frequency equivalent circuit model of the PZT-5H element and using the electric field responses derived in Section 4.4, Section 4.8 identifies the nature of the charge distribution in the piezoelectric medium and electrodes, and describes the source of the charge that drives the spatial mean electric field response. Section 4.9 and Section 4.10 describe the solutions of the coupled linear piezoelectric and heat diffusion equations with the appropriate boundary conditions that yield the spatial mean temperatures in the substrate and piezoelectric medium in response to the skin surface temperature. Two cases are considered: direct substrate surface-skin contact and indirect substrate surface-skin contact where the skin temperature is measured through a prosthetic polymer liner. Finally, in Section 4.11 and Section 4.12, the output voltage response models of the sensor element to an applied temperature at the substrate surface and applied axial stress respectively are presented.

4.2 PZT-5H sensor element

The piezoelectric temperature sensor element selected is a commercially available Murata (Type 7BB-27-4) diaphragm consisting of a dry-pressed and sintered PZT layer poled along the 3-axis normal to the surface with silver electrodes on the top and bottom faces perpendicular to the axial direction (3-axis) and bonded to a brass substrate. The type of PZT is not known, nor is this information available from Murata. However, it is likely that the material used is PZT-5H, which is commonly used for this type of application. The manufacturer specified flexure mode resonant frequency is $4.6kHz$ with a low frequency capacitance of $20nF \pm 30\%$ measured at $1kHz$. Using electronic callipers, the diameters of the PZT film and electrode are found to be $20mm$ and $18.2mm$, respectively. The total thickness is $0.53mm$ made up of $0.3mm$ brass substrate and $0.23mm$ PZT-5H media. PZT

piezoelectric technology has the inherent advantage of being applicable to both temperature and interface pressure measurement. In this thesis it will be shown that the large constant strain pyroelectric coefficient and piezoelectric constants of PZT-5H materials in tandem with appropriate signal conditioning make possible the measurement of temperature at frequencies in the range of sub μHz to a few Hz suitable for use within the confinement of a prosthetic socket [84].

4.3 Prototype sensor configuration

A proposed sensor prosthetic socket-mounting configuration that uses the Murata Type 7BB-27-4 diaphragm element is shown in Figure 4.1. For use directly against the skin, the sensor element may be embedded in a prosthetic liner rather than the prosthetic socket.

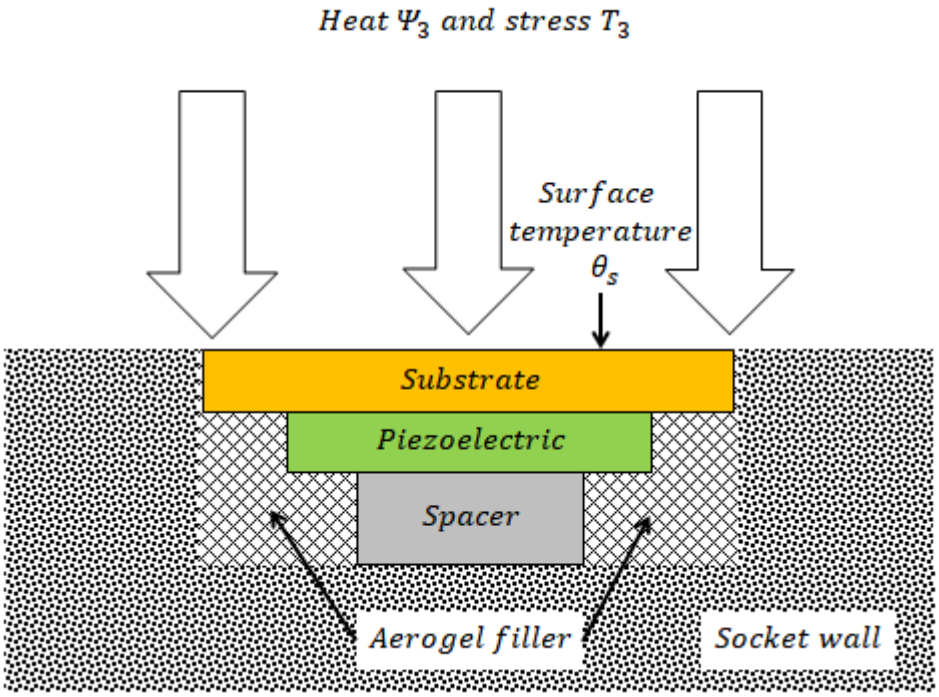

Figure 4.1 Configuration of prosthetic socket temperature or pressure sensor embedded into the socket wall (or elastomer liner)

While this thesis concentrates on the use of the sensor element to measure temperature changes, the aim is ultimately to use the same piezoelectric technology to measure both applied axial stress (pressure) and temperature simultaneously using

the same sensor element. In the case that temperature only is measured, the spacer shown is unnecessary and a low thermal conductivity support collar flexibly bonded to the bare underside circumferential width of the substrate is introduced to support and affix the sensor element. It is important that the support collar has a high stiffness to avoid an unwanted flexure response. It is proposed that an aerogel filler is used to loosely fill the cavity left by the removal of the spacer to ensure that the sensing element is thermally insulated at the lower electrode.

In the case of axial stress measurement, it is necessary to negate the effect of temperature changes in the piezoelectric and substrate media on the response. To achieve this, it is proposed that a narrow circumferential channel with a diameter $1/\sqrt{2}$ of the diameter of the piezoelectric electrode is etched through the electrode and piezoelectric medium such that two electrically isolated piezoelectric volumes are created with equal surface area on the same substrate. The inner piezoelectric volume is subject to the applied axial stress via the spacer. The spacer transfers the normal stress load to the socket wall and it is proposed that the spacer is fabricated from a stiff aerogel material. Such strong, rigid aerogel materials are now available, are inexpensive and are characterised as having extremely low thermal conductivity [85]. The outer piezoelectric volume is isolated with respect to the applied axial stress in the inner piezoelectric medium, but remains subject to the effect of the applied axial stress in the substrate. The axial stress response component is obtained by subtracting the two sensor responses at the inner and outer electrodes, assuming that both sensor volumes are subject to the same surface temperature and exhibit the same temperature response such that the effects of temperature changes in the piezoelectric and substrate media are negated. However, a caveat to this method is that since the surface area is reduced by 50%, then the response charge is also reduced by 50%. In addition, the effect of temperature is differenced out only at the signal conditioning stage, leading to the possibility of a significant reduction in the useful range of the sensor, or at worst saturation at the intermediate signal conditioning stages. It is therefore necessary that the sensor element is adequately thermally insulated to minimise this effect. Furthermore, a reduction in the axial stress response will result since the response contribution due to the substrate axial stress is negated together with the temperature response.

Notwithstanding the problems of reduced measurement range or saturation discussed above, it is in principle possible to measure both temperature and axial stress simultaneously. This can be achieved by taking the difference between the inner sensor response, which is the sum of both temperature and applied axial stress responses, and an amplitude scaled value of the temperature independent axial stress response described above such that the stress response is negated leaving only the temperature response. It is therefore in principle possible to measure both temperature and applied axial stress simultaneously and independently using the same piezoelectric element.

For both skin temperature and / or applied axial stress measurement, it may not be desirable to place the sensor substrate on the skin to measure the skin temperature directly. In the case that the PZT-5H sensor element must be used directly against the skin, there are requirements to ensure that the surface in contact with the skin is safe and hypoallergenic to avoid allergic skin reactions, and that the sensor element is protected from skin moisture. Polydimethylsiloxane (PDMS) silicone rubber, which is a commonly used coating for medical applications such as medical implants, is proposed as a suitable coating for the sensor element. PDMS is an elastomer at low temperatures and has the required properties of being hydrophobic, hypoallergenic and safe for use in medically applications. PDMS has the desirable mechanical property of having a very low Young's modulus, which is a necessary requirement to ensure the substrate of the piezoelectric element can expand freely in response to a temperature change. With the thermal conductivity and specific heat capacity of PDMS equal to $0.15\,Wm^{-1}K^{-1}$ and $1460\,Jkg^{-1}K^{-1}$ respectively, the diffusion coefficient is low and a possible detrimental effect on the conduction of heat to the sensor surface and therefore the sensor response must be considered. However, if it is ensured that the coating is thin enough then the severity of the effect on the sensor response can be mitigated. The application of a PDMS surface coating as described in [86] is conveniently achieved using a spray on technique that can apply thin surface coating thicknesses down to approximately $1\mu m$. At this thickness, the effect on the sensor response is estimated to be negligible.

The development of the sensor element response model follows a path of analysis that starts by considering a general symmetrical transverse isotropic piezoelectric device poled along the axial 3-direction with rigidly bonded isotropic substrate. All assumptions and observations are described and justified. The solution is dependent on the appropriate boundary conditions chosen and in the case of the sensor used within a prosthetic socket, the socket wall is assumed to provide ideal insulation such that the heat flow across the socket wall boundary can be assumed to be negligibly close to zero. In practice this can be closely approximated by using very low thermal conductivity aerogel materials to fill the space between the sensor and socket wall, as discussed above.

4.4 Sensor element electric field model

4.4.1 Initial considerations

The relevant state equations for both the piezoelectric and substrate media are solved for the electric field response in this section. The required output voltage of the piezoelectric element is then given by $V_o = -l_p \bar{E}_3$. In the analysis, it is assumed that at the low frequencies of interest, the effect of the inertial masses of the piezoelectric and substrate media are negligible. That is to assume that the acoustic wave produced within both the piezoelectric and substrate media in response to an applied stress or temperature change has a wavelength very much larger than the dimensions of the sensor. The dependences of the instantaneous stresses, strains and electric field are therefore considered to be due to the instantaneous spatial temperature distribution and applied axial stress only.

In the development of mathematical models, the shear stress and strain components and associated elastic constants are omitted since the electric displacement and electric field response to shear stress in PZT is zero [87].

With reference to Figure 4.1 in Section 4.3, the outer electrode of the device furthest away from the measurement surface is assumed to be thermally insulated such that heat flow out of the device in the axial direction and into the external environment is negligible. No change in the entropy of the internal or external

environment therefore takes place via this route. It is further assumed that the sides of the substrate and PZT materials are sufficiently insulated or that the temperature of the adjacent area is close to that across the area of the sensor surface such that heat flow is along the axial 3-direction only with heat flow along the transverse directions being considered negligible.

4.4.2 Relevant state equations

The state Equations 3.22, 3.23 and 3.35 developed in Chapter 3 and used in the following analysis are repeated below for clarity.

$$\boldsymbol{T} = \boldsymbol{c}^{E}\boldsymbol{S} - \boldsymbol{e}^{t}\boldsymbol{E} - \boldsymbol{\gamma}^{E}\Delta\theta \tag{3.22}$$

$$\boldsymbol{D} = \boldsymbol{e}\boldsymbol{S} + \boldsymbol{\varepsilon}^{S}\boldsymbol{E} + \boldsymbol{p}^{S}\Delta\theta \tag{3.23}$$

$$\boldsymbol{T}_{b} = \boldsymbol{c}_{b}\boldsymbol{S}_{b} - \boldsymbol{\gamma}_{b}\Delta\theta_{b} \tag{3.35}$$

The electric displacement $\boldsymbol{D}$ can be set to zero without loss of generality with the effect of an external displacement charge being included later by the introduction of an additional term to the permittivity in the case of derivation from spatially averaged equations, or to the primary pyroelectric term in the case of derivation from spatially dependent equations. The effect of the input impedance of the external signal conditioning electronics can be included in the corresponding output voltage response by considering an external impedance in parallel with the dielectric resistance. Furthermore, an internal dielectric leakage can be included by the introduction of an additional term to the permittivity for both spatially dependent and spatially averaged cases.

4.4.3 Choice of independent variable form

In the development of the sensor model it initially seems preferable to use either the strain-charge ($\boldsymbol{S} - \boldsymbol{D}$) or stress-charge ($\boldsymbol{T} - \boldsymbol{D}$) independent variable form of the piezoelectric constitutive equations and diffusion equations given by Equation (A4.1) or (A4.2) respectively rather than the strain-voltage ($\boldsymbol{S} - \boldsymbol{E}$) form given by

Equations 3.22, 3.23 and 3.42 since setting D to zero appears to reduce the complexity of the analysis. However, it is desirable that the sensor electric field response be found such that the material constants are in the form of constant electric field and constant strain. The investigation into the individual effects of temperature on both the static electrical capacitance (from the constant strain permittivity ε_{33}^{S}) and mechanical equivalent capacitances that will be discussed in Chapter 5 can be more easily extracted from the solution using the strain-voltage ($\boldsymbol{S}-\boldsymbol{E}$) form.

In addition, since expansion of the piezoelectric matrices is necessary to solve for the electric field response, the conversion of the solution of the electric field from constant electric displacement values to constant electric field values for the stiffness and thermal stress coefficients involves considerably more work than using the $\boldsymbol{S}-\boldsymbol{E}$ independent variables form of the constitutive equations from the outset. Throughout the following analysis the $\boldsymbol{S}-\boldsymbol{E}$ form is therefore used.

4.4.4 Analysis – Electric field model

In the following analysis the solution for the electric field response of a general transverse isotropic piezoelectric device in the configuration discussed in Section 4.3 to the application of a change in temperature at the external surface of the substrate and an axial compressive stress along the polar x_3 axis is derived. The strain in the 1- and 2-axes, which is denoted by S, is also derived for application in the analysis of Section 4.9. While the analysis is developed with application to a PZT-5H piezoelectric device with a brass substrate in mind, it is however general and applicable to any piezoelectric ceramic/polymer and substrate combination where the substrate is isotropic and the piezoelectric medium is transverse isotropic. The solution is easily modified to be applicable to alternative isotropies via a re-definition of the substrate and piezoelectric stiffness matrix components.

The PZT-5H element is symmetrical in the transverse 1-2 plane and as a transverse isotropic material the device will therefore be subject to equal stress and strain along the transverse 1- and 2- axes such that $S_1 = S_2 = S$ and transverse stresses $T_1 = T_2 = T$. In addition, the thermal expansion coefficient, Young's moduli, Poisson's ratios and permittivities are identical in the 1- and 2-axes but are in

general different along the polar 3-axis. The analysis to follow assumes rectangular coordinates and a rectilinear form, however the solutions are equally applicable to devices with an annular form where the use of cylindrical co-ordinates will yield an identical result. The surface temperature measurand θ_s is assumed to be constant along the transverse 1- and 2- axes and heat flow is assumed to be one dimensional and to be directed along the polar 3-axis denoted by x_3. The assumption of one dimensional heat flow is justified since θ_s is considered to be constant along the substrate surface and the outside edges of the sensor are insulated with a low thermal conductivity material.

Expanding the matrices of Equations 3.32 and 3.23 yields Equations 4.1 to 4.3 for the piezoelectric medium transverse stress, stress applied along the polar x_3 axis and the electric displacement. The variables T and S are the stress and strain in both transverse 1- and 2- axes due to transverse symmetry, and the subscript 3 indicates a variable acting axially along the 3-axis.

$$T = (c_{11}^E + c_{12}^E)\left(S - \varphi_{p1}^E \Delta\theta\right) + c_{31}^E\left(S_3 - \varphi_{p3}^E \Delta\theta\right) - e_{31}E_3 \tag{4.1}$$

$$T_3 = 2c_{31}^E\left(S - \varphi_{p1}^E \Delta\theta\right) + c_{33}^E\left(S_3 - \varphi_{p3}^E \Delta\theta\right) - e_{33}E_3 \tag{4.2}$$

$$D_3 = 2e_{31}S + e_{33}S_3 + \varepsilon_{33}^S E_3 + p^S \Delta\theta \tag{4.3}$$

Noting that the symmetry of the substrate implies that as with the piezoelectric film the transverse strains $S_{b1} = S_{b2} = S_b$ and transverse stresses $T_{b1} = T_{b2} = T_b$, then the equivalent Equations for the substrate are found by expanding the isotropic Hooke's law relationship given by Equation 3.35 to yield Equation 4.4 and Equation 4.5.

$$T_b = \frac{E_b}{(1+\mu_b)(1-2\mu_b)}(S_b + \mu_b S_{b3} - (1+\mu_b)\varphi_b \Delta\theta_b) \tag{4.4}$$

$$T_{b3} = \frac{E_b}{(1+\mu_b)(1-2\mu_b)}(2\mu_b S_b + (1-\mu_b)S_{b3} - (1+\mu_b)\varphi_b \Delta\theta_b) \tag{4.5}$$

By substitution and rearrangement using Equation 4.4 and Equation 4.5, the stress T_b in the 1- and 2- axes and the strain S_{b3} in the 3-axis of the substrate material are given by Equation 4.6 and Equation 4.7 respectively.

$$T_b = \frac{E_b}{(1-\mu_b)}\left(S_b + \frac{\mu_b}{E_b}T_{b3} - \varphi_b \Delta\theta_b\right) \tag{4.6}$$

$$S_{b3} = \frac{(1+\mu_b)(1-2\mu_b)}{E_b(1-\mu_b)}T_{b3} - \frac{2\mu_b}{(1-\mu_b)}S_b + \frac{(1+\mu_b)}{(1-\mu_b)}\varphi_b \Delta\theta_b \tag{4.7}$$

The constants E_b and μ_b are the Young's modulus and Poisson's ratio of the substrate respectively. The subscript b is maintained for all variables and constants to differentiate these values from those in the piezoelectric film.

Heat flow along the axial x_3 dimension produces a temperature gradient within both substrate and piezoelectric media. Since both materials are considered to be Hookean in nature over the range of the applied stimuli, then the transverse stresses T and T_{b1}, and the temperature gradient varies both with time, t and x_3 while the transverse strains S and S_{b1} vary only with t and are invariant with respect to x_3. On the other hand, at the low frequency excitation considered, the applied axial stresses T_3 and T_{b3} vary with t only and are invariant with respect to x_3 while the strain S_3 and S_{b3} vary both with t and x_3. Furthermore, since the thermal expansion coefficient, stiffnesses and thicknesses of both substrate and piezoelectric medium are in general different, and since the temperature varies with x_3 in both materials, there will exist a radius of curvature due to the different coefficients of thermal expansion, Young's moduli and thickness of both the substrate and piezoelectric materials. However, since the temperature changes considered are small and since the PZT-5H-brass substrate is relatively thick when compared to, for example the thickness of a bimetal strip circuit breaker, the curvature K (reciprocal of the bending radius) is considered to be negligible. The curvature was approximated as $K = 0.004\ (m^{-1})$ for a temperature change of $20K$ by using the thickness dimensions, Young's moduli and the coefficients of thermal expansion of the brass substrate and PZT-5H [88],[89].

It is assumed that the piezoelectric material is rigidly bonded to the brass substrate, and that the piezoelectric and substrate bi-layer bending radius under a temperature change is infinite such that $K \approx 0$. The force equilibrium of the transverse forces then infers that the sum of the transverse axes forces with respect to the axial x_3 dimension in both the piezoelectric material and brass substrate is zero such that Equation 4.8 is satisfied. A_b and A_p are the cross-sectional areas in both the

1-3 and 2-3 planes of the substrate and piezoelectric medium respectively (or in the case of an annular device, the cross sectional areas of the diameters), and l_b and l_p are the thicknesses of the substrate and piezoelectric film respectively. The definite integrals are necessary since the transverse stresses T_b of the substrate and T of the piezoelectric film vary with respect to x_3.

$$\int_{-l_b}^{l_p} dF = \int_{-l_b}^{0} T_b dA_b + \int_{0}^{l_p} T dA_p = 0 \tag{4.8}$$

Taking the reference origin at the substrate-piezoelectric film interface, and noting that the transverse stresses are equal in the x_1 and x_2 transverse dimensions of both piezoelectric film and substrate (although this is not a necessary condition for the general validity of Equation 4.8), then the sum of the forces can be written as Equation 4.9. The terms l_b and l_p are the thicknesses of the substrate and piezoelectric film respectively.

$$\int_{-l_b}^{l_p} dF = \frac{A_b}{l_b} \int_{-l_b}^{0} T_b \, dx_3 + \frac{A_p}{l_p} \int_{0}^{l_p} T \, dx_3 = 0 \tag{4.9}$$

Equation 4.9 is equivalent to the sum of the average forces in the substrate and piezoelectric materials and can therefore be written as Equation 4.10 where the over-bar denotes dimensional averaging with respect to the axial x_3 direction over the respective dimension intervals.

$$\int_{-l_b}^{l_p} dF = \bar{T}_b A_b + \bar{T} A_p = 0 \tag{4.10}$$

The relationship between the spatial mean transverse stresses is therefore given by $\bar{T} = -\bar{T}_b \, A_b / A_p$. Writing Equations 4.1 to 4.3 in dimensional average form with respect to x_3 and taking Laplace transforms with respect to time throughout yields Equations 4.11 to 4.13 where the integration is evaluated over the limits $0 \rightarrow l_p$ along the x_3 axis in the piezoelectric medium. When Kelvin-Voigt type viscous friction effects are considered and included in the stiffness terms then it is assumed that all strain terms have zero initial conditions such that $S_b(0^-)$, $S(0^-)$, $S_{b3}(0^-)$ and $S_3(0^-)$ and their first derivatives at $t = 0^-$ are zero. However, since the effect of viscous friction is directly proportional to frequency, it is of little interest at the low frequencies under consideration. The customary (s) notation, where s is the

Laplace variable, which is widely used to indicate the Laplace domain, is omitted to reduce notation, it being implicitly understood that all functions and coefficients are in the Laplace domain unless otherwise indicated.

$$\bar{T} = (c_{11}^E + c_{12}^E)\left(S - \varphi_{p1}^E \Delta\bar{\theta}\right) + c_{31}^E(\bar{S}_3 - \varphi_{p3}^E \Delta\bar{\theta}) - e_{31}\bar{E}_3 \tag{4.11}$$

$$T_3 = 2c_{31}^E\left(S - \varphi_{p1}^E \Delta\bar{\theta}\right) + c_{33}^E(\bar{S}_3 - \varphi_{p3}^E \Delta\bar{\theta}) - e_{33}\bar{E}_3 \tag{4.12}$$

$$D_3 = 2e_{31}S + e_{33}\bar{S}_3 + \varepsilon_{33}^s\bar{E}_3 + p^s\Delta\bar{\theta} \tag{4.13}$$

Since the transverse strain S and the applied axial stress T_3 at the low frequencies and small temperature change under consideration are independent of x_3 and are functions of s only, the over-bar is unnecessary for these terms and it is therefore omitted in Equations 4.11 to 4.13.

Writing Equation 4.6 in the dimensional average form with respect to x_3 yields Equation 4.14 where dimensional averaging is evaluated over the limits $-l_b \to 0$ along the x_3 axis in the substrate. As before, the over-bar is omitted in S_b and T_{b3} since, as with the piezoelectric medium, at low frequency these variables are functions of time only.

$$\bar{T}_b = \frac{E_b}{(1-\mu_b)}\left(S_b + \frac{\mu_b}{E_b}T_{b3} - \varphi_b\Delta\bar{\theta}_b\right) \tag{4.14}$$

Substituting $\bar{T} = -\bar{T}_b\, A_b/A_p$ into Equation 3.49 and noting that $S_b = S$ yields Equation 4.15.

$$\bar{T} = -\frac{E_b A_b}{(1-\mu_b)A_p}\left(S + \frac{\mu_b}{E_b}T_{b3} - \varphi_b\Delta\bar{\theta}_b\right) \tag{4.15}$$

Substituting Equation 4.15 into Equation 4.11 yields Equation 4.16.

$$-\frac{E_b A_b}{(1-\mu_b)A_p}\left(S_b + \frac{\mu_b}{E_b}T_{b3} - \varphi_b\Delta\bar{\theta}_b\right) =$$

$$(c_{11}^E + c_{12}^E)\left(S - \varphi_{p1}^E\Delta\bar{\theta}\right) + c_{31}^E\left(\bar{S}_3 - \varphi_{p3}^E\Delta\bar{\theta}\right) - e_{31}\bar{E}_3 \tag{4.16}$$

Setting $D_3 = 0$ for the present to simplify the calculation, the simultaneous solution of Equation 4.16 together with Equations 4.12 and 4.13 with selected variables of $\bar{E}_3$, $\bar{S}_3$ and S can now be found for the required $\bar{E}_3$ and S in terms of

$\Delta\bar{\theta}_b$, $\Delta\bar{\theta}$, T_{b3} and T_3 which are independent of x_3 and are functions of s only. The required solutions of S and $\bar{E}_3$ in the Laplace domain are given by Equation 4.17 and Equation 4.18. The coefficients C_4 to C_7 used in Equation 4.17, which are in general functions of the Laplace variable s, are defined in Appendix A.7. The terms α and β are defined in Appendix A.1.

The solutions were obtained by writing a Matlab script that uses the 'solve' functionality that allows for the necessary requirement of symbolic characters.

$$S = C_4\Delta\bar{\theta} + C_5\Delta\bar{\theta}_b + C_6T_{b3} + C_7T_3 = C_4\Delta\bar{\theta} + C_5\Delta\bar{\theta}_b + \left(C_6\frac{A_{ps}}{A_{bs}} + C_7\right)T_3 \qquad (4.17)$$

$$\bar{E}_3 = \frac{\left(\frac{\beta E_b A_b \varphi_{p1}^E}{E_b A_b + \alpha(1-\mu_b)A_p} - 2e_{31}\varphi_{p1}^E - e_{33}\varphi_{p3}^E - p^S\right)\Delta\bar{\theta} - \frac{\beta\left(E_b A_b \varphi_b \Delta\bar{\theta}_b - (1-\mu_b)A_p\frac{c_{31}^E}{c_{33}^E}T_3 - \mu_b A_b T_{b3}\right)}{E_b A_b + \alpha(1-\mu_b)A_p} - \frac{e_{33}}{c_{33}^E}T_3}{\frac{(1-\mu_b)\beta^2 A_p}{2(E_b A_b + \alpha(1-\mu_b)A_p)} + \frac{e_{33}^2}{c_{33}^E} + \varepsilon_{33}^S{}'} \qquad (4.18)$$

At the low frequencies of interest, the applied axial force is spatially independent in both substrate and piezoelectric media and therefore T_{b3} and T_3 are related by $T_{b3}A_{bs} = T_3A_{ps}$ where A_{bs} and A_{ps} are the surface areas of the substrate and piezoelectric media respectively. T_{b3} can therefore be substituted by $T_{b3} = T_3\,A_{ps}/A_{bs}$ to yield Equation 4.19.

$$\bar{E}_3 = \frac{\left(\frac{\beta E_b A_b \varphi_{p1}^E}{E_b A_b + \alpha(1-\mu_b)A_p} - 2e_{31}\varphi_{p1}^E - e_{33}\varphi_{p3}^E - p^S\right)\Delta\bar{\theta} - \frac{\beta E_b A_b \varphi_b \Delta\bar{\theta}_b - \beta\left((1-\mu_b)A_p\frac{c_{31}^E}{c_{33}^E} + \mu_b A_b\frac{A_{ps}}{A_{bs}}\right)T_3}{E_b A_b + \alpha(1-\mu_b)A_p} - \frac{e_{33}}{c_{33}^E}T_3}{\frac{(1-\mu_b)\beta^2 A_p}{2(E_b A_b + \alpha(1-\mu_b)A_p)} + \frac{e_{33}^2}{c_{33}^E} + \varepsilon_{33}^S{}'} \qquad (4.19)$$

The terms α and c_{31}^E/c_{33}^E in Equation 4.19 may be replaced by $E_{p1}^E/\left(1-\mu_{p1}^E\right)$ and $\mu_{p3}^E/\left(1-\mu_{p1}^E\right)$ respectively to produce a tidier notational form for $\bar{E}_3$ given by Equation 4.20, however the form given by Equation 4.18 is retained to reduce notation and facilitate readability. The Young's modulus and Poisson's ratio terms E_{p1}^E, μ_{p1}^E and μ_{p3}^E are discussed in Appendix A.5.

$$\bar{E}_3 =$$

$$\frac{\left(\frac{\beta E_b A_b \varphi_{p1}^E}{E_b A_b + \alpha(1-\mu_b)A_p} - 2e_{31}\varphi_{p1}^E - e_{33}\varphi_{p3}^E - p^S\right)\Delta\bar{\theta} - \frac{\beta\left(1-\mu_{p1}^E\right)E_b A_b \varphi_b \Delta\bar{\theta}_b - \beta\left(\left(1-\mu_b\right)\mu_{p3}^E A_p - \left(1-\mu_{p1}^E\right)\mu_b A_b \frac{A_{ps}}{A_{bs}}\right)T_3}{\left(1-\mu_{p1}^E\right)E_b A_b + (1-\mu_b)E_{p1}^E A_p} - \frac{e_{33}}{c_{33}^E}T_3}{\frac{\left(1-\mu_{p1}^E\right)(1-\mu_b)\beta^2 A_p}{2\left(\left(1-\mu_{p1}^E\right)E_b A_b + (1-\mu_b)E_{p1}^E A_p\right)} + \frac{e_{33}^2}{c_{33}^E} + \varepsilon_{33}^S}'$$

(4.20)

The spatially dependent E_3 given by Equation 4.21 is obtained from Equation 4.2 and Equation 4.3 with S substituted by Equation 4.17 and D_3 reintroduced by noting that $D_3 = -\delta_s \bar{E}_3/s$. The reintroduction of D_3 and definition of δ_s is discussed further below.

$$E_3 = \frac{-\frac{e_{33}}{c_{33}^E}T_3 - \beta\left(C_4\Delta\bar{\theta} + C_5\Delta\bar{\theta}_b + C_6 T_{b3} + C_7 T_3\right) - \left(e_{33}\left(\frac{2c_{31}^E}{c_{33}^E}\varphi_{p1}^E + \varphi_{p3}^E\right) + P^S\right)\Delta\theta - \delta_s\bar{E}_3/s}{\frac{e_{33}^2}{c_{33}^E} + \varepsilon_{33}^S}$$

$$= \frac{-\frac{e_{33}}{c_{33}^E}T_3 - \beta\left(C_4\Delta\bar{\theta} + C_5\Delta\bar{\theta}_b + \left(C_6\frac{A_{ps}}{A_{bs}} + C_7\right)T_3\right) - \left(e_{33}\left(\frac{2c_{31}^E}{c_{33}^E}\varphi_{p1}^E + \varphi_{p3}^E\right) + P^S\right)\Delta\theta - \delta_s\bar{E}_3/s}{\frac{e_{33}^2}{c_{33}^E} + \varepsilon_{33}^S} \quad (4.21)$$

By subtracting Equation 4.21 from its spatial averaged version with respect to x_3 yields Equation 4.22 that relates the difference of E_3 and $\Delta\theta$ from their respective spatial mean values. Equation 4.22 is useful for determining the time dependent volume space charge density distribution in the piezoelectric medium discussed in Section 4.8.

$$(E_3 - \bar{E}_3) = -\frac{\left(e_{33}\left(\frac{2c_{31}^E}{c_{33}^E}\varphi_{p1}^E + \varphi_{p3}^E\right) + P^S\right)}{\frac{e_{33}^2}{c_{33}^E} + \varepsilon_{33}^S}(\Delta\theta - \Delta\bar{\theta}) \quad (4.22)$$

The electric displacement D_3 can be conveniently written in the Laplace domain as $D_3 = -\delta_s \bar{E}_3/s$ or equivalently in the time-domain as $D_3(t) = -\delta_s\bar{E}_3(t) * U(t)$ where $\delta_s = l_p/R_s A_s$ is defined as the equivalent electrical conductivity associated with an external resistance R_s connected externally across the piezoelectric element electrodes using the electrode surface area A_s and thickness l_p of the piezoelectric element. More specifically, the input resistance of a follow-on

signal-conditioning amplifier can be represented by R_s. The term $U(t)$ is the Heaviside step function and the symbol $*$ denotes time-domain convolution. The dash superscript in the permittivity term $\varepsilon_{33}^{S}{}'$ of Equations 4.18 to 4.20 for the spatially averaged electric field indicates that the electric displacement $D_3 = -\delta_s \bar{E}_3/s$ due to the equivalent conductivity δ_s may be added directly to the internal conductivity δ_{33} of the piezoelectric medium and included in the frequency dependent part of $\varepsilon_{33}^{S}{}'$. In the same way, the effect of a non-zero electric displacement D_3 may also be included directly in the permittivity terms of coefficients C_4 to C_7. On the other hand, in Equation 4.21 and Equation 4.22, δ_s cannot be added directly to δ_{33} in the denominator permittivity term but must be included in the numerator as the term $-c_{33}^{E}\delta_s \bar{E}_3/s$ shown in Equation 4.21. The electric displacement term does not appear in Equation 4.22, which is independent of the external electric displacement and the external mechanical clamping effects of the substrate.

The use of the Laplace domain throughout allows $p^S \Delta\theta$ to be replaced by $(p^S \Delta\theta + \delta_s \bar{E}_3/s)$ or equivalently for spatially averaged Equations, the permittivity ε_{33}^{S} to be replaced with $\varepsilon_{33}^{S}{}' = (\varepsilon_{33}^{S} + \delta_s/s)$, thereby simplifying the notation used and maintaining compatibility with the follow on analysis and solution of the heat diffusion equations discussed in Section 3.7 and Section 3.8. The direct substitution of ε_{33}^{S} with $\varepsilon_{33}^{S}{}' = (\varepsilon_{33}^{S} + \delta_s/s)$ reduces the algebraic manipulation required and is valid since C_4 to C_7 and $\bar{E}_3$ are obtained using the spatially averaged Equations 4.12, 4.13 and 4.16.

The sensor output voltage, given by $V_o = -l_p \bar{E}_3$, is ultimately required in the measurement of the sensor response and therefore it is the spatial mean of the electric field that is of specific interest. Equation 4.21 is therefore of little direct use in the analysis to follow, however in Section 4.4, Equation 4.22 is used together with Equation 4.18 to describe the nature of the spatial charge density in the piezoelectric medium and electrodes.

4.5 Effect of the substrate adhesive

The efficacy of the adhesive used to bond the piezoelectric electrode to the substrate is essential to ensure good mechanical coupling between the substrate and piezoelectric electrode. The mechanical effect of the adhesive layer on the mechanical response of the sensor element is analysed by applying a force equilibrium analysis and applying the relevant material properties of the piezoelectric medium, substrate and adhesive. It is assumed that the brass substrate is rigidly bonded to the PZT medium bottom electrode using an electrically conductive epoxy resin adhesive, and that the maximum temperature the sensor will be subjected to is below that of the adhesive glass transition temperature such that the adhesive remains in its vitreous or 'glass' form and behaves according to Hooke's law.

Equation 4.15, which is repeated below for clarity, does not take into account the effect of the substrate-piezoelectric electrode interface adhesive.

$$\bar{T} = -\frac{E_b A_b}{(1-\mu_b)A_p}\left(S + \frac{\mu_b}{E_b}T_{b3} - \varphi_b \Delta\bar{\theta}_b\right) \tag{4.15}$$

In the derivation of Equation 4.15 it was assumed that curvature due to thermal expansion is negligible such that the stresses in the 1- and 2- directions parallel to the sensor surface are constant along the 3-axis in each material layer and this is also assumed here. It is further assumed that the adhesive is exposed only to temperatures below its glass transition temperature, which is denoted by θ_g, such that the adhesive is always in its vitreous form. By setting the applied axial stress T_{b3} to zero, Equation 4.15 becomes Equation 4.23.

$$\bar{T} = -\frac{E_b A_b}{(1-\mu_b)A_p}(S - \varphi_b \Delta\bar{\theta}_b) = -\alpha_b \frac{A_b}{A_p}(S - \varphi_b \Delta\bar{\theta}_b) \tag{4.23}$$

Applying force equilibrium conditions that include the adhesive layer yields Equation 4.24.

$$\bar{T} = -\left(\frac{E_b A_b}{(1-\mu_b)A_p} + \frac{E_a A_a}{(1-\mu_a)A_p}\right)\left(S - \frac{E_b A_b \varphi_b (1-\mu_a) + E_a A_a \varphi_a (1-\mu_b)}{E_b A_b (1-\mu_a) + E_a A_a (1-\mu_b)}\Delta\bar{\theta}_b\right) \tag{4.24}$$

It can be seen that the effect of the adhesive is to modify Equation 4.23 such

that α_b and φ_b are replaced by the effective values denoted by α_{b-eff} and φ_{b-eff}. $\bar{T}$ is the spatial mean stress in the PZT along the 1- and 2- axes, S is the strain along the 1- and 2- axes in the substrate, PZT and adhesive, $\Delta\bar{\theta}_b$ is the spatial mean temperature in the substrate, E_a is the Young's modulus of the adhesive, and φ_a is the thermal expansion coefficient of the adhesive. The effect of the adhesive layer is therefore equivalent to replacing α_b and φ_b in Equation 4.24 such that:

$$\alpha_b \rightarrow \frac{E_b}{(1-\mu_b)} + \frac{E_a A_a}{(1-\mu_a)A_b} = \alpha_{b-eff}; \quad \varphi_b \rightarrow \frac{E_b A_b \varphi_b (1-\mu_a) + E_a A_a \varphi_a (1-\mu_b)}{E_b A_b (1-\mu_a) + E_a A_a (1-\mu_b)} = \varphi_{b-eff}$$

The coefficient of thermal expansion of conductive epoxy adhesives below the glass transition temperature is typically 50% greater than that of the brass substrate, however the thickness and Young's modulus of the adhesive layer are much lower than that of the substrate and PZT film. The adhesive type and adhesive layer thickness are not published by or available from the manufacturer of the PZT element (Murata). However, it is highly likely that the adhesive used is a type of electrically conductive epoxy resin commonly used in this application. Using the mechanical and thermal properties of a common conducting silver epoxy, Epo-Tek H20E [90], a typical Poisson's ratio for Epo-tek epoxy adhesives [91], and a typical adhesive thickness used in the PZT element, the relevant properties of the adhesive are estimated and given in Table 4.1 together with the relevant material properties and dimensions of the adhesive and substrate.

	Epo-Tek H20E adhesive	Substrate
Young's modulus	$E_a = 5.6GPa$	$E_b = 110GPa$
Poisson's ratio	$\mu_a = 0.3$	$\mu_b = 0.34$
Thermal expansion coefficient	$\varphi_a = 31 \times 10^{-6} K^{-1}$	$\varphi_b = 19 \times 10^{-6} K^{-1}$
Glass transition temperature	$\theta_g : > 80°C$	–
Thickness	$l_a = 20\mu m$	$l_b = 300\mu m$
Width	$w_a = 20mm$	$w_b = 27mm$
Diametric cross-sectional area	$A_a = 0.4 \times 10^{-6}\, m^2$	$A_b = 8.1 \times 10^{-6}\, m^2$

Table 4.1 Adhesive and substrate material properties and dimensions

Substituting the data from Table 4.1 into Equation 4.23 and Equation 4.24 and noting that the cross-sectional area of the piezoelectric medium is $A_p = 4.6 \times 10^{-6}\ m^2$ yields Equation 4.25 and 4.26 for the spatial mean stress in the piezoelectric medium without and with the effect of the adhesive, respectively.

$$\bar{T} = -2.935 \times 10^{11}(S - 19.000 \times 10^{-6}\Delta\bar{\theta}_b) \tag{4.25}$$

$$\bar{T} = -2.942 \times 10^{11}(S - 19.066 \times 10^{-6}\Delta\bar{\theta}_b) \tag{4.26}$$

Comparing Equation 4.25 with Equation 4.26 it is clear that α_{beff} differs from α_b and φ_{beff} differs from φ_b by less than 0.24% and 0.35% respectively. Assuming that the adhesive specification is similar to that listed above and given that the sensor element will be exposed to temperatures considerably less than θ_g, it can therefore be stated that it is reasonable to neglect the adhesive layer for temperatures below the glass transition temperature of the adhesive. At temperatures above θ_g, the substrate will become progressively mechanically decoupled from the piezoelectric medium, affecting the sensor response.

4.6 Effect of the substrate on the effective pyroelectric coefficient

With reference to Equation 4.18 the coefficients that contribute to the total pyroelectric effect, which are denoted by P_1 to P_4, are given by Equations 4.27 to 4.30 respectively where the temperature variables in brackets indicate the piezoelectric or substrate temperature applicable to each coefficient.

$$P_1 = p^s \qquad \text{Primary pyroelectric effect } (\Delta\bar{\theta}) \tag{4.27}$$

$$P_2 = 2e_{31}\varphi_{p1}^E + e_{33}\varphi_{p3}^E \qquad \text{Secondary pyroelectric effect } (\Delta\bar{\theta}) \tag{4.28}$$

$$P_3 = -\frac{\beta E_b A_b \varphi_{p1}^E}{E_b A_b + \alpha(1-\mu_b)A_p} \qquad \text{Substrate clamping effect } (\Delta\bar{\theta}) \tag{4.29}$$

$$P_4 = \frac{\beta E_b A_b \varphi_b}{E_b A_b + \alpha(1-\mu_b)A_p} \qquad \text{Substrate clamping effect } (\Delta\bar{\theta}_b) \tag{4.30}$$

P_1 is the primary pyroelectric coefficient at constant strain (mechanically clamped) which is solely attributable to a temperature-induced change in polarisation. P_2 is the secondary pyroelectric coefficient at constant electric field, which is solely due to thermal expansion and the piezoelectric effect in the absence of a substrate. P_3 and P_4 are additional pyroelectric effects due to substrate clamping. It can be seen that as expected, the substrate clamping effects vanish as the cross-sectional area of the substrate $A_b \to 0$. The constant stress primary pyroelectric coefficient for free thermal expansion in the piezoelectric medium is given by $P^T = P_1 + P_2$.

For a spatially uniform temperature change throughout the piezoelectric and substrate media, the effective pyroelectric coefficient for uniform temperature is denoted by $P_{eff} = P_1 + P_2 + P_3 + P_4$ and is given by Equation 4.31.

$$P_{eff} = \frac{\beta(\varphi_b - \varphi_p)E_b A_b}{E_b A_b + \alpha(1-\mu_b)A_p} + 2e_{31}\varphi_{p1}^E + e_{33}\varphi_{p3}^E + P^s \tag{4.31}$$

Using published data for PZT-5H and brass, which is listed in Appendix A.1 and was obtained from [88],[92],[93],[94], the pyroelectric coefficients were calculated and are given in Table 4.2.

$P_1 \approx -300$ to $-400 \mu C m^{-2} K^{-1}$	$P_2 \approx 41 \mu C m^{-2} K^{-1}$
$P_3 \approx 145 \mu C m^{-2} K^{-1}$	$P_4 \approx -687 \mu C m^{-2} K^{-1}$

Table 4.2 PZT-5H element pyroelectric coefficients

Using P_1 to P_4 in Table 4.2, P_{eff} can therefore be approximated as being in the range of $P_{eff} \approx -800$ to $-900 \mu C m^{-2} K^{-1}$. On the other hand, in the absence of the substrate, the effective pyroelectric coefficient is equal to $P^T = P_1 + P_2$ and therefore the effective pyroelectric coefficient can be approximated in the range of ≈ -260 to $-360\, \mu C m^{-2} K^{-1}$. The effect of substrate clamping is therefore to increase the effective pyroelectric coefficient to approximately 2.8 × the value of the constant stress pyroelectric coefficient, P^T.

In the absence of a substrate, the ratio of primary pyroelectric coefficient to secondary pyroelectric coefficient is approximately $10:1$ with the secondary effect acting to reduce the total constant stress pyroelectric coefficient, P^T compared to the constant strain primary pyroelectric coefficient, P^S. When the effect of the brass substrate is included as an additional secondary pyroelectric coefficient, which is given by $P_3 + P_4$, the total contribution of the secondary pyroelectric coefficient is therefore $P_2 + P_3 + P_4 \approx -500\mu C m^{-2} K^{-1}$, which has the same sign and is between $\sim 25\%$ and $\sim 70\%$ greater than the primary pyroelectric coefficient, P^S. Assuming an average value for P^S such that $P^S = -350\mu C m^{-2} K^{-1}$, the ratio of the secondary pyroelectric effect to the primary pyroelectric effect is therefore approximately $1.4:1$. The enhanced secondary response is largely due to thermal expansion in the brass substrate that is dominant due to its large Young's modulus of approximately $110GPa$, and a coefficient of thermal expansion greater than $4\times$ that of PZT in the 1- and 2-axes. It can therefore be stated that the pyroelectric response of the sensor is significantly enhanced by a factor of approximately $2.8\times$ due to thermal expansion in the brass substrate.

4.7 Equivalent circuit model – low frequency

Applying the relationship $V_o = -l_p \bar{E}_3$ to Equation 4.18 and writing in Laplace form such that $\varepsilon_{33}^{S\,\prime} = (\varepsilon_{33}^S + \delta_{33}/s)$ yields Equation 4.32 for the output voltage, V_o of the piezoelectric element where A_s is the surface area of the piezoelectric element electrodes.

$$V_o = A_s \frac{\left(2e_{31}\varphi_{p1}^E + e_{33}\varphi_{p3}^E + p^S - \frac{\beta E_b A_b \varphi_{p1}^E}{E_b A_b + \alpha(1-\mu_b)A_p}\right)\Delta\bar{\theta} + \frac{\beta E_b A_b \varphi_b \Delta\bar{\theta}_b - \beta\left((1-\mu_b)A_p \frac{c_{31}^E}{c_{33}^E} + \mu_b A_b \frac{A_{ps}}{A_{bs}}\right)T_3}{E_b A_b + \alpha(1-\mu_b)A_p} + \frac{e_{33}}{c_{33}^E}T_3}{\frac{A_s}{l_p}\left(\frac{(1-\mu_b)\beta^2 A_p}{2(E_b A_b + \alpha(1-\mu_b)A_p)} + \frac{e_{33}^2}{c_{33}^E} + \varepsilon_{33}^{S\,\prime}\right)} \tag{4.32}$$

It can be seen that in the case of zero internal and external conductivity such that $\delta_{33} = 0$ and $\delta_s = 0$, that Equation 4.32 is of the form of the parallel plate

capacitor equation given by $\mathrm{V} = \mathrm{Q}/\mathrm{C}$ where V is the voltage, Q is the charge and C is the capacitance. V_o may therefore be considered as due to a charge equal to the numerator of Equation 4.32 applied to a capacitor with capacitance equal to the denominator of Equation 4.32. By including the internal conductivity δ_{33}, an equivalent low frequency circuit model for the piezoelectric element can therefore be described by Figure 4.2 where C_p, R_p and Q are given by Equations 4.33 to 4.35 respectively. In Equation 4.33, the constant strain permittivity term stated excludes the δ_{33}/s term, and this term is instead represented by R_p in the model. If the substrate is notionally removed by setting $A_b = 0$, such that the piezoelectric medium would be allowed to move freely in all directions, the resultant term inside the brackets of Equation 4.33, given by $(\beta^2/2\alpha + e_{33}^2/c_{33}^E + \varepsilon_{33}^S)$ is the constant stress permittivity ε_{33}^T. Using the material constants given in Appendix A.1, the constant stress capacitance given by $A_s\varepsilon_{33}^T/l_p$ is approximately 50% higher than the low frequency clamped capacitance, C_p and therefore substrate clamping reduces the low frequency capacitance of the sensor element. The term $2e_{31}\varphi_{p1}^E + e_{33}\varphi_{p3}^E + p^S$ in Equation 4.35 is the constant stress pyroelectric coefficient p^T. The effect of substrate clamping on the pyroelectric coefficients is discussed in Section 4.6 above.

$$C_p = \frac{A_s}{l_p}\left(\frac{(1-\mu_b)\beta^2 A_p}{2\left(E_b A_b + \alpha(1-\mu_b)A_p\right)} + \frac{e_{33}^2}{c_{33}^E} + \varepsilon_{33}^S\right) \tag{4.33}$$

$$R_p = \frac{l_p}{\delta_{33} A_s} \tag{4.34}$$

$$\mathrm{Q} = A_s\left[\begin{array}{l}\left(2e_{31}\varphi_{p1}^E + e_{33}\varphi_{p3}^E + p^S - \frac{\beta E_b A_b \varphi_{p1}^E}{E_b A_b + \alpha(1-\mu_b)A_p}\right)\Delta\bar{\theta} + \\ \qquad \frac{\beta E_b A_b \varphi_b \Delta\bar{\theta}_b - \beta\left((1-\mu_b)A_p\frac{c_{31}^E}{c_{33}^E} + \mu_b A_b\frac{A_{ps}}{A_{bs}}\right)T_3}{E_b A_b + \alpha(1-\mu_b)A_p} + \frac{e_{33}}{c_{33}^E}T_3\end{array}\right] \tag{4.35}$$

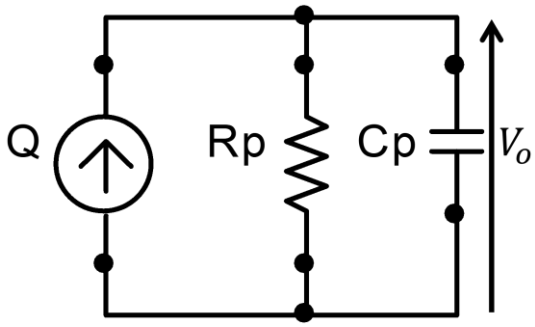

Figure 4.2 Sensor element low frequency equivalent circuit model

The equivalent circuit model shown in Figure 4.2 is used as the input model for the signal conditioning amplifier designs that are discussed in Chapter 6. The equivalent circuit model can also be written in the Laplace domain by replacing $j\omega$ with s. It is of interest to define the nature of the charge term Q described by Equation 4.35 and this is discussed in Section 4.8.

4.8 Definition of the charge term Q and charge distribution

4.8.1 Dielectric polarisation equations

In charge mode signal conditioning it is the free charge that flows between the piezoelectric sensor element electrodes, via the charge amplifier, in response to a change in the polarisation within the piezoelectric medium that yields a measure of surface temperature and applied axial stress. The change in polarisation due to a change in temperature is, in general, spatially dependent and results in the formation of surface and spatially dependent volume bound and free charge densities within the piezoelectric medium, and when externally connected also an additional surface free charge density on the piezoelectric element electrodes. Given this complexity, it is of interest to define the precise nature of the charge Q given by Equation 4.35, which is involved with the temperature and applied stress measurands, and the temporal and spatial distribution of the charge within the non-ideal piezoelectric medium and on the electrodes. The electric field, electric displacement and polarisation terms in the following analysis are given as Laplace transforms with respect to the time variable to reduce notation.

Equation 4.18 and Equation 4.22 given in Section 4.4.4 describe the spatial mean electric field denoted by $\bar{E}_3$, and difference of the spatially dependent electric field from the spatial mean electric field denoted by $(E_3 - \bar{E}_3)$ respectively. Summing these equations gives the total spatially dependent electric field in terms of the spatially dependent and spatial mean temperatures, and the applied axial stress, all of which are also functions of time. The nature and distribution of all bound and free charges in the piezoelectric medium and on the electrodes are identified by treating the contributions due to Equation 4.18 and Equation 4.22 separately and using superposition to obtain the instantaneous total charge distribution of bound and free charges.

Writing $\varepsilon_{33}^{S\,\prime}$ as $\varepsilon_{33}^{S\,\prime} = \varepsilon_o + \varepsilon_o\chi_{33}^S + \delta_{33}/s + \delta_s/s$ and $\varepsilon_{33}^S = \varepsilon_o + \varepsilon_o\chi_{33}^S + \delta_{33}/s$, Equation 4.18 and Equation 4.22 can be re-organised in the form of the general dielectric equation for polarised media given by $D = \varepsilon_o E + P$, where D, E, P and ε_o denote the electric displacement field, electric field, polarisation field and permittivity of free space respectively to yield Equation 4.36 and Equation 4.37. Q is as defined in Section 4.7 and A_s is the surface area of one electrode.

$$-\frac{\delta_s}{s}\bar{E}_3 = \varepsilon_o\bar{E}_3 + \left(\frac{(1-\mu_b)\beta^2 A_p}{2\left(E_b A_b + \alpha(1-\mu_b)A_p\right)} + \frac{e_{33}^2}{c_{33}^E} + \varepsilon_o\chi_{33}^S\right)\bar{E}_3 + \frac{\mathrm{Q}}{A_s} - \left(-\frac{\delta_{33}}{s}\right)\bar{E}_3 \quad (4.36)$$

$$0 = \varepsilon_o(E_3 - \bar{E}_3) + \left(\frac{e_{33}^2}{c_{33}^E} + \varepsilon_o\chi_{33}^S\right)(E_3 - \bar{E}_3) + \left(e_{33}\left(\frac{c_{31}^E}{c_{33}^E}\varphi_{p1}^E + \varphi_{p3}^E\right) + P^S\right)(\Delta\theta - \Delta\bar{\theta}) - \left(-\frac{\delta_{33}}{s}\right)(E_3 - \bar{E}_3) \quad (4.37)$$

Equation 4.36 and Equation 4.37 are used in Sections 4.8.2 and 4.8.3 to solve the surface and volume charge densities respectively.

4.8.2 Surface charge densities

By inspection of Equation 4.36 it can be seen that D is given by $-\delta_s\,\bar{E}_3/s$ and P is given by $\left(\frac{(1-\mu_b)\beta^2 A_p}{2\left(E_b A_b + \alpha(1-\mu_b)A_p\right)} + \frac{e_{33}^2}{c_{33}^E} + \varepsilon_o\chi_{33}^S\right)\bar{E}_3 + \frac{\mathrm{Q}}{A_s}$. The term $-\delta_{33}\,\bar{E}_3/s$ represents an electric displacement field component due to free charge on the surface of the

piezoelectric medium. Equation 4.36 can be written as Equation 4.38 by taking the divergence throughout.

$$-\frac{\delta_s}{s}\nabla.\bar{E}_3 = \varepsilon_o\nabla.\bar{E}_3 + \left(\frac{(1-\mu_b)\beta^2 A_p}{2\left(E_b A_b + \alpha(1-\mu_b)A_p\right)} + \frac{e_{33}^2}{c_{33}^E} + \varepsilon_o\chi_{33}^S\right)\nabla.\bar{E}_3 + \frac{1}{A_s}\nabla.\mathrm{Q} - \left(-\frac{\delta_{33}}{s}\right)\nabla.\bar{E}_3 \quad (4.38)$$

Equation 4.39 gives the divergence theorem for a field, $\boldsymbol{G}$ where $\boldsymbol{G}$ passes through a closed surface of area A that encloses a volume V and the vector $\boldsymbol{n}$ is the unit normal to the surface.

$$\iiint_V \nabla.\boldsymbol{G}\, dV = \oiint_A \boldsymbol{G}.\boldsymbol{n}\, dA \quad (4.39)$$

Since that by definition $\bar{E}_3$ is constant with respect to x_3 through the thickness of the piezoelectric medium and electrodes and are zero elsewhere, it can be stated that the divergence of $\bar{E}_3$ and the component of the polarisation field dependent on Q are zero within the body of the piezoelectric medium. Externally, the divergence of $\bar{E}_3$ and Q is infinite at the electrode-piezoelectric medium boundaries and therefore the volume charge density within the piezoelectric medium due to Equation 4.38 is zero such that charge exists only on the electrodes and piezoelectric surfaces.

Integrating Equation 4.38 over the piezoelectric volume and applying the divergence theorem yields Equation 4.40 where $\bar{J}_3$ is the spatial mean current density given by $\bar{J}_3 = \delta_{33}\bar{E}_3$.

$$-\frac{\delta_s}{s}\oiint_A \bar{E}_3.n\, dA = \varepsilon_o \oiint_A \bar{E}_3.n\, dA + \left(\frac{(1-\mu_b)\beta^2 A_p}{2\left(E_b A_b + \alpha(1-\mu_b)A_p\right)} + \frac{e_{33}^2}{c_{33}^E} + \varepsilon_o\chi_{33}^S\right)\oiint_A \bar{E}_3.n\, dA + \frac{1}{A_s}\oiint_A \mathrm{Q}.n\, dA + \frac{1}{s}\oiint_A \bar{J}_3.n\, dA \quad (4.40)$$

All terms in Equation 4.40 are in the form of Gauss's law such that the total charge, free charge and bound charge in the piezoelectric medium and electrodes due to the spatial mean polarisation and electric field can be written directly as Equations 4.41 to 4.43 respectively. The total charge $\overline{\mathrm{Q}}_\mathrm{t}$ is given by $\overline{\mathrm{Q}}_\mathrm{t} = \overline{\mathrm{Q}}_\mathrm{b} + \overline{\mathrm{Q}}_\mathrm{f}$ where $\overline{\mathrm{Q}}_\mathrm{b}$ is the bound charge and $\overline{\mathrm{Q}}_\mathrm{f}$ is the electric displacement free charge.

$$\overline{\mathrm{Q}}_{\mathrm{t}} = \varepsilon_o \oiint_A \overline{E}_3 . n \, dA \tag{4.41}$$

$$\overline{\mathrm{Q}}_{\mathrm{b}} = -\left(\frac{(1-\mu_b)\beta^2 A_p}{2\left(E_b A_b + \alpha(1-\mu_b)A_p\right)} + \frac{e_{33}^2}{c_{33}^E} + \varepsilon_o \chi_{33}^S \right) \oiint_A \overline{E}_3 . n \, dA - \frac{1}{A_s} \oiint_A \mathrm{Q} . n \, dA \tag{4.42}$$

$$\overline{\mathrm{Q}}_{\mathrm{f}} = -\frac{\sigma_s}{s} \oiint_A \overline{E}_3 . n \, dA - \frac{1}{s} \oiint_A \bar{J}_3 . n \, dA = -\frac{(\delta_s + \delta_{33})}{s} \oiint_A \overline{E}_3 . n \, dA \tag{4.43}$$

Since all fields are one-dimensional, are considered to be spatially constant, and exist only between the electrodes along the polar x_3 axis perpendicular to the integration surface, then $\overline{\mathrm{Q}}_{\mathrm{t}}$, $\overline{\mathrm{Q}}_{\mathrm{b}}$ and $\overline{\mathrm{Q}}_{\mathrm{f}}$ can be written as Equations 4.44 to 4.46 respectively, where the surface area of integration is over one electrode only.

$$\overline{\mathrm{Q}}_{\mathrm{t}} = \varepsilon_o A_s \bar{E}_3 \tag{4.44}$$

$$\overline{\mathrm{Q}}_{\mathrm{b}} = -\left(\frac{(1-\mu_b)\beta^2 A_p}{2\left(E_b A_b + \alpha(1-\mu_b)A_p\right)} + \frac{e_{33}^2}{c_{33}^E} + \varepsilon_o \chi_{33}^S \right) A_s \bar{E}_3 - \mathrm{Q} \tag{4.45}$$

$$\overline{\mathrm{Q}}_{\mathrm{f}} = -\frac{(\delta_s + \delta_{33})}{s} A_s \bar{E}_3 \tag{4.46}$$

The spatial mean component of the electric, displacement and polarisation fields begin on one electrode and end on the other, and by definition are constant throughout the thickness of the piezoelectric material. The location of all free charge due to the spatial mean field components therefore exists on the electrode at the electrode-piezoelectric surface boundaries only, while the location of all bound charge is on the surface of the piezoelectric medium only. All charges can therefore be described as surface charge densities. Furthermore, the surface free and bound charge on the opposite piezoelectric surface and electrode are equal and opposite in sign since the spatial mean electric and polarisation fields are in the opposite direction relative to the piezoelectric and electrode surface normal vectors.

Noting that since all fields are considered to be one-dimensional and exist only along the polar x_3 axis perpendicular to the integration surface, and using the definition of divergence, Equation 4.38 can be written as Equation 4.47.

$$-\frac{\delta_s}{s}\frac{\partial \bar{E}_3}{\partial x_3} = \varepsilon_o \frac{\partial \bar{E}_3}{\partial x_3} + \left(\frac{(1-\mu_b)\beta^2 A_p}{2\left(E_b A_b + \alpha(1-\mu_b)A_p\right)} + \frac{e_{33}^2}{c_{33}^E} + \varepsilon_o \chi_{33}^S \right) \frac{\partial \bar{E}_3}{\partial x_3} + \frac{1}{A_s}\frac{\partial \mathrm{Q}}{\partial x_3} + \frac{\delta_{33}}{s}\frac{\partial \bar{E}_3}{\partial x_3} \tag{4.47}$$

By comparing Equation 4.38 and Equation 4.47 and using the divergence theorem, the total, bound and free volume charge densities denoted by $\bar{\sigma}_t$, $\bar{\sigma}_b$ and $\bar{\sigma}_f$ respectively (C/m^3) due to the spatially averaged fields in the piezoelectric medium can be written as Equation 4.48 to Equation 4.50 respectively.

$$\bar{\sigma}_t = \varepsilon_o \frac{\partial \bar{E}_3}{\partial x_3} \tag{4.48}$$

$$\bar{\sigma}_b = -\left(\frac{(1-\mu_b)\beta^2 A_p}{2\left(E_b A_b + \alpha(1-\mu_b)A_p\right)} + \frac{e_{33}^2}{c_{33}^E} + \varepsilon_o \chi_{33}^S \right) \frac{\partial \bar{E}_3}{\partial x_3} - \frac{1}{A_s} \frac{\partial Q}{\partial x_3} \tag{4.49}$$

$$\bar{\sigma}_f = -\frac{(\delta_s + \delta_{33})}{s} \frac{\partial \bar{E}_3}{\partial x_3} \tag{4.50}$$

Since all fields are zero outside the piezoelectric medium, the $\bar{E}_3$ and Q dependent polarisation components can be described spatially by using the Heaviside step function denoted by U such that $\bar{E}_3 = \bar{E}_3\left[U(x_3) - U\left(x_3 - l_p\right)\right]$ and $\mathrm{Q} = \mathrm{Q}\left[U(x_3) - U\left(x_3 - l_p\right)\right]$, where l_p is the thickness of the piezoelectric medium. Taking spatial Laplace transforms of $\bar{E}_3$ and Q and denoting the spatial Laplace variable as p yields $\bar{E}_3(p) = \bar{E}_3\,(1 - e^{-px_3})/p$ and $\mathrm{Q}(p) = \mathrm{Q}\,(1 - e^{-px_3})/p$. The spatial Laplace transform of the differential with respect to x_3 of $\bar{E}_3$ and Q is therefore given by Equation 4.51 and Equation 4.52.

$$\mathcal{L}\left\{\frac{\partial \bar{E}_3}{\partial x_3}\right\} = \bar{E}_3(1 - e^{-px_3}) \tag{4.51}$$

$$\mathcal{L}\left\{\frac{\partial \mathrm{Q}}{\partial x_3}\right\} = \mathrm{Q}(1 - e^{-px_3}) \tag{4.52}$$

Inverse spatial Laplace transforming Equation 4.51 and Equation 4.52 yields Equation 4.53 and Equation 4.54 where δ denotes the Dirac delta function.

$$\frac{\partial \bar{E}_3}{\partial x_3} = \bar{E}_3\left[\delta(x_3) - \delta\left(x_3 - l_p\right)\right] \tag{4.53}$$

$$\frac{\partial Q}{\partial x_3} = Q\left[\delta(x_3) - \delta\left(x_3 - l_p\right)\right] \tag{4.54}$$

Substituting Equation 4.53 and Equation 4.54 into $\bar{\sigma}_t$, $\bar{\sigma}_b$ and $\bar{\sigma}_f$ yields Equations 4.55 to 4.57.

$$\bar{\sigma}_t = \varepsilon_o \bar{E}_3 \left[\delta(x_3) - \delta\left(x_3 - l_p\right)\right] \tag{4.55}$$

$$\bar{\sigma}_b = -\left[\left(\frac{(1-\mu_b)\beta^2 A_p}{2\left(E_b A_b + \alpha(1-\mu_b)A_p\right)} + \frac{e_{33}^2}{c_{33}^E} + \varepsilon_o \chi_{33}^S\right)\bar{E}_3 - \frac{1}{A_s}Q\right]\left[\delta(x_3) - \delta\left(x_3 - l_p\right)\right] \tag{4.56}$$

$$\bar{\sigma}_f = -\frac{(\delta_s + \delta_{33})}{s}\bar{E}_3\left[\delta(x_3) - \delta\left(x_3 - l_p\right)\right] \tag{4.57}$$

Considering the charge at $x_3 = 0$ only and noting that the area under a delta function is defined as unity, integration over the volume of the piezoelectric medium yields Equations 4.58 to 4.60 that as expected are identical to Equations 4.44 to 4.46 respectively. It can be seen that at $x_3 = l_p$ all charges are equal and opposite of those at $x_3 = 0$ as discussed above.

$$\overline{\mathrm{Q}}_t = \varepsilon_o A_s \bar{E}_3 \tag{4.58}$$

$$\overline{\mathrm{Q}}_b = -\left(\frac{(1-\mu_b)\beta^2 A_p}{2\left(E_b A_b + \alpha(1-\mu_b)A_p\right)} + \frac{e_{33}^2}{c_{33}^E} + \varepsilon_o \chi_{33}^S\right) A_s \bar{E}_3 - \mathrm{Q} \tag{4.59}$$

$$\overline{\mathrm{Q}}_f = -\frac{(\delta_s + \delta_{33})}{s} A_s \bar{E}_3 \tag{4.60}$$

It can be seen from Equation 4.59 that the bound charge $\overline{\mathrm{Q}}_\mathrm{b}$ is given by the negative sum of a term due to a spatial mean electric field dependent dielectric polarisation and the term Q due to a spatial mean temperature change and applied axial stress induced polarisation.

The charge term Q of the equivalent circuit shown in Figure 4.2 is therefore defined as the negative bound charge that is induced on the surface of the dielectric medium at the electrode boundary in response to the spatial mean of a polarisation distribution that is due only to the applied temperature change and/or axial stress polarisation components. It can furthermore be stated that after the application of temperature change or applied axial stress polarisation, $\overline{\mathrm{E}}_3$ will decay to zero as $\mathrm{t} \to \infty$, and as it does so the total charge $\overline{\mathrm{Q}}_\mathrm{t}$ will also tend to zero while the electric displacement free charge $\overline{\mathrm{Q}}_\mathrm{f}$ will tend toward Q.

4.8.3 Volume charge densities

By inspection of Equation 4.37 it can be seen that the electric displacement, D due to the difference $(E_3 - \bar{E}_3)$ electric field is zero and P is given by $\left(\frac{e_{33}^2}{c_{33}^E} + \varepsilon_o \chi_{33}^S\right)(E_3 - \bar{E}_3) + \left(e_{33}\left(\frac{c_{31}^E}{c_{33}^E}\varphi_{p1}^E + \varphi_{p3}^E\right) + P^S\right)(\Delta\theta - \Delta\bar{\theta})$. An additional electric displacement component due to a free charge distribution in the piezoelectric medium is represented by the term $-\delta_{33}\,(E_3 - \bar{E}_3)/s$.

Taking the divergence of Equation 4.37 yields Equation 4.61.

$$0 = \varepsilon_o \nabla.(E_3 - \bar{E}_3) + \left(\frac{e_{33}^2}{c_{33}^E} + \varepsilon_o \chi_{33}^S\right)\nabla.(E_3 - \bar{E}_3)$$

$$+\left(e_{33}\left(\frac{c_{31}^E}{c_{33}^E}\varphi_{p1}^E + \varphi_{p3}^E\right) + P^S\right)\nabla.(\Delta\theta - \Delta\bar{\theta}) + \frac{\delta_{33}}{s}\nabla.(E_3 - \bar{E}_3) \tag{4.61}$$

The total, bound and free volume charge densities that exist only within the body of the piezoelectric medium and which are denoted by σ_t, σ_b and σ_f respectively can be written directly by inspection of Equation 4.61 to yield Equations 4.62 to 4.64.

$$\sigma_t = \varepsilon_o \nabla.(E_3 - \bar{E}_3) \tag{4.62}$$

$$\sigma_b = -\left(\frac{e_{33}^2}{c_{33}^E} + \varepsilon_o \chi_{33}^S\right)\nabla.(E_3 - \bar{E}_3) - \left(e_{33}\left(\frac{c_{31}^E}{c_{33}^E}\varphi_{p1}^E + \varphi_{p3}^E\right) + P^S\right)\nabla.(\Delta\theta - \Delta\bar{\theta}) \tag{4.63}$$

$$\sigma_f = -\frac{\delta_{33}}{s}\nabla.(E_3 - \bar{E}_3) \tag{4.64}$$

It can therefore be stated that after the application of spatially dependent polarisation due to spatially dependent temperature change, the difference electric field $(E_3 - \bar{E}_3)$ will decay to zero everywhere within the piezoelectric medium as $t \to \infty$. As it does so, the spatially dependent total volume charge density σ_t will also tend to zero and the spatially dependent electric displacement free charge volume density σ_f will tend toward the spatially dependent negative volume bound charge density, $-\sigma_b$ everywhere in the piezoelectric medium. The applied axial stress T_3 has

no bearing on the volume charge densities since the applied stress is considered constant throughout the piezoelectric medium at the low frequencies of interest and therefore produces surface charge densities only. Similarly, the external conductivity δ_s also has no bearing on the volume free charge density since it results in a surface free charge density only.

In the steady state, as the electric field decays to zero everywhere in the piezoelectric medium, a free charge distribution will form within the body of the piezoelectric which is equal in magnitude and opposite in sign to the bound charge distribution at every point.

4.9 Temperature response model – substrate surface

4.9.1 Temperature response – Laplace form

To find an expression for the sensor output voltage response using the spatial mean electric field equation given by Equation 4.18, which was derived in Section 4.44, such that $V_o = -l_p \bar{E}_3$, it is necessary to solve the heat diffusion equations for $\Delta\theta$ and $\Delta\theta_b$ given by Equation 3.42 and Equation 3.47. These are repeated below for ease of reference.

$$\frac{\partial \Delta\theta}{\partial t} = K^{S,E} \frac{\partial^2 \Delta\theta}{\partial x_3^2} - \frac{\theta_o}{\boldsymbol{\rho} C_{sp}^{S,E}} \left(\boldsymbol{\gamma}^{E,t} \frac{\partial \boldsymbol{S}}{\partial t} + \boldsymbol{p}^{S,t} \frac{\partial \boldsymbol{E}}{\partial t} \right) \tag{3.42}$$

$$\frac{\partial \Delta\theta_b}{\partial t} = K_b^S \frac{\partial^2 \Delta\theta_b}{\partial x_3^2} - \frac{\theta_o}{\rho_b C_{spb}^S} \boldsymbol{\gamma}_b^t \frac{\partial \boldsymbol{S}_b}{\partial t} \tag{3.47}$$

In this section, the heat diffusion equations are solved under the constraints of the boundary conditions dictated by the sensor configuration. To solve the diffusion equations, it is necessary that these are written in a form such that only the temperatures $\Delta\theta$ and $\Delta\theta_b$ are functions of x_3. The elastic-dielectric coupling term $\boldsymbol{\gamma}^{E,t}\boldsymbol{S} + \boldsymbol{p}^{S,t}\boldsymbol{E}$ and elastic coupling term $\boldsymbol{\gamma}_b^t \boldsymbol{S}_b$ and the diffusion Equations 3.42 and 3.47 which are functions of both t and x_3 must therefore be written in terms of $\Delta\bar{\theta}_b$, $\Delta\bar{\theta}$, T_{b3}, T_3, which are functions of time only, and their respective temperatures $\Delta\theta$ and $\Delta\theta_b$, which are functions of t and x_3.

Creating the new scalar variable $\lambda = \lambda(x_3, s)$ to denote $\boldsymbol{\gamma}^{E,t}\boldsymbol{S} + \boldsymbol{p}^{S,t}\boldsymbol{E}$ and expanding yields Equation 4.65. Equations 4.2 and 4.3 are repeated below for ease of reference.

$$\lambda = 2\left(\varphi_{p1}^{E}(c_{11}^{E} + c_{12}^{E}) + \varphi_{p3}^{E}c_{31}^{E}\right)S + \left(\varphi_{p3}^{E}c_{33}^{E} + 2\varphi_{p1}^{E}c_{31}^{E}\right)S_3 + p^S E_3 \tag{4.65}$$

$$T_3 = 2c_{31}^{E}\left(S - \varphi_{p1}^{E}\Delta\theta\right) + c_{33}^{E}\left(S_3 - \varphi_{p3}^{E}\Delta\theta\right) - e_{33}E_3 \tag{4.2}$$

$$D_3 = 2e_{31}S + e_{33}S_3 + \varepsilon_{33}^{S}E_3 + p^S\Delta\theta \tag{4.3}$$

By taking temporal Laplace transforms of Equation 4.2 and Equation 4.3, Equation 4.65 can now be solved simultaneously using the variables λ, S_3, and E_3 together with Equation 4.2 and Equation 4.3, while setting $D_3 = 0$ to simplify the solution, to obtain λ in terms of S, $\Delta\theta$ and T_3 as given by Equation 4.66 where all variables and coefficients are functions of the Laplace variable s. The Laplace domain coefficients C_1 to C_3 are defined in Appendix A.7. The solution also yields the spatially dependent strain and electric field variables S_3 and E_3 and verifying that E_3 is the same as Equation 4.21 calculated in Section 4.4.4 is a useful check that the calculation is correct. The coupling term λ of the piezoelectric material is now in the desired form where only $\Delta\theta$ is a function of x_3.

$$\lambda = C_1 S + C_2\Delta\theta + C_3 T_3 \tag{4.66}$$

In contrast to the direct inclusion of D_3 in ε_{33}^{S} described above for C_4 to C_7 and $\bar{E}_3$, the electric displacement $D_3 = -\delta_s\,\bar{E}_3/s$ cannot be included directly via adjustment of ε_{33}^{S} in coefficients C_1 to C_3 since these are obtained using Equations 4.2, 4.3 and 4.65 where the electric field E_3 and axial strain S_3 are now spatially dependent. Only an internal electrical conductivity associated with a leakage conduction current within the piezoelectric medium may be accounted for in this way. However, by inspection of Equation 4.3, it can be seen that D_3 may be accounted for by replacing $p^S\Delta\theta$ by $(p^S\Delta\theta + \delta_s\,\bar{E}_3/s)$ in the $C_2\Delta\theta$ term of Equation 4.66 yielding an adjusted term $C_2\Delta\theta + \kappa$ that replaces $C_2\Delta\theta$ and is given by Equation 4.67. No adjustment is required for coefficients C_1 and C_3 since these do not contain terms in $p^S\Delta\theta$.

$$C_2\Delta\theta + \kappa = \frac{\varepsilon_{33}^S\left(2c_{31}^E\varphi_{p1}^E + c_{33}^E\varphi_{p3}^E\right)^2\Delta\theta - \left(e_{33}\left(2c_{31}^E\varphi_{p1}^E + c_{33}^E\varphi_{p3}^E\right) + c_{33}^E p^S\right)\left(p^S\Delta\theta + \delta_s\bar{E}_3/s\right)}{c_{33}^E\varepsilon_{33}^S + e_{33}^2} \quad (4.67)$$

To include the external electric displacement, the term κ must therefore be added to Equation 4.66 such that $\lambda \to \lambda + \kappa$ to yield Equation 4.68 where S has been substituted by Equation 4.17. The term κ (in Laplace domain form) is found by inspection from Equation 4.67 and is given by Equation 4.69. C_{14} is defined in Appendix A.7.

$$\lambda = C_1(C_4\Delta\bar{\theta} + C_5\Delta\bar{\theta}_b + C_6T_{b3}) + C_2\Delta\theta + \kappa + (C_3 + C_1C_7)T_3 \quad (4.68)$$

$$\kappa = -C_{14}\delta_s\frac{\bar{E}_3}{s} \quad (4.69)$$

By inspection of the Laplace domain Equation 4.18, the spatially averaged electric field response $\bar{E}_3$ can be written as Equation 4.70 where the Laplace domain coefficients C_{10} to C_{13} are defined in Appendix A.7.

$$\bar{E}_3 = C_{10}\Delta\bar{\theta} + C_{11}\Delta\bar{\theta}_b + C_{12}T_{b3} + C_{13}T_3 \quad (4.70)$$

For Equation 4.69 to be valid, the spatially averaged electric field $\bar{E}_3$ must also include the effect of the electric displacement by the replacement of occurrences of ε_{33}^S in coefficients C_{10} to C_{13} by $\varepsilon_{33}^{S\,\prime} = (\varepsilon_{33}^S + \delta_s/s)$.

Substituting Equation 4.70 into Equation 4.69 yields Equation 4.71.

$$\kappa = -\frac{\delta_s C_{14}}{s}(C_{10}\Delta\bar{\theta} + C_{11}\Delta\bar{\theta}_b + C_{12}T_{b3} + C_{13}T_3) \quad (4.71)$$

Substituting Equation 4.71 into Equation 4.68 and rearranging yields Equation 4.72 for λ that includes the effect of a electric displacement where occurrences of ε_{33}^S in the coefficients C_4 to C_7 have been replaced by $\varepsilon_{33}^{S\,\prime} = (\varepsilon_{33}^S + \delta_s/s)$.

$$\lambda = C_2\Delta\theta + \left(C_1C_4 - C_{14}C_{10}\frac{\delta_s}{s}\right)\Delta\bar{\theta} + \left(C_1C_5 - C_{14}C_{11}\frac{\delta_s}{s}\right)\Delta\bar{\theta}_b + \left(C_1C_6 - C_{14}C_{12}\frac{\delta_s}{s}\right)T_{b3} + \left(C_3 + C_1C_7 - C_{14}C_{13}\frac{\delta_s}{s}\right)T_3 \quad (4.72)$$

Equation 4.72 can also be written in the time-domain as Equation 4.73 where the coefficients $C_1(t)$ to $C_7(t)$ and $C_{10}(t)$ to $C_{14}(t)$ are now the impulse responses or inverse transforms of the Laplace domain coefficients.

$$\lambda(x_3,t) = C_2(t) * \Delta\theta(x_3,t) + \begin{pmatrix} C_1(t) * C_4(t) \\ -\delta_s C_{14}(t) * C_{10}(t) * U(t) \end{pmatrix} * \Delta\bar{\theta}(t)$$

$$+ \begin{pmatrix} C_1(t) * C_5(t) \\ -\delta_s C_{14}(t) * C_{11}(t) * U(t) \end{pmatrix} * \Delta\bar{\theta}_b(t) + \begin{pmatrix} C_1(t) * C_6(t) \\ -\delta_s C_{14}(t) * C_{12}(t) * U(t) \end{pmatrix} * T_{b3}(t)$$

$$+ \begin{pmatrix} C_3(t) + C_1(t) * C_7(t) \\ -\delta_s C_{14}(t) * C_{13}(t) * U(t) \end{pmatrix} * T_3(t) \quad (4.73)$$

Similarly for the substrate, defining a new scalar variable $\lambda_b = \lambda_b(x_3,t)$ to denote $\gamma_b^t S_b$ and expanding using Hooke's law for an isotropic material defined in Appendix A.5 yields Equation 4.74. Equation 4.7 is repeated below for ease of reference.

$$\lambda_b = \frac{E_b \varphi_b}{(1-2\mu_b)}(2S_b + S_{b3}) \quad (4.74)$$

$$S_{b3} = \frac{(1+\mu_b)(1-2\mu_b)}{E_b(1-\mu_b)} T_{b3} - \frac{2\mu_b}{(1-\mu_b)} S_b + \frac{(1+\mu_b)}{(1-\mu_b)} \varphi_b \Delta\theta_b \quad (4.7)$$

Taking Laplace transforms of Equations 4.74 and 4.7, and as before omitting the (s) notation, it being implicit that all variables and coefficients are in the Laplace domain unless otherwise stated, and using the definition of Hooke's law for an isotropic material allows S_{b3} to be obtained in terms of variables where only temperature is a function of x_3. Equation 4.75 is found by substituting for S_{b3} in Equation 4.74 using the Laplace transform of Equation 4.7.

$$\lambda_b = \frac{2E_b \varphi_b}{(1-\mu_b)} \left(S_b + \frac{(1+\mu_b)}{2E_b} T_{b3} + \frac{\varphi_b(1+\mu_b)}{2(1-2\mu_b)} \Delta\theta_b \right) \quad (4.75)$$

Noting that $S_b = S$ and substituting Equation 4.17 into 4.75 yields Equation 4.76 where, as before occurrences of ε_{33}^S in the (Laplace domain) coefficients C_4 to C_7 are replaced by $\varepsilon_{33}^{S\,\prime} = (\varepsilon_{33}^S + \delta_s/s)$.

$$\lambda_b = \frac{2E_b \varphi_b}{(1-\mu_b)} \left(C_4 \Delta\bar{\theta} + C_5 \Delta\bar{\theta}_b + \left(\frac{(1+\mu_b)}{2E_b} + C_6 \right) T_{b3} + C_7 T_3 + \frac{\varphi_b(1+\mu_b)}{2(1-2\mu_b)} \Delta\theta_b \right) \quad (4.76)$$

The coupling term λ_b of the substrate is now in the desired form where only $\Delta\theta_b$ is a function of x_3. Equation 4.76 can also be written in the time-domain as Equation 4.77 where the coefficients $C_4(t)$ to $C_7(t)$ are the impulse responses or inverse transforms of the Laplace domain coefficients.

$$\lambda_b(x_3,t) = \frac{2E_b\varphi_b}{(1-\mu_b)}(t) * \left(\begin{array}{c} C_4(t) * \Delta\bar{\theta}(t) + C_5(t) * \Delta\bar{\theta}_b(t) + \left(\frac{(1+\mu_b)}{2E_b} + C_6(t)\right) * T_{b3}(t) + \\ C_7(t) * T_3(t) + \frac{\varphi_b(1+\mu_b)}{2(1-2\mu_b)} * \Delta\theta_b(t) \end{array} \right) \tag{4.77}$$

The time-domain expressions for λ and λ_b given by Equation 4.73 and Equation 4.77 respectively may now be substituted into Equation 3.42 and Equation 3.47 respectively to yield Equations 4.78 and 4.79 respectively where $*$ denotes time-domain convolution. For generality it is assumed that $\theta_o/\rho C_{sp}^{S,E}$, $\theta_o/\rho_b C_{spb}^{S}$ K_b^S and $K^{S,E}$ are not necessarily constant such that their impulse responses are not necessarily weighted Dirac delta functions.

$$\frac{\partial\Delta\theta(x_3,t)}{\partial t} = K^{S,E} * \frac{\partial^2\Delta\theta(x_3,t)}{\partial x_3^2} - \frac{\theta_o}{\rho C_{sp}^{S,E}} * \frac{\partial}{\partial t}\lambda(x_3,t) \tag{4.78}$$

$$\frac{\partial\Delta\theta_b(x_3,t)}{\partial t} = K_b^S * \frac{\partial^2\Delta\theta_b(x_3,t)}{\partial x_3^2} - \frac{\theta_o}{\rho_b C_{spb}^{S}} * \frac{\partial}{\partial t}\lambda_b(x_3,t) \tag{4.79}$$

Assuming zero initial conditions at $t = 0$, taking Laplace transforms, and substituting Equation 4.76 and Equation 4.68 into Equation 4.78 and Equation 4.79 respectively yields Equation 4.80 and Equation 4.81 respectively where, the (s) and (x_3, s) notation have been omitted for brevity.

$$s\Delta\theta = K^{S,E}\frac{\partial^2\Delta\theta}{\partial x_3^2} - s\frac{\theta_o}{\rho C_{sp}^{S,E}}\left(\begin{array}{c} C_2\Delta\theta + \left(C_1C_4 - C_{14}C_{10}\frac{\delta_s}{s}\right)\Delta\bar{\theta} + \left(C_1C_5 - C_{14}C_{11}\frac{\delta_s}{s}\right)\Delta\bar{\theta}_b \\ + \left(C_1C_6 - C_{14}C_{12}\frac{\delta_s}{s}\right)T_{b3} + \left(C_3 + C_1C_7 - C_{14}C_{13}\frac{\delta_s}{s}\right)T_3 \end{array} \right) \tag{4.80}$$

$s\Delta\theta_b =$

$$K_b^S \frac{\partial^2 \Delta\theta_b}{\partial x_3^2} - s\frac{\theta_o}{\rho_b C_{spb}^S}\frac{2E_b\varphi_b}{(1-\mu_b)}\begin{pmatrix}\frac{\varphi_b(1+\mu_b)}{2(1-2\mu_b)}\Delta\theta_b + C_4\Delta\bar{\theta} + C_5\Delta\bar{\theta}_b \\ +C_7T_3 + \left(\frac{(1+\mu_b)}{2E_b} + C_6\right)T_{b3}\end{pmatrix} \tag{4.81}$$

Moving the $\Delta\theta$ and $\Delta\theta_b$ terms on the right hand sides of Equation 4.80 and Equation 4.81 to the left hand side and rationalising yields Equation 4.82 and Equation 4.83 where $K_{eff}^{S,E}$ and K_{effb}^{S} are the effective diffusion coefficients of the piezoelectric and substrate media due to dielectric-elastic-thermal coupling and elastic-thermal coupling respectively. The effective diffusion coefficients together with two new coefficients, C_8 and C_9 are defined in Table 4.3.

$K_{eff}^{S,E} = \frac{k_p}{\rho c_{sp}^{S,E} + C_2\theta_o}\left(\frac{m^2}{s}\right)$	$K_{effb}^{S} = \frac{k_b(1-\mu_b)(1-2\mu_b)}{\rho_b C_{spb}^S(1-\mu_b)(1-2\mu_b)+\theta_o\varphi_b^2E_b(1+\mu_b)}\left(\frac{m^2}{s}\right)$
$C_8 = \frac{\theta_o}{\rho c_{sp}^{S,E} + C_2\theta_o}\left(\frac{K^2m^2}{N}\right)$	$C_9 = \frac{2\theta_o\varphi_bE_b(1-2\mu_b)}{\rho_b c_{spb}^S(1-\mu_b)(1-2\mu_b)+\theta_o\varphi_b^2E_b(1+\mu_b)}\ (K)$

Table 4.3 Diffusion equation coefficients

$s\Delta\theta =$

$$K_{eff}^{S,E}\frac{\partial^2\Delta\theta}{\partial x_3^2} - sC_8\begin{pmatrix}\left(C_1C_4 - C_{14}C_{10}\frac{\delta_s}{s}\right)\Delta\bar{\theta} + \left(C_1C_5 - C_{14}C_{11}\frac{\delta_s}{s}\right)\Delta\bar{\theta}_b \\ +\left(C_1C_6 - C_{14}C_{12}\frac{\delta_s}{s}\right)T_{b3} + \left(C_3 + C_1C_7 - C_{14}C_{13}\frac{\delta_s}{s}\right)T_3\end{pmatrix} \tag{4.82}$$

$$s\Delta\theta_b = K_{effb}^{S}\frac{\partial^2\Delta\theta_b}{\partial x_3^2} - sC_9\begin{pmatrix}C_4\Delta\bar{\theta} + C_5\Delta\bar{\theta}_b + C_7T_3 \\ +\left(\frac{(1+\mu_b)}{2E_b} + C_6\right)T_{b3}\end{pmatrix} \tag{4.83}$$

Equation 4.82 and Equation 4.83 can now be solved for $\Delta\theta$ and $\Delta\theta_b$ under constraint of the relevant boundary conditions. The spatial average temperatures, $\Delta\bar{\theta}$ and $\Delta\bar{\theta}_b$ are then obtained by integrating these results over the respective thicknesses of each media. By substitution of $\Delta\bar{\theta}$ and $\Delta\bar{\theta}_b$ into Equation 4.18 with $V_o = -l_p\bar{E}_3$,

the piezoelectric output voltage response to a change in surface temperature and/or applied stress is obtained.

Defining the coupling terms $\eta(s)$ and $\xi(s)$ in Table 4.4 as follows allows Equation 4.82 and Equation 4.83 to be written as Equation 4.84 and Equation 4.85 respectively.

$\eta(s) = C_8 \begin{pmatrix} \left(C_1C_4 - C_{14}C_{10}\frac{\delta_s}{s}\right)\Delta\bar{\theta} \\ +\left(C_1C_5 - C_{14}C_{11}\frac{\delta_s}{s}\right)\Delta\bar{\theta}_b \\ +\left(C_1C_6 - C_{14}C_{12}\frac{\delta_s}{s}\right)T_{b3} \\ +\left(C_3 + C_1C_7 - C_{14}C_{13}\frac{\delta_s}{s}\right)T_3 \end{pmatrix}$	$\xi(s) = C_9\begin{pmatrix} C_4\Delta\bar{\theta} + C_5\Delta\bar{\theta}_b + C_7T_3 \\ +\left(\frac{(1+\mu_b)}{2E_b} + C_6\right)T_{b3} \end{pmatrix}$

Table 4.4 Laplace domain coupling terms

$$s\Delta\theta(x_3,s) = K_{eff}^{S,E}\frac{\partial^2\Delta\theta(x_3,s)}{\partial x_3^2} - s\eta(s) \tag{4.84}$$

$$s\Delta\theta_b(x_3,s) = K_{effb}^{S}\frac{\partial^2\Delta\theta_b(x_3,s)}{\partial x_3^2} - s\xi(s) \tag{4.85}$$

Equation 4.84 and Equation 4.85 can also be written in the time-domain by taking the inverse Laplace transform of Equation 4.82 and Equation 4.83 to yield Equation 4.86 and Equation 4.87 respectively.

$$\frac{\partial\Delta\theta(x_3,t)}{\partial t} = K_{eff}^{S,E}(t) * \frac{\partial^2\Delta\theta(x_3,t)}{\partial x_3^2} - C_8(t) * \frac{\partial}{\partial t}\begin{pmatrix} \begin{pmatrix} C_1(t) * C_4(t) \\ -\delta_s C_{14}(t) * C_{10}(t) * U(t) \end{pmatrix} * \Delta\bar{\theta}(t) \\ +\begin{pmatrix} C_1(t) * C_5(t) \\ -\delta_s C_{14}(t) * C_{11}(t) * U(t) \end{pmatrix} * \Delta\bar{\theta}_b(t) \\ +\begin{pmatrix} C_1(t) * C_6(t) \\ -\delta_s C_{14}(t) * C_{12}(t) * U(t) \end{pmatrix} * T_{b3}(t) \\ +\begin{pmatrix} C_3(t) + C_1(t) * C_7(t) \\ -\delta_s C_{14}(t) * C_{13}(t) * U(t) \end{pmatrix} * T_3(t) \end{pmatrix} \tag{4.86}$$

$$\frac{\partial \Delta\theta_b(x_3,t)}{\partial t} =$$

$$K^S_{effb}(t) * \frac{\partial^2 \Delta\theta_b(x_3,t)}{\partial x_3^2} - C_9(t) * \frac{\partial}{\partial t}\left(\begin{array}{c} C_4(t) * \Delta\bar{\theta}(t) + C_5(t) * \Delta\bar{\theta}_b(t) + \\ \left(\frac{(1+\mu_b)}{2E_b}(t) + C_6(t)\right) * T_{b3}(t) + C_7(t) * T_3(t) \end{array}\right) \quad (4.87)$$

Equation 4.86 and Equation 4.87 are now solved for temporal initial conditions that are assumed to be zero and boundary conditions that are as shown in Figure 4.3.

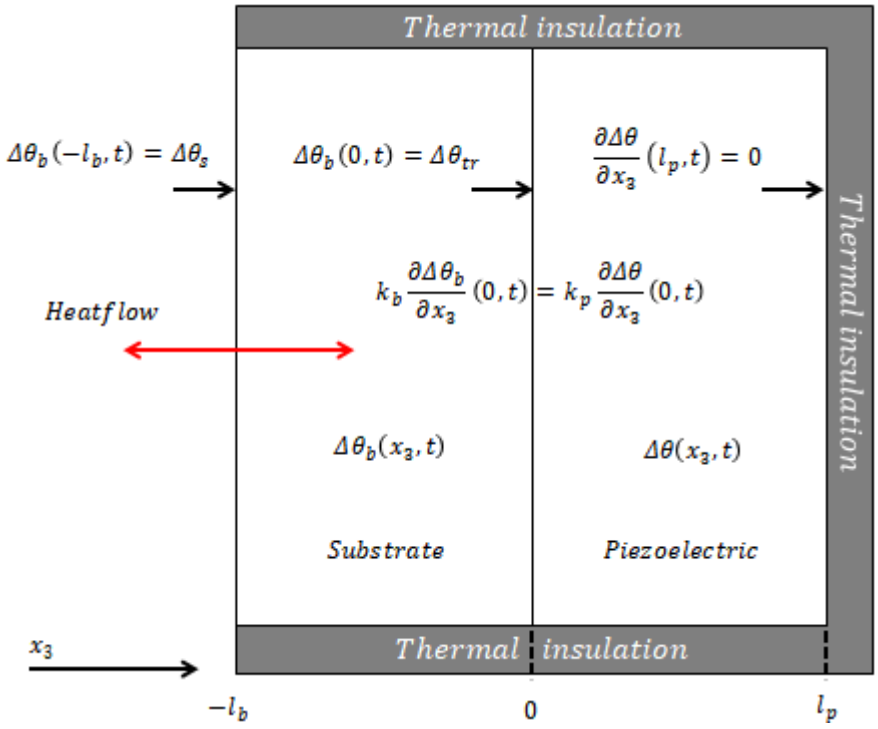

Figure 4.3 Sensor configuration and boundary conditions

It is assumed that a negligible amount of heat flows across the boundary at $x_3 = l_p$ and therefore the temperature gradient at $x_3 = l_p$ is assumed to be zero such that $\frac{\partial\Delta\theta}{\partial x_3}(l_p,t) = 0$. Furthermore, since heat flow across a boundary is continuous, then $k_b\frac{\partial\Delta\theta_b}{\partial x_3}(0,t) = k_p\frac{\partial\Delta\theta}{\partial x_3}(0,t)$.

Starting with Equation 4.86 and Equation 4.87, the coupling terms of the piezoelectric and substrate are now denoted by $\eta'(t)$ and $\xi'(t)$ and are given in Table 4.5.

$\eta'(t) =$ $\begin{pmatrix} C_1(t) * C_4(t) \\ -\delta_s C_{14}(t) * C_{10}(t) * U(t) \end{pmatrix} * \Delta\bar{\theta}(t) +$ $\begin{pmatrix} C_1(t) * C_5(t) \\ -\delta_s C_{14}(t) * C_{11}(t) * U(t) \end{pmatrix} * \Delta\bar{\theta}_b(t) +$ $\begin{pmatrix} C_1(t) * C_6(t) \\ -\delta_s C_{14}(t) * C_{12}(t) * U(t) \end{pmatrix} * T_{b3}(t) +$ $\begin{pmatrix} C_3(t) + C_1(t) * C_7(t) \\ -\delta_s C_{14}(t) * C_{13}(t) * U(t) \end{pmatrix} * T_3(t)$	$\xi'(t) =$ $\begin{pmatrix} C_4(t) * \Delta\bar{\theta}(t) \\ +C_5(t) * \Delta\bar{\theta}_b(t) \\ +\left(\frac{(1+\mu_b)}{2E_b} + C_6(t)\right) * T_{b3}(t) \\ +C_7(t) * T_3(t) \end{pmatrix}$

Table 4.5 Time-domain coupling terms

Substituting the time-domain coupling terms into Equation 4.86 and Equation 4.87 respectively yields Equation 4.88 and Equation 4.89.

$$\frac{\partial \Delta\theta(x_3,t)}{\partial t} = K_{eff}^{S,E}(t) * \frac{\partial^2 \Delta\theta(x_3,t)}{\partial x_3^2} - C_8(t) * \frac{\partial \eta'(t)}{\partial t} \tag{4.88}$$

$$\frac{\partial \Delta\theta_b(x_3,t)}{\partial t} = K_{effb}^{S}(t) * \frac{\partial^2 \Delta\theta_b(x_3,t)}{\partial x_3^2} - C_9(t) * \frac{\partial \xi'(t)}{\partial t} \tag{4.89}$$

Equation 4.88 and Equation 4.89 are second order non-homogenous partial differential equations and are now solved using the double Laplace transform method [95] applied to both temporal and spatial variables. As verification of this method, the 'variation of parameters' method was also applied to the spatial variable after taking Laplace transforms with respect to time. As expected, the analysis yielded the same solution for the given boundary and initial conditions, confirming the validity of the spatial Laplace method.

Starting with Equation 4.88 for the piezoelectric medium and taking the Laplace transform with respect to the time variable and assuming zero initial conditions such that in the time-domain $\Delta\theta(x_3, 0) = \eta(0) = 0$, recovers Equation 4.84, which is repeated below, where $\eta(s) = C_8(s)\eta'(s)$.

$$s\Delta\theta(x_3,s) = K_{eff}^{S,E}\frac{\partial^2\Delta\theta(x_3,s)}{\partial x_3^2} - s\eta(s) \tag{4.84}$$

Defining a spatial Laplace variable p, and taking the spatial Laplace transform of Equation 4.84 yields Equation 4.90, where the dash superscript denotes the spatial derivative.

$$s\Delta\theta(p,s) = K_{eff}^{S,E}\left(p^2\Delta\theta(p,s) - p\Delta\theta(0,s) - \Delta\theta'(0,s)\right) - \frac{s}{p}\eta(s) \tag{4.90}$$

Rearranging Equation 4.90 and rationalising yields Equation 4.91.

$$\Delta\theta(p,s) = \frac{p\Delta\theta(0,s)+\Delta\theta'(0,s)}{\left(p-\sqrt{\frac{s}{K_{eff}^{S,E}}}\right)\left(p+\sqrt{\frac{s}{K_{eff}^{S,E}}}\right)} + \frac{s\eta(s)}{pK_{eff}^{S,E}\left(p-\sqrt{\frac{s}{K_{eff}^{S,E}}}\right)\left(p+\sqrt{\frac{s}{K_{eff}^{S,E}}}\right)} \tag{4.91}$$

Equation 4.92 is found by expressing Equation 4.91 as a sum of partial fractions.

$$\Delta\theta(p,s) = \frac{A}{2\left(p-\sqrt{\frac{s}{K_{eff}^{S,E}}}\right)} + \frac{B}{2\left(p+\sqrt{\frac{s}{K_{eff}^{S,E}}}\right)} + \eta(s)\left[\frac{1}{2\left(p-\sqrt{\frac{s}{K_{eff}^{S,E}}}\right)} + \frac{1}{2\left(p+\sqrt{\frac{s}{K_{eff}^{S,E}}}\right)} - \frac{1}{p}\right] \tag{4.92}$$

The terms A and B are given by:

$$A = \Delta\theta(0,s) + \sqrt{\frac{K_{eff}^{S,E}}{s}}\Delta\theta'(0,s); \qquad B = \Delta\theta(0,s) - \sqrt{\frac{K_{eff}^{S,E}}{s}}\Delta\theta'(0,s)$$

Inverse Laplace transforming Equation 4.92 with respect to the spatial variable yields Equation 4.93. This solution is valid on the interval $0 \le x_3 \le l_p$ since $\Delta\theta(x_3,s)$ is defined only within these limits.

$$\Delta\theta(x_3,s) = \left[\frac{A}{2}e^{\sqrt{\frac{s}{K_{eff}^{S,E}}}x_3} + \frac{B}{2}e^{-\sqrt{\frac{s}{K_{eff}^{S,E}}}x_3}\right] + \eta(s)\left[\frac{1}{2}e^{\sqrt{\frac{s}{K_{eff}^{S,E}}}x_3} + \frac{1}{2}e^{-\sqrt{\frac{s}{K_{eff}^{S,E}}}x_3} - 1\right] \tag{4.93}$$

With reference to Figure 4.3, the boundary conditions are $\frac{\partial \Delta\theta}{\partial x_3}\left(l_p, s\right) = 0$ and $\Delta\theta(0,s) = \Delta\theta_{tr}(s)$, where $\Delta\theta_{tr}(s)$ is the temporal Laplace transform of the transition or common boundary temperature of the two media.

Setting $x_3 = 0$ yields Equation 4.94.

$$\Delta\theta(0,s) = \Delta\theta_{tr}(s) = \frac{A+B}{2} \tag{4.94}$$

Equation 4.94 can be confirmed by substituting the expressions for A and B containing the Laplace $x_3 = 0$ spatial initial conditions into Equation 4.94 to yield the left hand side as expected. Differentiating Equation 4.93 with respect to x_3 and setting equal to zero with x_3 set to $x_3 = l_p$ yields Equation 4.95.

$$0 = Ae^{\sqrt{\frac{s}{K^{S,E}_{eff}}}l_p} - Be^{-\sqrt{\frac{s}{K^{S,E}_{eff}}}l_p} + \eta(s)\left(e^{\sqrt{\frac{s}{K^{S,E}_{eff}}}l_p} - e^{-\sqrt{\frac{s}{K^{S,E}_{eff}}}l_p}\right) \tag{4.95}$$

Solving for A and B using Equation 4.94 and Equation 4.95 yields Equation 4.96 and Equation 4.97 respectively.

$$A = \frac{2\Delta\theta_{tr}(s)e^{-\sqrt{\frac{s}{K^{S,E}_{eff}}}l_p} - \eta(s)\left(e^{\sqrt{\frac{s}{K^{S,E}_{eff}}}l_p} - e^{-\sqrt{\frac{s}{K^{S,E}_{eff}}}l_p}\right)}{e^{\sqrt{\frac{s}{K^{S,E}_{eff}}}l_p} + e^{-\sqrt{\frac{s}{K^{S,E}_{eff}}}l_p}} \tag{4.96}$$

$$B = \frac{2\Delta\theta_{tr}(s)e^{\sqrt{\frac{s}{K^{S,E}_{eff}}}l_p} + \eta(s)\left(e^{\sqrt{\frac{s}{K^{S,E}_{eff}}}l_p} - e^{-\sqrt{\frac{s}{K^{S,E}_{eff}}}l_p}\right)}{e^{\sqrt{\frac{s}{K^{S,E}_{eff}}}l_p} + e^{-\sqrt{\frac{s}{K^{S,E}_{eff}}}l_p}} \tag{4.97}$$

Substituting Equation 4.96 and Equation 4.97 into Equation 4.93 and writing the exponential terms in hyperbolic form yields the spatial temperature distribution, $\Delta\theta(x_3, s)$given by Equation 4.98, which is valid over the interval $0 \leq x_3 \leq l_p$.

$$\Delta\theta(x_3,s)=\frac{\Delta\theta_{tr}(s)cosh\sqrt{\frac{s}{K_{eff}^{S,E}}}(x_3-l_p)\ +\eta(s)\left(cosh\sqrt{\frac{s}{K_{eff}^{S,E}}}(x_3-l_p)\ -cosh\sqrt{\frac{s}{K_{eff}^{S,E}}}l_p\right)}{cosh\sqrt{\frac{s}{K_{eff}^{S,E}}}l_p} \quad (4.98)$$

The spatial average $\Delta\bar{\theta}(s)$ required to determine the electric field response is given by $\Delta\bar{\theta}(s)=\frac{1}{l_p}\int_0^{l_p}\Delta\theta(x_3,s)dx_3$ yielding Equation 4.99.

$$\Delta\bar{\theta}(s)=\frac{\frac{\Delta\theta_{tr}(s)}{l_p}\sqrt{\frac{K_{eff}^{S,E}}{s}}sinh\sqrt{\frac{s}{K_{eff}^{S,E}}}l_p\ +\frac{\eta(s)}{l_p}\left(\sqrt{\frac{K_{eff}^{S,E}}{s}}sinh\sqrt{\frac{s}{K_{eff}^{S,E}}}l_p-l_p\,cosh\sqrt{\frac{s}{K_{eff}^{S,E}}}l_p\right)}{cosh\sqrt{\frac{s}{K_{eff}^{S,E}}}l_p} \quad (4.99)$$

The solution of Equation 4.89 for the substrate follows a similar procedure, however since the substrate temperature interval starts at $x_3=-l_b$ rather than zero, an axis transformation of $X_3=x_3+l_b$ is necessary to shift the spatial temperature distribution by $-l_b$ before applying the spatial Laplace transform to Equation 4.89.

Taking the temporal Laplace transform with respect to time of the spatially shifted Equation 4.89 for the substrate and setting zero initial conditions such that $\Delta\theta_b(X_3,0)=0$, yields Equation 4.100 where $\xi(s)=C_9(s)\xi'(s)$.

$$s\Delta\theta_b(X_3,s)=K_{effb}^{S}\frac{\partial^2\Delta\theta(X_3,s)}{\partial X_3^2}-s\xi(s) \quad (4.100)$$

Applying the spatial shift and taking spatial Laplace transforms with respect to X_3 yields Equation 4.101.

$$s\Delta\theta_b(p,s)e^{pl_b}=K_{effb}^{S}\left(p^2\Delta\theta_b(p,s)-p\Delta\theta_b(-l_b,s)-\Delta\theta_b{}'(-l_b,s)\right)e^{pl_b}$$
$$-\frac{s}{p}\xi(s)e^{pl_b} \quad (4.101)$$

The e^{pl_b} spatial shift factor is common to every term in Equation 4.101 and can therefore be cancelled throughout, it being understood that the inverse spatial Laplace transform of $\Delta\theta_b(p,s)$ is in terms of X_3 and that the axis shift $X_3\rightarrow x_3+l_b$ must be substituted after inverse Laplace transformation. This is equivalent to requiring the inverse Laplace transform of $\Delta\theta_b(p,s)e^{pl_b}$ without the spatial

transformation. In Equation 4.101, cases of $-l_b$ shown in brackets are left in terms of x_3 and have equivalent X_3 values of zero. Equation 4.101 can therefore be written as Equation 4.102.

$$s\Delta\theta_b(p,s) = K^S_{effb}\left(p^2\Delta\theta_b(p,s) - p\Delta\theta_b(0,s) - \Delta\theta_b{}'(0,s)\right) - \frac{s}{p}\xi(s) \qquad (4.102)$$

Rearranging Equation 4.102 and rationalising yields Equation 4.103.

$$\Delta\theta_b(p,s) = \frac{p\Delta\theta_b(0,s)+\Delta\theta_b{}'(0,s)}{\left(p-\sqrt{\frac{s}{K^S_{effb}}}\right)\left(p+\sqrt{\frac{s}{K^S_{effb}}}\right)} + \frac{s\xi(s)}{pK^{S,E}_{eff}\left(p-\sqrt{\frac{s}{K^S_{effb}}}\right)\left(p+\sqrt{\frac{s}{K^S_{effb}}}\right)} \qquad (4.103)$$

Equation 4.104 is found by expressing Equation 4.103 as a sum of partial fractions.

$$\Delta\theta_b(p,s) = \frac{A'}{2\left(p-\sqrt{\frac{s}{K^S_{effb}}}\right)} + \frac{B'}{2\left(p+\sqrt{\frac{s}{K^S_{effb}}}\right)} + \\ +\xi(s)\left[\frac{1}{2\left(p-\sqrt{\frac{s}{K^S_{effb}}}\right)} + \frac{1}{2\left(p+\sqrt{\frac{s}{K^S_{effb}}}\right)} - \frac{1}{p}\right] \qquad (4.104)$$

The terms A' and B' are given by:

$$A' = \Delta\theta_b(0,s) + \sqrt{\frac{K^S_{effb}}{s}}\Delta\theta_b'(0,s); \quad B' = \Delta\theta_b(0,s) - \sqrt{\frac{K^S_{effb}}{s}}\Delta\theta_b'(0,s)$$

Inverse Laplace transforming Equation 4.104 with respect to the spatial variable yields Equation 4.105. This solution is valid on the interval $0 \le X_3 \le l_b$ since $\Delta\theta(X_3,s)$ is defined only within these limits.

$$\Delta\theta_b(X_3,s) = \left[\frac{A'}{2}e^{\sqrt{\frac{s}{K^S_{effb}}}X_3} + \frac{B'}{2}e^{-\sqrt{\frac{s}{K^S_{effb}}}X_3}\right] + \xi(s)\left[\frac{1}{2}e^{\sqrt{\frac{s}{K^S_{effb}}}X_3} + \frac{1}{2}e^{-\sqrt{\frac{s}{K^S_{effb}}}X_3} - 1\right]$$

(4.105)

Substituting the spatial shift $X_3 = x_3 + l_b$ into Equation 4.105 yields Equation 4.106.

$$\Delta\theta_b(x_3, s) = \left[\frac{A'}{2} e^{\sqrt{\frac{s}{K^S_{effb}}}(x_3+l_b)} + \frac{B'}{2} e^{-\sqrt{\frac{s}{K^S_{effb}}}(x_3+l_b)}\right] + \\ +\xi(s)\left[\frac{1}{2} e^{\sqrt{\frac{s}{K^S_{effb}}}(x_3+l_b)} + \frac{1}{2} e^{-\sqrt{\frac{s}{K^S_{effb}}}(x_3+l_b)} - 1\right] \quad (4.106)$$

The terms A' and B' are now given by:

$$A' = \Delta\theta_b(-l_b, s) + \sqrt{\frac{K^S_{effb}}{s}}\Delta\theta'_b(-l_b, s); \quad B' = \Delta\theta_b(-l_b, s) - \sqrt{\frac{K^S_{effb}}{s}}\Delta\theta'_b(-l_b, s)$$

This solution is valid on the interval $-l_b \le x_3 \le 0$ since $\Delta\theta_b(x_3, s)$ is defined only within these limits. With reference to Figure 4.3, the boundary conditions are $\Delta\theta_b(0, s) = \Delta\theta_{tr}(s)$ and $\Delta\theta_b(-l_b, s) = \Delta\theta_s(s)$, where $\Delta\theta_s(s)$ is the temporal Laplace transform of the temperature measurand.

Setting $x_3 = -l_b$ yields Equation 4.107.

$$\Delta\theta(-l_b, s) = \Delta\theta_s(s) = \frac{A'+B'}{2} \quad (4.107)$$

Equation 4.107 can be confirmed by substituting the expressions for A' and B' above containing the Laplace $x_3 = -l_b$ spatial initial conditions into Equation 4.107 to yield the left hand side as expected. Setting $x_3 = 0$ yields Equation 4.108.

$$\Delta\theta_b(0, s) = \Delta\theta_{tr}(s) = \left[\frac{A'}{2} e^{\sqrt{\frac{s}{K^S_{effb}}}l_b} + \frac{B'}{2} e^{-\sqrt{\frac{s}{K^S_{effb}}}l_b}\right] + \\ +\xi(s)\left[\frac{1}{2} e^{\sqrt{\frac{s}{K^S_{effb}}}l_b} + \frac{1}{2} e^{-\sqrt{\frac{s}{K^S_{effb}}}l_b} - 1\right] \quad (4.108)$$

Solving for A' and B' using Equation 4.107 and Equation 4.108 yields Equation 4.109 and Equation 4.110 respectively.

$$A' = \frac{2\Delta\theta_{tr}(s) - 2\Delta\theta_s(s)e^{-\sqrt{\frac{s}{K^S_{effb}}}l_b} - \xi(s)\left(e^{\sqrt{\frac{s}{K^S_{effb}}}l_b} + e^{-\sqrt{\frac{s}{K^S_{effb}}}l_b} - 2\right)}{e^{\sqrt{\frac{s}{K^S_{effb}}}l_b} - e^{-\sqrt{\frac{s}{K^S_{effb}}}l_b}} \tag{4.109}$$

$$B' = \frac{2\Delta s(s)e^{\sqrt{\frac{s}{K^S_{effb}}}l_b} - 2\Delta\theta_{tr}(s) + \xi(s)\left(e^{\sqrt{\frac{s}{K^S_{effb}}}l_b} + e^{-\sqrt{\frac{s}{K^S_{effb}}}l_b} - 2\right)}{e^{\sqrt{\frac{s}{K^S_{effb}}}l_b} - e^{-\sqrt{\frac{s}{K^S_{effb}}}l_b}} \tag{4.110}$$

Substituting Equation 4.109 and Equation 4.110 into Equation 4.106 and writing the exponential terms in hyperbolic form yields the spatial temperature distribution, $\Delta\theta_b(x_3, s)$given by Equation 4.111, which is valid for $-l_b \leq x_3 \leq 0$.

$$\Delta\theta_b(x_3, s) = \frac{\Delta\theta_{tr}(s)\sinh\sqrt{\frac{s}{K^S_{effb}}}(x_3 + l_b) - \Delta\theta_s(s)\sinh\sqrt{\frac{s}{K^S_{effb}}}x_3 - \xi(s)\left(\sinh\sqrt{\frac{s}{K^S_{effb}}}x_3 - \sinh\sqrt{\frac{s}{K^S_{effb}}}(x_3 + l_b) + \sinh\sqrt{\frac{s}{K^S_{effb}}}l_b\right)}{\sinh\sqrt{\frac{s}{K^S_{effb}}}l_b} \tag{4.111}$$

The spatial average $\Delta\bar{\theta}_b(s)$ required to determine the electric field response is given by $\Delta\bar{\theta}_b(s) = \frac{1}{l_b}\int_{-l_b}^{0}\Delta\theta_b(x_3, s)dx_3$ and is given by Equation 4.112.

$$\Delta\bar{\theta}_b(s) = \sqrt{\frac{K^S_{effb}}{s}}\frac{\left(\cosh\sqrt{\frac{s}{K^S_{effb}}}l_b - 1\right)}{l_b\sinh\sqrt{\frac{s}{K^S_{effb}}}l_b}\left(\Delta\theta_s(s) + \Delta\theta_{tr}(s) + 2\xi(s)\right) - \xi(s) \tag{4.112}$$

Before Equation 4.99 and Equation 4.112 can be substituted into Equation 4.18 to determine the electric field response, $\Delta\theta_{tr}(s)$ must first be factored out of the solutions. With reference to Figure 4.3, this is achieved by noting that at the $x_3 = 0$

material boundary, the heat flow in the brass substrate is equal to the heat flow in the piezoelectric medium. Equating heat flows at the boundary yields Equation 4.113.

$$k_b \frac{\partial \Delta\theta_b}{\partial x_3}(0,s) = k_p \frac{\partial \Delta\theta}{\partial x_3}(0,s) \tag{4.113}$$

Differentiating Equation 4.98 and Equation 4.111, setting $x_3 = 0$, and substituting into Equation 4.113 and rearranging yields Equation 4.114 for $\Delta\theta_{tr}(s)$.

$$\Delta\theta_{tr}(s) = \frac{\begin{pmatrix} k_b\sqrt{K_{eff}^{S,E}}\ cosh\sqrt{\frac{s}{K_{eff}^{S,E}}}l_p\ \Delta\theta_s(s) - \xi(s) k_b\sqrt{K_{eff}^{S,E}}\left(cosh\sqrt{\frac{s}{K_{effb}^{S}}}l_b - 1\right) cosh\sqrt{\frac{s}{K_{eff}^{S,E}}}l_p \\ -\eta(s) k_p\sqrt{K_{effb}^{S}}\ sinh\sqrt{\frac{s}{K_{effb}^{S}}}l_b\ sinh\sqrt{\frac{s}{K_{eff}^{S,E}}}l_p \end{pmatrix}}{k_p\sqrt{K_{effb}^{S}}\ sinh\sqrt{\frac{s}{K_{effb}^{S}}}l_b\ sinh\sqrt{\frac{s}{K_{eff}^{S,E}}}l_p + k_b\sqrt{K_{eff}^{S,E}}\ cosh\sqrt{\frac{s}{K_{effb}^{S}}}l_b\ cosh\sqrt{\frac{s}{K_{eff}^{S,E}}}l_p} \tag{4.114}$$

Substituting Equation 4.114 for $\Delta\theta_{tr}(s)$ into Equation 4.99 and Equation 4.112, rationalising and rearranging yields the final equations given by Equation 4.115 and Equation 4.116 for the one dimensional spatial averages with respect to the x_3 axis of $\Delta\theta(x_3, s)$and $\Delta\theta_b(x_3, s)$ given by $\Delta\bar{\theta}(s)$ and $\Delta\bar{\theta}_b(s)$ respectively.

$$\Delta\bar{\theta}(s) =$$

$$\frac{1}{l_p}\sqrt{\frac{K_{eff}^{S,E}}{s}}\left(\frac{k_b\sqrt{K_{eff}^{S,E}}\ sinh\sqrt{\frac{s}{K_{eff}^{S,E}}}l_p\left(\Delta\theta_s(s) + \xi(s) + \left(\eta(s) - \xi(s)\right) cosh\sqrt{\frac{s}{K_{effb}^{S}}}l_b\right)}{k_p\sqrt{K_{effb}^{S}}\ sinh\sqrt{\frac{s}{K_{effb}^{S}}}l_b\ sinh\sqrt{\frac{s}{K_{eff}^{S,E}}}l_p + k_b\sqrt{K_{eff}^{S,E}}\ cosh\sqrt{\frac{s}{K_{effb}^{S}}}l_b\ cosh\sqrt{\frac{s}{K_{eff}^{S,E}}}l_p}\right) - \eta(s) \tag{4.115}$$

$$\Delta\bar{\theta}_b(s) =$$

$$\frac{1}{l_b}\sqrt{\frac{K_{effb}^{S}}{s}}\left(\frac{k_b\sqrt{K_{eff}^{S,E}}\left(\Delta\theta_s(s)+\xi(s)\right)sinh\sqrt{\frac{s}{K_{effb}^{S}}}l_b\ cosh\sqrt{\frac{s}{K_{eff}^{S,E}}}l_p+ k_p\sqrt{K_{effb}^{S}}\left(\Delta\theta_s(s)+2\xi(s)-\eta(s)\right)\left(cosh\sqrt{\frac{s}{K_{effb}^{S}}}l_b-1\right)sinh\sqrt{\frac{s}{K_{eff}^{S,E}}}l_p}{k_p\sqrt{K_{effb}^{S}}\ sinh\sqrt{\frac{s}{K_{effb}^{S}}}l_b\ sinh\sqrt{\frac{s}{K_{eff}^{S,E}}}l_p+k_b\sqrt{K_{eff}^{S,E}}\ cosh\sqrt{\frac{s}{K_{effb}^{S}}}l_b\ cosh\sqrt{\frac{s}{K_{eff}^{S,E}}}l_p}\right)-\xi(s)$$

(4.116)

The significance of the coupling terms in Equation 4.115 and Equation 4.116 are investigated by substituting the values of coefficients C_1 to C_{14} for PZT 5H and brass given in Appendix A.7 into the coupling terms $\eta(s)$ and $\xi(s)$ for the extreme cases of $\delta_s = 0$ and $\delta_s \to \infty$. As discussed in Section 4.9.2, the electrical conductivity of PZT-5H is extremely low and it is therefore assumed that $\delta_{33} = 0$.

The expressions for the short circuit values of $\eta(s)$ and $\xi(s)$ denoted by $\eta(s)_{oc}$ and $\xi(s)_{oc}$ ($\delta_s = 0$) are evaluated as follows:

$$\eta(s)_{oc} =$$

$$1.65\times10^{-5}\Delta\bar{\theta} + 52.1\times10^{-5}\Delta\bar{\theta}_b + 123.1\times10^{-11}T_3 - 8.48\times10^{-11}T_{b3}$$

$$\xi(s)_{oc} =$$

$$2.39\times10^{-11}\Delta\bar{\theta} + 75.4\times10^{-11}\Delta\bar{\theta}_b - 5.65\times10^{-17}T_3 + 23.2\times10^{-17}T_{b3}$$

The expressions for the short circuit values of $\eta(s)$ and $\xi(s)$ denoted by $\eta(s)_{sc}$ and $\xi(s)_{sc}$ ($\delta_s \to \infty$) are evaluated as follows:

$$\eta(s)_{sc} =$$

$$3.14\times10^{-4}\Delta\bar{\theta} + 11.38\times10^{-4}\Delta\bar{\theta}_b + 9.72\times10^{-10}T_3 - 1.47\times10^{-10}T_{b3}$$

$$\xi(s)_{sc} =$$

$$5.21\times10^{-11}\Delta\bar{\theta} + 85.85\times10^{-11}\Delta\bar{\theta}_b - 10\times10^{-17}T_3 + 21.53\times10^{-17}T_{b3}$$

Noting that the temperature measurand $\Delta\theta_s$ and the spatial average temperatures in both media are of the same order of magnitude, then comparing the $\Delta\bar{\theta}$ and $\Delta\bar{\theta}_b$ coupling terms in $\eta(s)$ and $\xi(s)$ to $\Delta\theta_s$ in Equation 4.115 and Equation 4.116 for $\Delta\bar{\theta}$ and $\Delta\bar{\theta}_b$ indicates extremely weak coupling under both open-circuit and short-circuit conditions. The temperature terms in $\eta(s)$ are approximately 4 and 3 orders of magnitude less than $\Delta\bar{\theta}$ in the piezoelectric medium under open circuit and short circuit conditions respectively; and around 9 orders of magnitude less than $\Delta\bar{\theta}_b$ in the substrate under both open and short circuit conditions. Furthermore, the coupling axial stress terms in $\eta(s)$ and $\xi(s)$ are at least 3 orders and 10 orders of magnitude respectively less than the contribution of the applied axial stress terms in Equation 4.18. The coupling terms can therefore be neglected and Equation 4.115 and Equation 4.116 reduce to Equation 4.117 and Equation 4.118 respectively.

$$\Delta\bar{\theta}(s) \cong \sqrt{\frac{K_{eff}^{S,E}}{s}}\frac{\Delta\theta_s(s)}{l_p}\left(\frac{k_b\sqrt{K_{eff}^{S,E}}\sinh\sqrt{\frac{s}{K_{eff}^{S,E}}}l_p}{k_p\sqrt{K_{effb}^{S}}\sinh\sqrt{\frac{s}{K_{effb}^{S}}}l_b\sinh\sqrt{\frac{s}{K_{eff}^{S,E}}}l_p+k_b\sqrt{K_{eff}^{S,E}}\cosh\sqrt{\frac{s}{K_{effb}^{S}}}l_b\cosh\sqrt{\frac{s}{K_{eff}^{S,E}}}l_p}\right) \tag{4.117}$$

$$\Delta\bar{\theta}_b(s) \cong \sqrt{\frac{K_{effb}^{S}}{s}}\frac{\Delta\theta_s(s)}{l_b}\left(\frac{k_b\sqrt{K_{eff}^{S,E}}\sinh\sqrt{\frac{s}{K_{effb}^{S}}}l_b\cosh\sqrt{\frac{s}{K_{eff}^{S,E}}}l_p+k_p\sqrt{K_{effb}^{S}}\left(\cosh\sqrt{\frac{s}{K_{effb}^{S}}}l_b-1\right)\sinh\sqrt{\frac{s}{K_{eff}^{S,E}}}l_p}{k_p\sqrt{K_{effb}^{S}}\sinh\sqrt{\frac{s}{K_{effb}^{S}}}l_b\sinh\sqrt{\frac{s}{K_{eff}^{S,E}}}l_p+k_b\sqrt{K_{eff}^{S,E}}\cosh\sqrt{\frac{s}{K_{effb}^{S}}}l_b\cosh\sqrt{\frac{s}{K_{eff}^{S,E}}}l_p}\right) \tag{4.118}$$

Equation 4.117 and Equation 4.118 form the Laplace transform transfer functions relating the applied surface temperature measurand $\Delta\theta_s(s)$, to the one dimensional spatial average temperatures of the piezoelectric and substrate materials $\Delta\bar{\theta}(s)$ and $\Delta\bar{\theta}_b(s)$ with respect to the x_3 axis respectively. It is possible to find the transient response for an applied temperature $\Delta\theta_s(s)$ using Equation 4.117 and Equation 4.118; however, the exact fractional inverse Laplace transform function required is not available on commercially available software such as Matlab or

Octave to date. To obtain an approximation of the time-frequency response of the sensor, a Padé approximant method of sufficient order is introduced in Chapter 7 to obtain a close approximation to the exact solution.

4.9.2 Effect of coupling on the diffusion coefficients

The diffusion coefficients $K_{eff}^{S,E}$ and K_{effb}^{S} are those evaluated at constant transverse strain, constant axial stress and constant spatial average temperatures. They are dependent only on the respective properties of the piezoelectric and substrate media and, since the substrate and piezoelectric media are solids, they are intuitively expected to be close to $K^{S,E}$ and K_b^S respectively. Substituting published piezoelectric and substrate constants given in Appendix A.1 and assuming $\theta_o = 300K$, the effective diffusion coefficients $K_{eff}^{S,E}$ of the piezoelectric medium and K_{effb}^{S} of the substrate are found to differ from the uncoupled diffusion coefficients by approximately -2.5% in the substrate; and -0.25% in the piezoelectric medium for $\delta_{33} \to 0$ and -0.12% for $\delta_{33} \to \infty$. It is considered that particularly for the substrate, this difference while small cannot be neglected and it is therefore the effective diffusion coefficients that are used henceforth. The electrical conductivity of PZT-5H is extremely low and the value of $K_{eff}^{S,E}$ as $\delta_{33} \to 0$ is assumed for the analyses to follow.

From the above definition of $K_{eff}^{S,E}$ it can be seen that since C_2 is dependent on the internal conductivity δ_{33} but independent of an externally connected equivalent conductivity δ_s then so must $K_{eff}^{S,E}$ be. This result is tenable since it is reasonable that in the linear theory considered, the value of $K_{eff}^{S,E}$ is a property of the piezoelectric medium and should not depend on external stimuli or on properties external to the piezoelectric medium. On the other hand, under short circuit conditions, it is reasonable that $K_{eff}^{S,E}$ should remain dependent on the internal conductivity δ_{33} since it is the spatially averaged electric field $\bar{E}_3$ that is forced to zero and not necessarily the instantaneous value of E_3. E_3 has a spatial dependence in the piezoelectric

medium that is generally non-zero everywhere, even under fictive ideal short-circuit conditions where $\delta_s \to \infty$.

4.9.3 Temperature response – Fourier form

The steady state response is readily obtained since both of the transfer functions $\Delta\bar{\theta}(s)/\Delta\theta_s(s)$ and $\Delta\bar{\theta}_b(s)/\Delta\theta_s(s)$, which are obtained from Equation 4.117 and Equation 4.118 respectively, contain only real poles such that the roots of the denominators have values of $s < 0$ and they are therefore inherently stable. It can therefore be stated that the Laplace transform region of convergence of the impulse responses of $\Delta\bar{\theta}(s)$ and $\Delta\bar{\theta}_b(s)$ includes the $j\omega$ axis. It is therefore valid to allow substitution of $s = j\omega$ in Equation 4.117 and Equation 4.118 to yield the frequency-domain Fourier transfer function relationships. Noting that $\sqrt{j} = \pm(1+j)/\sqrt{2}$ such that $\sqrt{s} = \sqrt{j\omega} = \pm(1+j)\sqrt{\omega/2}$, and substituting into Equation 4.117 and Equation 4.118 yields Equation 4.119 and Equation 4.120 respectively. The choice of using + or − throughout in the substitution is arbitrary and either will yield the same result.

$$\Delta\bar{\theta}(j\omega) \cong \frac{(1-j)\Delta\theta_s(j\omega)}{l_p}\sqrt{\frac{K_{eff}^{S,E}}{2\omega}}\left(\frac{k_b\sqrt{K_{eff}^{S,E}}\,\sinh(1+j)\sqrt{\frac{\omega}{2K_{eff}^{S,E}}}l_p}{\begin{matrix}k_p\sqrt{K_{effb}^{S}}\,\sinh(1+j)\sqrt{\frac{\omega}{2K_{effb}^{S}}}l_b\,\sinh(1+j)\sqrt{\frac{\omega}{2K_{eff}^{S,E}}}l_p+\\ k_b\sqrt{K_{eff}^{S,E}}\,\cosh(1+j)\sqrt{\frac{\omega}{2K_{effb}^{S}}}l_b\,\cosh(1+j)\sqrt{\frac{\omega}{2K_{eff}^{S,E}}}l_p\end{matrix}}\right) \quad (4.119)$$

$$\Delta\bar{\theta}_b(j\omega) \cong \frac{(1-j)\Delta\theta_s(j\omega)}{l_b}\sqrt{\frac{K_{effb}^{S}}{2\omega}}\left(\frac{\begin{matrix}k_b\sqrt{K_{eff}^{S,E}}\,\sinh(1+j)\sqrt{\frac{\omega}{2K_{effb}^{S}}}l_b\,\cosh(1+j)\sqrt{\frac{\omega}{2K_{eff}^{S,E}}}l_p+\\ k_p\sqrt{K_{effb}^{S}}\left(\cosh(1+j)\sqrt{\frac{\omega}{2K_{effb}^{S}}}l_b-1\right)\sinh(1+j)\sqrt{\frac{\omega}{2K_{eff}^{S,E}}}l_p\end{matrix}}{\begin{matrix}k_p\sqrt{K_{effb}^{S}}\,\sinh(1+j)\sqrt{\frac{\omega}{2K_{effb}^{S}}}l_b\,\sinh(1+j)\sqrt{\frac{\omega}{2K_{eff}^{S,E}}}l_p+\\ k_b\sqrt{K_{eff}^{S,E}}\,\cosh(1+j)\sqrt{\frac{\omega}{2K_{effb}^{S}}}l_b\,\cosh(1+j)\sqrt{\frac{\omega}{2K_{eff}^{S,E}}}l_p\end{matrix}}\right) \quad (4.120)$$

Assuming steady state sinusoidal temperature excitation, Equation 4.119 and Equation 4.120 are used to obtain the steady state response where the amplitude and phase responses are readily obtained to allow the steady state phase delay, phase and amplitude response behaviours to be investigated.

4.10 Temperature response models – elastomer liner surface

4.10.1 Initial considerations

Under circumstances where the sensor cannot be in direct contact with the skin for which the temperature is to be measured, for example when contact with the metallic substrate may cause skin reactions leading to inflammation, it may be necessary to measure temperature through an elastomer socket liner. Furthermore, it is normal for an elastomer liner to be worn between the prosthetic socket and surface of the skin to improve comfort and reduce injury due to an imperfect fit. The effects of such a liner on the response of the sensor are therefore investigated.

It is assumed that there is negligible mechanical coupling at the liner/sensor interface and that therefore only thermal coupling needs be included in the analysis. This assumption is justified intuitively by considering that the elastomer has a maximum Young's Modulus at least 3 orders of magnitude less than that of brass or PZT, and is not rigidly bonded to the sensor element substrate. The elastomer is therefore unlikely to offer significant resistance to changes in the transverse strain due to thermal expansion, or to axial stress loading applied to the sensor through the elastomer in the mechanically coupled substrate and piezoelectric media.

4.10.2 Thermal conductivity of prosthetic socket liners

The thermal conductivity of various commonly used elastomer liners is given in [96]. The lowest thermal conductivities are found with liners such as the Pelite and Syncor Durosleeve at $0.085\,Wm^{-1}K^{-1}$ which are constructed of closed cell foam, and the highest thermal conductivity measured is $0.266\,Wm^{-1}K^{-1}$ for the Ossur icecross comfort plus sensil gel, which is constructed from silicone gel. The most

commonly used and commercially available elastomer liners have thermal conductivities of approximately $0.2\,Wm^{-1}K^{-1}$ [97]. The thermal diffusion coefficient for these materials is therefore low when compared to the metallic substrate and PZT media despite the partially mitigating properties of relatively low specific heat capacities and densities. Since such liners are much thicker compared to the piezoelectric and substrate media and have a thickness typically between $2mm$ and $8mm$, it is therefore intuitive that measuring temperature through such materials will be problematic. This problem is discussed further in Section 4.10.3.

4.10.3 Elastomer liner temperature response

With the lowest thermal conductivity, lowest diffusion coefficient and the greatest thickness, the liner will have by far the greatest influence on the transient and steady state responses of the sensor. It is therefore important to consider the transient response of the liner to an applied temperature change. When measuring temperature through a medium, it is desirable to have as large a thermal conductivity and as low a thickness, density and specific heat capacity as possible to minimise significant amplitude and phase effects in the measured temperature. It is intuitive that measuring temperature through elastomer prosthetic socket liners will produce long duration transients with significant amplitude errors and phase distortion in the measured response. Chapter 7 presents a thorough treatment of this problem, which is due to elastomer liners poor heat conductivity coefficients and large thicknesses relative to the sensor element substrate and piezoelectric media. A Gaussian predictive model based on a machine learning algorithm that partially mitigates this problem, allowing a meaningful estimate of skin temperature from measurements made at the liner / prosthetic socket interface is described in [98].

4.10.4 Temperature response models – Laplace form

Noting that analysis of the liner involves a similar set of thermal boundary conditions as those used above to determine the substrate temperature distribution $\Delta\theta_b(x_3, s)$ given by Equation 4.111, the temperature distribution in the elastomer

liner, $\Delta\theta_e(x_3, s)$ can be written immediately as Equation 4.121. The elastomer liner thickness is denoted by l_e and extends from $x_3 = -l_b$ to $x_3 = -(l_b + l_e)$. The terms K_e and $\Delta\theta_{skin}(s)$ are the diffusion coefficient of the elastomer and skin temperature measurand respectively.

$$\Delta\theta_e(x_3, s) = \frac{\Delta\theta_s(s)\ sinh\sqrt{\frac{s}{K_e}}(x_3+l_b+l_e) - \Delta\theta_{skin}(s)\ sinh\sqrt{\frac{s}{K_e}}(x_3+l_b)}{sinh\sqrt{\frac{s}{K_e}}l_e} \tag{4.121}$$

Before the effect of the elastomer can be included in Equation 4.18 to obtain the required output voltage response, it is necessary to factor $\Delta\theta_s(s)$ out of the solutions. This is realised by noting that at the $x_3 = -l_b$ material boundary, the heat flow in the substrate is equal to the heat flow in the elastomer liner. Equating heat flows at the boundary yields Equation 4.122 where k_e and $\Delta\theta_e$ are the thermal conductivity and spatial temperature distribution in the elastomer liner respectively.

$$k_b \frac{\partial\Delta\theta_b}{\partial x_3}(-l_b, s) = k_e \frac{\partial\Delta\theta_e}{\partial x_3}(-l_b, s) \tag{4.122}$$

Differentiating Equation 4.111 and Equation 4.121 and by setting $x_3 = -l_b$, followed by substitution into Equation 4.122 and rearranging yields Equation 4.123 for $\Delta\theta_s(s)$.

$$\Delta\theta_s(s) = \frac{k_e\sqrt{K^S_{effb}}\ sinh\sqrt{\frac{s}{K^S_{effb}}}l_b\ \Delta\theta_{skin}(s) + k_b\sqrt{K_e}\ sinh\sqrt{\frac{s}{K_e}}l_e\ \Delta\theta'_{tr}(s)}{k_b\sqrt{K_e}\ sinh\sqrt{\frac{s}{K_e}}l_e\ cosh\sqrt{\frac{s}{K^S_{effb}}}l_b + k_e\sqrt{K^S_{effb}}\ sinh\sqrt{\frac{s}{K^S_{effb}}}l_b\ cosh\sqrt{\frac{s}{K_e}}l_e} \tag{4.123}$$

Where $\Delta\theta'_{tr}(s)$ is given by Equation 4.124 and is equal to Equation 4.114 with the insignificant η and ξ coupling terms neglected.

$$\Delta\theta'_{tr}(s) = \frac{\left(k_b\sqrt{K^{S,E}_{eff}}\ cosh\sqrt{\frac{s}{K^{S,E}_{eff}}}l_p\ \Delta\theta_s(s)\right)}{k_p\sqrt{K^S_{effb}}\ sinh\sqrt{\frac{s}{K^S_{effb}}}l_b\ sinh\sqrt{\frac{s}{K^{S,E}_{eff}}}l_p + k_b\sqrt{K^{S,E}_{eff}}\ cosh\sqrt{\frac{s}{K^S_{effb}}}l_b\ cosh\sqrt{\frac{s}{K^{S,E}_{eff}}}l_p} \tag{4.124}$$

Substituting Equation 4.124 into Equation 4.123 and rearranging yields Equation 4.125 for the temperature $\Delta\theta_s(s)$ at the elastomer-substrate boundary.

$$\Delta\theta_s(s) = \frac{b(s)k_e\sqrt{K_{effb}^S}\ sinh\sqrt{\frac{s}{K_{effb}^S}}l_b\,\Delta\theta_{skin}(s)}{a(s)b(s)-k_b^2\sqrt{K_eK_{eff}^{S,E}}\ sinh\sqrt{\frac{s}{K_e}}l_e\,cosh\sqrt{\frac{s}{K_{eff}^{S,E}}}l_p} \tag{4.125}$$

The terms $a(s)$ and $b(s)$are given by Equation 4.126 and Equation 4.127 respectively.

$$a(s) = k_b\sqrt{K_e}\ sinh\sqrt{\frac{s}{K_e}}l_e\ cosh\sqrt{\frac{s}{K_{effb}^S}}l_b\ + \\ k_e\sqrt{K_{effb}^S}\ sinh\sqrt{\frac{s}{K_{effb}^S}}l_b\ cosh\sqrt{\frac{s}{K_e}}l_e \tag{4.126}$$

$$b(s) = k_p\sqrt{K_{effb}^S}\ sinh\sqrt{\frac{s}{K_{effb}^S}}l_b\ sinh\sqrt{\frac{s}{K_{eff}^{S,E}}}l_p\ + \\ k_b\sqrt{K_{eff}^{S,E}}\ cosh\sqrt{\frac{s}{K_{effb}^S}}l_b\ cosh\sqrt{\frac{s}{K_{eff}^{S,E}}}l_p \tag{4.127}$$

Finally, substituting Equation 4.125 into Equation 4.117 and Equation 4.118 yields Equation 4.128 and Equation 4.129 for the spatial average temperatures in the substrate and piezoelectric materials respectively that include the effect of the elastomer liner placed between the substrate and surface temperature measurand.

$$\Delta\bar{\theta}(s) \cong \sqrt{\frac{K_{eff}^{S,E}}{s}}\frac{\Delta\theta_{skin}(s)}{l_p}\frac{k_b\,k_e\sqrt{K_{eff}^{S,E}K_{effb}^S}\,sinh\sqrt{\frac{s}{K_{eff}^{S,E}}}l_p\,sinh\sqrt{\frac{s}{K_{effb}^S}}l_b}{a(s)b(s)-k_b^2\sqrt{K_eK_{eff}^{S,E}}\ sinh\sqrt{\frac{s}{K_e}}l_e\,cosh\sqrt{\frac{s}{K_{eff}^{S,E}}}l_p} \tag{4.128}$$

$$\Delta\bar{\theta}_b(s) \cong \sqrt{\frac{K_{effb}^S}{s}}\frac{\Delta\theta_{skin}(s)}{l_b}\frac{\begin{pmatrix} k_b\,k_e\sqrt{K_{eff}^{S,E}K_{effb}^S}\,sinh^2\sqrt{\frac{s}{K_{effb}^S}}l_b\ cosh\sqrt{\frac{s}{K_{eff}^{S,E}}}l_p \\ +k_pk_eK_{effb}^S\left(cosh\sqrt{\frac{s}{K_{effb}^S}}l_b-1\right)sinh\sqrt{\frac{s}{K_{eff}^{S,E}}}l_p\ sinh\sqrt{\frac{s}{K_{effb}^S}}l_b \end{pmatrix}}{a(s)b(s)-k_b^2\sqrt{K_eK_{eff}^{S,E}}\ sinh\sqrt{\frac{s}{K_e}}l_e\,cosh\sqrt{\frac{s}{K_{eff}^{S,E}}}l_p} \tag{4.129}$$

Equation 4.128 and Equation 4.129 reduce to Equation 4.117 and Equation 4.118 respectively when l_e is set to zero.

4.10.5 Temperature response models – Fourier form

For transfer functions in the Laplace variable that have zero initial conditions at $t = 0^-$, such as those developed above, the substitution of $s = j\omega$ may be made to yield the Fourier transfer function. An additional requirement for the validity of the substitution of $s = j\omega$ is that the Laplace domain input signals that have the $j\omega$ axis within their region of convergence. However if the $j\omega$ axis lies on the boundary of the region of convergence, then the Fourier transform of the input signal may exist, such as with the Heaviside step function or step sinusoid, but the substitution of $s = j\omega$ while valid for the transfer functions is invalid for the input signal. In general the Fourier transform of time-domain input and response signals are valid on the interval $-\infty < t < \infty$ and therefore the Fourier transform expressions are useful for determining the steady state frequency response directly rather than calculating the inverse Laplace transform and allowing $t \to \infty$. Letting $s = j\omega$ yields Equation 4.130 and Equation 4.131 for the Fourier transfer functions of the spatial average temperature in the piezoelectric and substrate media respectively.

$$\Delta\bar{\theta}(j\omega) \cong$$

$$\frac{\Delta\theta_{skin}(j\omega)(1-j)}{l_p}\sqrt{\frac{K_{eff}^{S,E}}{2\omega}}\frac{k_b\,k_e\sqrt{K_{eff}^{S,E}K_{effb}^{S}}\sinh(1+j)\sqrt{\frac{\omega}{2K_{eff}^{S,E}}}l_p\sinh(1+j)\sqrt{\frac{\omega}{2K_{effb}^{S}}}l_b}{a(j\omega)b(j\omega)-k_b^2\sqrt{K_eK_{eff}^{S,E}}\sinh(1+j)\sqrt{\frac{\omega}{2K_e}}l_e\cosh(1+j)\sqrt{\frac{\omega}{2K_{eff}^{S,E}}}l_p} \tag{4.130}$$

$$\Delta\bar{\theta}_b(j\omega) \cong \frac{\Delta\theta_{skin}(j\omega)(1-j)}{l_b}\sqrt{\frac{K_{effb}^{S}}{2\omega}}\times$$

$$\frac{\begin{pmatrix} k_b\,k_e\sqrt{K_{eff}^{S,E}K_{effb}^{S}}\sinh^2(1+j)\sqrt{\frac{\omega}{2K_{effb}^{S}}}l_b\,\cosh(1+j)\sqrt{\frac{\omega}{2K_{eff}^{S,E}}}l_p \\ +k_pk_eK_{effb}^{S}\left(\cosh(1+j)\sqrt{\frac{\omega}{2K_{effb}^{S}}}l_b-1\right)\sinh(1+j)\sqrt{\frac{\omega}{2K_{eff}^{S,E}}}l_p\,\sinh(1+j)\sqrt{\frac{\omega}{2K_{effb}^{S}}}l_b \end{pmatrix}}{a(j\omega)b(j\omega)-k_b^2\sqrt{K_eK_{eff}^{S,E}}\sinh(1+j)\sqrt{\frac{\omega}{2K_e}}l_e\cosh(1+j)\sqrt{\frac{\omega}{2K_{eff}^{S,E}}}l_p} \tag{4.131}$$

The terms $a(j\omega)$ and $b(j\omega)$ are given by Equation 4.132 and Equation 4.133 respectively.

$$a(j\omega) = k_b\sqrt{K_e}\,\sinh(1+j)\sqrt{\frac{\omega}{2K_e}}l_e\,\cosh(1+j)\sqrt{\frac{\omega}{2K^S_{effb}}}l_b$$

$$+k_e\sqrt{K^S_{effb}}\;sinh(1+j)\sqrt{\frac{\omega}{2K^S_{effb}}}l_b\;\;cosh(1+j)\sqrt{\frac{\omega}{2K_e}}l_e \qquad (4.132)$$

$$b(j\omega) = k_p\sqrt{K^S_{effb}}\;sinh(1+j)\sqrt{\frac{\omega}{2K^S_{effb}}}l_b\;\;sinh(1+j)\sqrt{\frac{\omega}{2K^{S,E}_{eff}}}l_p$$

$$+k_b\sqrt{K^{S,E}_{eff}}\;cosh(1+j)\sqrt{\frac{\omega}{2K^S_{effb}}}l_b\;\;cosh(1+j)\sqrt{\frac{\omega}{2K^{S,E}_{eff}}}l_p \qquad (4.133)$$

Equation 4.130 and Equation 4.131 reduce to Equation 4.119 and Equation 4.120 respectively when l_e is set to zero.

4.10.6 Limiting case $l_b, l_p \ll l_e$

For the case that $l_b,\ l_p \ll l_e$ then $\Delta\bar{\theta}(s) \cong \Delta\bar{\theta}_b(s) \cong \Delta\theta_s(s)$ and Equation 4.128 and Equation 4.129 reduce to Equation 4.134 which is exact in the limit $l_b,\ l_p \to 0$.

$$\Delta\bar{\theta}(s) \cong \Delta\bar{\theta}_b(s) \cong \Delta\theta_s(s) \cong \frac{\Delta\theta_{skin}(s)}{\cosh\sqrt{\frac{s}{K_e}}l_e} \qquad (4.134)$$

In Fourier form Equation 4.134 is written as Equation 4.135.

$$\Delta\bar{\theta}(j\omega) \cong \Delta\bar{\theta}_b(j\omega) \cong \Delta\theta_s(j\omega) \cong \frac{\Delta\theta_{skin}(j\omega)}{\cosh(1+j)\sqrt{\frac{\omega}{2K_e}}l_e} \qquad (4.135)$$

Equation 4.134 and Equation 4.135 are identical to the limiting case of heat flow through the liner where the sensor thickness is considered to be negligible or alternatively that the thermal conductivities of both the substrate and piezoelectric materials are considered to be high such that the temperature of the sensor can be considered to be uniform throughout. In Equation 4.134 and Equation 4.135, the piezoelectric external boundary condition of zero heat flow out of the external

surface is preserved and the same result can be obtained by considering the liner alone with the zero heat flow boundary condition on its external surface.

The precise time-domain response of Equation 4.134 to a driving surface temperature $\Delta\theta_{skin}(t)$ can be found using standard tables of fractional calculus Laplace transforms. In Chapter 7, the response of Equation 4.134 is calculated for the case that $\Delta\theta_{skin}(t)$ is a general complex sinusoid and the results are used to validate the Padé approximant method used to determine the sensor response.

4.11 Final sensor element response models – temperature

4.11.1 Voltage response – Laplace form

Writing the spatially averaged electric field given by Equation 4.18 with the axial applied T_3 and T_{b3} terms set to zero and representing low frequency dielectric loss such that ${\varepsilon_{33}^S}' = (\varepsilon_{33}^S + \delta_{33}/s)$ where δ_{33} is the conductivity of the piezoelectric medium in the axial 3-dimension yields Equation 4.136.

$$\bar{E}_3(s) = \left.\frac{\left(\frac{\beta E_b A_b \varphi_{p1}^E}{E_b A_b + \alpha(1-\mu_b)A_p} - 2e_{31}\varphi_{p1}^E - e_{33}\varphi_{p3}^E - P^S\right)\Delta\bar{\theta}(s) - \frac{\beta E_b A_b \varphi_b}{E_b A_b + \alpha(1-\mu_b)A_p}\Delta\bar{\theta}_b(s)}{\frac{(1-\mu_b)\beta^2 A_p}{2(E_b A_b + \alpha(1-\mu_b)A_p)} + \frac{e_{33}^2}{c_{33}^E} + \varepsilon_{33}^S + \frac{\delta_{33}}{s}}\right|_{T_3, T_{b3}=0} \tag{4.136}$$

The corresponding sensor element output voltage given by $V_o(s) = -l_p\bar{E}_3(s)$ yields Equation 4.137. Equation 4.137 is identical to Equation 4.32 for the equivalent circuit voltage discussed in Section 4.7 with the T_3 and T_{b3} terms set to zero and ${\varepsilon_{33}^S}'$ replaced by $(\varepsilon_{33}^S + \delta_{33}/s)$.

$$V_o(s) = l_p \left.\frac{\left(2e_{31}\varphi_{p1}^E + e_{33}\varphi_{p3}^E + P^S - \frac{\beta E_b A_b \varphi_{p1}^E}{E_b A_b + \alpha(1-\mu_b)A_p}\right)\Delta\bar{\theta}(s) + \frac{\beta E_b A_b \varphi_b}{E_b A_b + \alpha(1-\mu_b)A_p}\Delta\bar{\theta}_b(s)}{\frac{(1-\mu_b)\beta^2 A_p}{2(E_b A_b + \alpha(1-\mu_b)A_p)} + \frac{e_{33}^2}{c_{33}^E} + \varepsilon_{33}^S + \frac{\delta_{33}}{s}}\right|_{T_3, T_{b3}=0} \tag{4.137}$$

The influence of an electric displacement due to for example the input resistance of external signal conditioning electronics is re-introduced into Equation 4.137 by including an external resistor R_s connected across the piezoelectric medium. The corresponding electric displacement is $D_3(s) = V_o(s)/j\omega A_s R_s$ or in terms of the displacement current $I_o(s) = j\omega A_s D_3(s) = V_o(s)/R_s$. The inclusion of the resistor is equivalent to adding an equivalent electrical conductivity $\delta_s = l_p/R_s A_s$ to δ_{33} in Equation 4.137 where A_s is the surface area of the silver electrodes. Writing $\delta_{33} = l_p/R_p A_s$ where R_p is the resistance of the piezoelectric medium in the axial 3-dimension yields Equation 4.138.

$$V_o(s) = l_p \frac{\left(2e_{31}\varphi_{p1}^E + e_{33}\varphi_{p3}^E + P^S - \frac{\beta E_b A_b \varphi_{p1}^E}{E_b A_b + \alpha(1-\mu_b)A_p}\right)\Delta\bar{\theta}(s) + \frac{\beta E_b A_b \varphi_b}{E_b A_b + \alpha(1-\mu_b)A_p}\Delta\bar{\theta}_b(s)}{\frac{(1-\mu_b)\beta^2 A_p}{2(E_b A_b + \alpha(1-\mu_b)A_p)} + \frac{e_{33}^2}{c_{33}^E} + \varepsilon_{33}^S + \frac{l_p}{sA_s}\left(\frac{1}{R_p} + \frac{1}{R_s}\right)}_{T_3, T_{b3}=0}$$

(4.138)

The corresponding electric displacement and resulting current in the presence of an external resistor R_s are given by Equation 4.139 and 4.140 respectively where $D_3(s) = V_o(s)/sA_s R_s$ and $I_o(s) = sA_s D_3(s)$.

$$D_3(s) = l_p \frac{\left(2e_{31}\varphi_{p1}^E + e_{33}\varphi_{p3}^E + P^S - \frac{\beta E_b A_b \varphi_{p1}^E}{E_b A_b + \alpha(1-\mu_b)A_p}\right)\Delta\bar{\theta}(s) + \frac{\beta E_b A_b \varphi_b}{E_b A_b + \alpha(1-\mu_b)A_p}\Delta\bar{\theta}_b(s)}{sA_s R_s\left(\frac{(1-\mu_b)\beta^2 A_p}{2(E_b A_b + \alpha(1-\mu_b)A_p)} + \frac{e_{33}^2}{c_{33}^E} + \varepsilon_{33}^S\right) + l_p\left(\frac{R_s}{R_p} + 1\right)}_{T_3, T_{b3}=0}$$

(4.139)

$$I_o(s) = sA_s l_p \frac{\left(2e_{31}\varphi_{p1}^E + e_{33}\varphi_{p3}^E + P^S - \frac{\beta E_b A_b \varphi_{p1}^E}{E_b A_b + \alpha(1-\mu_b)A_p}\right)\Delta\bar{\theta}(s) + \frac{\beta E_b A_b \varphi_b}{E_b A_b + \alpha(1-\mu_b)A_p}\Delta\bar{\theta}_b(s)}{sA_s R_s\left(\frac{(1-\mu_b)\beta^2 A_p}{2(E_b A_b + \alpha(1-\mu_b)A_p)} + \frac{e_{33}^2}{c_{33}^E} + \varepsilon_{33}^S\right) + l_p\left(\frac{R_s}{R_p} + 1\right)}_{T_3, T_{b3}=0}$$

(4.140)

Equations 4.117 and 4.118 or alternatively Equation 4.128 and Equation 4.129 to include the effect of the elastomer liner can now be substituted into Equation 4.138 to yield the final sensor output voltage response of the sensor

element to a temperature change $\Delta\theta_{skin}(s)$ with and without a liner respectively. Alternatively, under 'short-circuit' or virtual earth signal conditioning input conditions such that $R_s \to 0$, Equation 4.139 and Equation 4.140 yield the sensor electric displacement charge and displacement current response respectively to a forcing temperature change $\Delta\theta_{skin}(s)$ at the liner surface. The Laplace form is specifically applicable to determining the combined transient response of the sensor element and signal-conditioning amplifier and is used in the transient analysis presented in Chapter 7.

4.11.2 Voltage response – Fourier form

The corresponding Fourier form of Equation 4.136 to Equation 4.140 is given by letting $s = j\omega$ to yield Equation 4.141 to Equation 4.145 respectively.

$$\bar{E}_3(j\omega) = \frac{\left(\frac{\beta E_b A_b \varphi_{p1}^E}{E_b A_b + \alpha(1-\mu_b)A_p} - 2e_{31}\varphi_{p1}^E - e_{33}\varphi_{p3}^E - P^S\right)\Delta\bar{\theta}(j\omega) - \frac{\beta E_b A_b \varphi_b}{E_b A_b + \alpha(1-\mu_b)A_p}\Delta\bar{\theta}_b(j\omega)}{\frac{(1-\mu_b)\beta^2 A_p}{2(E_b A_b + \alpha(1-\mu_b)A_p)} + \frac{e_{33}^2}{c_{33}^E} + \varepsilon_{33}^S + \frac{\delta_{33}}{j\omega}}_{T_3, T_{b3}=0} \tag{4.141}$$

The corresponding sensor element output voltage given by $V_o(j\omega) = -l_p\bar{E}_3(j\omega)$ yields Equation 4.142 and Equation 4.143.

$$V_o(j\omega) = l_p \frac{\left(2e_{31}\varphi_{p1}^E + e_{33}\varphi_{p3}^E + P^S - \frac{\beta E_b A_b \varphi_{p1}^E}{E_b A_b + \alpha(1-\mu_b)A_p}\right)\Delta\bar{\theta}(j\omega) + \frac{\beta E_b A_b \varphi_b}{E_b A_b + \alpha(1-\mu_b)A_p}\Delta\bar{\theta}_b(j\omega)}{\frac{(1-\mu_b)\beta^2 A_p}{2(E_b A_b + \alpha(1-\mu_b)A_p)} + \frac{e_{33}^2}{c_{33}^E} + \varepsilon_{33}^S + \frac{\delta_{33}}{j\omega}}_{T_3, T_{b3}=0} \tag{4.142}$$

$$V_o(j\omega) = l_p \frac{\left(2e_{31}\varphi_{p1}^E + e_{33}\varphi_{p3}^E + P^S - \frac{\beta E_b A_b \varphi_{p1}^E}{E_b A_b + \alpha(1-\mu_b)A_p}\right)\Delta\bar{\theta}(j\omega) + \frac{\beta E_b A_b \varphi_b}{E_b A_b + \alpha(1-\mu_b)A_p}\Delta\bar{\theta}_b(j\omega)}{\frac{(1-\mu_b)\beta^2 A_p}{2(E_b A_b + \alpha(1-\mu_b)A_p)} + \frac{e_{33}^2}{c_{33}^E} + \varepsilon_{33}^S + \frac{l_p}{j\omega A_S}\left(\frac{1}{R_p} + \frac{1}{R_S}\right)}_{T_3, T_{b3}=0} \tag{4.143}$$

The corresponding electric displacement and resulting current in the presence of an external resistor R_s are given by Equation 4.144 and 4.145 respectively where $D_3(j\omega) = V_o(j\omega)/j\omega A_s R_s$ and $I_o(j\omega) = j\omega A_s D_3(j\omega)$.

$$D_3(j\omega) = l_p \frac{\left(2e_{31}\varphi_{p1}^E + e_{33}\varphi_{p3}^E + P^S - \frac{\beta E_b A_b \varphi_{p1}^E}{E_b A_b + \alpha(1-\mu_b)A_p}\right)\Delta\bar{\theta}(j\omega) + \frac{\beta E_b A_b \varphi_b}{E_b A_b + \alpha(1-\mu_b)A_p}\Delta\bar{\theta}_b(j\omega)}{j\omega A_s R_s\left(\frac{(1-\mu_b)\beta^2 A_p}{2(E_b A_b + \alpha(1-\mu_b)A_p)} + \frac{e_{33}^2}{c_{33}^E} + \varepsilon_{33}^S\right) + l_p\left(\frac{R_s}{R_p}+1\right)}_{T_3, T_{b3}=0} \tag{4.144}$$

$$I_o(j\omega) = j\omega A_s l_p \frac{\left(2e_{31}\varphi_{p1}^E + e_{33}\varphi_{p3}^E + P^S - \frac{\beta E_b A_b \varphi_{p1}^E}{E_b A_b + \alpha(1-\mu_b)A_p}\right)\Delta\bar{\theta}(j\omega) + \frac{\beta E_b A_b \varphi_b}{E_b A_b + \alpha(1-\mu_b)A_p}\Delta\bar{\theta}_b(j\omega)}{j\omega A_s R_s\left(\frac{(1-\mu_b)\beta^2 A_p}{2(E_b A_b + \alpha(1-\mu_b)A_p)} + \frac{e_{33}^2}{c_{33}^E} + \varepsilon_{33}^S\right) + l_p\left(\frac{R_s}{R_p}+1\right)}_{T_3, T_{b3}=0} \tag{4.145}$$

4.12 Final sensor element response models – axial stress (pressure)

4.12.1 Voltage response – Laplace form

To consider the response of the sensor to an applied stress, $\Delta\bar{\theta}_b(s)$ and $\Delta\bar{\theta}(s)$ can be set to zero in Equation 4.18 before using the analysis discussed above to yield Equation 4.146 for the spatially averaged electric field response due to the applied stress T_3. The relationship $T_{b3} = T_3\, A_{ps}/A_{bs}$ equating the axial forces is used where A_{ps} and A_{bs} are the surface areas of the piezoelectric and substrate media perpendicular to the 3-axis respectively. The double dash superscript indicates zero temperature change.

$$\bar{E}_3(s) = \frac{\frac{\beta\left((1-\mu_b)A_p\frac{c_{31}^E}{c_{33}^E} + \mu_b A_b \frac{A_{ps}}{A_{bs}}\right)}{E_b A_b + \alpha(1-\mu_b)A_p} - \frac{e_{33}}{c_{33}^E}}{\frac{(1-\mu_b)\beta^2 A_p}{2(E_b A_b + \alpha(1-\mu_b)A_p)} + \frac{e_{33}^2}{c_{33}^E} + \varepsilon_{33}^S + \frac{\delta_{33}}{s}} T_3(s)_{\Delta\bar{\theta}, \Delta\bar{\theta}_b = 0} \tag{4.146}$$

Equation 4.147 therefore gives the corresponding sensor output voltage.

$$V_o(s) = l_p \frac{\frac{e_{33}}{c_{33}^E} - \frac{\beta\left((1-\mu_b)A_p\frac{c_{31}^E}{c_{33}^E} + \mu_b A_b \frac{A_{ps}}{A_{bs}}\right)}{E_b A_b + \alpha(1-\mu_b)A_p}}{\frac{(1-\mu_b)\beta^2 A_p}{2(E_b A_b + \alpha(1-\mu_b)A_p)} + \frac{e_{33}^2}{c_{33}^E} + \varepsilon_{33}^S + \frac{\delta_{33}}{s}} T_3(s)_{\Delta\bar{\theta},\Delta\bar{\theta}_b=0} \tag{4.147}$$

By the same argument as the surface temperature response, the influence of an electric displacement due to for example the input resistance of external signal conditioning electronics can be re-introduced into Equation 4.147 by including a notional resistor R_s in parallel with the piezoelectric medium to yield Equation 4.148.

$$V_o(s) = l_p \frac{\frac{e_{33}}{c_{33}^E} - \frac{\beta\left((1-\mu_b)A_p\frac{c_{31}^E}{c_{33}^E} + \mu_b A_b \frac{A_{ps}}{A_{bs}}\right)}{E_b A_b + \alpha(1-\mu_b)A_p}}{\frac{(1-\mu_b)\beta^2 A_p}{2(E_b A_b + \alpha(1-\mu_b)A_p)} + \frac{e_{33}^2}{c_{33}^E} + \varepsilon_{33}^S + \frac{l_p}{sA_s}\left(\frac{1}{R_p} + \frac{1}{R_s}\right)} T_3(s)_{\Delta\bar{\theta},\Delta\bar{\theta}_b=0} \tag{4.148}$$

Equations 4.149 and Equation 4.150 therefore give the corresponding electric displacement and displacement current respectively.

$$D_3(s) = l_p \frac{\frac{e_{33}}{c_{33}^E} - \frac{\beta\left((1-\mu_b)A_p\frac{c_{31}^E}{c_{33}^E} + \mu_b A_b \frac{A_{ps}}{A_{bs}}\right)}{E_b A_b + \alpha(1-\mu_b)A_p}}{sA_s R_s\left(\frac{(1-\mu_b)\beta^2 A_p}{2(E_b A_b + \alpha(1-\mu_b)A_p)} + \frac{e_{33}^2}{c_{33}^E} + \varepsilon_{33}^S\right) + l_p\left(\frac{R_s}{R_p}+1\right)} T_3(s)_{\Delta\bar{\theta},\Delta\bar{\theta}_b=0} \tag{4.149}$$

$$I_o(s) = sA_s l_p \frac{\frac{e_{33}}{c_{33}^E} - \frac{\beta\left((1-\mu_b)A_p\frac{c_{31}^E}{c_{33}^E} + \mu_b A_b \frac{A_{ps}}{A_{bs}}\right)}{E_b A_b + \alpha(1-\mu_b)A_p}}{sA_s R_s\left(\frac{(1-\mu_b)\beta^2 A_p}{2(E_b A_b + \alpha(1-\mu_b)A_p)} + \frac{e_{33}^2}{c_{33}^E} + \varepsilon_{33}^S\right) + l_p\left(\frac{R_s}{R_p}+1\right)} T_3(s)_{\Delta\bar{\theta},\Delta\bar{\theta}_b=0} \tag{4.150}$$

Since β is negative, the effect of substrate clamping tends to reduce the sensor element response to an applied stress as E_b or A_b is increased.

4.12.2 Voltage response – Fourier form

The corresponding Fourier forms of Equation 4.146 to Equation 4.150 are given by letting $s = j\omega$ to yield Equation 4.151 to Equation 4.160 respectively.

$$\bar{E}_3(j\omega) = \frac{\frac{\beta\left((1-\mu_b)A_p\frac{c_{31}^E}{c_{33}^E}+\mu_b A_b\frac{A_{ps}}{A_{bs}}\right)}{E_bA_b+\alpha(1-\mu_b)A_p} - \frac{e_{33}}{c_{33}^E}}{\frac{(1-\mu_b)\beta^2A_p}{2(E_bA_b+\alpha(1-\mu_b)A_p)} + \frac{e_{33}^2}{c_{33}^E} + \varepsilon_{33}^S + \frac{\delta_{33}}{j\omega}} T_3(j\omega)_{\Delta\bar{\theta},\Delta\bar{\theta}_b=0} \quad (4.151)$$

$$V_o(j\omega) = l_p \frac{\frac{e_{33}}{c_{33}^E} - \frac{\beta\left((1-\mu_b)A_p\frac{c_{31}^E}{c_{33}^E}+\mu_b A_b\frac{A_{ps}}{A_{bs}}\right)}{E_bA_b+\alpha(1-\mu_b)A_p}}{\frac{(1-\mu_b)\beta^2A_p}{2(E_bA_b+\alpha(1-\mu_b)A_p)} + \frac{e_{33}^2}{c_{33}^E} + \varepsilon_{33}^S + \frac{\delta_{33}}{j\omega}} T_3(j\omega)_{\Delta\bar{\theta},\Delta\bar{\theta}_b=0} \quad (4.152)$$

$$V_o(j\omega) = l_p \frac{\frac{e_{33}}{c_{33}^E} - \frac{\beta\left((1-\mu_b)A_p\frac{c_{31}^E}{c_{33}^E}+\mu_b A_b\frac{A_{ps}}{A_{bs}}\right)}{E_bA_b+\alpha(1-\mu_b)A_p}}{\frac{(1-\mu_b)\beta^2A_p}{2(E_bA_b+\alpha(1-\mu_b)A_p)} + \frac{e_{33}^2}{c_{33}^E} + \varepsilon_{33}^S + \frac{l_p}{j\omega A_S}\left(\frac{1}{R_p}+\frac{1}{R_S}\right)} T_3(j\omega)_{\Delta\bar{\theta},\Delta\bar{\theta}_b=0} \quad (4.153)$$

$$D_3(j\omega) = l_p \frac{\frac{e_{33}}{c_{33}^E} - \frac{\beta\left((1-\mu_b)A_p\frac{c_{31}^E}{c_{33}^E}+\mu_b A_b\frac{A_{ps}}{A_{bs}}\right)}{E_bA_b+\alpha(1-\mu_b)A_p}}{j\omega A_sR_s\left(\frac{(1-\mu_b)\beta^2A_p}{2(E_bA_b+\alpha(1-\mu_b)A_p)} + \frac{e_{33}^2}{c_{33}^E} + \varepsilon_{33}^S\right) + l_p\left(\frac{R_s}{R_p}+1\right)} T_3(j\omega)_{\Delta\bar{\theta},\Delta\bar{\theta}_b=0} \quad (4.154)$$

$$I_o(j\omega) = j\omega A_s l_p \frac{\frac{e_{33}}{c_{33}^E} - \frac{\beta\left((1-\mu_b)A_p\frac{c_{31}^E}{c_{33}^E}+\mu_b A_b\frac{A_{ps}}{A_{bs}}\right)}{E_bA_b+\alpha(1-\mu_b)A_p}}{j\omega A_sR_s\left(\frac{(1-\mu_b)\beta^2A_p}{2(E_bA_b+\alpha(1-\mu_b)A_p)} + \frac{e_{33}^2}{c_{33}^E} + \varepsilon_{33}^S\right) + l_p\left(\frac{R_s}{R_p}+1\right)} T_3(j\omega)_{\Delta\bar{\theta},\Delta\bar{\theta}_b=0} \quad (4.155)$$

4.13 Conclusions

Models describing the low frequency response of the sensor element to a temperature change and/or applied axial stress under substrate clamping conditions have been developed. The models include the effect of substrate clamping and both internal equivalent resistance that represents dielectric leakage and an externally connected resistance that represents the input resistance of a follow-on signal conditioning amplifier. The effect of the adhesive used to bond the substrate and electroded piezoelectric media have a negligible mechanical effect on the sensor element response when the adhesive temperature is kept below the glass transition temperature and it can therefore be reasonably assumed that the piezoelectric medium is rigidly bonded to the substrate. While this assumption holds, the observed

effective pyroelectric response is approximately 180% greater than the constant stress pyroelectric coefficient that would be observed in the absence of substrate clamping. At temperatures above the glass transition temperature, it can be expected that the observed pyroelectric response will be significantly reduced and it is therefore important that the sensor element is not exposed to temperatures above approximately $80°C$. At low frequency, the piezoelectric element can be adequately modelled as a shunt-connected capacitor and resistor in parallel with a current source, which represents the rate of change of the negative piezoelectric medium bound surface charge due to a temperature change or applied axial stress.

The effect of substrate clamping on the low frequency sensor element capacitance is to decrease it by approximately 30% compared to the constant stress capacitance value that would otherwise be observed in the absence of the substrate.

While response models for both applied axial stress and temperature have been derived, the research presented in this thesis concentrates on the use of the temperature response models of the PZT-5H sensor element to investigate the signal conditioning output voltage response.

Chapter 5

Temperature dependence of Clamped and LF immittances

5.1 Introduction

This chapter describes the investigation into the collective temperature dependency of the material constants in terms of the clamped (constant strain), total low frequency and mechanical low frequency capacitances denoted by C_o, C_p and C_m respectively. The temperature within a transtibial prosthetic socket typically varies within the range $25°C$ to $35°C$ [99] and it is therefore necessary to investigate the temperature dependence of the C_o, C_p and C_m over this temperature range. The low frequency PZT-5H sensor element capacitance is dependent on the clamped permittivity and piezoelectric constants of the PZT; and stiffness matrix elements of both PZT and substrate. The pyroelectric charge generated is also dependent on the piezoelectric constants and stiffness matrix elements of both PZT and substrate via the effective pyroelectric coefficient, P_{eff} given by Equation 4.31 and this is investigated further in Chapter 7, Section 7.5. By inspection of Equation 4.33 in

Section 4.7 the capacitances C_o, C_m and C_p are given by Equations 5.1 to 5.3 respectively.

$$C_o = \frac{A_s \varepsilon_{33}^S}{l_p} \tag{5.1}$$

$$C_m = \frac{A_s}{l_p}\left(\frac{(1-\mu_b)\beta^2 A_p}{2\left(E_b A_b + \alpha(1-\mu_b)A_p\right)} + \frac{e_{33}^2}{c_{33}^E}\right) \tag{5.2}$$

$$C_p = \frac{A_s}{l_p}\left(\frac{(1-\mu_b)\beta^2 A_p}{2\left(E_b A_b + \alpha(1-\mu_b)A_p\right)} + \frac{e_{33}^2}{c_{33}^E} + \varepsilon_{33}^S\right) \tag{5.3}$$

The clamped capacitance C_o is a purely electrical capacitance dependent only on the dimensions of the piezoelectric medium and constant strain permittivity while C_m is a purely mechanical contribution to the total equivalent capacitance denoted by C_p and given by $C_p = C_o + C_m$. C_p is the low frequency capacitance and is equal to the $1kHz$ capacitance specification for the PZT-5H Murata Type 7BB-27-4 diaphragm element $(20nF \pm 30\%)$ as discussed in Section 4.2. It can be seen from Equation 5.3 that removal of the substrate by setting $A_b = 0$ yields Equation 5.4 for the constant stress permittivity denoted by ε_{33}^T. The constant stress permittivity is observed at low frequency when the piezoelectric medium is allowed to strain freely in all dimensions such that $A_b = 0$.

$$\varepsilon_{33}^T = \varepsilon_{33}^S + \frac{\beta^2}{2\alpha} + \frac{e_{33}^2}{c_{33}^E} \tag{5.4}$$

In the linear theory leading to the piezoelectric and substrate equations of state described in Chapter 3, it is assumed that the material constants of both piezoelectric and substrate media are constant for a small temperature change $\Delta\theta$. To test this assumption, the temperature dependency of the sensor element capacitances over the temperature range $20°C$ to $40°C$ for which the sensor is required to operate were therefore investigated. A significant temperature dependency in the capacitances infers an undesirable temperature dependent gain and cut-on frequency leading to a non-linear sensor element output voltage response V_o. An observed change in capacitance may not only be related to the temperature dependence of the dielectric constant, but also temperature dependence of the stiffness coefficients of

the substrate and piezoelectric media and possibly the stress-charge piezoelectric coefficients.

Section 5.2 describes the mathematical modelling of the low frequency and series resonance admittances, while Section 5.3 describes the experimental set-up and experimental procedure. Section 5.4 presents the measurement results and the extraction of the sensor element capacitances at steady state temperatures of $20°C$ to $40°C$ in increments of $5°C$.

5.2 Immittance modelling

5.2.1 Low frequency admittance

To investigate the effect of temperature on the performance of the sensor a low frequency immittance model is presented that allows the low frequency capacitance C_p to be measured, where the effect of the inertial masses of the brass substrate and PZT body can be neglected. The clamped (or constant strain) capacitance C_o is extracted using the Butterworth Van Dyke (BVD) piezoelectric resonator model [100]. The low frequency electrical equivalent mechanical capacitance C_m can then be obtained from $C_m = C_p - C_0$.

Under the conditions that $T_3 = 0$ and that the measurement temperature is held temporally and spatially constant throughout the piezoelectric material over the period of measurement, such that $\Delta\theta(x_3, t) = \Delta\bar{\theta} = 0$, $E_3(x_3, t) = \bar{E}_3(t)$ and $S_3(x_3, t) = \bar{S}_3(t)$, then Equations 5.96, 5.97 and 5.99 reduce to Equations 5.5, 5.6 and 5.7, respectively.

$$0 = 2c_{31}^E S + c_{33}^E S_3 - e_{33}E_3 \tag{5.5}$$

$$D_3 = 2e_{31}S + e_{33}S_3 + \varepsilon_{33}^S E_3 \tag{5.6}$$

$$-\frac{E_b}{(1-\mu_b)}\frac{A_b}{A_p}S = (c_{11}^E + c_{12}^E)S + c_{31}^E S_3 - e_{31}E_3 \tag{5.7}$$

By algebraic manipulation of Equation 5.5 and 5.7, both S and S_3 can be found in terms of E_3. Further substitution into Equation 5.6 yields Equation 5.8.

$$\frac{D_3}{E_3} = \frac{(1-\mu_b)\beta^2 A_p}{2\left(E_b A_b + \alpha(1-\mu_b)A_p\right)} + \frac{e_{33}^2}{c_{33}^E} + \varepsilon_{33}^S \tag{5.8}$$

For an applied voltage V that gives rise to a current I, and noting that $D_3 = -I/j\omega A_s$ where A_s is the surface area of the electrodes, and $E_3 = -V/l_p$, then the low frequency admittance denoted by $Y_{lf} = I/V$ is given by Equation 5.9.

$$Y_{lf} = \frac{j\omega A_s}{l_p}\left[\frac{(1-\mu_b)\beta^2 A_p}{2(E_b A_b + \alpha(1-\mu_b)A_p)} + \frac{e_{33}^2}{c_{33}^E} + \varepsilon_{33}^S\right] \tag{5.9}$$

The low frequency immittance can be written $Y_{lf} = G_{lf} + jB_{lf}$, where G_{lf} is the low frequency conductance (S), and B_{lf} is the low frequency susceptance (S). When Equation 5.9 is compared with Equation 5.3, it is apparent that the measured low frequency susceptance B_{lf} is equal to ωC_p and that C_p can therefore be obtained by measuring the gradient of a B_{lf}-ω plot. In the derivation of Y_{lf} dielectric and mechanical losses are considered to be negligible and therefore the admittance is purely susceptive. This is a reasonable assumption in the low frequency regime however if required, mechanical and electrical losses can be introduced by treating the material constants as complex, resulting in an additional real valued conductance term.

5.2.2 Series resonance admittance

When excited by an AC signal, the PZT sensor element becomes a resonator that may be described using the well-known BVD model shown in Figure 5.1 that is valid only for a narrow range of frequencies around a resonance. R_s, C_s and L_s form the mechanical arm and account for mechanical damping and acoustic losses, stiffness and inertial mass respectively. The value and interpretation of R_s, C_s and L_s is dependent on the resonance mode, clamping and mass loading by the substrate, however C_o always represents the mechanically clamped capacitance $C_o = A_s\varepsilon_{33}^S/l_p$ of the sensor [101].

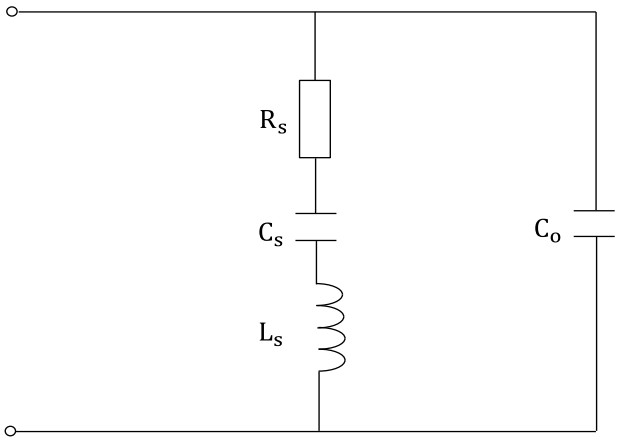

Figure 5.1 BVD electrical equivalent model of a piezoelectric resonator

Equation 5.10 describes the admittance, Y of the BVD model such that $Y = G + jB$ near a resonance where G is the conductance (S) and B is the susceptance (S).

$$Y = \frac{R_S + j\left(\omega C_0 R_S^2 - \left(\omega L_s - \frac{1}{\omega C_S}\right)\left(1 + \frac{C_O}{C_S} - \omega^2 C_0 L_s\right)\right)}{R_S^2 + \left(\omega L_s - \frac{1}{\omega C_S}\right)^2} \tag{5.10}$$

At series resonance, $\omega_s = 1/\sqrt{L_s C_s}$ and the conductance G reaches a peak value while the susceptance, B is equal to $\omega_s C_0$ where ω_s is the series resonance frequency ($rads^{-1}$). The clamped capacitance C_0 of the piezoelectric sensor element is therefore the measured value of capacitance at the series resonance frequency where the measured conductance G reaches its peak.

5.3 Methodology

5.3.1 Experimental set-up

A block diagram of the experimental set-up is shown in Figure 5.2.

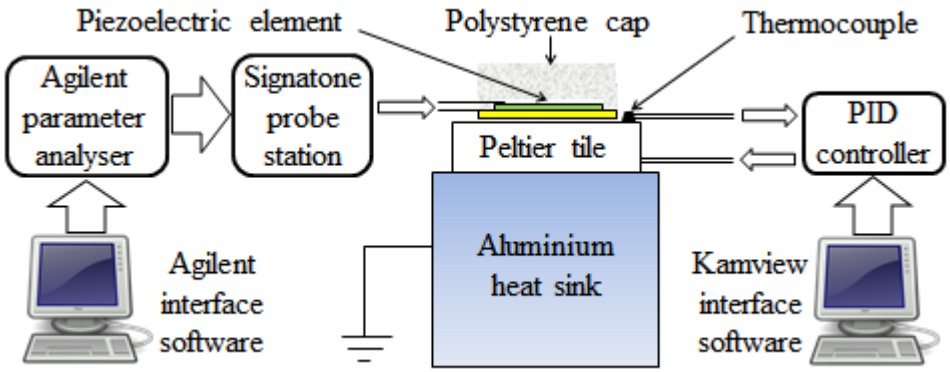

Figure 5.2 Immittance measurement set-up

The PZT sensor element is supplied pre-fitted with aluminium flying leads. A $100mv$ ac signal was applied to the sensor via the flying leads using an Agilent B1500A parameter analyser connected via a Signatone probe station. The terminations of the sensor element flying leads were fixed to a glass slide using Agar electrically conducting silver paste to form electrodes. The electrodes were connected to the parameter analyser via probes lowered onto the dried silver paste electrodes. The probe station was mounted on a vibration isolation table to avoid corruption of the measured immittance due to currents induced by vibration.

The sensor element was placed substrate down on a European Thermodynamics Peltier tile and aluminium heat sink assembly, and affixed using RS Heat Sink Compound Plus paste to limit mechanical loading and ensure good thermal conduction over the entire brass substrate surface. The paste also served to suppress the large amplitude $4.6kHz$ flexure-resonance mode, ensuring uncorrupted low frequency immittance measurements.

Room convection currents that can give rise to a non-uniform temperature distribution in the sensor element during impedance measurements will result in the measurement of a pyroelectric current by the parameter analyser. This current is in

addition to that generated by the parameter analyser and will result in erroneous instantaneous impedance measurements. To minimise this error, the sensor was shielded by placing the entire experimental set-up inside the probe station and covering the sensor element with a cap fashioned from expanded polystyrene. Care was taken to ensure the polystyrene cap did not contact the surface of the PZT sensor element. The very low thermal conductivity of expanded polystyrene reduces the occurrence of steady state temperature gradients and axial heat flows within the piezoelectric and substrate materials that would otherwise exist due to a temperature difference between the Peltier tile / substrate interface and sensor element top electrode.

5.3.2 Experimental procedure

The temperature dependencies of the clamped capacitance C_o and low frequency capacitance C_p are investigated by measuring the impedance of the sensor isothermally over a high frequency range $60kHz$ to $200kHz$ to include the first resonance, and over a low frequency range $1kHz$ to $9kHz$ respectively. The temperature was varied in steps of $5°C$ over the range $20°C$ to $40°C$. It is assumed that the piezoelectric, elastic and dielectric constants are constant over the measurement frequency ranges and that the resistivity of the electrodes and resistance of the supply cable are negligible.

The temperature of the Peltier tile was controlled using a KamView proportional-integrator-differentiator (PID) controller, with the target temperature being selected using the KamView user interface. The Peltier tile temperature feedback signal was implemented by the use of a thermocouple attached to the Peltier tile surface. The risk of condensation on the sensor was avoided by ensuring that the ambient temperature was maintained below the minimum measurement temperature and that the Peltier temperature did not drop below ambient temperature during its hunting period.

The temperature was increased in $5°C$ steps over a temperature range of $20°C$ to $40°C$. Prior to each impedance measurement, the temperature was allowed to stabilise for $15\ minutes$ to avoid pyroelectric effects and to ensure a constant and

uniform temperature throughout the body of the sensor. Secondly, the PZT element was manually short-circuited via a small resistor that was briefly connected across the silver paste electrodes to ensure the required initial condition of zero spatial mean electric field.

5.4 Immittance measurements

5.4.1 Low frequency admmitance - extraction of C_p

The low frequency admittance measurements for the temperature range $20°C$ to $40°C$ are shown in Figure 5.3. The constant B/f relationship over the $1-9kHz$ range at all temperatures confirms that the low frequency admittance is largely susceptive.

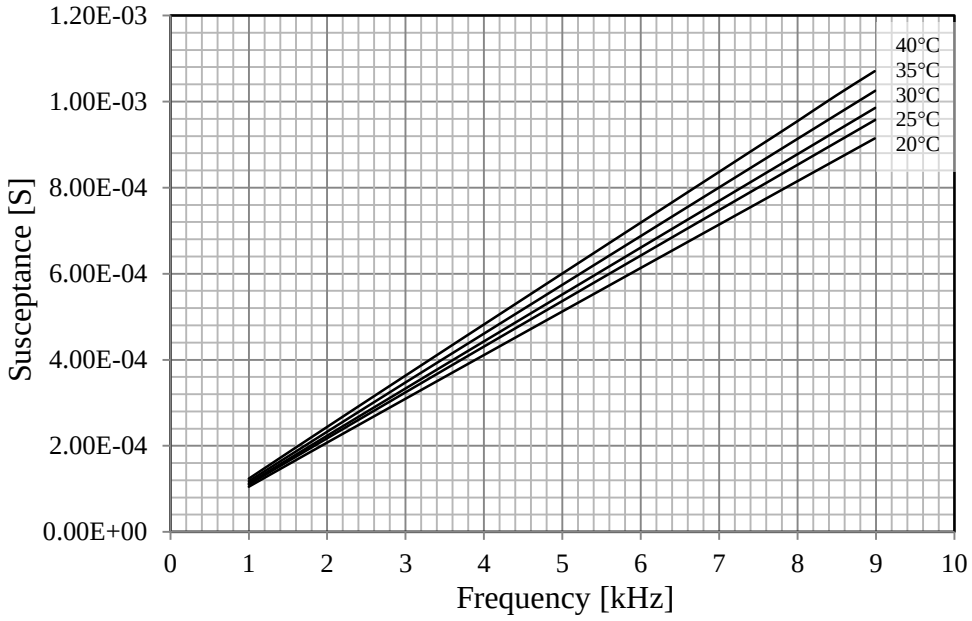

Figure 5.3 Susceptance vs frequency at $20°C$ to 40°

At frequencies under $9kHz$, the effect of damping loss and inertial mass in the PZT film and brass substrate can therefore be considered negligible. It can therefore be inferred that since the influence of the inertial mass reduces with frequency that at frequencies below $1kHz$ the inertial mass will also have a negligible effect and that the B/f relationship will remain linear down to DC. The

low frequency capacitance C_p is extracted from Figure 5.3 by fitting a linear trend line at each temperature using Excel. C_p is then determined from $C_p = \Delta B/2\pi\Delta f$.

The DC resistivity of PZT materials is also known to vary significantly with temperature over the range of interest [69],[94]. As frequency is reduced, the measured resistivity, which is inversely proportional to the conductivity and conductance, increases almost asymptotically. Since the minimum frequency the Agilent B1500A analyser is can measure at is $1kHz$, it is not possible to obtain a meaningful measurement of the DC resistivity by extrapolation of the immittance measurements. However, the measured conductance and equivalent resistance of the PZT sensor element at $1kHz$ over the temperature range $25°C$ to $35°C$ indicates that the conductance tends to increase with temperature as shown in Figure 5.4.

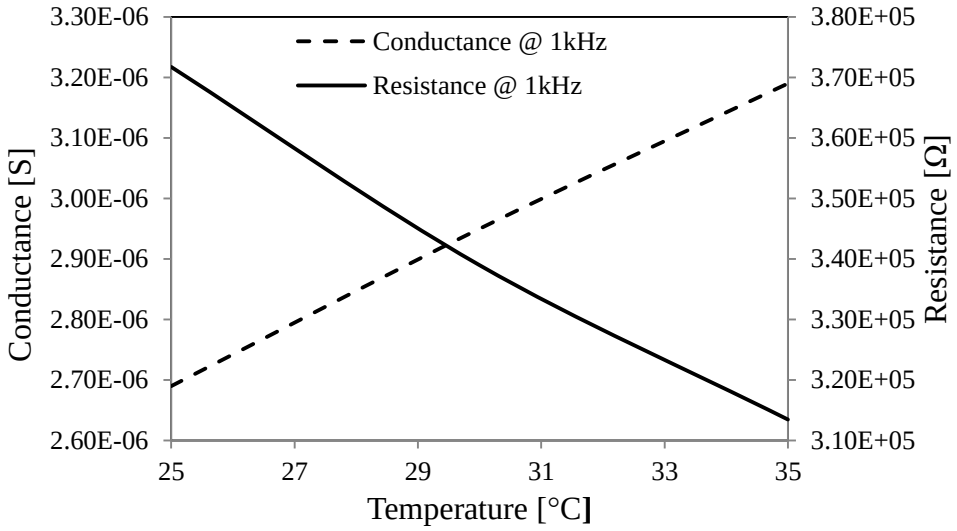

Figure 5.4 Conductance and resistance at $25°C$ to $35°C$ and $1kHz$

It can be seen from Figure 5.4 that the conductance increases by approximately 20% at $35°C$ compared to the value at $25°C$.

5.4.2 Series resonance admmitance - extraction of C_o

The piezoelectric PZT film is thin relative to its diameter and therefore radial modes are excited at frequencies below that of the thickness resonant modes. The first vibration resonance observed and used to determine C_o is therefore radial. The

use of the first radial vibration mode ensures a clean measurement uncorrupted by the coincidence of thickness mode and higher frequency radial mode resonances.

The admittance results for the temperature range $20°C$ to $40°C$ were compared with the BVD model admittance described by Equation 5.10. At series resonance the term $(\omega L_s - 1/\ \omega_s C_s)$ in the denominator of Equation 5.10 equals zero and the conductance G reaches its peak value while the susceptance B reduces to $\omega_s C_0$ where ω_s is the series resonance frequency. The conductance G and capacitance B/ω measurements at temperatures of $20°C$ to $40°C$ in steps of $10°C$ for the first radial mode are shown in Figure 5.5 a) to e) respectively. The constant strain capacitances C_o at each temperature are therefore found directly by reading off the value of B/ω at the peak value of G.

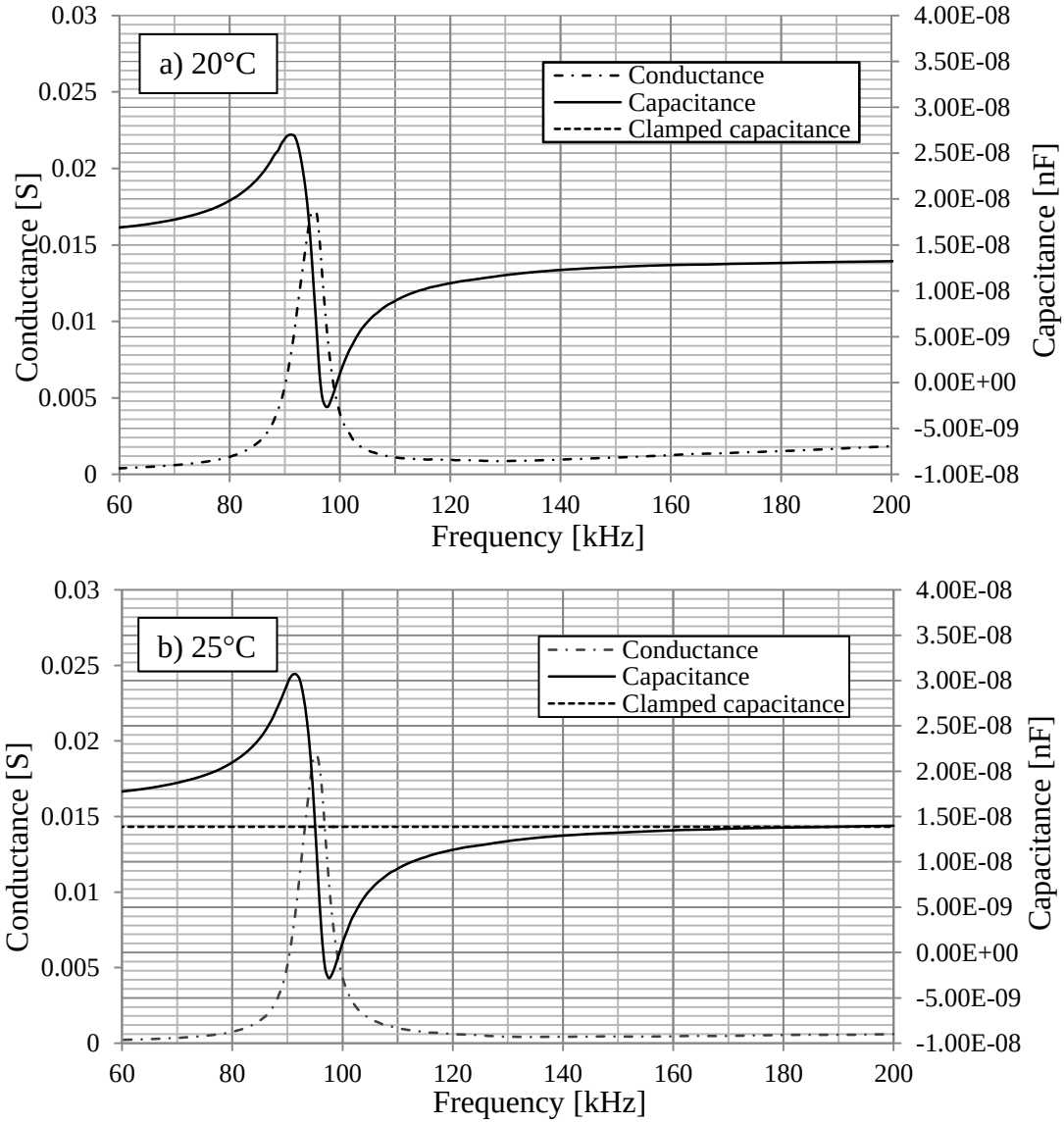

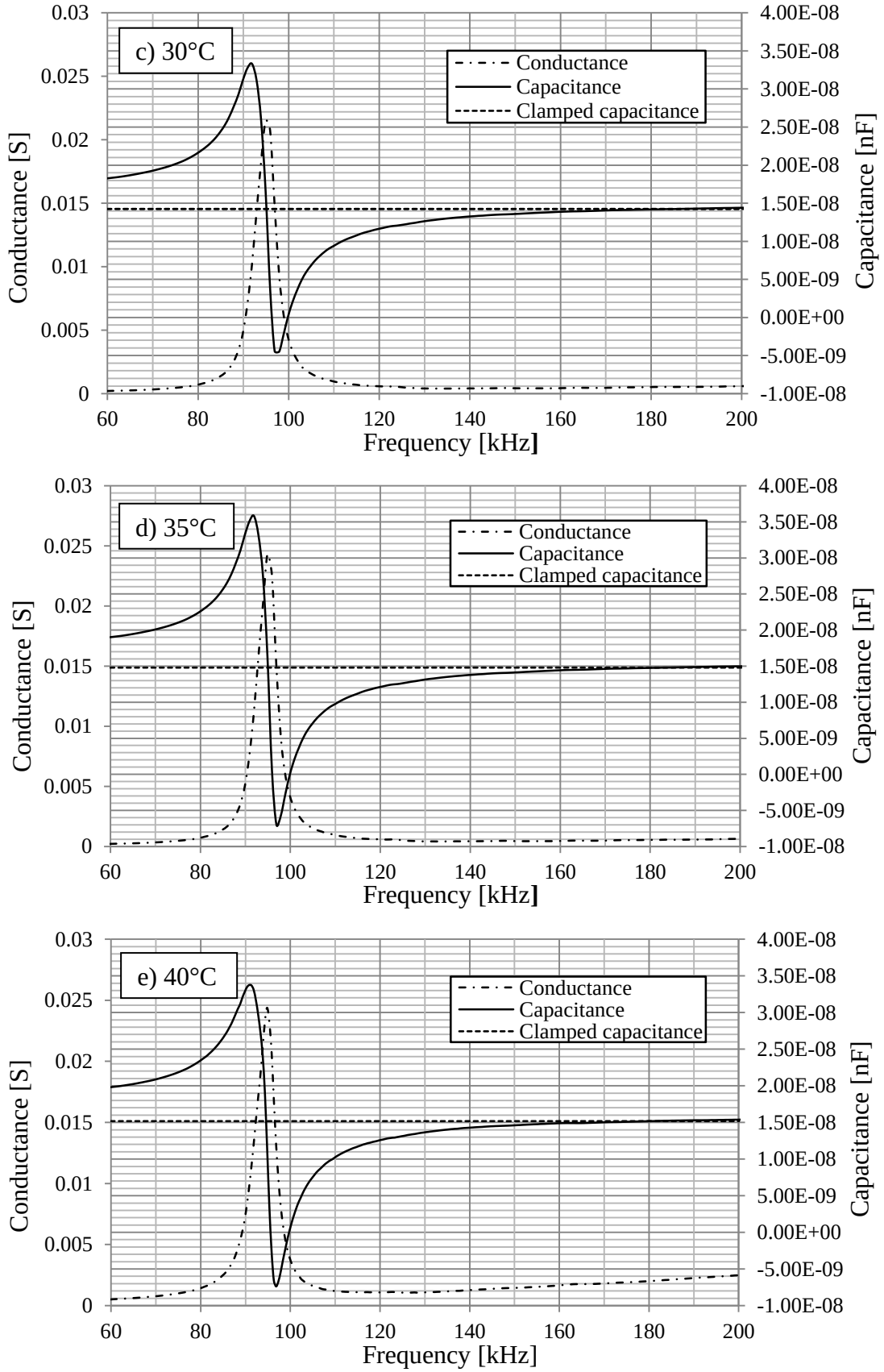

Figure 5.5 Conductance and capacitance measured at a) $20°C$ to e) $40°C$

Confirmation of C_o was made by noting that C_o is also approximately equal to the capacitance at $2\omega_a$ equal to $B(2\omega_a)/2\omega_a$ where ω_a is the anti-resonance frequency that occurs at the BVD model maximum impedance (minimum admittance) [102]. The value of ω_a is higher but very close to the series resonance ω_s, and since the measured capacitance is invariant with frequency at around $2\omega_a$, a confirmation of C_o can be made by comparing C_o to the capacitance at a frequency of $200kHz$ for each of the capacitance plots in Figure 5.5.

5.4.3 Capacitance temperature dependence

Figure 5.6 shows the measured low frequency capacitance, clamped capacitance and low frequency mechanical capacitance of the PZT sensor element. The mechanical capacitance, C_m is calculated by subtracting the measure clamped capacitance from the low frequency capacitance such that $C_m = C_p - C_o$.

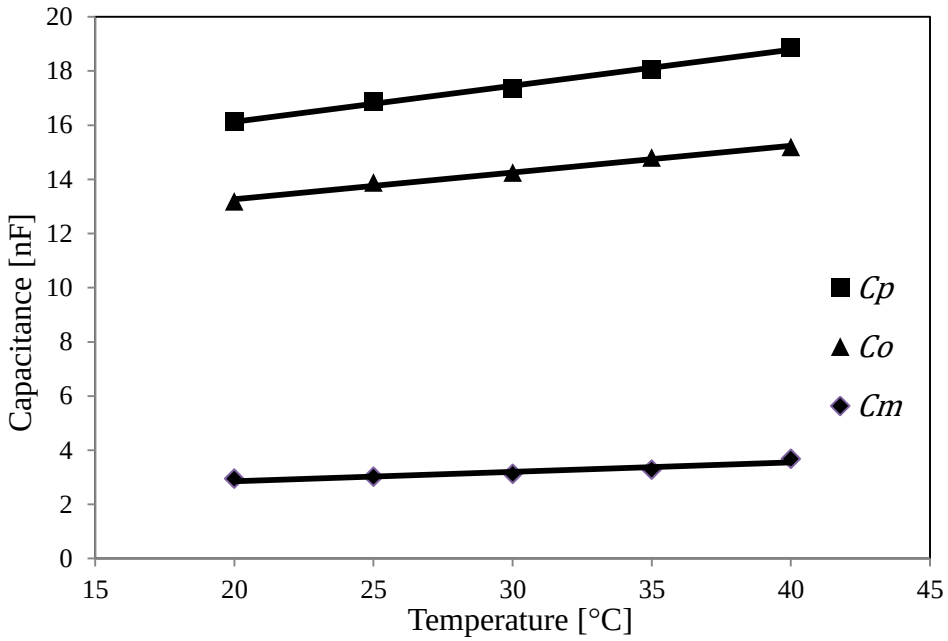

Figure 5.6 Sensor element total, clamped and mechanical capacitances as a function of temperature

Table 5.1 gives the values of C_p, C_o and C_m as a function of temperature.

$\theta[°C]$	$C_p\ [nF]$	$C_o\ [nF]$	$C_m = C_p - C_o\ [nF]$
20	16.12	13.18	2.94
25	16.88	13.87	3.01
30	17.36	14.24	3.12
35	18.06	14.79	3.27
40	18.86	15.18	3.68

Table 5.1 Sensor element total, clamped and mechanical capacitances

It can be seen from Table 5.1 that over the temperature range $20°C - 40°C$, the low frequency, clamped and mechanical capacitances rise by 17%, 15.2% and 25.2% respectively. The measured value of C_o at $20°C$ is in the proximity of the room temperature nominal value calculated from $C_o = A_s\varepsilon_{33}^S/l_p = 14.7nF$ using the material constants of PZT-5H given in Appendix A.1. However, the measured value of $C_p = 16.12nF$ at $20°C$ is considerably lower than the low frequency capacitance $C_p = 22.7nF$ at room temperature, which is calculated using Equation 4.33. While both values of C_p are comfortably within the $C_p = 20nF \pm 30\%$ manufacturer specification, it is useful to speculate on the reason for this difference.

The nominal calculated value of $C_m = C_p - C_o$ is $C_m = 8nF$, which is considerably higher than the measured value of $C_m = 2.94nF$. By inspection of Equation 4.33 it can be seen that C_m is dependent on e_{33}^2 and β^2, where β is proportional to e_{31} and e_{33}. It is therefore suggested that the reduced value of C_m may be due to reduced values of the published e_{31} and e_{33} values given in Appendix A1. A reduction of 40% in both values of e_{31} and e_{33} would yield the value of C_m observed.

5.5 Conclusions

It has been demonstrated that C_p , C_o and C_m exhibit an approximately linear relationship with temperature and that all capacitances show a significant increase with increasing temperature over the range $20°C - 40°C$. The observed increases in

capacitance are not only be related to the temperature dependence of the dielectric constant, but also temperature dependence of the stiffness coefficients of the substrate and piezoelectric media and possibly the stress-charge piezoelectric coefficients. C_o exhibits the largest absolute increase of $2nF$ while C_m exhibits the greatest percentage increase at 25.2% over the temperature range $20°C - 40°C$ suggesting that the constant strain permittivity increases approximately linearly with temperature while the stiffnesses of the piezoelectric and substrate media reduce with temperature over the temperature range $20°C - 40°C$, assuming that the stress-charge piezoelectric coefficients remain approximately constant. In addition, it is shown that the conductance increases by approximately 20% over the temperature range $25°C$ to $35°C$ and therefore the time constant, which is dependent on the conductance and capacitance of the sensor element will also be temperature dependent. These temperature dependencies indicate an undesirable temperature dependent gain, time constant and therefore cut-on frequency that will produce a non-linear sensor element voltage response V_o over the temperature range $20°C - 40°C$.

It is worth noting that the effective pyroelectric coefficient, P_{eff} discussed in Section 4.6 is also dependent on the stiffness coefficients of the substrate and piezoelectric media and the stress-charge piezoelectric coefficients. It too may therefore exhibit a significant temperature dependence over the temperature range $20°C - 40°C$. This is discussed further in Chapter 7, Section 7.5, where linearity in response over this temperature range is investigated.

Chapter 6

Signal conditioning and e-Health platform

6.1 Introduction

From the results of Chapter 5, it is desirable that the significant temperature dependence of the sensor capacitances, C_p , C_o and C_m are mitigated. The use of charge-mode signal conditioning effectively provides a low impedance 'virtual earth' input that greatly reduces the influence of C_p , C_o and C_m and therefore their temperature dependence on the measured response.

This chapter describes the bipolar and unipolar charge amplifier designs developed, built and used in the characterisation of the PZT-5H piezoelectric sensor element and for sensor response measurements. In addition, an enhanced open loop gain design that can mitigate the effect of reduced dielectric resistance in the sensor element is presented.

Section 6.3.2 describes a proof of concept $5V$ unipolar design that provides portability, has low power consumption, low cost, and that can be operated from a

single regulated $5V$ power source supplied by an Arduino Uno platform. In addition, this design is capable of being operated with large time constants to allow continuous operation over an $8\ hour$ time period while maintaining low measurement error with respect to response voltage decay and output voltage drift. A DC bias of $2.5V$ allows the measurement of both positive and negative temperature changes. This design is used in Chapter 7, Section 7.5, to investigate the linearity of the PZT-5H piezoelectric element over a temperature range up to and exceeding the required maximum temperature change that would be applied in use.

Section 6.3.3 describes the bipolar design built as a proof of concept to demonstrate the feasibility of temperature change measurement using a PZT-5H piezoelectric element. This design is used to measure the overall sensor response to a rapid change in temperature applied to the substrate of the piezoelectric element by a proportional integrator differentiator (PID) controlled Peltier device as described in Chapter 7, Section 7.3.

A unipolar charge amplifier design with a similar specification to the unipolar design discussed in Section 6.3.2, but with the addition of an enhanced open loop gain, is discussed in Section 6.3.4. The enhanced open loop gain reduces the possible effects of piezoelectric medium resistivity degradation, which is described in Section 6.3.2, and reduces the sensitivity to open loop gain variations due to temperature and manufacturing tolerances.

Section 6.4.2 addresses the effect and mitigation of op-amp input bias currents while Section 6.4.3 and Section 6.4.4 address the effect and mitigation of the input referred offset voltage and bias voltage drift respectively. Section 6.4.5 describes the method for voltage drift compensation while Section 6.5 describes a comprehensive noise model applicable to the three charge amplifier designs and gives a theoretical estimate for the signal to noise ratio. The e-Health platform that is used in the experimental analyses to push the measured data to a server database.is discussed in Section 6.6.

6.2 Choice of signal conditioning method

It is required that the sensor element signal conditioning operates from a unipolar $5V$ supply and that time constant is large enough to provide a faithful representation of the measured signal over an operating time of $8\,hours$. The low frequency resistivity of PZT-5H at $25°C$ is greater than $10^{11}\Omega$m [103] and therefore by using the area of the electrodes $A_s = 2.6 \times 10^{-4}m^2$ and thickness of the PZT-5H $l_p = 0.23 \times 10^{-3}$, the dielectric resistance, R_p given by Equation 4.34 can be estimated at greater than $90G\Omega$. The nominal low frequency capacitance C_p of the sensor, calculated using Equation 4.33 and the material constants given in Appendix A.1, is $22.7nF$ at room temperature. The time constant of the sensor element denoted by τ is therefore $\tau \approx 2000$s. Even using the fictive ideal case voltage-mode signal conditioning where the input impedance of the signal conditioning electronics can be considered infinite, this sensor time constant is several orders of magnitude too low to produce a useful sensor where it is required that the sensor operate over a period of several hours. In addition, the manufacturer specified tolerance of $C_p = 20nF \pm 30\%$ means that the time constant and gain will vary considerably between devices. Furthermore, an input shunt resistance may be required to provide a necessary path for unavoidable amplifier bias currents at the high impedance input. Since this shunt resistance is in parallel with the sensor dielectric resistance, the actual time constant will be lower and the cut-on frequency higher than the ideal case. In addition, the voltage generated is around $8V/K - 9V/K$ precluding the use of the desired $5V$ supply and measurement over the temperature range $20°C - 40°C$, and the temperature dependence of R_p indicates that the sensor time constant will be significantly reduced at the higher temperatures in the $20°C - 40°C$ measurement range. The significant temperature dependence of C_p and R_p demonstrated in Chapter 5 suggests that an undesirable temperature dependent gain and cut-on frequency leading to a non-linear sensor element voltage response V_o is likely over the temperature range $20°C - 40°C$.

In principle, a large capacitance can be shunt-connected to the sensor element to reduce the gain, increase the time constant and mitigate the significant temperature dependence of C_p. While the shunt capacitance will reduce the gain and increase the

time constant, the required time constant is difficult to achieve. This is due to the limiting value of R_p and the capacitance value / insulation resistance trade-off associated with the polypropylene capacitors, where the specified insulation resistance tends to reduce with increasing nominal capacitance value.

The option of charge-mode signal conditioning is therefore chosen rather than voltage-mode signal conditioning. The near virtual earth input of charge-mode signal conditioning effectively isolates the temperature dependent sensor element low frequency impedance from the charge-mode signal conditioning amplifier voltage response. The feedback network impedances of the charge amplification stages now determine the decay time constant observed at the output of the charge-mode amplifier with the required time constant being realised by appropriate design. For use as part of a practical sensor, it is necessary that the unipolar charge amplifier design discussed in Section 6.3.2 is capable of operating with a time constant large enough to provide the necessary signal conditioning to record continuous in-situ measurements of temperature change without significant signal decay over a useful measurement period, while meeting the required specification. As discussed in Section 2.5, this specification requires a continuous measurement duration of approximately $8\ hours$ with an output voltage signal decay of less than 2%.

Charge mode amplification in particular is prone to the effects of triboelectric cable noise since the output voltage is proportional to the instantaneous free charge at the feedback capacitor, which is the sum of the charge due to the temperature change or axial stress measurand and triboelectric charges. While triboelectric cable noise can be reduced by the use of a well-anchored low noise amplifier connecting cable, it cannot be completely eliminated since installation of the sensor element within a prosthetic socket means that some cable movement is inevitable during wear. Furthermore, since the sensor would be used in the external environment, it is not possible to eliminate the risk of signal corruption due to external electromagnetic interference. The use of a differential input was therefore specified for the signal conditioning amplifier designs to reduce the effect of common-mode triboelectric cable noise and induced electromagnetic interference from external sources, that are both present and correlated at both input lines and that appear at the inverting inputs of the charge amplification stages.

6.3 Charge mode signal conditioning design

6.3.1 Choice of components

The $1\mu F$ and $1.5\mu F$ feedback capacitors used in the charge amplification stages are metalised polypropylene types with a tolerance of $\pm 5\%$, chosen for their very high insulation resistance. Since large feedback resistors are required to be used in parallel with the feedback capacitors, it is important that the insulation resistance is high to avoid a significant reduction in the time constant of the charge amplification stages. The voltage divider noise reduction and power supply noise reduction capacitors are ceramic types to provide compact size with large capacitances at low cost. For the power supply, noise reduction capacitances of $0.1\mu F$ and $1\mu F$ were connected between ground and each of the $\pm V_{cc}$ power supply inputs for the bipolar design, and between ground and $+V_{cc}$ for the unipolar design, while ceramic $0.47\mu F$ capacitors are connected between the voltage divider central point and ground to reduce input noise. The requirement of using large feedback resistors lays the amplifier prone to large output voltage swings due to op-amp bias currents and input offset voltages. It is therefore crucial that these are maintained as low as possible. Texas LMC 6081 op-amps were chosen since these specify a very low typical input bias current of $10fA$, typical input offset bias current of $5fA$ and typical input offset voltage of $150\mu V$. All resistors are low noise metal film types, have a low temperature coefficient and provide good temperature stability. The large feedback resistors are thick film types with a $\pm 1\%$ tolerance and all other circuit resistors are thin film types with a $\pm 0.1\%$ tolerance and low temperature coefficients. The R_{pot-1} and R_{pot-2} potentiometers are 25 turn 250Ω trimmers that allow fine resolution voltage compensation via the voltage dividers if required. The nominal values of the components chosen for the amplifier designs given in Section 6.3.2 and Section 6.3.3 to realise a difference amplifier DC gain of $G = R_3/R_2 = 0.5$ are given as follows:

$R_1 = 221k\Omega$	$R_3 = 100k\Omega$	$R_s = 100\Omega$	$R_{d1} = 100k\Omega$	$C_f = 1.5\mu F$
$R_2 = 200k\Omega$	$R_4 = 110k\Omega$	$R_f = 1G\Omega$	$R_{d2} = 221k\Omega$	$C_n = 0.47\mu F$

For the unipolar design, the resistor component values of R_1, R_2 and R_3 were selected to realise low power consumption in the voltage dividers by allowing the use of sufficiently large resistors R_{d1} and R_{d2}.

6.3.2 Unipolar charge amplifier design

The schematic diagram for the unipolar $5V$ single supply charge amplifier is shown in Figure 6.1. This amplifier is designed to be portable, have low power consumption and to operate in tandem with the wearable platform as described in Section 6.6. This design was used for the accumulative voltage response measurements discussed in Chapter 7, Section 7.5. The op-amps power supply and associated additional ceramic power supply noise reduction capacitors are omitted from the schematic for clarity.

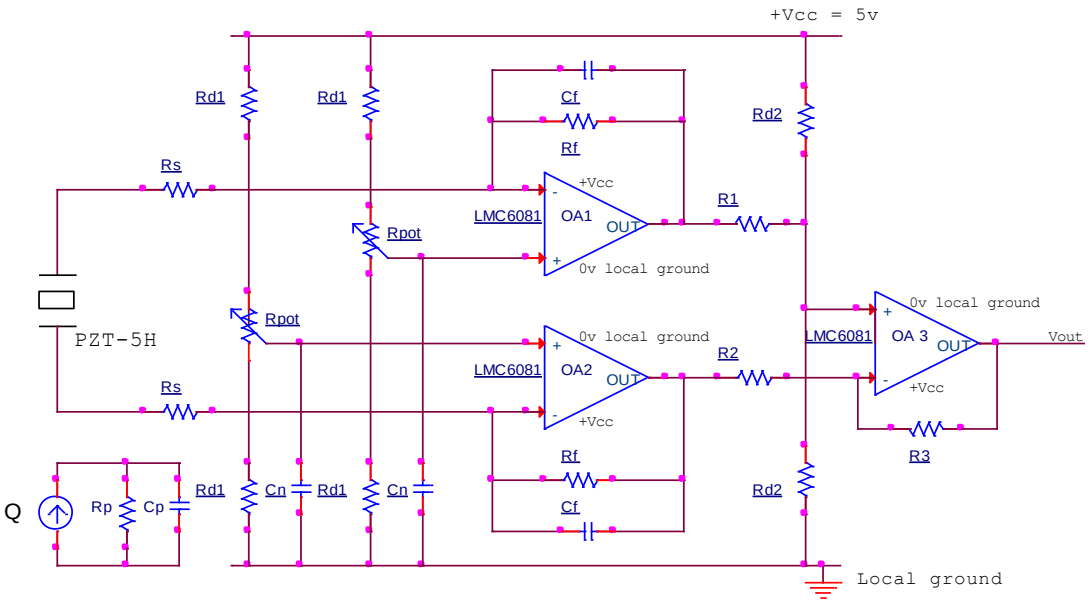

Figure 6.1 Unipolar charge amplifier schematic with PZT-5H model inset

Circuit analysis of the schematic Figure 6.1 yields Equation 6.1 for the frequency-domain output voltage of the charge amplifier stages at OA1 and OA2 which are denoted by $V_{OA1}(j\omega)$ and $V_{OA2}(j\omega)$ respectively where $Z_p = 1/C_p\left(j\omega + 1/R_pC_p\right)$ and $Z_f = 1/C_f\left(j\omega + 1/R_fC_f\right)$. The terms A_v and $\hat{A}_v$ are the frequency dependent and DC open loop gains of OA1 and OA2 respectively where

A_v is represented by a single pole with a $-3dB$ cut off frequency ω_c such that $A_v = \hat{A}_v/(1 + j\omega/\omega_c)$. The gain-bandwidth product of OA1 and OA2 is given by $GBP = \omega_c \hat{A}_v$ and is defined as the OA open loop unity gain frequency.

$$V_{OA1}(j\omega),\ V_{OA2}(j\omega) = \mp \frac{j\omega \mathrm{Q}(j\omega) A_v \left(\frac{Z_p Z_f}{Z_p + 2Z_f + 2R_s}\right)}{1 + A_v \left(\frac{Z_p + 2R_s}{Z_p + 2Z_f + 2R_s}\right)} + \left(\frac{\hat{A}_v}{\hat{A}_v + 1}\right)\frac{V_{cc}}{2} \tag{6.1}$$

The charge $\mathrm{Q}(j\omega)$ is given by Equation 6.2 and the charge $-\mathrm{Q}(j\omega)$ is the frequency dependent dielectric bound charge (C) produced by the PZT-5H element. As discussed in Section 4.8, the charge $-\mathrm{Q}(j\omega)$ exists on the surface of the piezoelectric medium, and is produced in response to a change in polarisation due to a temperature distribution or applied stress stimulus such that $\overline{\mathrm{Q}}_\mathrm{b}(j\omega) = -\mathrm{Q}(j\omega)$. Under all conditions, $\overline{\mathrm{Q}}_\mathrm{b}(j\omega)$ depends only on the spatial mean of the piezoelectric polarisation and not on the particular spatial distribution of the polarisation or on the electric field polarisation of the dielectric. Under ideal short-circuit conditions such that $R_s = 0$ and if the substitution $\hat{A}_v \to \infty$ is valid, then $\mathrm{Q}(j\omega)$ is precisely equal to the electric displacement given by $A_s D_3(j\omega)$.

$$\mathrm{Q}(j\omega) = A_s \left[\begin{array}{l} \left(2e_{31}\varphi_{p1}^E + e_{33}\varphi_{p3}^E + p^s - \frac{\beta E_b A_b \varphi_{p1}^E}{E_b A_b + \alpha(1-\mu_b)A_p}\right)\Delta\bar{\theta}(j\omega) + \\ \frac{\beta E_b A_b \varphi_b \Delta\bar{\theta}_b(j\omega) - \beta\left((1-\mu_b)A_p \frac{c_{31}^E}{c_{33}^E} + \mu_b A_b \frac{A_{ps}}{A_{bs}}\right)T_3(j\omega)}{E_b A_b + \alpha(1-\mu_b)A_p} + \frac{e_{33}}{c_{33}^E} T_3(j\omega) \end{array} \right] \tag{6.2}$$

Circuit analysis of the final difference amplifier stage yields Equation 6.3.

$$V_{out}(j\omega) = \frac{GBP\left(\left(\frac{R_{d2}}{2R_1 + R_{d2}}\right)V_{OA2}(j\omega) - \left(\frac{R_3}{R_2 + R_3}\right)V_{OA1}(j\omega)\right)}{j\omega + GBP\left(\frac{R_2}{R_2 + R_3}\right)} + \frac{V_{cc}(R_2 + R_3)}{2R_2\left(1 + \frac{R_{d2}}{2R_1}\right)} \tag{6.3}$$

Setting $R_{d2} = 2R_1R_3/R_2$ yields Equation 6.4. The voltage gain is now equal for both $V_{OA1}(j\omega)$ and $V_{OA2}(j\omega)$ and the bias voltage $V_{cc}/2$ which is common mode is therefore negated. The output voltage V_{out} is therefore proportional to $\left(V_{OA1}(j\omega) - V_{OA2}(j\omega)\right)$ as required for sensor operation.

$$V_{out}(j\omega) = \frac{GBP\left(\frac{R_3}{R_2+R_3}\right)\left(V_{OA2}(j\omega)-V_{OA1}(j\omega)\right)}{j\omega+GBP\left(\frac{R_2}{R_2+R_3}\right)} + \frac{V_{cc}}{2} \tag{6.4}$$

The required bias voltage at V_{out} is restored by means of the voltage divider resistors R_{d2} and the DC closed loop gain of the difference amplifier is given by $G = R_3/R_2$. Noting the necessary condition that $G = R_3/R_2 = R_{d2}/2R_1$ to maintain equal gain for both V_{OA1} and V_{OA2}, then adjustment of G while at the same time maintaining equal gain is conveniently achieved by increasing or decreasing both R_1 and R_2 by the same ratio, keeping R_{d2} and R_3 constant. When the cut-off frequency of the charge amplifier stages is sufficiently less than $GBP(R_2/(R_2+R_3))$, then V_{out} is given by Equation 6.5.

$$V_{out}(j\omega) \cong \left(\frac{R_3}{R_2}\right)\left(V_{OA2}(j\omega) - V_{OA1}(j\omega)\right) + \frac{V_{cc}}{2} \tag{6.5}$$

When $\hat{A}_v$ is large enough and the inequality $R_f/R_p \ll \hat{A}_v$ is satisfied, then by substitution of $Z_p = 1/C_p\left(j\omega + 1/R_pC_p\right)$ and $Z_f = 1/C_f\left(j\omega + 1/R_fC_f\right)$ and applying the amplifier design observations that $C_p \ll C_f$, $1/R_pC_p \ll GBP$, $1/R_fC_f \ll GBP$, $R_s \ll R_p$ and $R_s \ll R_f$ then Equation 6.1 for $V_{OA1}(j\omega)$ and $V_{OA2}(j\omega)$ can be simplified and given by Equation 6.6 where the approximation $\hat{A}_v/\left(\hat{A}_v+1\right) \approx 1$ has been made. This is easily justified by noting that the typical data sheet values for $\hat{A}_v$ are approximately 3.5×10^5 and 1.4×10^6 for the LMC6081 op-amp when sinking and sourcing current respectively.

$$V_{OA1}(j\omega),\ V_{OA2}(j\omega) = \mp\frac{j\omega A_s \mathrm{Q}(j\omega)}{2R_sC_pC_f\left(j\omega+\frac{1}{R_fC_f}\right)\left(j\omega+\frac{1}{2R_sC_p}+\frac{1}{R_pC_p}\right)} + \frac{V_{cc}}{2} \tag{6.6}$$

Equation 6.6 is also obtained by letting $A_v \to \infty$ in Equation 6.1. Since $2R_sC_p \ll R_fC_f$, $2R_sC_p \ll R_pC_p$ and $R_s \ll R_p$ then by inspection of Equation 6.6, the amplifier time decay constant is $\tau_d = R_fC_f$, the steady state $-3dB$ cut-on frequency is $\omega_{c-on} = 1/R_fC_f$, the rise time is $\tau_r \cong 2R_sC_p$ and the $-3dB$ steady state cut-off frequency is $\omega_{c-off} \cong 1/2R_sC_p$. Substituting for $V_{OA1}(j\omega)$ and $V_{OA2}(j\omega)$ given by Equation 6.6 into Equation 6.4 and Equation 6.5 yields Equation 6.7 for $V_{out}(j\omega)$.

$$V_{out}(j\omega) = \frac{j\omega \mathrm{Q}(j\omega) GBP\left(\frac{R_3}{R_2+R_3}\right)}{R_s C_p C_f \left(j\omega + GBP\left(\frac{R_2}{R_2+R_3}\right)\right)\left(j\omega + \frac{1}{R_f C_f}\right)\left(j\omega + \frac{1}{2R_s C_p}\right)} + \frac{V_{cc}}{2}$$

$$\cong \frac{R_3 j\omega \mathrm{Q}(j\omega)}{R_2 R_s C_p C_f \left(j\omega + \frac{1}{R_f C_f}\right)\left(j\omega + \frac{1}{2R_s C_p}\right)} + \frac{V_{cc}}{2} \quad (6.7)$$

Equation 6.7 describes the desired $V_{out}(j\omega)$ response characteristic where the value of R_f is chosen large enough to achieve the desired decay time constant, being limited only by bias current and input offset voltage considerations; and the value of R_s is ideally chosen as small as possible while maintaining its purpose of providing sufficient additional ESD protection for OA1 and OA2. The output voltage response given by Equation 6.7 is used with V_{cc} set to zero in the time-frequency sensor response analysis described in Chapter 7 where it is assumed that the $-3dB$ cut-off frequency of the charge amplifier stages is sufficiently lower than $GBP(R_2/(R_2 + R_3))$. This approximation is reasonable since for the LMC6081 opamp, $GBP = 2.6\pi \times 10^6\ rads^{-1}$ and with $G = R_3/R_2 = R_{d1}/2R_1$ set to $G = 0.5$ as is the case for the accumulative voltage response measurements described in Chapter 7, the $-3dB$ cut-off frequency is given by $GBP(R_2/(R_2 + R_3)) = 5.45 \times 10^6\ rads^{-1}$. This is over one order of magnitude greater than the $-3dB$ cut-off frequency of the charge amplifier stages of $1/2R_sC_p = 2.5 \times 10^5\ rads^{-1}$.

However, if the inequality $R_f/R_p \ll \hat{A}_v$ is not satisfied then Equation 6.7 is no longer valid. Reduced piezoelectric resistivity and therefore reduced R_p can occur due to the presence of moisture [104] or crack formation, which is primarily due to prolonged applied cyclic stress, but that can be accelerated by conditions of high humidity such as that present in a prosthetic socket [105]. Since it is required that R_f is large, it is desirable to investigate the influence of a reduced equivalent dielectric resistance R_p on the voltage output response. The following analysis avoids the generalisation that the substitution, $\hat{A}_v \to \infty$ is valid and describes the influence of the feedback resistances R_f and R_p on amplifier performance by comparison with the ideal model of Equation 6.7.

Describing A_v as being represented by a single pole with a $-3dB$ cut off frequency ω_c such that $A_v = \hat{A}_v/(1 + j\omega/\omega_c)$, and applying the amplifier design

observations that $C_p \ll C_f$, $1/R_pC_p \ll GBP$, $1/R_fC_f \ll GBP$, $R_s \ll R_p$ and $R_s \ll R_f$ then Equation 6.1 can be simplified and written as Equation 6.8. Some very small terms and a pole at a frequency much greater than $1/2R_sC_p$ that have a negligible effect on the response are omitted. Some small terms are retained such that $V_{OA1}(j\omega)$ and $V_{OA2}(j\omega)$ algebraically approach the desired response characteristic of Equation 6.7 precisely in the limit as $\hat{A}_v \to \infty$, and by inference as $GBP \to \infty$.

$$V_{OA1}(j\omega),\ V_{OA2}(j\omega) = \mp \frac{j\omega Q(j\omega) GBP}{C_f\left(1+2R_sC_pGBP\right)\left(j\omega+\frac{GBP\left(1+2\frac{R_s}{R_p}+2\frac{R_sC_p}{R_fC_f}\right)}{2\left(1+2R_sC_pGBP\right)}-\varrho\right)\left(j\omega+\frac{GBP\left(1+2\frac{R_s}{R_p}+2\frac{R_sC_p}{R_fC_f}\right)}{2\left(1+2R_sC_pGBP\right)}+\varrho\right)} + \frac{V_{cc}}{2} \tag{6.8}$$

The denominator constant, denoted by ϱ, is given by Equation 6.9.

$$\varrho = \sqrt{\left(\frac{GBP\left(1+2\frac{R_s}{R_p}+2\frac{R_sC_p}{R_fC_f}\right)}{2\left(1+2R_sC_pGBP\right)}\right)^2 - \frac{GBP\left(\hat{A}_v\left(R_p+2R_s\right)+2R_f\right)}{\left(1+2R_sC_pGBP\right)\hat{A}_vR_pR_fC_f}} \tag{6.9}$$

Equation 6.10 therefore gives the difference voltage $\left(V_{OA1}(j\omega) - V_{OA2}(j\omega)\right)$.

$$\left(V_{OA1}(j\omega) - V_{OA2}(j\omega)\right) = \frac{-2j\omega Q(j\omega) GBP}{C_f\left(1+2R_sC_pGBP\right)\left(j\omega+\frac{GBP\left(1+2\frac{R_s}{R_p}+2\frac{R_sC_p}{R_fC_f}\right)}{2\left(1+2R_sC_pGBP\right)}-\varrho\right)\left(j\omega+\frac{GBP\left(1+2\frac{R_s}{R_p}+2\frac{R_sC_p}{R_fC_f}\right)}{2\left(1+2R_sC_pGBP\right)}+\varrho\right)} \tag{6.10}$$

Substituting Equation 6.10 into Equation 6.4 yields the output voltage given by Equation 6.11.

$$V_{out}(j\omega) = \frac{2j\omega Q(j\omega)(GBP)^2\left(\frac{R_3}{R_2+R_3}\right)}{C_f\left(1+2R_sC_pGBP\right)\left(j\omega+GBP\left(\frac{R_2}{R_2+R_3}\right)\right)\left(j\omega+\frac{GBP\left(1+2\frac{R_s}{R_p}+2\frac{R_sC_p}{R_fC_f}\right)}{2\left(1+2R_sC_pGBP\right)}-\varrho\right)\left(j\omega+\frac{GBP\left(1+2\frac{R_s}{R_p}+2\frac{R_sC_p}{R_fC_f}\right)}{2\left(1+2R_sC_pGBP\right)}+\varrho\right)} + \frac{V_{cc}}{2} \tag{6.11}$$

When the difference amplifier cut-off frequency given by $GBP\,R_2/(R_2+R_3)$ is sufficiently greater than the cut-off frequency of the charge amplifier stages, then $V_{out}(j\omega)$ reduces to Equation 6.12.

$$V_{out}(j\omega)=\frac{2j\omega A_s Q(j\omega)GBP\,R_3}{C_f R_2\left(1+2R_sC_pGBP\right)\left(j\omega+\frac{GBP\left(1+2\frac{R_s}{R_p}+2\frac{R_sC_p}{R_fC_f}\right)}{2\left(1+2R_sC_pGBP\right)}-\varrho\right)\left(j\omega+\frac{GBP\left(1+2\frac{R_s}{R_p}+2\frac{R_sC_p}{R_fC_f}\right)}{2\left(1+2R_sC_pGBP\right)}+\varrho\right)}+\frac{V_{cc}}{2} \tag{6.12}$$

As discussed above, to achieve the large charge amplifier output voltage time constant required for an extended period of use of $8\,hours$, a large value for R_f is required such that in the expression for ϱ given by Equation 6.9 it cannot be generally assumed that $R_f/R_p \ll \hat{A}_v$ or that letting $\hat{A}_v \to \infty$ is valid. By inspection of Equation 6.12, the undesired consequences of this condition not being satisfied are that the decay time constant denoted by τ_d of the charge amplifier stages are reduced while the rise time denoted by τ_r is increased. In addition, the passband closed loop gain of the charge amplifier stages and therefore V_{out} are reduced by an attenuation factor denoted by A_r given by $A_r=\tau_r GBP/\left(1+2R_sC_pGBP\right)$, where $A_r \leq 1$.

Furthermore, the bandwidth is reduced such that the steady state $-3dB$ cut-off frequency ω_{c-off} is reduced while the steady state $-3dB$ cut-on frequency ω_{c-on} is increased under the design observations discussed above. It is worth noting that in the case that R_s is set to zero, then ω_{c-off} is ultimately limited to the GBP of OA1 and OA2, and the rise time at $V_{OA1}(j\omega)$ and $V_{OA2}(j\omega)$ is therefore of the order $\tau_r \cong 1/GBP$. By inspection of Equation 6.12, τ_d and τ_r are given by Equation 6.13 and Equation 6.14, respectively.

$$\tau_d = \frac{2\left(1+2R_sC_pGBP\right)}{GBP\left(1+2\frac{R_s}{R_p}+2\frac{R_sC_p}{R_fC_f}\right)-\sqrt{\left(GBP\left(1+2\frac{R_s}{R_p}+2\frac{R_sC_p}{R_fC_f}\right)\right)^2-4GBP\left(\hat{A}_v\left(R_p+2R_s\right)+2R_f\right)\left(1+2R_sC_pGBP\right)/\left(\hat{A}_vR_pR_fC_f\right)}}$$

$$\cong \frac{2\left(1+2R_sC_pGBP\right)}{GBP-\sqrt{(GBP)^2-\frac{4GBP\left(\hat{A}_vR_p+2R_f\right)\left(1+2R_sC_pGBP\right)}{\left(\hat{A}_vR_pR_fC_f\right)}}}_{R_p,R_f \gg 2R_s} = R_fC_f \underset{GBP\to\infty}{\hat{A}_v\to\infty} \tag{6.13}$$

$$\tau_r = \frac{2\left(1+2R_sC_pGBP\right)}{GBP\left(1+2\frac{R_S}{R_p}+2\frac{R_SC_p}{R_fC_f}\right)+\sqrt{\left(GBP\left(1+2\frac{R_S}{R_p}+2\frac{R_SC_p}{R_fC_f}\right)\right)^2-4GBP\left(\hat{A}_v\left(R_p+2R_s\right)+2R_f\right)\left(1+2R_sC_pGBP\right)/\left(\hat{A}_vR_pR_fC_f\right)}}$$

$$= \frac{2\left(1+2R_sC_pGBP\right)}{GBP+\sqrt{(GBP)^2-4GBP\left(\hat{A}_vR_p+2R_f\right)\left(1+2R_sC_pGBP\right)/\left(\hat{A}_vR_pR_fC_f\right)}} \underset{R_p,R_f\gg 2R_s}{\cong} \frac{1+2R_sC_pGBP}{GBP}$$

$$= 2R_sC_p \underset{GBP\to\infty}{\hat{A}_v\to\infty} \qquad (6.14)$$

To investigate the influence of R_f on the gain factor, decay time constant and rise time, A_r, τ_d and τ_r are calculated for the cases that $R_f = 1G\Omega$ and $R_f = 1T\Omega$ using the component values listed in Table 6.1 with the results given in Table 6.2 and Table 6.3. $R_f = 1G\Omega$ is used in the laboratory measurements described in Chapter 7 while $R_f = 1T\Omega$ is required for continuous use for a period of 8 $hours$ with no more than 2% signal decay. Four test values of $\hat{A}_v$ are quoted on the LMC6081 data sheet for load resistances of 600Ω and $2k\Omega$ under conditions of sourcing and sinking current. The lowest value of $\hat{A}_v$ is when sinking current from a load of 600Ω, and the highest value is when sourcing current into a load of $2k\Omega$. The loads presented by the difference amplification stage at OA3 and 'seen' by the outputs of both OA1 and OA2 are much greater than $2k\Omega$ and it is therefore the sourcing and sinking values of $\hat{A}_v$ at a load of $2k\Omega$ that are relevant to the analysis.

It is easily shown that for all three of the signal conditioning differential designs presented, that regardless of the DC bias, when the output of OA1 is sourcing current, then the output of OA2 is sinking current and vice versa. It is therefore important that both the current sourcing and sinking values of $\hat{A}_v$ are considered in the analysis. The value of $R_p = 90G\Omega$ listed in Table 6.1 is the estimated equivalent resistance at DC of the PZT-5H element at a temperature of $25°C$, which was calculated using the sensor element dimensions and an estimate of $10^{11}\Omega m$ for the room temperature DC resistivity of PZT-5H from [103],[106].

$R_s = 100\Omega$	$R_p = 90G\Omega$	$C_p = 20nF$
$C_f = 1.5\mu F$	$GBP = 2.6\pi \times 10^6\ rads^{-1}$	$\hat{A}_v = 1.4 \times 10^6 - sourcing$ $\hat{A}_v = 3.5 \times 10^5 - sinking$

Table 6.1 Charge amplification stage and sensor characteristics, $R_p = 90G\Omega$

$\hat{A}_v = 1.4 \times 10^6 - sourcing$		
R_f	$1G\Omega$	$1T\Omega$
A_r	1	1
$A_r - ideal$	1	1
τ_d	$1500s$	$1.5 \times 10^6 s$
$\tau_d - ideal = R_f C_f$	$1500s$	$1.5 \times 10^6 s$
τ_r	$4.01\mu s$	$4.01\mu s$
$\tau_r - ideal = 2R_s C_p$	$4\mu s$	$4\mu s$

Table 6.2 Decay time constant, rise time and gain factor (sourcing), $R_p = 90G\Omega$

$\hat{A}_v = 3.5 \times 10^5 - sinking$		
R_f	$1G\Omega$	$1T\Omega$
A_r	1	1
$A_r - ideal$	1	1
τ_d	$1500s$	$1.5 \times 10^6 s$
$\tau_d - ideal = R_f C_f$	$1500s$	$1.5 \times 10^6 s$
τ_r	$4.01\mu s$	$4.01\mu s$
$\tau_r - ideal = 2R_s C_p$	$4\mu s$	$4\mu s$

Table 6.3 Decay time constant, rise time and gain factor (sinking), $R_p = 90G\Omega$

It can be seen from Table 6.2 and Table 6.3 that for $R_p = 90G\Omega$, both values of R_f and $\hat{A}_v$ yield values of G_r and τ_d that are equal to the ideal model values while τ_r is almost equal to the ideal model value. The approximation $\hat{A}_v \to \infty$ is therefore valid in this case.

Considering a significantly reduced dielectric resistance such that $R_p = 100M\Omega$, which could be the case for example if the PZT-5H sensor patch was significantly degraded by for example exposure to moisture or cracking, G_r, τ_d and

τ_r are calculated for the cases that $R_f = 1G\Omega$ and $R_f = 1T\Omega$ using the component values listed in Table 6.4 with the results given in Table 6.5 and Table 6.6.

$R_s = 100\Omega$	$R_p = 100M\Omega$	$C_p = 20nF$
$C_f = 1.5\mu F$	$GBP = 2.6\pi \times 10^6\ rads^{-1}$	$\hat{A}_v = 1.4 \times 10^6 - sourcing$ $\hat{A}_v = 3.5 \times 10^5 - sinking$

Table 6.4 Charge amplification stage and sensor characteristics, $R_p = 100M\Omega$

$\hat{A}_v = 1.4 \times 10^6 - sourcing$		
R_f	$1G\Omega$	$1T\Omega$
A_r	1	1
$A_r - ideal$	1	1
τ_d	$1500s$	$1.479 \times 10^6 s$
$\tau_d - ideal = R_f C_f$	$1500s$	$1.5 \times 10^6 s$
τ_r	$4.01\mu s$	$4.01\mu s$
$\tau_r - ideal = 2R_s C_p$	$4\mu s$	$4\mu s$

Table 6.5 Decay time constant, rise time and gain factor, sourcing, $R_p = 100M\Omega$

$\hat{A}_v = 3.5 \times 10^5 - sinking$		
R_f	$1G\Omega$	$1T\Omega$
A_r	1	1
$A_r - ideal$	1	1
τ_d	$1500s$	$1.419 \times 10^6 s$
$\tau_d - ideal = R_f C_f$	$1500s$	$1.5 \times 10^6 s$
τ_r	$4.01\mu s$	$4.01\mu s$
$\tau_r - ideal = 2R_s C_p$	$4\mu s$	$4\mu s$

Table 6.6 Decay time constant, rise time and gain factor, sinking, $R_p = 100M\Omega$

From both Table 6.5 and Table 6.6 it can be seen that at $R_f = 1G\Omega$, the decay time constant τ_d and gain constant G_r are equal to the ideal values while the rise time τ_r is very close to the ideal value. In this case, the approximation $\hat{A}_v \to \infty$ is therefore valid. Equation 6.6 may therefore be used to accurately describe the charge amplifier response at $V_{OA1}(j\omega)$ and $V_{OA2}(j\omega)$ when $R_f = 1G\Omega$. However when $R_f = 1T\Omega$, the decay time constant is reduced by approximately 1.5% of the

required value given by $\tau_d = R_f C_f$ when OA1 and OA2 are sourcing current and reduced by approximately 6% of the ideal value when OA1 or OA2 are sinking current. The steady state $-3dB$ cut-on frequency ω_{c-on} is therefore increased by approximately 1.5% when sourcing current and increased by approximately 6.4% when sinking current, while τ_r and the steady state $-3dB$ cut-off frequency ω_{c-off} are unchanged compared with the values at $R_p = 90G\Omega$. Considering a step input at $t = 0$, the sourcing and sinking values of τ_d given in Table 6.6 for $R_f = 1T\Omega$ correspond to an output signal decay greater than the maximum 2% permitted decay after the period $t = 8\,hours$ specification.

Since the sensor period of use is during the initial period of its decay transient period, then the effect on ω_{c-on}, which applies in the steady state is of little interest, while the modestly increased τ_r and reduction in ω_{c-off} will have no significant effect on the measurement at the low frequencies of interest. While the decay time constant at $R_p = 90G\Omega$ for both current sinking and sourcing are equal to the ideal model values, a reduced R_p due to degradation or reduced values of $\hat{A}_v$ due to manufacturing tolerances could significantly reduce τ_d when $R_f = 1T\Omega$. At $R_f = 1T\Omega$, this output signal decay will be greater than the maximum 2% permitted decay specification, reducing the period for which the sensor may be used continuously without incurring significant measurement error. It is worth noting that the equivalent DC internal resistance R_p of the PZT-5H element is significantly temperature dependent, changing by approximately 10% over the temperature range of 20℃ to 40℃, however the effect on τ_d, τ_r and A_r is insignificant and can be neglected.

It is therefore desirable to reduce the possibility of a reduced τ_d due to a significantly reduced R_p or variations in $\hat{A}_v$ due to manufacturing tolerances. This can be achieved by increasing the effective value of the $\hat{A}_v$ associated with OA1 and OA2, such that the condition $R_f/R_p \ll \hat{A}_v$ is realised at a reduced R_p, and the approximation $\hat{A}_v \to \infty$ therefore remains valid. In addition to restoring the decay time constant to $\tau_d = R_f C_f$ and the cut-on frequency to $\omega_{c-on} = 1/R_f C_f$, sufficiently increasing $\hat{A}_v$ and therefore the GBP provides the additional advantage of further improving the desired response at $V_{OA1}(j\omega)$ and $V_{OA2}(j\omega)$ by ensuring that

the rise time and cut-off frequency are equal to the ideal values of $\tau_r = 2R_sC_p$ and $\omega_{c-off} = 1/2R_sC_p$ respectively. A circuit design with enhanced open loop gain developed to solve this problem is discussed further in Section 6.3.4.

6.3.3 Bipolar charge amplifier design

The schematic diagram for the charge amplifier developed for use in the laboratory investigation that is described in Section 7.3 to measure the transient temperature response of the PZT-5H piezoelectric element is shown in Figure 6.2. With a maximum supply voltage of $V_{cc} = \pm 18V$, this design allows large temperature swings to be measured without saturating the amplifier output. The op-amps power supply and associated ceramic noise reduction capacitors are omitted for clarity.

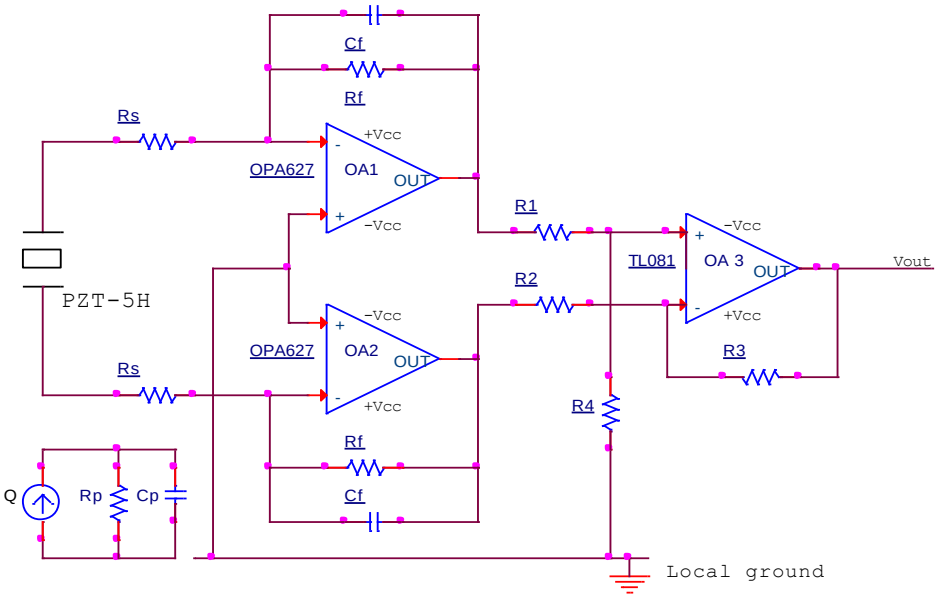

Figure 6.2 Bipolar charge amplifier schematic

Circuit analysis of the schematic in Figure 6.2 yields Equation 6.15 for the frequency-domain output voltage of the charge amplifier stages at OA1 and OA2 which are denoted by $V_{OA1}(j\omega)$ and $V_{OA2}(j\omega)$ respectively where as before $Z_p = 1/C_p\left(j\omega + 1/R_pC_p\right)$ and $Z_f = 1/C_f\left(j\omega + 1/R_fC_f\right)$. The term A_v is the frequency dependent open loop gain of OA1 and OA2 respectively.

$$V_{OA1}(j\omega),\ V_{OA2}(j\omega) = \mp \frac{j\omega \mathrm{Q}(j\omega) A_v \left(\frac{Z_p Z_f}{Z_p + 2Z_f + 2R_s}\right)}{1 + A_v \left(\frac{Z_p + 2R_s}{Z_p + 2Z_f + 2R_s}\right)} \tag{6.15}$$

Assuming that $R_f/R_p \ll \hat{A}_v$, and describing A_v as being represented by a single pole with a $-3dB$ cut off frequency ω_c such that $A_v = \hat{A}_v/(1 + j\omega/\omega_c)$ where $GBP = \omega_c \hat{A}_v$ is the gain-bandwidth product of OA1 and OA2, and applying the amplifier design observations that $C_p \ll C_f$, $1/R_p C_p \ll GBP$, $1/R_f C_f \ll GBP$, $R_s \ll R_p$ and $R_s \ll R_f$ then Equation 6.15 can be written as Equation 6.16.

$$V_{OA1}(j\omega),\ V_{OA2}(j\omega) = \mp \frac{j\omega A_s \mathrm{Q}(j\omega)}{2R_s C_p C_f \left(j\omega + \frac{1}{R_f C_f}\right)\left(j\omega + \frac{1}{2R_s C_p} + \frac{1}{R_p C_p}\right)} \tag{6.16}$$

Circuit analysis of the final difference amplifier stage yields Equation 6.17.

$$V_{out}(j\omega) = \frac{GBP\left(\left(\frac{R_4}{R_1 + R_4}\right) V_{OA2}(j\omega) - \left(\frac{R_3}{R_2 + R_3}\right) V_{OA1}(j\omega)\right)}{j\omega + GBP\left(\frac{R_2}{R_2 + R_3}\right)} \tag{6.17}$$

Setting $R_4 = R_1 R_3/R_2$ yields Equation 6.18.

$$V_{out}(j\omega) = \frac{GBP\left(\frac{R_3}{R_2 + R_3}\right)\left(V_{OA2}(j\omega) - V_{OA1}(j\omega)\right)}{j\omega + GBP\left(\frac{R_2}{R_2 + R_3}\right)} \tag{6.18}$$

The voltage gain is now equal for both $V_{OA1}(j\omega)$ and $V_{OA2}(j\omega)$ and the Common mode voltages are negated. The output voltage V_{out} is therefore proportional to $\left(V_{OA1}(j\omega) - V_{OA2}(j\omega)\right)$ as required for sensor operation. The forward gain, which is equal to the DC closed loop gain of the difference amplifier is given by $G = R_3/R_2$. Noting the necessary condition that $G = R_3/R_2 = R_4/R_1$ to maintain equal gain for both $V_{OA1}(j\omega)$ and $V_{OA2}(j\omega)$, then adjustment of G is conveniently achieved by increasing or decreasing both R_1 and R_2 by the same ratio, while keeping R_4 and R_3 constant.

When the $-3dB$ cut-off frequency of the charge amplifier stages is very much less than $GBP(R_2/(R_2 + R_3))$ then V_{out} can be described by Equation 6.19.

$$V_{out}(j\omega) \cong \left(\frac{R_3}{R_2}\right)\left(V_{OA2}(j\omega) - V_{OA1}(j\omega)\right) \tag{6.19}$$

Substituting for $V_{OA1}(j\omega)$ and $V_{OA2}(j\omega)$ given by Equation 6.16 into Equation 6.18 and Equation 6.19 yields Equation 6.20 for V_{out}.

$$V_{out}(j\omega) = \frac{j\omega \mathrm{Q}(j\omega) GBP\left(\frac{R_3}{R_2+R_3}\right)}{R_s C_p C_f \left(j\omega + GBP\left(\frac{R_2}{R_2+R_3}\right)\right)\left(j\omega + \frac{1}{R_f C_f}\right)\left(j\omega + \frac{1}{2R_s C_p} + \frac{1}{R_p C_p}\right)}$$

$$\cong \frac{R_3 j\omega A_s \mathrm{Q}(j\omega)}{R_2 R_s C_p C_f \left(j\omega + \frac{1}{R_f C_f}\right)\left(j\omega + \frac{1}{2R_s C_p} + \frac{1}{R_p C_p}\right)} \qquad (6.20)$$

Equation 6.20 is used for the transient voltage response measurements described in Chapter 7 with the forward difference stage gain, which is given by $G = R_3/R_2 = R_4/R_1$, set to $G = 1$, and where it is assumed that the $-3dB$ cut-off frequency of the charge amplifier stages is sufficiently lower than $GBP(R_2/(R_2 + R_3))$. This is a reasonable assumption since for the TL081 opamp $GBP = 6\pi \times 10^6\ rads^{-1}$ and with $R_3/R_2 = 1$ the $-3dB$ cut-off is given by $GBP(R_2/(R_2 + R_3)) = 3\pi \times 10^6\ rads^{-1}$ compared to the $-3dB$ cut-off frequency of the charge amplifier stages of $1/2R_sC_p = 2.5 \times 10^5\ rads^{-1}$.

6.3.4 Unipolar charge amplifier design – enhanced open loop gain

The design shown in the schematic of Figure 6.3 allows the native $\hat{A}_v$ of OA1 and OA2 to be increased to realise the required condition that $R_f/R_p \ll \hat{A}_v$ when using very large feedback resistances together with a sensor element that may have or develop reduced resistivity as described in Section 6.3.2. The effect of compromised resistivity is considered by assuming a reduced equivalent sensor element insulation resistance R_p such that $R_p = 100M\Omega$. This approach has the additional advantage that the GBP, by inference, is also increased.

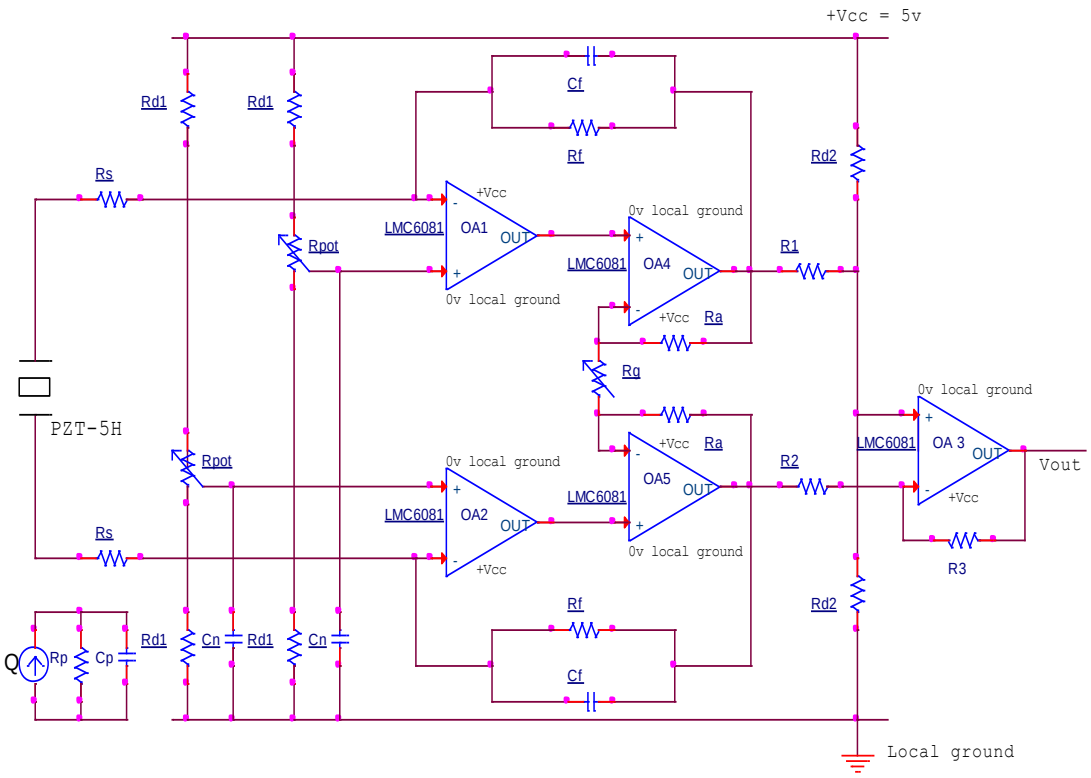

Figure 6.3 Unipolar charge amplifier schematic – enhanced open loop gain

The solution is achieved by the introduction of a non-inverting buffer gain stage formed by op-amps OA4 and OA5, and resistors R_a and R_g. As discussed in Section 6.3.2, satisfying this condition is desirable to ensure that the decay time constant achieved is sufficiently close to $\tau_d \cong R_f C_f$. Circuit analysis of the schematic Figure 6.3 yields Equation 6.21 for the frequency-domain output voltage of the charge amplifier stages at OA4 and OA5, where A_{vg} and $\hat{A}_{vg}$ are the frequency dependent and DC open loop gains of OA4 and OA5 respectively.

$$V_{OA1}(j\omega),\ V_{OA2}(j\omega) = \frac{\mp j\omega Q(j\omega)\left(\frac{Z_p Z_f}{Z_p+2Z_f+2R_S}\right)A_v\left(\frac{A_{vg}}{1+A_{vg}\left(\frac{R_g}{2R_a+R_g}\right)}\right)}{1+\left(\frac{Z_p+2R_S}{Z_p+2Z_f+2R_S}\right)A_v\left(\frac{A_{vg}}{1+A_{vg}\left(\frac{R_g}{2R_a+R_g}\right)}\right)} + \left(\frac{\hat{A}_v\left(\frac{\hat{A}_{vg}}{\hat{A}_{vg}+1}\right)}{\hat{A}_v\left(\frac{\hat{A}_{vg}}{\hat{A}_{vg}+1}\right)+1}\right)\frac{V_{cc}}{2} \tag{6.21}$$

By comparing Equation 6.21 to Equation 6.1 in Section 6.3.2, it can be seen that for the signal term, A_v is effectively substituted by Equation 6.22 for A_{ve}, where

A_{ve} is the equivalent frequency dependent open loop gain, and for the voltage bias term, $\hat{A}_v$ is substituted by $\hat{A}_v\hat{A}_{vg}/(\hat{A}_{vg}+1)$.

$$A_{ve} = A_v\left(\frac{A_{vg}}{1+A_{vg}\left(\frac{R_g}{2R_a+R_g}\right)}\right) \tag{6.22}$$

Assuming OA4 and OA5 have identical $-3dB$ open loop cut-off frequency and open loop gains as OA1 and OA2 such that $A_{vg} = \hat{A}_v/(1+j\omega/\omega_c)$, then the gain of the then A_{ve} can be described by Equation 6.23.

$$A_{ve} = \frac{\hat{A}_v}{\left(1+j\frac{\omega}{\omega_c}\right)}\left(\frac{\frac{\hat{A}_v}{\left(1+j\frac{\omega}{\omega_c}\right)}}{1+\frac{\hat{A}_v}{\left(1+j\frac{\omega}{\omega_c}\right)}\left(\frac{Rg}{2R_a+R_g}\right)}\right) = \frac{\omega_c\hat{A}_v}{(j\omega+\omega_c)}\left(\frac{\omega_c\hat{A}_v}{j\omega+\omega_c\left(1+\hat{A}_v\left(\frac{R_g}{2R_a+R_g}\right)\right)}\right) \tag{6.23}$$

Defining a gain enhancement factor $G_g = 1+2R_a/R_g$, and noting that $\hat{A}_v \gg 1$ and that the pole at $\omega_c\left(1+\hat{A}_vR_g/(2R_a+R_g)\right)$ is very much greater than ω_c, whether OA4 and OA5 are sourcing or sinking current, yields Equation 6.24 where A_{ve} denotes the frequency dependent enhanced open loop gain. It can be seen that the open loop cut-off frequency ω_c remains unchanged while the open loop gain $\hat{A}_{ve}$ and the GBP are increased by the gain enhancement factor to $G_g\hat{A}_v$ and G_gGBP respectively.

$$A_{ve} = \frac{\hat{A}_{ve}}{\left(1+j\frac{\omega}{\omega_c}\right)} = G_g\frac{\hat{A}_v}{\left(1+j\frac{\omega}{\omega_c}\right)} = G_g\frac{GBP}{(j\omega+\omega_c)} \tag{6.24}$$

The open loop $-3dB$ cut-off frequency therefore remains unchanged and, noting that $\hat{A}_{vg} \gg 1$, the bias voltage at $V_{OA1}(j\omega)$ and $V_{OA2}(j\omega)$ also remains unchanged at $V_{cc}/2$. In addition to effectively increasing the open loop gain and GBP of OA1 and OA2, a further advantage of the open loop gain enhancement solution is that the outputs of both OA1 and OA2 'see' a very high input impedance at the non-inverting inputs of OA4 and OA5 respectively. They are therefore electrically buffered from the input impedances of the difference amplifier stage at OA3. The relevant open loop sourcing and sinking gains are therefore independent of the input impedances at OA3 and are always the higher of the LMC6081 data-sheet values vis-à-vis load impedance conditions.

To investigate the influence of G_g on the gain factor A_r, decay time constant, τ_r and rise time, τ_d, these are calculated for $R_f = 1G\Omega$ and $R_f = 1T\Omega$ and for the cases $G_g = 10$ and $G_g = 100$. The enhanced specifications for $G_g = 10$ are given in Table 6.7 where both the GBP and $\hat{A}_v$ are increased by a factor of $G_g = 10$. The results for the cases that OA1 and OA2 are sinking current and sourcing current are given in Table 6.8 and Table 6.9 respectively.

$R_s = 100\Omega$	$R_p = 100M\Omega$	$C_p = 20nF$
$C_f = 1.5\mu F$	$GBP = 2.6\pi \times 10^7\ rads^{-1}$	$\hat{A}_{ve} = 1.4 \times 10^7$- source $\hat{A}_{ve} = 3.5 \times 10^6$- sink

Table 6.7 Charge amplification stage and sensor characteristics $G_g = 10$

$\hat{A}_{ve} = 1.4 \times 10^7 - sourcing$		
R_f	$1G\Omega$	$1T\Omega$
A_r	1	1
$A_r - ideal$	1	1
τ_d	$1500s$	$1.498 \times 10^6 s$
$\tau_d - ideal = R_f C_f$	$1500s$	$1.5 \times 10^6 s$
τ_r	$4.012\mu s$	$4.012\mu s$
$\tau_r - ideal = 2R_s C_p$	$4\mu s$	$4\mu s$

Table 6.8 Decay time constant, rise time and gain factor (sourcing) $G_g = 10$

$\hat{A}_{ve} = 3.5 \times 10^6 - sinking$		
R_f	$1G\Omega$	$1T\Omega$
A_r	1	1
$A_r - ideal$	1	1
τ_d	$1500s$	$1.491 \times 10^6 s$
$\tau_d - ideal = R_f C_f$	$1500s$	$1.5 \times 10^6 s$
τ_r	$4.012\mu s$	$4.012\mu s$
$\tau_r - ideal = 2R_s C_p$	$4\mu s$	$4\mu s$

Table 6.9 Decay time constant, rise time and gain factor (sinking) $G_g = 10$

The enhanced specifications for $G_g = 100$ are given in Table 6.10 where both the GBP and $\hat{A}_v$ are increased by a factor of $G_g = 100$.

$R_s = 100\Omega$	$R_p = 100M\Omega$	$C_p = 20nF$
$C_f = 1.5\mu F$	$GBP = 2.6\pi \times 10^8\ rads^{-1}$	$\hat{A}_{ve} = 1.4 \times 10^8$- source $\hat{A}_{ve} = 3.5 \times 10^7$- sink

Table 6.10 Charge amplification stage and sensor characteristics $G_g = 100$

The results for the cases that OA1 and OA2 are sinking current and sourcing current are given in Table 6.11 and Table 6.12 respectively.

$\hat{A}_{ve} = 1.4 \times 10^8 - sourcing$		
R_f	$1G\Omega$	$1T\Omega$
A_r	1	0.999
$A_r - ideal$	1	1
τ_d	$1500s$	$1.5 \times 10^6 s$
$\tau_d - ideal = R_f C_f$	$1500s$	$1.5 \times 10^6 s$
τ_r	$4.001\mu s$	$4.001\mu s$
$\tau_r - ideal = 2R_s C_p$	$4\mu s$	$4\mu s$

Table 6.11 Decay time constant, rise time and gain factor (sourcing) $G_g = 100$

$\hat{A}_{ve} = 3.5 \times 10^7 - sinking$		
R_f	$1G\Omega$	$1T\Omega$
A_r	1	1
$A_r - ideal$	1	1
τ_d	$1500s$	$1.5 \times 10^6 s$
$\tau_d - ideal = R_f C_f$	$1500s$	$1.5 \times 10^6 s$
τ_r	$4.001\mu s$	$4.001\mu s$
$\tau_r - ideal = 2R_s C_p$	$4\mu s$	$4\mu s$

Table 6.12 Decay time constant, rise time and gain factor (sinking) $G_g = 100$

It can be seen from Table 6.8 and Table 6.9 that setting $G_g = 10$ is sufficient to ensure the decay time constant, τ_d is high enough to meet the required response specification for $R_f = 1T\Omega$ when the dielectric insulation resistance is reduced to $R_p = 100M\Omega$. From Table 6.11 and Table 6.12 it can be seen that increasing the gain enhancement to $G_g = 100$ further improves the response by increasing τ_d and reducing τ_r toward the ideal values thus ensuring immunity to a reduced sensor

dielectric resistance, and immunity to a reduced sensitivity in the signal response to variations in the typical data sheet values of $\hat{A}_v$ and GBP. It can therefore be stated that if R_p is significantly reduced to $R_p = 100M\Omega$, and large feedback resistances of $R_f = 1T\Omega$ are used at the charge amplifier stages, then the signal conditioning decay time constant specification is adequate to meet the required signal conditioning specification when the gain enhancement factor is set to $G_g = 10$. The response is further improved toward the ideal response given by Equation 6.6 when the gain enhancement factor is set to $G_g = 100$.

6.4 Op-amp drift and offsets

6.4.1 Initial considerations

All signal conditioning amplifiers exhibit drift that leads to a steady state DC output voltage component even in the absence of an input signal. This output voltage appears as an offset that increases or 'drifts' over time and adds to the measured signal. The drift originates from two main sources: a mismatch in transistor and resistor components due to manufacturing tolerances, and bias currents that exist at the inputs to semiconductor components such as transistors and op-amps. The presence of $1/f$ noise, also called pink noise, will also result in a slow drift in the output voltage over long periods [107]. However, for the specified required eight hours of operation, $1/f$ noise drift is insignificant and can be safely ignored. In charge-mode signal conditioning amplifiers, these components result in a small and almost immediate output voltage offset component in addition to a steady drift in the output voltage over a time period of the same order of magnitude as the amplifier time constant. It is therefore necessary to ensure that the maximum drift over the measurement period is limited to avoid significant error in measurement.

In circuits constructed using op-amps, the specifications required to allow analysis of drift and offset voltage are the input referred offset voltage denoted V_{os}, which is due to manufacturing tolerances, the input offset bias current denoted by $i_{b-os} = (i_b^- - i_b^+)$, which is the difference between the bias currents at the inverting and non-inverting terminals, and the bias current at the non-inverting input denoted

by i_b^+. In the following analysis, the steady state and transient output offset or 'drift' voltages for the differential charge-mode amplifier design schematic shown in Figure 6.1 for two different sensor insulation resistances denoted R_p are calculated. The low frequency resistivity of PZT-5H at 25℃ is greater than $10^{11}\Omega$m [103] and therefore by using the area of the electrodes $A_s = 2.6 \times 10^{-4} m^2$ and thickness of the PZT-5H given by $l_p = 0.23 \times 10^{-3}$, the dielectric resistance can be estimated at greater than $90G\Omega$. A nominal value of $R_p = 90G\Omega$ was therefore assumed, while a value of $R_p = 100M\Omega$ is used to consider the possibility of degradation in R_p as described in Section 6.2.4. The op-amp specifications used are taken from the published Texas instruments LMC6081 op-amp data sheet. The ESD resistors denoted by R_s are much smaller than R_p and are henceforth ignored.

6.4.2 Op-amp bias currents

Inverting input bias currents i_b^-

The input bias current specifications given for all op-amps are modelled as flowing from the inverting and non-inverting inputs to ground. Equation 6.25 and Equation 6.26 give the steady state output voltages of OA1 and OA2 due to the non-inverting input bias currents where i_{b1}^- and i_{b2}^- are the bias currents at the inverting inputs of OA1 and OA2 respectively, R_{f1} and R_{f2} are the feedback resistances at OA1 and OA2 respectively, and $\hat{A}_{v1}$ and $\hat{A}_{v2}$ are the open loop DC gains of OA1 and OA2 respectively. The values of R_f and $\hat{A}_v$ for each charge amplifier stage are initially assumed to be different to allow for component tolerances.

$$V_{OA1-i_b^-} = i_{b1}^- R_{f1} + \frac{\hat{A}_{v1} i_{b2}^- R_{f2} - \hat{A}_{v2} i_{b1}^- R_{f1}}{\frac{R_{f2}}{R_{f1}}\hat{A}_{v1} + \left(\frac{R_p}{R_{f1}}\hat{A}_{v1} + 1\right)\hat{A}_{v2}} = \left[i_{b1}^- R_f + \frac{(i_{b2}^- - i_{b1}^-)R_f}{\frac{R_p}{R_f}\hat{A}_v + 2} \right]_{\substack{\hat{A}_{v1}=\hat{A}_{v2}=\hat{A}_v \\ R_{f1}=R_{f2}=R_f}} \quad (6.25)$$

$$V_{OA2-i_b^-} = i_{b2}^- R_{f2} + \frac{\hat{A}_{v2} i_{b1}^- R_{f1} - \hat{A}_{v1} i_{b2}^- R_{f2}}{\frac{R_{f1}}{R_{f2}}\hat{A}_{v2} + \left(\frac{R_p}{R_{f2}}\hat{A}_{v2} + 1\right)\hat{A}_{v1}} = \left[i_{b2}^- R_f + \frac{(i_{b1}^- - i_{b2}^-)R_f}{\frac{R_p}{R_f}\hat{A}_v + 2} \right]_{\substack{\hat{A}_{v1}=\hat{A}_{v2}=\hat{A}_v \\ R_{f1}=R_{f2}=R_f}} \quad (6.26)$$

The charge amplifier output is proportional to $\left(V_{OA1-i_b^-} - V_{OA2-i_b^-}\right)$ and it is therefore necessary that the output voltage due to the input offset voltage is kept small enough to avoid error. While it is important that $\left(V_{OA1-i_b^-} - V_{OA2-i_b^-}\right)$ is small, it is equally important that both $V_{OA1-i_b^-}$ and $V_{OA2-i_b^-}$ are also sufficiently small to avoid curtailment of the available measurement range at OA1 and OA2.

Non--inverting input bias currents i_b^+

Equation 6.27 and Equation 6.28 give the steady state output voltages of OA1 and OA2 respectively due to the non-inverting input bias currents. The terms i_{b1}^+ and i_{b2}^+ are the bias currents at the non-inverting inputs of OA1 and OA2 respectively, and R_a and R_b are the voltage divider resistances between the non-inverting terminals and local ground 'seen' by the non-inverting input bias currents respectively. R_a and R_b are given by $R_a = a'\left(R_{d1u-1} + (1-a)R_{pot-1}\right) \cong R_{d1}/2$ and $R_b = b'\left(R_{d1u-2} + (1-b)R_{pot-2}\right) \cong R_{d1}/2$ where R_{d1u-1} and R_{d1u-2} are the upper voltage divider resistors of the voltage dividers, R_{pot-1} and R_{pot-2} are the potentiometers between the upper and lower voltage divider resistors, a and b are the resistance fractions of R_{pot-1} and R_{pot-2} respectively, and $a'$and b' are the overall resistance fractions of the voltage dividers. These terms are described fully in Section 6.4.5.

$$V_{OA1-i_b^+} = -i_{b1}^+ R_a - \frac{\hat{A}_{v1} i_{b2}^+ R_b + \hat{A}_{v1}\hat{A}_{v2}\left(i_{b1}^+ R_a - i_{b2}^+ R_b\right) - \hat{A}_{v2} i_{b1}^+ R_a}{\frac{R_{f2}}{R_{f1}}\hat{A}_{v1} + \left(\frac{R_p}{R_{f1}}\hat{A}_{v1} + 1\right)\hat{A}_{v2}}$$

$$\cong -\left[i_{b1}^+ R_a + \frac{i_{b2}^+ R_b + \hat{A}_v\left(i_{b1}^+ R_a - i_{b2}^+ R_b\right) - i_{b1}^+ R_a}{\frac{R_p}{R_f}\hat{A}_v + 2} \right]_{\substack{\hat{A}_{v1}=\hat{A}_{v2}=\hat{A}_v \\ R_{f1}=R_{f2}=R_f}} \tag{6.27}$$

$$V_{OA2-i_b^+} = -i_{b2}^+ R_b - \frac{\hat{A}_{v2} i_{b1}^+ R_a + \hat{A}_{v1}\hat{A}_{v2}\left(i_{b2}^+ R_b - i_{b1}^+ R_a\right) - \hat{A}_{v1} i_{b2}^+ R_b}{\frac{R_{f1}}{R_{f2}}\hat{A}_{v2} + \left(\frac{R_p}{R_{f2}}\hat{A}_{v2} + 1\right)\hat{A}_{v1}}$$

$$\cong -\left[i_{b2}^+ R_b + \frac{i_{b1}^+ R_a + \hat{A}_v\left(i_{b2}^+ R_b - i_{b1}^+ R_a\right) - i_{b2}^+ R_b}{\frac{R_p}{R_f}\hat{A}_v + 2} \right]_{\substack{\hat{A}_{v1}=\hat{A}_{v2}=\hat{A}_v \\ R_{f1}=R_{f2}=R_f}} \tag{6.28}$$

Total bias currents i_b

The maximum output voltages due to the bias currents occur when the feedback resistors and open loop gains are equal and maximal such that $\hat{A}_{v1} = \hat{A}_{v2} = \hat{A}_v = 1.4 \times 10^6$ and $R_{f1} = R_{f2} = R_f = (1 + 5\%)T\Omega$ or $(1 + 5\%)G\Omega$ (maximum tolerance values). Setting these values therefore represents a worst-case scenario. Letting $R_a = R_b = R_{d1}/2$, the total steady state output voltages at $V_{OA1}$and V_{OA2} due both the inverting and non-inverting input bias currents are given in terms of the input bias current and input offset bias current specifications by Equation 6.29 and Equation 6.30 respectively. The terms $i_{b1-os} = (i_{b1}^- - i_{b1}^+)$ and $i_{b2-os} = (i_{b2}^- - i_{b2}^+)$ are the input offset bias currents of OA1 and OA2 respectively, and i_{b1}^+ and i_{b2}^+ are the input bias currents of OA1 and OA2 respectively.

$$V_{OA1-i_b} = i_{b1-os}R_f + i_{b1}^+ \frac{R_f\left(\frac{R_p}{R_f}\hat{A}_v+1\right)-\frac{R_{d1}}{2}\hat{A}_v\left(\frac{R_p}{R_f}+1\right)}{\frac{R_p}{R_f}\hat{A}_v+2} + \frac{(i_{b2-os}-i_{b1-os})R_f+i_{b2}^+\left(R_f+\frac{R_{d1}}{2}\hat{A}_v\right)}{\frac{R_p}{R_f}\hat{A}_v+2} \quad (6.29)$$

$$V_{OA2-i_b} = i_{b2-os}R_f + i_{b2}^+ \frac{R_f\left(\frac{R_p}{R_f}\hat{A}_v+1\right)-\frac{R_{d1}}{2}\hat{A}_v\left(\frac{R_p}{R_f}+1\right)}{\frac{R_p}{R_f}\hat{A}_v+2} + \frac{(i_{b1-os}-i_{b2-os})R_f+i_{b1}^+\left(R_f+\frac{R_{d1}}{2}\hat{A}_v\right)}{\frac{R_p}{R_f}\hat{A}_v+2} \quad (6.30)$$

The following analysis considers two cases of the amplifier output voltages generated by the input bias currents: when the inequality $R_{f1,2}/R_p \ll \hat{A}_{v1,2}$ is true and when it is false. PZT materials exhibit high DC resistivity at room temperature [103],[106] such that for the values of $R_{f1,2}$ used in the amplifier design, $R_{f1}/R_p \ll \hat{A}_{v1}$ and $R_{f2}/R_p \ll \hat{A}_{v2}$ are always true over the temperature range of interest. However, consideration of a significantly reduced dielectric resistance R_p such that $R_{f1}/R_p \ll \hat{A}_{v1}$ and $R_{f2}/R_p \ll \hat{A}_{v2}$ are false which would be the case for example if high feedback resistances R_f were used and the insulation resistance of

the PZT-5H sensor patch R_p was significantly degraded by for example exposure to moisture or cracking as discussed in Section 6.3.2.

When $R_{f1}/R_p \ll \hat{A}_{v1}$ and $R_{f2}/R_p \ll \hat{A}_{v2}$ are true, the approximations $\hat{A}_{v1},\ \hat{A}_{v2} \to \infty$ can be made and it can therefore be seen that Equation 6.29 and Equation 6.30 reduce to Equation 6.31 and Equation 6.32 respectively.

$$V_{OA1-i_b} = i_{b1-os}R_f + i_{b1}^{+}\left[R_f - \frac{R_{d1}}{2}\left(\frac{R_f}{R_p}+1\right)\right] + i_{b2}^{+}\frac{R_{d1}}{2}\left(\frac{R_f}{R_p}\right)$$

$$\cong R_f(i_{b1-os} + i_{b1}^{+})_{R_{d1}\ll R_p,\, R_f} = R_f(i_{b1}^{-})_{R_{d1}\ll R_p,\, R_f} \qquad (6.31)$$

$$V_{OA2-i_b} = i_{b2-os}R_f + i_{b2}^{+}\left[R_f - \frac{R_{d1}}{2}\left(\frac{R_f}{R_p}+1\right)\right] + i_{b1}^{+}\frac{R_{d1}}{2}\left(\frac{R_f}{R_p}\right)$$

$$\cong R_f(i_{b2-os} + i_{b2}^{+})_{R_{d1}\ll R_p,\, R_f} = R_f(i_{b2}^{-})_{R_{d1}\ll R_p,\, R_f} \qquad (6.32)$$

It can be seen from Equation 6.31 and Equation 6.32 that the steady state output voltage due to the bias currents i_{b1}^{+} and i_{b2}^{+} respectively can be negated by selecting the voltage divider resistors R_{d1} equal to twice the value of the parallel combination of R_f and R_p such that $R_{d1} = 2R_fR_p/(R_f + R_p) \cong 2R_p$. However, it can be seen from Equation 6.31 that negating the i_{b1}^{+} bias current term in this way has the consequence of increasing the offset voltage due to i_{b2}^{+} to $i_{b2}^{+}R_f$ and therefore for the case that $i_{b1}^{+} \cong i_{b1}^{-}$, no overall reduction in offset voltage is gained. Furthermore, selecting a large value of $R_{d1} \cong 2R_p$ for the four voltage divider resistors with the low tolerance required would be both expensive and incur an unacceptably long $V_{cc}/2$ bias voltage rise-time of $C_nR_{d1}/2 \approx 12\ hours$.

Noting that for the amplifier design, $R_{d1} \ll R_p$, $R_{d1} \ll R_f$, and $C_p \ll C_f$, the corresponding output voltages including the voltage drift with respect to time are therefore approximated by Equation 6.33 and Equation 6.34 where as before the nominal value of C_f is used such that $C_{f1} = C_{f2} = C_f$. Since the time constant $R_{d1}C_n/2$ formed by the noise reducing capacitor ($C_n = 0.47\mu F$) and voltage divider resistances ($R_{d1} = 100k\Omega$) is approximately $0.02s$, the effect of C_n on the output voltages is vanishingly small and is therefore neglected.

$$V_{OA1-i_b} \cong R_f \left(1 - e^{-\frac{t}{R_f C_f}}\right)(i_{b1-os} + i_{b1}^{+})_{R_{d1} \ll R_p, R_f} \tag{6.33}$$

$$V_{OA2-i_b} \cong R_f \left(1 - e^{-\frac{t}{R_f C_f}}\right)(i_{b2-os} + i_{b2}^{+})_{R_{d1} \ll R_p, R_f} \tag{6.34}$$

The maximum offset voltages due to the bias currents that can be expected at $t = 0$ and in the steady state in the case of $R_f = (1 + 5\%)G\Omega$ and, at $t = 0$, in the steady state and after 8 $hours$ of transient drift in the case of $R_f = (1 + 5\%)T\Omega$ are shown in Table 6.13. The nominal values of $C_p = 20nF$ and $C_f = 1.5\mu F$ are assumed for the transient drift calculation. The LMC6081 op-amps used in the unipolar designs have a very low typical bias current of approximately $10fA$ and offset bias current of approximately $5fA$.

$R_p = 90G\Omega,\ i_{b1,2-os} = 5fA, i_{b1,2}^{+} = 10fA$					
$R_{f1} = R_{f2} = R_f$ / Bias current drift	$1.05G\Omega$ $steady\ state$	$1.05G\Omega$ $t = 0$	$1.05T\Omega$ $steady\ state$	$1.05T\Omega$ $t = 8hr$	$1.05T\Omega$ $t = 0$
$Maximum\ V_{OA1-i_b}$	$0.016mV$	$\approx 0V$	$15.75mV$	$0.285mV$	$\approx 0V$
$Maximum\ V_{OA2-i_b}$	$0.016mV$	$\approx 0V$	$15.75mV$	$0.285mV$	$\approx 0V$

Table 6.13 Expected maximum voltage drift at $R_p = 90G\Omega$ due to bias currents

It can be seen from Table 6.13 that the magnitude of the maximum drift voltages at the outputs of OA1 and OA2 after a typical 8 $hour$ sensor operating period with $R_{f1} = R_{f2} = (1 + 5\%)T\Omega$ are given by $0.285mV$, while the steady state drift voltage with $R_{f1} = R_{f2} = (1 + 5\%)G\Omega$ (maximum tolerance value) are given by $0.016mV$. Since the sensitivity of the sensor and amplifier when used to measure temperature is $0.15V/K$, then with $R_{f1} = R_{f2} = (1 + 5\%)T\Omega$ a measurement error of less than $2.6mK$ can be expected at $t = 8\ hours$, while it can be seen that the steady state drift voltage is negligible with $R_{f1} = R_{f2} = (1 + 5\%)G\Omega$. It is therefore

clear that the resulting voltage offsets are insignificant and may be ignored when $R_p = 90G\Omega$.

When $R_f/R_p \ll \hat{A}_v$ is not true, then the approximation $A_v \to \infty$ cannot be made and Equation 6.29 and Equation 6.30 must be used directly. Equation 6.35 and Equation 6.36 give the corresponding time dependent voltage drifts due to the bias currents and offset bias currents.

$$V_{OA1-i_b} = R_f\left(1 - e^{-\frac{t}{R_f C_f}}\right) i_{b1-os} +$$

$$+\frac{R_f}{2}\left[\left(1 - e^{-\frac{t}{R_f C_f}}\right) + \frac{\hat{A}_v R_p}{(\hat{A}_v R_p + 2R_f)}\left(1 - e^{-\frac{t}{C_f}\left(\frac{1}{R_f}+\frac{2}{\hat{A}_v R_p}\right)}\right)\right] i_{b1}^{+}$$

$$-\frac{R_{d1}}{2}\left[e^{-\frac{t}{C_f}\left(\frac{1}{R_f}+\frac{2}{\hat{A}_v R_p}\right)} + \frac{\hat{A}_v(R_p + R_f)}{(\hat{A}_v R_p + 2R_f)}\left(1 - e^{-\frac{t}{C_f}\left(\frac{1}{R_f}+\frac{2}{\hat{A}_v R_p}\right)}\right)\right] i_{b1}^{+}$$

$$+\frac{R_f}{2}\left[\left(1 - e^{-\frac{t}{R_f C_f}}\right) - \frac{\hat{A}_v R_p}{(\hat{A}_v R_p + 2R_f)}\left(1 - e^{-\frac{t}{C_f}\left(\frac{1}{R_f}+\frac{2}{\hat{A}_v R_p}\right)}\right)\right](i_{b2-os} - i_{b1-os} + i_{b2}^{+})$$

$$+\frac{R_{d1}}{2}\left[\left(\frac{C_p}{C_f}\right)e^{-\frac{t}{C_f}\left(\frac{1}{R_f}+\frac{2}{\hat{A}_v R_p}\right)} + \frac{\hat{A}_v R_f}{(\hat{A}_v R_p + 2R_f)}\left(1 - e^{-\frac{t}{C_f}\left(\frac{1}{R_f}+\frac{2}{\hat{A}_v R_p}\right)}\right)\right] i_{b2}^{+} \qquad (6.35)$$

$$V_{OA2-i_b} = R_f\left(1 - e^{-\frac{t}{R_f C_f}}\right) i_{b2-os} +$$

$$+\frac{R_f}{2}\left[\left(1 - e^{-\frac{t}{R_f C_f}}\right) + \frac{\hat{A}_v R_p}{(\hat{A}_v R_p + 2R_f)}\left(1 - e^{-\frac{t}{C_f}\left(\frac{1}{R_f}+\frac{2}{\hat{A}_v R_p}\right)}\right)\right] i_{b2}^{+}$$

$$-\frac{R_{d1}}{2}\left[e^{-\frac{t}{C_f}\left(\frac{1}{R_f}+\frac{2}{\hat{A}_v R_p}\right)} + \frac{\hat{A}_v(R_p + R_f)}{(\hat{A}_v R_p + 2R_f)}\left(1 - e^{-\frac{t}{C_f}\left(\frac{1}{R_f}+\frac{2}{\hat{A}_v R_p}\right)}\right)\right] i_{b2}^{+}$$

$$+\frac{R_f}{2}\left[\left(1 - e^{-\frac{t}{R_f C_f}}\right) - \frac{\hat{A}_v R_p}{(\hat{A}_v R_p + 2R_f)}\left(1 - e^{-\frac{t}{C_f}\left(\frac{1}{R_f}+\frac{2}{\hat{A}_v R_p}\right)}\right)\right](i_{b1-os} - i_{b2-os} + i_{b1}^{+})$$

$$+\frac{R_{d1}}{2}\left[\left(\frac{C_p}{C_f}\right)e^{-\frac{t}{C_f}\left(\frac{1}{R_f}+\frac{2}{\hat{A}_v R_p}\right)} + \frac{\hat{A}_v R_f}{(\hat{A}_v R_p + 2R_f)}\left(1 - e^{-\frac{t}{C_f}\left(\frac{1}{R_f}+\frac{2}{\hat{A}_v R_p}\right)}\right)\right] i_{b1}^{+} \qquad (6.36)$$

The second and final terms can be neglected since $R_{d1} \ll R_p$ and $C_p \ll C_f$ and therefore Equation 6.35 and Equation 6.36 can be reduced to Equation 6.37 and Equation 6.38 respectively.

$$V_{OA1-i_b} \cong R_f\left(1 - e^{-\frac{t}{R_f C_f}}\right) i_{b1-os} +$$

$$+\frac{R_f}{2}\left[\left(1 - e^{-\frac{t}{R_f C_f}}\right) + \frac{\hat{A}_v R_p}{(\hat{A}_v R_p + 2R_f)}\left(1 - e^{-\frac{t}{C_f}\left(\frac{1}{R_f} + \frac{2}{\hat{A}_v R_p}\right)}\right)\right] i_{b1}^{+}$$

$$+\frac{R_f}{2}\left[\left(1 - e^{-\frac{t}{R_f C_f}}\right) - \frac{\hat{A}_v R_p}{(\hat{A}_v R_p + 2R_f)}\left(1 - e^{-\frac{t}{C_f}\left(\frac{1}{R_f} + \frac{2}{\hat{A}_v R_p}\right)}\right)\right] (i_{b2-os} - i_{b1-os} + i_{b2}^{+})$$

(6.37)

$$V_{OA2-i_b} \cong R_f\left(1 - e^{-\frac{t}{R_f C_f}}\right) i_{b2-os} +$$

$$+\frac{R_f}{2}\left[\left(1 - e^{-\frac{t}{R_f C_f}}\right) + \frac{\hat{A}_v R_p}{(\hat{A}_v R_p + 2R_f)}\left(1 - e^{-\frac{t}{C_f}\left(\frac{1}{R_f} + \frac{2}{\hat{A}_v R_p}\right)}\right)\right] i_{b2}^{+}$$

$$+\frac{R_f}{2}\left[\left(1 - e^{-\frac{t}{R_f C_f}}\right) - \frac{\hat{A}_v R_p}{(\hat{A}_v R_p + 2R_f)}\left(1 - e^{-\frac{t}{C_f}\left(\frac{1}{R_f} + \frac{2}{\hat{A}_v R_p}\right)}\right)\right] (i_{b1-os} - i_{b2-os} + i_{b1}^{+})$$

(6.38)

The maximum drift voltages due to the bias currents that can be expected at $t = 0$ and in the steady state in the case of $R_f = (1 + 5\%)G\Omega$ and, at $t = 0$, in the steady state and after 8 $hours$ of transient drift in the case of $R_f = (1 + 5\%)T\Omega$ are shown in Table 6.14 for datasheet specified typical values of the input bias current and input offset bias current.

$R_p = 100M\Omega,\ i_{b1,2-os} = 5fA, i_{b1,2}^{+} = 10fA$					
$R_{f1} = R_{f2} = R_f$ / Bias current drift	$1.05G\Omega$ $steady\ state$	$1.05G\Omega$ $t = 0$	$1.05T\Omega$ $steady\ state$	$1.05T\Omega$ $t = 8hr$	$1.05T\Omega$ $t = 0$
$Maximum\ V_{OA1-i_b}$	$0.016mV$	$\approx 0V$	$15.75mV$	$0.285mV$	$\approx 0V$
$Maximum\ V_{OA2-i_b}$	$0.016mV$	$\approx 0V$	$15.75mV$	$0.285mV$	$\approx 0V$

Table 6.14 Expected maximum voltage drift at $R_p = 100M\Omega$ due to bias currents

It can be seen from Table 6.14 that the magnitude of the maximum steady state drift voltages when $R_{f1} = R_{f2} = (1 + 5\%)G\Omega$ is $0.016mV$. This value of feedback resistor is used for the experimental investigations described in Chapter 7 and since all experiment measurement durations are less than $3\ minutes$ and the magnitude of the offset drift voltage due to bias currents at $3\ minutes$ is $0.0017mV$, the effect of the bias currents may therefore be neglected. The steady state drift voltage after an $8\ hour$ sensor operating period with $R_{f1} = R_{f2} = (1 + 5\%)T\Omega$ rises to approximately $0.29mV$. Since the sensitivity of the sensor and amplifier when used to measure temperature is $0.15V/K$, it is clear that the resulting voltage offsets are insignificant and that these may also be neglected. By comparing Table 6.13 and Table 6.14 it can be seen that a reduction in R_p does not result in a change in the drift voltages. The drift voltages are insensitive, although not independent, of R_p over the range $0 \leq R_p \leq \infty$. For the extremes of $R_p = 0$ and $R_p = \infty$, with $R_f = 1.05G\Omega$, the steady state and $t = 8\ hour$ values of both V_{OA1-i_b} and V_{OA2-i_b} are $15.75mV$ at $R_p = 0$, and $0.285mV$ at $R_p = \infty$. The insensitivity of the output drift voltage to the value of R_p is due to the contribution of the bias currents at the inverting inputs of OA1 and OA2, which are dominant and produce an output drift voltage that is independent of R_p. The contribution of the bias and offset bias currents to the overall drift voltages can therefore be neglected for all values of R_p.

6.4.3 Op-amp input-offset voltages V_{os}

The input offset voltages are modelled as voltage sources in series with either the inverting or the non-inverting terminals of each of the op-amps. To comply with convention, the polarity of V_{os} toward the non-inverting input is positive if referred to the non-inverting terminal, while the polarity of V_{os} toward the inverting terminal is negative if referred to the inverting terminal. The value of input offset voltage V_{os} quoted in the data sheet for the LMC6081 has a typical value of $150\mu V$ that can therefore be referred either to the non-inverting terminal as $+V_{os}$ or equivalently to the inverting terminal as $-V_{os}$. While the published input offset voltage can be considered relatively low, the current induced through R_s and the sensing element dielectric resistance R_p by the input offset voltages also flow through the feedback resistors R_f resulting in output voltages at OA1 and OA2. Since the feedback resistors R_f are necessarily large to achieve the required time constants, then if R_p is sufficiently low relative to R_f, a significant drift leading to a steady state output voltage offset will occur. However, this drift can be negated using a voltage compensation scheme if necessary.

The steady state output voltages of OA1 and OA2 due to V_{cc}, V_{os1} and V_{os2} are derived and given in the following analysis. The DC open loop gains denoted by $\hat{A}_{v1}$ and $\hat{A}_{v2}$, and the feedback resistors denoted by R_{f1} and R_{f2} associated with the single charge amplifier stages formed by OA1 and OA2 respectively are considered to be different to reflect manufacturing tolerances. The input offset voltages of OA1 and OA2 are denoted by V_{os1} and V_{os2} respectively and are also in general different due to manufacturing tolerances. When R_p is small or R_{f1} and R_{f2} are large such that the ratios R_{f1}/R_p and R_{f2}/R_p approach the same order as the open loop gains then the standard approximation $\hat{A}_{v1},\ \hat{A}_{21} \to \infty$ cannot be made and the high steady state voltage gain, mitigated in part by the finite open loop gain may nevertheless result in significant output voltage offsets at the output of OA1 and OA2.

As shown in Figure 6.1, voltage offset compensation, if required, is achieved using two 25 turn 250Ω trimmer type potentiometers R_{pot-1} and R_{pot-2} at each of the non-inverting inputs of OA1 and OA2 to provide fine adjustment of the bias voltages applied to the non-inverting inputs of OA1 and OA2. These trimmers

provide voltage compensation of the input offset voltage; voltage compensation due to the error in the bias voltage supplied by the voltage divider resistors R_{d1} due to resistor tolerances of $\pm 0.1\%$; and voltage compensation due to the difference in the inverting input voltages of OA1 and OA2 due to tolerances in the values of the open loop gains. The compensation scheme described above cannot in general be used to compensate for drift due to the bias currents at the inverting and non-inverting inputs of OA1 and OA2. However, as described in Section 6.4.2, since the LMC6081 op-amps typically have very low bias current specifications, the bias current drifts are insignificant and can be neglected.

The upper and lower voltage divider resistors supplying the non-inverting input of OA1 are denoted by R_{d1u-1} and R_{d1l-1}, and those supplying OA2 are denoted by R_{d1u-2} and R_{d1l-2} respectively to reflect that these are in general different due to resistor tolerances. Denoting the proportion of R_{pot} appearing between the non-inverting input of OA1 and R_{d1l-1} as aR_{pot-1}, and OA2 and R_{d1l-2} as bR_{pot-2} where a and b can take values between zero and one, then the steady state output voltages of OA1 and OA2, denoted by V_{OA1-os} and V_{OA2-os} are given by Equation 6.39 and Equation 6.40 respectively where a' and b' are given by:

$$a' = \left(aR_{pot-1}+R_{d1l-1}\right)/\left(R_{pot-1}+R_{d1u-1}+R_{d1l-1}\right)$$

$$b' = \left(bR_{pot-2}+R_{d1l-2}\right)/\left(R_{pot-2}+R_{d1u-2}+R_{d1l-2}\right)$$

$$V_{OA1-os} =$$

$$a'V_{cc} + V_{os1} + \frac{b'\hat{A}_{v1}+\hat{A}_{v1}\hat{A}_{v2}(a'-b')-a'\hat{A}_{v2}}{\frac{R_{f2}}{R_{f1}}\hat{A}_{v1}+\left(\frac{R_p}{R_{f1}}\hat{A}_{v1}+1\right)\hat{A}_{v2}}V_{cc} + \frac{V_{os2}\hat{A}_{v1}+\hat{A}_{v1}\hat{A}_{v2}(V_{os1}-V_{os2})-V_{os1}\hat{A}_{v2}}{\frac{R_{f2}}{R_{f1}}\hat{A}_{v1}+\left(\frac{R_p}{R_{f1}}\hat{A}_{v1}+1\right)\hat{A}_{v2}} \quad (6.39)$$

$$V_{OA2-os} =$$

$$b'V_{cc} + V_{os2} + \frac{a'\hat{A}_{v2}+\hat{A}_{v1}\hat{A}_{v2}(b'-a')-b'\hat{A}_{v1}}{\frac{R_{f1}}{R_{f2}}\hat{A}_{v2}+\left(\frac{R_p}{R_{f2}}\hat{A}_{v2}+1\right)\hat{A}_{v1}}V_{cc} + \frac{V_{os1}\hat{A}_{v2}+\hat{A}_{v1}\hat{A}_{v2}(V_{os2}-V_{os1})-V_{os2}\hat{A}_{v1}}{\frac{R_{f1}}{R_{f2}}\hat{A}_{v2}+\left(\frac{R_p}{R_{f2}}\hat{A}_{v2}+1\right)\hat{A}_{v1}} \quad (6.40)$$

The following analysis considers the two cases of the amplifier output voltages generated by the offset voltages when the inequalities $R_{f1}/R_p \ll A_{v1}$ and $R_{f2}/R_p \ll A_{v2}$ are true and when they are false. All PZT materials exhibit high DC

resistivity such that for the values of $R_{f1,2}$ used in the amplifier design, $R_{f1}/R_p \ll \hat{A}_{v1}$ and $R_{f2}/R_p \ll \hat{A}_{v2}$ are always true. However, consideration of a significantly reduced R_p such that $R_{f1}/R_p \ll A_{v1}$ and $R_{f2}/R_p \ll A_{v2}$ are false which would be the case for example if high feedback resistances R_f were used and the insulation resistance of the PZT-5H sensor element, R_p was significantly degraded by for example exposure to moisture or cracking.

When $R_{f1}/R_p \ll \hat{A}_{v1}$ and $R_{f2}/R_p \ll \hat{A}_{v2}$ are true, the approximations $\hat{A}_{v1}, \hat{A}_{v2} \to \infty$ can be made and it can therefore be seen that Equation 6.39 and Equation 6.40 reduce to Equation 6.41 and Equation 6.42 respectively.

$$V_{OA1-os} = a'V_{cc} + \frac{R_{f1}}{R_p}(a' - b')V_{cc} + V_{os1} + \frac{R_{f1}}{R_p}(V_{os1} - V_{os2}) \tag{6.41}$$

$$V_{OA2-os} = b'V_{cc} + \frac{R_{f2}}{R_p}(b' - a')V_{cc} + V_{os2} + \frac{R_{f2}}{R_p}(V_{os2} - V_{os1}) \tag{6.42}$$

By correcting for voltage divider resistor tolerances at the non-inverting inputs of OA1 and OA2 without compensating for the input offset voltage voltages such that $a' = b' = 0.5$, Equation 6.41 and Equation 6.42 can be reduced to Equation 6.43 and Equation 6.44.

$$V_{OA1-os} = \frac{V_{cc}}{2} + V_{os1} + \frac{R_{f1}}{R_p}(V_{os1} - V_{os2}) \tag{6.43}$$

$$V_{OA2-os} = \frac{V_{cc}}{2} + V_{os2} + \frac{R_{f2}}{R_p}(V_{os2} - V_{os1}) \tag{6.44}$$

When V_{os1} is precisely equal to V_{os2} and $a' = b' = 0.5$, then $V_{OA1-os} = V_{cc}/2 + V_{os1}$ and $V_{OA2-os} = V_{cc}/2 + V_{os2}$ and the output voltages are limited to the value of the respective input offset voltages and desired bias voltage. Since the input offset voltage of the LMC6081 is typically equal to approximately $150\mu V$ with a specified limit of $350\mu V$, then in this case no voltage compensation is required. However, due to manufacturing tolerances, it cannot be assumed that $(V_{os1} - V_{os2})$ is zero or close to zero.

The drift with respect to time can be estimated by considering that if the amplifier is switched on at $t = 0$, then the voltages at the outputs of OA1 and OA2, that include the time-dependent drift due to the offset voltages, are given by Equation

6.45 and Equation 6.46 respectively. A very short rise time in the drift components that occur at switch-on due to the ESD R_s resistors and the frequency dependence of OA1 and OA2 are omitted for clarity.

$$V_{OA1-os} = \frac{V_{cc}}{2} + V_{os1} + \left[\frac{R_{f1}}{R_p}\left(1 - e^{-\frac{t}{R_{f1}C_{f1}}}\right) + \frac{C_p}{C_{f1}}e^{-\frac{t}{R_{f1}C_{f1}}}\right](V_{os1} - V_{os2}) \quad (6.45)$$

$$V_{OA2-os} = \frac{V_{cc}}{2} + V_{os2} + \left[\frac{R_{f2}}{R_p}\left(1 - e^{-\frac{t}{R_{f2}C_{f2}}}\right) + \frac{C_p}{C_{f2}}e^{-\frac{t}{R_{f2}C_{f2}}}\right](V_{os2} - V_{os1}) \quad (6.46)$$

It can be seen that at $t = 0$ there is an 'immediate' component of drift given by $(C_p/C_{f1})(V_{os1} - V_{os2})$ at the output of OA1 and $(C_p/C_{f2})(V_{os2} - V_{os1})$ at the output of OA2. As $t \to \infty$ the drift components at the outputs of OA1 and OA2 are given by $(R_{f1}/R_p)(V_{os1} - V_{os2})$ and $(R_{f2}/R_p)(V_{os2} - V_{os1})$ respectively. Since $C_p \ll C_{f1}, C_{f2}$ the 'immediate' component can be neglected. The feedback resistors R_{f1} and R_{f2} have tolerances of $\pm 5\%$, and the typical limit values of V_{os1} and V_{os2} for the LMC6081 op-amps are $150\mu V$ and $350\mu V$ respectively. The largest output voltage swing due to the offset voltages is therefore given by letting the difference in the voltage offset voltages be $V_{os1} - V_{os2} = 200\mu V$, and by allowing the values of R_{f1} and R_{f2} to be equal and 5% greater than their nominal values. The nominal values of $C_p = 20nF$ and $C_f = 1.5\mu F$ are assumed for the transient drift calculation.

To achieve the necessary amplifier operating time constants for a continuous measurement period of 8 $hours$ with a specification of a maximum 2% signal decay, and for use in laboratory measurements, feedback resistances with nominal values of $R_f = 1T\Omega$ and $R_f = 1G\Omega$ respectively are required. The insulation resistance of the PZT-5H sensor element is estimated to be greater than $R_p = 90G\Omega$ which is calculated using the estimate of the DC resistivity of PZT-5H discussed in Section 6.2 and the dimensions of the piezoelectric element. The maximum output drift voltages that can be expected (excluding the bias voltage $V_{cc}/2$) in the steady state in the case of $R_{f1} = R_{f2} = (1 + 5\%)G\Omega$ and, in the case of $R_{f1} = R_{f2} = (1 + 5\%)T\Omega$ in the steady state and after 8 $hours$ of transient drift are shown in Table 6.15.

$R_p = 90G\Omega,\ V_{os1} = 150\mu V, V_{os2} = 350\mu V$					
$R_{f1} = R_{f2} = R_f$ / Drift voltage	$1.05G\Omega$ $steady\ state$	$1.05G\Omega$ $t = 0$	$1.05T\Omega$ $steady\ state$	$1.05T\Omega$ $t = 8hrs$	$1.05T\Omega$ $t = 0$
$Maximum\ V_{OA1-drift}$	$2.45mV$	$0.353mV$	$2.68mV$	$0.395mV$	$0.353mV$
$Maximum\ V_{OA2-drift}$	$-1.95mV$	$0.147mV$	$-2.18mV$	$0.105mV$	$0.147mV$

Table 6.15 Expected maximum voltage drift at $R_p = 90G\Omega$ due to $V_{os1}$and V_{os2}

It can be seen that the maximum drift voltages after a typical $8\ hour$ sensor operating period with $R_{f1} = R_{f2} = 1T\Omega\ (nominal)$ or in the steady state with $R_{f1} = R_{f2} = 1G\Omega\ (nominal)$ are less than $1mV$. Since the sensitivity of the sensor and amplifier when used to measure temperature is approximately $0.15V/K$, it is clear that the resulting voltage offsets are insignificant and that voltage compensation is not required for either value of feedback resistor.

When $R_{f1}/R_p \ll \hat{A}_{v1}$ and $R_{f2}/R_p \ll \hat{A}_{v2}$ are not true, the approximations $\hat{A}_{v1},\ \hat{A}_{v2} \to \infty$ cannot be made. This would be the case for example if high feedback resistances R_f were used and the insulation resistance of the PZT-5H sensor patch R_p was significantly degraded by for example exposure to moisture or cracking. From Equation 6.39 and Equation 6.40 it can be deduced that the maximum offset drifts at OA1 and OA2 occur when both of the open loop gains are equal and maximal such that $\hat{A}_{v1} = \hat{A}_{v2} = \hat{A}_v = 1.4 \times 10^6$, Equation 6.39 and Equation 6.40 reduce to Equation 6.47 and Equation 6.48 respectively.

$$V_{OA1-os} = a'V_{cc} + V_{os1} + \frac{b'-a'+\hat{A}_v(a'-b')}{\left(\frac{R_p}{R_{f1}}\hat{A}_v+\frac{R_{f2}}{R_{f1}}+1\right)}V_{cc} + \frac{V_{os2}-V_{os1}+\hat{A}_v(V_{os1}-V_{os2})}{\left(\frac{R_p}{R_{f1}}\hat{A}_v+\frac{R_{f2}}{R_{f1}}+1\right)} \tag{6.47}$$

$$V_{OA2-os} = b'V_{cc} + V_{os2} + \frac{a'-b'+\hat{A}_v(b'-a')}{\left(\frac{R_p}{R_{f2}}\hat{A}_v+\frac{R_{f1}}{R_{f2}}+1\right)}V_{cc} + \frac{V_{os1}-V_{os2}+\hat{A}_v(V_{os2}-V_{os1})}{\left(\frac{R_p}{R_{f2}}\hat{A}_v+\frac{R_{f1}}{R_{f2}}+1\right)} \tag{6.48}$$

As before, correcting for the voltage divider resistor tolerances at the non-inverting inputs of OA1 and OA2 without voltage offset compensation such that

$a' = b' = 0.5$, Equation 6.47 and Equation 6.48 can be reduced to Equation 6.49 and Equation 6.50 respectively.

$$V_{OA1-os} = \frac{V_{cc}}{2} + V_{os1} + \frac{V_{os2} - V_{os1} + \hat{A}_v(V_{os1} - V_{os2})}{\left(\frac{R_p}{R_{f1}}\hat{A}_v + \frac{R_{f2}}{R_{f1}} + 1\right)} \tag{6.49}$$

$$V_{OA2-os} = \frac{V_{cc}}{2} + V_{os2} + \frac{V_{os1} - V_{os2} + \hat{A}_v(V_{os2} - V_{os1})}{\left(\frac{R_p}{R_{f2}}\hat{A}_v + \frac{R_{f1}}{R_{f2}} + 1\right)} \tag{6.50}$$

The maximum voltage drift occurs when $R_{f1} = R_{f2} = R_f$ are 5% above the nominal values. Letting $R_{f1} = R_{f2} = R_f$, Equation 6.49 and Equation 6.50 reduce to Equation 6.51 and Equation 6.52 respectively.

$$V_{OA1-os} = \frac{V_{cc}}{2} + V_{os1} + \frac{V_{os2} - V_{os1} + \hat{A}_v(V_{os1} - V_{os2})}{\left(\frac{R_p}{R_f}\hat{A}_v + 2\right)} \tag{6.51}$$

$$V_{OA2-os} = \frac{V_{cc}}{2} + V_{os2} + \frac{V_{os1} - V_{os2} + \hat{A}_v(V_{os2} - V_{os1})}{\left(\frac{R_p}{R_f}\hat{A}_v + 2\right)} \tag{6.52}$$

Equation 6.53 and Equation 6.54 approximate the corresponding output voltages, including the voltage drift due to the offset voltages with respect to time.

$$V_{OA1-os} =$$

$$\frac{V_{cc}}{2} + V_{os1} + \left[\frac{\hat{A}_v R_f}{(\hat{A}_v R_p + 2R_f)}\left(1 - e^{-\frac{t}{C_f}\left(\frac{1}{R_f} + \frac{2}{\hat{A}_v R_p}\right)}\right) + \frac{C_p}{C_f}e^{-\frac{t}{C_f}\left(\frac{1}{R_f} + \frac{2}{\hat{A}_v R_p}\right)}\right](V_{os1} - V_{os2}) \tag{6.53}$$

$$V_{OA2-os} =$$

$$\frac{V_{cc}}{2} + V_{os2} + \left[\frac{\hat{A}_v R_f}{(\hat{A}_v R_p + 2R_f)}\left(1 - e^{-\frac{t}{C_f}\left(\frac{1}{R_f} + \frac{2}{\hat{A}_v R_p}\right)}\right) + \frac{C_p}{C_f}e^{-\frac{t}{C_f}\left(\frac{1}{R_f} + \frac{2}{\hat{A}_v R_p}\right)}\right](V_{os2} - V_{os1}) \tag{6.54}$$

As in Section 6.4.2, it can be seen that at $t = 0$ there is an 'immediate' component of drift given by $(C_p/C_f)(V_{os1} - V_{os2})$ at the output of OA1 and $(C_p/C_f)(V_{os2} - V_{os1})$ at the output of OA2. As $t \to \infty$ the drift components at the outputs of OA1 and OA2 are given by $\pm(\hat{A}_v R_f/(\hat{A}_v R_p + 2R_f))(V_{os1} - V_{os2})$ respectively. Since $C_p \ll C_f$ this 'immediate' component can, as previously, be neglected. As above, the difference in the offset voltages is assumed to be $V_{os1} - V_{os2} = 200\mu V$ and the feedback resistors R_f are assumed to be 5% greater than their nominal values to achieve the maximum voltage drift. The nominal values of $C_p = 20nF$ and $C_f = 1.5\mu F$ are used for the transient drift calculation.

The piezoelectric element is now assumed to have a lower insulation resistance of $R_p = 100M\Omega$ to simulate the effect of insulation resistance degradation. The maximum output drift voltages that can be expected (excluding the bias voltage $V_{cc}/2$) in the steady state and, in the case of $R_{f1} = R_{f2} = R_f = (1 + 5\%)T\Omega$ in the steady state and after $8\,hours$ of transient drift are shown in Table 6.16.

$R_p = 100M\Omega,\ V_{os1} = 150\mu V, V_{os2} = 350\mu V$					
$R_{f1} = R_{f2} = R_f$ / Drift voltage	$1.05G\Omega$ $steady\ state$	$1.05G\Omega$ $t = 0$	$1.05T\Omega$ $steady\ state$	$1.05T\Omega$ $t = 8hr$	$1.05T\Omega$ $t = 0$
$Maximum\ V_{OA1-drift}$	$2.45mV$	$0.353mV$	$2.07V$	$38.4mV$	$0.353mV$
$Maximum\ V_{OA2-drift}$	$-1.95mV$	$0.147mV$	$-2.07V$	$-37.9mV$	$0.147mV$

Table 6.16 Expected maximum voltage drift at $R_p = 100M\Omega$ due to $V_{os1}$and V_{os2}

It can be seen from Table 6.16 that when $R_p = 100M\Omega$, the maximum drift voltages after a typical $8\,hour$ sensor operating period with $R_f = 1T\Omega\ (nominal)$ are significant. The sensitivity of the sensor and charge-mode conditioning amplifier when used to measure temperature is $0.15V/K$ and therefore using $R_f = 1T\Omega\ (nominal)$ feedback resistors, a measurement drift error of approximately $0.25K$ will occur at the end of an $8\,hour$ measurement period. It is clear that

replacement of the piezoelectric sensor element is necessary in this case. Alternatively, the use of voltage compensation will mitigate the increasing drift voltage over the measurement period. Lower values of R_p will result in a greater drift with the drift following an approximately inversely proportional relationship to R_p. The output voltage of OA3 due to the input offset voltage V_{os3} is given by $V_{OA3-os} = V_{os3}(1 + R_3/R_2)$. Since the ratio of R_3 and R_2 is given by $R_3/R_2 = 0.5$ for the difference amplifier gain of $G = 0.5$, then V_{OA3-os} is typically less than $0.3mV$ and can therefore be neglected.

6.4.4 Bias voltage drift

It can be seen from Equation 6.39 and Equation 6.40 given in Section 6.4.3 that a similar drift in the DC bias at the outputs of OA1 and OA2 will occur for the general case that separate voltage dividers are used at OA1 and OA2. In this case the bias voltages are uncompensated such that $a' \neq b'$ due to the voltage divider resistor tolerances of $\pm 0.1\%$. While this is small, a significant offset voltage may develop at the amplifier output when R_{f1}/R_p and R_{f2}/R_p are large. By inspection of Equation 6.39 and Equation 6.40, the steady state DC bias voltages at the outputs of OA1 and OA2 can be written as Equation 6.55 and Equation 6.56.

$$V_{OA1-DC\ bias} = a'V_{cc} + \frac{b'\hat{A}_{v1} + \hat{A}_{v1}\hat{A}_{v2}(a'-b') - a'\hat{A}_{v2}}{\frac{R_{f2}}{R_{f1}}\hat{A}_{v1} + \left(\frac{R_p}{R_{f1}}\hat{A}_{v1} + 1\right)\hat{A}_{v2}} V_{cc} \tag{6.55}$$

$$V_{OA2-DC\ bias} = b'V_{cc} + \frac{a'\hat{A}_{v2} + \hat{A}_{v1}\hat{A}_{v2}(b'-a') - b'\hat{A}_{v1}}{\frac{R_{f1}}{R_{f2}}\hat{A}_{v2} + \left(\frac{R_p}{R_{f2}}\hat{A}_{v2} + 1\right)\hat{A}_{v1}} V_{cc} \tag{6.56}$$

The worst case values for the voltage divider fractions are $a' = 0.5005$ and $b' = 0.4995$ or vice-versa. As before, the maximum offset drifts at OA1 and OA2 occur when both of the open loop gains are equal and maximal such that $\hat{A}_{v1} = \hat{A}_{v2} = \hat{A}_v = 1.4 \times 10^6$ and $R_{f1} = R_{f2} = R_f = (1 + 5\%)T\Omega$. The bias voltages given by Equation 6.55 and Equation 6.56 therefore reduce to Equation 6.57 and Equation 6.58 respectively.

$$V_{OA1-DC\ bias} = a'V_{cc} + \frac{b'-a'+\hat{A}_v(a'-b')}{\left(\frac{R_p}{R_f}\hat{A}_v+2\right)}V_{cc} \tag{6.57}$$

$$V_{OA2-DC\ bias} = b'V_{cc} + \frac{a'-b'+\hat{A}_v(b'-a')}{\left(\frac{R_p}{R_f}\hat{A}_v+2\right)}V_{cc} \tag{6.58}$$

When $R_f/R_p \ll \hat{A}_v$ is true, the approximation $A_v \to \infty$ can be made and therefore Equation 6.57 and Equation 6.58 reduce to Equation 6.59 and Equation 6.60 respectively.

$$V_{OA1-DC\ bias} = a'V_{cc} + \frac{R_f}{R_p}(a'-b')V_{cc} \tag{6.59}$$

$$V_{OA2-DC\ bias} = b'V_{cc} + \frac{R_f}{R_p}(b'-a')V_{cc} \tag{6.60}$$

The corresponding output voltages including the voltage drift with respect to time is approximated by Equation 6.61 and Equation 6.62 respectively where, as previously, the nominal value of C_f is used such that $C_{f1} = C_{f2} = C_f$.

$$V_{OA1-DC\ bias} = a'V_{cc} + \left[\frac{R_f}{R_p}\left(1-e^{-\frac{t}{R_fC_f}}\right)+\frac{C_p}{C_f}e^{-\frac{t}{R_fC_f}}\right](a'-b')V_{cc} \tag{6.61}$$

$$V_{OA2-DC\ bias} = b'V_{cc} + \left[\frac{R_f}{R_p}\left(1-e^{-\frac{t}{R_fC_f}}\right)+\frac{C_p}{C_f}e^{-\frac{t}{R_fC_f}}\right](b'-a')V_{cc} \tag{6.62}$$

The maximum DC bias offset voltages that can be expected (excluding the bias voltage $V_{cc}/2 = 2.5V$) at $t = 0$ and in the steady state in the case of $R_f = (1+5\%)G\Omega$ and, at $t = 0$, in the steady state and after 8 $hours$ of transient drift in the case of $R_f = (1+5\%)T\Omega$ are shown in Table 6.17. The nominal values of $C_p = 20nF$ and $C_f = 1.5\mu F$ are used for the transient drift calculation.

$R_p = 90G\Omega,\ a' = 0.5005,\ b' = 0.4995$					
$R_{f1} = R_{f2} = R_f$ / Bias voltage offset	$1.05G\Omega$ $steady\ state$	$1.05G\Omega$ $t = 0$	$1.05T\Omega$ $steady\ state$	$1.05T\Omega$ $t = 8hr$	$1.05T\Omega$ $t = 0$
$Maximum\ V_{OA1-DC\ bias} - \frac{Vcc}{2}$	$2.56mV$	$2.57mV$	$60.8mV$	$3.62mV$	$2.57mV$
$Maximum\ V_{OA2-DC\ bias} - \frac{Vcc}{2}$	$-2.56mV$	$-2.57mV$	$-60.8mV$	$-3.62mV$	$-2.57mV$

Table 6.17 Expected maximum voltage drift at $R_p = 90G\Omega$ due to bias voltage

It can be seen from Table 6.17 that the magnitude of the maximum drift voltages given by $(3.62 - 2.57)mV$ after a typical $8\ hour$ sensor operating period with $R_f = 1T\Omega\ (nominal)$ is approximately $1mV$, and when $R_f = 1G\Omega\ (nominal)$ the steady state drift voltage is slightly less than the voltage offset due to the resistor tolerances at $t = 0$. Since the sensitivity of the sensor and amplifier when used to measure temperature is $0.15V/K$, it is clear that the resulting voltage offsets are insignificant and voltage compensation is therefore not required for either value of feedback resistor when $R_p = 90G\Omega$. When $R_f = 1G\Omega\ (nominal)$ the magnitude of the drift voltage in the steady state is given by $(2.57 - 2.56)mV = 0.01mV$. This drift is insignificant and therefore bias voltage compensation is not required.

When $R_f/R_p \ll \hat{A}_v$ is not true, such as may be the case for if high feedback resistances R_f were used and the insulation resistance of the PZT-5H sensor patch R_p was significantly degraded by for example exposure to moisture or cracking, then the approximation $A_v \to \infty$ cannot be made and Equation 6.57 and Equation 6.58 must be used directly. Equation 6.63 and Equation 6.64 approximate the corresponding output voltages, including the voltage drift due to the offset voltages with respect to time.

$$V_{OA1-os} =$$

$$a'V_{cc} + \left[\frac{\hat{A}_v R_f}{(\hat{A}_v R_p + 2R_f)}\left(1 - e^{-\frac{t}{C_f}\left(\frac{1}{R_f} + \frac{2}{\hat{A}_v R_p}\right)}\right) + \frac{C_p}{C_f}e^{-\frac{t}{C_f}\left(\frac{1}{R_f} + \frac{2}{\hat{A}_v R_p}\right)}\right](a' - b')V_{cc} \quad (6.63)$$

$$V_{OA2-os} =$$

$$b'V_{cc} + \left[\frac{\hat{A}_v R_f}{(\hat{A}_v R_p + 2R_f)}\left(1 - e^{-\frac{t}{C_f}\left(\frac{1}{R_f}+\frac{2}{\hat{A}_v R_p}\right)}\right) + \frac{C_p}{C_f}e^{-\frac{t}{C_f}\left(\frac{1}{R_f}+\frac{2}{\hat{A}_v R_p}\right)}\right](b' - a')V_{cc} \quad (6.64)$$

The maximum DC bias drift voltages that can be expected, excluding the bias voltage $V_{cc}/2 = 2.5V$, at $t = 0$ and in the steady state in the case of $R_f = (1 + 5\%)G\Omega$ and for the case of $R_f = (1 + 5\%)T\Omega$ at $t = 0$, after $8\,hours$ of transient drift and in the steady state are shown in Table 6.18.

$R_p = 100M\Omega,\ a' = 0.5005,\ b' = 0.4995$					
$R_{f1} = R_{f2} = R_f$ / Bias voltage offset	$1.05G\Omega$ $steady\ state$	$1.05G\Omega$ $t = 0$	$1.05T\Omega$ $steady\ state$	$1.05T\Omega$ $t = 8hr$	$1.05T\Omega$ $t = 0$
$Maximum\ V_{OA1-DC\ bias} - \frac{Vcc}{2}$	$55mV$	$2.57mV$	$51.7V$ $Limit\ 5V$	$0.95V$	$2.57mV$
$Maximum\ V_{OA2-DC\ bias} - \frac{Vcc}{2}$	$-55mV$	$-2.57mV$	$-51.7V$ $Limit\ 0V$	$-0.95V$	$-2.57mV$

Table 6.18 Expected maximum voltage drift at $R_p = 100M\Omega$ due to bias voltage

It can be seen from Table 6.18 that the magnitude of the maximum drift voltages after a typical $8\,hour$ sensor operating period with $R_{f1} = R_{f2} = 1T\Omega\ (nominal)$ are approximately $0.95V$. Since the sensitivity of the sensor and amplifier when used to measure temperature is $0.15V/K$, it is clear that the resulting voltage offsets are significant and that a significant measurement error that increases to approximately $6K$ over an $8\,hour$ measurement period will be incurred. Replacing the sensor element or applying voltage compensation is therefore necessary in this case. When $R_{f1} = R_{f2} = 1G\Omega\ (nominal)$ the steady state drift voltage is limited to $55mV$. At typical experimental measurement times of less than $3\,minutes$, the magnitude of the drift voltage is insignificant at $(8.23 - 2.57)mV \approx 6mV$ and therefore in this case bias voltage compensation is not required.

6.4.5 Voltage drift compensation

Under normal operating conditions such that $R_p = 90G\Omega$ for the PZT-5H sensor patch, voltage compensation using R_{pot-1} and R_{pot-2} serves the purpose of allowing compensation for the voltage divider resistor tolerances to ensure that the bias voltages at the outputs of OA1 and OA2 are precisely equal to $V_{cc}/2$. However, under the circumstances of a reduced R_p described in the sections above, it can also be used to simultaneously negate voltage drift by correcting for the input offset voltages and the effects of other component tolerances if necessary. Defining the fractions of R_{pot-1} and R_{pot-2} between the non-inverting inputs of OA1, OA2 and R_{d1l-1}, R_{d1l-2} respectively required to achieve voltage compensation such that V_{OA1-os} and $V_{OA2-os} = V_{cc}/2$ as $a_c R_{pot-1}$ and $b_c R_{pot-2}$ respectively, then a_c, b_c and the corresponding a_c' and b_c' are given by Equation 6.65 to Equation 6.68 respectively, where R_{d1u} and R_{d1l} refer to the upper and lower voltage divider resistors shown in Figure 6.1 respectively.

$$a_c = \frac{1}{2} + \frac{(R_{d1u-1} - R_{d1l-1})}{2R_{pot-1}} + \frac{(R_{pot-1} + R_{d1u-1} + R_{d1l-1})}{2R_{pot-1}} \left(\frac{V_{cc} - 2\hat{A}_{v1} V_{os1}}{\hat{A}_{v1} V_{cc}} \right) \tag{6.65}$$

$$b_c = \frac{1}{2} + \frac{(R_{d1u-2} - R_{d1l-2})}{2R_{pot-2}} + \frac{(R_{pot-2} + R_{d1u-2} + R_{d1l-2})}{2R_{pot-2}} \left(\frac{V_{cc} - 2\hat{A}_{v2} V_{os2}}{\hat{A}_{v2} V_{cc}} \right) \tag{6.66}$$

$$a_c' = \frac{1}{2} + \frac{1}{2\hat{A}_{v1}} - \frac{V_{os1}}{V_{cc}} \tag{6.67}$$

$$b_c' = \frac{1}{2} + \frac{1}{2\hat{A}_{v2}} - \frac{V_{os2}}{V_{cc}} \tag{6.68}$$

If $V_{cc} \ll \hat{A}_{v1} V_{os1}$ and $V_{cc} \ll \hat{A}_{v2} V_{os2}$ are true such that the assumptions $\hat{A}_{v1} \to \infty$ and $\hat{A}_{v2} \to \infty$ are valid, then Equation 6.65 to Equation 6.68 can be written as Equation 6.69 to Equation 6.72 respectively.

$$a_c = \frac{1}{2} + \frac{(R_{d1u-1} - R_{d1l-1})}{2R_{pot-1}} - \frac{(R_{pot-1} + R_{d1u-1} + R_{d1l-1}) V_{os1}}{V_{cc} R_{pot-1}} \tag{6.69}$$

$$b_c = \frac{1}{2} + \frac{(R_{d1u-2} - R_{d1l-2})}{2R_{pot-2}} - \frac{(R_{pot-2} + R_{d1u-2} + R_{d1l-2}) V_{os2}}{V_{cc} R_{pot-2}} \tag{6.70}$$

$$a_c' = \frac{1}{2} - \frac{V_{os1}}{V_{cc}} \tag{6.71}$$

$$b_c' = \frac{1}{2} - \frac{V_{os2}}{V_{cc}} \tag{6.72}$$

It can be seen that Equation 6.69 to Equation 6.72 are independent of R_p, R_{f1} and R_{f2} which is a direct result of the required voltage compensation reducing the current flowing through R_p, R_{f1} and R_{f2} to zero. It is however neither necessary nor practical to directly measure the open loop gains, input offset voltages, potentiometer resistances, and voltage divider resistances required to determine a_c and b_c.

The practical procedure employed allows the offset drift voltages to be significantly reduced where required. This method involves first adjusting both potentiometers R_{pot-1} and R_{pot-2} to the central stop such that $a = b = 0.5$ and removing the feedback capacitors C_{f1} and C_{f2} to exclude drift and observe the steady state output voltage offset directly. Measuring the voltages at the inverting outputs of OA1 and OA2 using an oscilloscope, the potentiometer R_{pot-1} is then adjusted until the oscilloscope measures precisely $V_{cc}/2$ at the output of OA1. This is then repeated for R_{pot-2} until the oscilloscope measures precisely $V_{cc}/2$ at the output of OA2. However, since the voltage at the output of OA1 is now changed, this procedure is repeated for several iterations until the output voltages at OA1 and OA2 are equal to $V_{cc}/2$. At the end of this process, both the outputs and voltages at the non-inverting inputs of OA1 and OA2 are equal to $V_{cc}/2$ and the current through the feedback resistors R_{f1} and R_{f2} must therefore be zero. The currents through R_s and the sensor are therefore also zero. The effect of voltage drift caused by component manufacturing tolerances and the input offset voltages is therefore significantly reduced.

6.5 Sensor and signal conditioning noise

6.5.1 Initial considerations

The noise due to Johnson, Shot, and $1/f$ noise sources produced by the resistors and semiconductor op-amps used in the charge amplifier designs result in an

output noise that limits the maximum signal resolution possible at the amplifier output. It is therefore important to estimate the total output mean squared noise power to ensure the SNR (signal to noise ratio) is sufficiently high to ensure sufficient signal resolution. This problem was investigated by developing a noise model of the unipolar amplifier shown in the schematic of Figure 6.1 to estimate the best achievable SNR at the amplifier output for a sensitivity of approximately $0.15\,V/K$ and a $1K$ temperature change. Finally, the minimum temperature that can be measured in the presence of the RMS noise, and in the presence of the ADC (analogue to digital converter) quantisation noise are considered in Section 6.5.5.

6.5.2 Theoretical considerations and methodology

All noise sources, Johnson noise, $1/f$ noise and Shot noise are assumed to be Gaussian random variables with the Johnson noise in external resistive components being modelled using either Thevenin or Norton equivalent circuits. The Thevenin equivalent is modelled as a noiseless resistor R in series with a mean squared noise voltage denoted by $\overline{|v_n|^2}$ where v_n is the instantaneous noise voltage and the Norton equivalent is modelled as a noiseless resistor in parallel with a mean squared noise current $\overline{|\imath_n|^2} = \overline{|v_n|^2}/R^2$. The mean squared noise voltage is also called the mean noise power and is defined as the power dissipated across a 1Ω resistor.

The two-sided PSD (power spectral density) of Johnson noise is given by $S_{Jv}(\omega) = 2RK\theta$ in voltage source form or $S_{Ji}(\omega) = 2K\theta/R$ in current source form where R is the resistance, K is Boltzmann's constant and θ is the absolute temperature. Shot noise, which is prevalent in semiconductor devices, is caused by quantum effects in a small electrical current that cause current fluctuations. Shot noise is modelled as a current source, and has a two-sided PSD given by $S_s(\omega) = I_b q_e$ where I_b is a semiconductor input bias current and q_e is the charge on an electron. For the case of an op-amp, there are bias currents at both inverting and non-inverting inputs. Finally, the $1/f$ noise, which is modelled as a voltage source, has one-sided PSD given by $S_{1/f}(\omega) = A_{1/f}/\omega$ where $A_{1/f}$ is a constant that is device specific.

While the following analysis considers resistor Johnson noise, the mathematical results are general and are equally valid for application to shot noise and $1/f$ noise sources where the approximation of Gaussian noise (AWGN) is valid. Assuming that Johnson noise is approximated by AWGN, then the power spectral density (PSD) denoted by $S_{Jv}(\omega)$ due to Johnson noise generated by a resistor, R is given by $S_{Jv}(\omega) = 2RK\theta\ (W/Hz)$ which can be considered flat over the entire frequency spectrum, where K is Boltzmann's constant and θ is the absolute temperature. The equivalent mean squared current PSD is given by $S_{Ji}(\omega) = 2K\theta/R\ \ (W/Hz)$. For an infinite bandwidth, the associated autocorrelation function is the inverse Fourier transform of $S_{Jv}(\omega)$ given by $A_{Jv}(\tau) = 2RK\theta\delta(\tau)$ where $\delta(\tau)$ is the Dirac delta function and τ is the autocorrelation delay. The associated signal power is given by the autocorrelation function at $\tau = 0$ and, as expected for an unrealisable infinite spectrum has infinite power and an autocorrelation of zero everywhere except at $\tau = 0$. The actual bandwidth of Johnson noise, $B(Hz)$ is given by $B = K\theta\pi^2/6h$ [108] where h is Planck's constant and that at room temperature $(\theta = 300K)$ yields $B = 10.28THz$.

Where the noise has a stated bandwidth and the cut-off is assumed to be sharp, then the PSD is given by $S_{Jv}(\omega) = 2RK\theta\big(U(\omega + 2\pi B) - U(\omega - 2\pi B)\big)$ where U is the Heaviside step function. The autocorrelation function can be found by taking the inverse Fourier transform of the PSD as shown by Equation 6.73 for general signals where $A(\tau)$ is the autocorrelation, T is the averaging period, $v(t)$ is the instantaneous voltage, $S(\omega)$ is the power spectral density and the superscript $*$ denotes complex conjugation. In the special case of periodic signals, T is the period of the signal. The autocorrelation function of the bandlimited noise source is therefore given by $A_{Jv}(\tau) = \mathcal{F}^{-1}\{S_{Jv}(\omega)\} = 4RK\theta Bsinc(2\pi B\tau)$ where $\mathcal{F}^{-1}$ indicates the inverse Fourier transform. Setting $\tau = 0$, the associated mean noise power is given by $P_n = A_{Jv}(0) = \overline{|v_n|^2} = 4RK\theta B$ which can also be written as $2BS_{Jv}(\omega)$. The RMS (root mean squared) noise voltage is therefore given by $2\sqrt{RK\theta B}$, or in terms of RMS noise voltage per unit $\sqrt{Hz}$ as $2\sqrt{RK\theta}$. The calculation of $\overline{|v_n|^2}$ above is equivalent to integrating $S_{Jv}(\omega)$ using Parseval's theorem for power signals, which is given by Equation 6.74.

$$A(\tau)= \lim_{T\to\infty} \frac{1}{T}\int_{-T/2}^{+T/2} v(t)v^*(t-\tau)dt = \frac{1}{2\pi}\int_{-\infty}^{+\infty} S(\omega)e^{j\omega\tau}d\,\omega \tag{6.73}$$

$$\overline{|v(t)|^2} = A(0) = \lim_{T\to\infty} \frac{1}{T}\int_{-T/2}^{+T/2}|v(t)|^2dt = \frac{1}{2\pi}\int_{-\infty}^{+\infty} S(\omega)d\,\omega \tag{6.74}$$

The noise output PSD, denoted by $S_O(\omega)$ from an LTI (linear time invariant) system denoted by $H(\omega)$ to an input noise $S(\omega)$ is given by $S_O(\omega) = |H(\omega)|^2 S(\omega)$. By substitution into Equation 6.74, the mean squared voltage at the output of the LTI system $\overline{|v_o|^2}$ may therefore be found using Equation 6.75.

$$\overline{|v_o|^2} = \frac{1}{2\pi}\int_{-\infty}^{+\infty}|H(\omega)|^2 S(\omega)d\,\omega \tag{6.75}$$

With knowledge of the PSD for each of the noise sources, Equation 6.75 is used in the following analysis to determine an estimate for the mean squared voltage for each of the Johnson, $1/f$ and shot noise sources and ultimately to provide an estimate for the signal to noise ratio at the amplifier output. The CMOS op-amps produce all three types of noise that are specified as input referred voltage and current noise PSD values. The input referred voltage noise contains both $1/f$ and Johnson noise while the input referred current noise describes shot noise only. All resistances are assumed to produce Johnson noise only, and all Johnson and shot noise sources are assumed to be uncorrelated AWGN noise with an infinite flat bandwidth and zero mean. The $1/f$ noise (or pink noise) sources are also assumed to be uncorrelated and Gaussian but with a minimum frequency dependent on the observation time. This lower limit is necessary since the operation of integrating over ω with limits that include $\omega = 0$ will yield an erroneous divergent result of infinite noise power, and is justified by noting that true DC is unattainable since an infinite observation period would be required to measure the mean squared noise voltage down to $\omega = 0$. An industry standard rule-of-thumb for the minimum noise frequency is taken as the reciprocal of the period of observation of the noise signal which is normally taken as between $10s$ and $1000s$. Taking the period of observation equal to the required continuous period of sensor operation as $8\,hours$, the rule of thumb minimum noise frequency limit can be stated as $f_{min} = 1/28800\ Hz$. The low frequency $1/f$ noise may be observed as a small signal drift over time at the sensor output if the observation period is long enough. In the

following noise analysis, the upper limit of frequency for the Johnson, shot noise and $1/f$ noise sources is taken as infinite. This choice simplifies the calculation of the output mean noise power and is justified by noting that the actual noise bandwidths are very much greater than would be passed by the $H(\omega)$ transfer functions presented to the noise sources that is, in any case, ultimately limited by the closed loop $-3dB$ cut-off frequency dictated by the op-amps.

Assuming an infinite noise bandwidth also gives a worst possible case scenario, it being the case that the actual noise will generally be a negligible amount lower than that estimated. The form of $|H(\omega)|^2$ is dependent on the position of each resistance and op-amp input in the amplifier circuit and is found for each noise source in turn using the principle of superposition by grounding all inputs and setting all other noise sources to zero such that all other resistors and opamps are considered noiseless.

The effect of noise attenuation due to the closed loop $-3dB$ cut-off frequency of the op-amps is taken into account by modelling the open loop gain $A_v(j\omega)$ with a single pole at the open loop $-3dB$ cut-off frequency ω_c such that $A_v(j\omega) = \hat{A}_v/(1 + j\omega/\omega_c)$ where $\hat{A}_v$ is the DC open loop gain specified in the LMC6081 op-amp data sheet. Furthermore, since all noise sources can reasonably be considered as independent and therefore uncorrelated to each other, the total mean squared noise voltage at the output is obtained simply by adding the individual mean squared noise contributions from each source together. The signal to noise ratio (SNR) is then calculated from $SNR = 10log\left(0.015^2/\overline{|v_o(t)|^2}\right)$ where $\overline{|v_o(t)|^2}$ is the total mean squared noise voltage at the output due to all noise sources.

The following noise analysis refers to the unipolar charge amplifier schematic shown in Figure 6.1 where the PZT piezoelectric element is modelled as a resistance R_p in parallel with a capacitance C_p as discussed in Section 4.7 and as shown on Figure 6.1 inset bottom left.

6.5.3 Resistor Johnson noise sources

Johnson noise due to voltage divider resistors R_{d1}

The frequency-domain Norton equivalent noise currents produced by each of the supply voltage divider resistors R_{d1} is denoted mathematically by $\mathcal{F}\{i_{R_{d1}}(t)\} = i_{R_{d1}}(j\omega)$ where $i_{R_{d1}}(t)$ is the instantaneous noise current, and the associated PSD of the mean squared noise current is given by $S_{R_{d1}}(\omega) = 2K\theta/R_{d1}$. The Fourier transform $\mathcal{F}\{i_{R_{d1}}(t)\}$ is not defined for stochastic noise processes and is introduced for mathematical purposes only.

Modelling the frequency dependent gain of OA1 and OA2 as $A_v(j\omega) = \hat{A}_v/(1 + j\omega/\omega_c)$, then the transfer function $\big(V_{OA1}(j\omega) - V_{OA2}(j\omega)\big)/i_{R_{d1}}(j\omega)$ is given by Equation 6.76 where C_n is a noise reduction capacitance, $GBP = \hat{A}_v\omega_c$ is the gain bandwidth product of the op-amps OA1 to OA3, which typically for the LMC6081 is $GBP = 2.6\pi \times 10^6\ rads^{-1}$ $(1.3MHz)$, and for the amplifier design, $C_p \ll C_f$, $1/R_pC_p \ll GBP$, $1/R_fC_f \ll GBP$, $R_s \ll R_p$ and $R_s \ll R_f$; and $\epsilon = \sqrt{\big(GBP/2\big(1 + 2R_sC_pGBP\big)\big)^2 - GBP\big(\hat{A}_vR_p + 2R_f\big)/\big(\big(1 + 2R_sC_pGBP\big)\hat{A}_vR_pR_fC_f\big)}$.

$$\frac{\big(V_{OA1}(j\omega) - V_{OA2}(j\omega)\big)}{i_{R_{d1}}(j\omega)} = \frac{GBP\left(j\omega + \frac{2R_f + R_p}{R_fR_pC_f}\right)}{C_n(j\omega + 2/C_nR_{d1})\big(1 + 2R_sC_pGBP\big)\left(j\omega + \frac{GBP}{2\big(1 + 2R_sC_pGBP\big)} - \epsilon\right)\left(j\omega + \frac{GBP}{2\big(1 + 2R_sC_pGBP\big)} + \epsilon\right)} \tag{6.76}$$

The final difference amplifier stage Fourier transfer function is given by Equation 6.77. Setting $R_{d2} = 2R_1R_3/R_2$, the closed loop gain common mode output voltage is negated and the output voltage, V_{out} is proportional to $\big(V_{OA1}(j\omega) - V_{OA1}(j\omega)\big)$ as required for sensor operation.

$$V_{out}(j\omega) = \frac{GBP \times \left(\left(\frac{R_{d2}}{2R_1 + R_{d2}}\right)V_{OA2}(j\omega) - \left(\frac{R_3}{R_2 + R_3}\right)V_{OA1}(j\omega)\right)}{j\omega + GBP\left(\frac{R_2}{R_2 + R_3}\right)} \tag{6.77}$$

Setting $R_{d2} = 2R_1R_3/R_2$, the output noise PSD at V_{out} due to the Johnson noise current $i_{R_{d1}}(t)$ is therefore given by Equation 6.78.

$$S_{OR_{d1}}(\omega) \cong$$

$$\frac{\frac{2K\theta}{R_{d1}}(GBP)^4\left(\frac{R_3}{R_2+R_3}\right)^2\left(\omega^2+\left(\frac{2R_f+R_p}{R_fR_pC_f}\right)^2\right)}{C_n^2\left(1+2R_sC_pGBP\right)^2(\omega^2+(2/C_nR_{d1})^2)\left(\omega^2+\left(\frac{R_2GBP}{R_2+R_3}\right)^2\right)\left(\omega^2+\left(\frac{GBP}{2\left(1+2R_sC_pGBP\right)}-\epsilon\right)^2\right)\left(\omega^2+\left(\frac{GBP}{2\left(1+2R_sC_pGBP\right)}+\epsilon\right)^2\right)}$$

(6.78)

The pole of Equation 6.78 associated with the difference amplifier stage occurs at a frequency of approximately $1.8\pi \times 10^6\, rads^{-1}$ where $R_2/(R_2+R_3) \approx 0.69$ for a normal operating gain of 0.5, while the pole associated with $C_n = 0.47uF$ and $R_{d1}/2 = 110.5k\Omega$ occurs at a much lower frequency of $19.25\, rads^{-1}$. The influence of the pole associated with the difference amplifier stage can therefore be considered negligible since the first order pole formed by C_n and R_{d1} attenuates the noise at a cut-off frequency very much lower than the GBP of the op-amps. Equation 6.78 for $S_{OR_{d1}}(\omega)$ can therefore be reduced to Equation 6.79 without significant error.

$$S_{OR_{d1}}(\omega) \cong$$

$$\frac{2K\theta(GBP)^2R_3^2\left(\omega^2+\left(\frac{2R_f+R_p}{R_fR_pC_f}\right)^2\right)}{R_{d1}R_2^2C_n^2\left(1+2R_sC_pGBP\right)^2(\omega^2+(2/C_nR_{d1})^2)\left(\omega^2+\left(\frac{GBP}{2\left(1+2R_sC_pGBP\right)}-\epsilon\right)^2\right)\left(\omega^2+\left(\frac{GBP}{2\left(1+2R_sC_pGBP\right)}+\epsilon\right)^2\right)}$$

(6.79)

Integrating Equation 6.79, the mean square voltage noise at V_{out} due to the input referred Johnson noise voltage produced by one voltage divider resistance R_{d1} is given by Equation 6.80, which is valid for $GBP \gg (2/C_nR_{d1})$.

$$\overline{\left|v_{R_{d1}}(t)\right|^2}_{R_{d2}=2R_1R_3/R_2} =$$

$$\frac{1}{2\pi}\int_{-\infty}^{\infty}\frac{\frac{2K\theta}{R_{d1}}(GBP)^2R_3^2\left(\omega^2+\left(\frac{2R_f+R_p}{R_fR_pC_f}\right)^2\right)}{R_2^2C_n^2\left(1+2R_sC_pGBP\right)^2(\omega^2+(2/C_nR_{d1})^2)\left(\omega^2+\left(\frac{GBP}{2\left(1+2R_sC_pGBP\right)}-\epsilon\right)^2\right)\left(\omega^2+\left(\frac{GBP}{2\left(1+2R_sC_pGBP\right)}+\epsilon\right)^2\right)}d\omega$$

$$\cong \frac{K\theta R_3^2}{2C_nR_2^2} + \frac{K\theta\hat{A}_v\left(2R_f+R_p\right)^2R_{d1}R_3^2}{4R_pR_fC_f\left(\hat{A}_vR_p+2R_f\right)R_2^2} \qquad (6.80)$$

From Equation 6.80 it can be seen that $\overline{\left|v_{R_{d1}}(t)\right|^2}$ is insensitive to R_s under the conditions $R_s \ll R_p$ and $R_s \ll R_f$ stated above. Noting that the noise sources associated with all four R_{d1} resistances associated with the two voltage dividers are uncorrelated with respect to each other, the total mean squared noise voltage at V_{out} due to all four R_{d1} resistors is therefore given by Equation 6.81.

$$\overline{\left|2v_{R_{d1}}(t)\right|^2}_{R_{d2}=2R_1R_3/R_2} \cong \frac{2K\theta R_3^2}{C_n R_2^2} + \frac{K\theta \hat{A}_v\left(2R_f+R_p\right)^2 R_{d1}R_3^2}{R_pR_fC_f\left(\hat{A}_vR_p+2R_f\right)R_2^2} \tag{6.81}$$

Johnson noise due to ESD resistors R_s

The output noise PSD due to one resistor R_s is given by Equation 6.82, where the analysis has been simplified by noting that for the amplifier design, $C_p \ll C_f$, $1/C_fR_f \ll GBP$, $R_s \ll R_p$ and $R_s \ll R_f$ and where $\epsilon = \sqrt{\left(GBP/2\left(1+2R_sC_pGBP\right)\right)^2 - GBP\left(\hat{A}_vR_p+2R_f\right)/\left(\left(1+2R_sC_pGBP\right)\hat{A}_vR_pR_fC_f\right)}$.

$$S_{OR_s}(\omega) = \frac{K\theta R_sC_p^2(GBP)^4\left(\omega^2+\left(\frac{1}{C_pR_p}\right)^2\right)\left(\frac{R_{d2}}{2R_1+R_{d2}}+\frac{R_3}{R_2+R_3}\right)^2}{2C_f^2\left(1+2R_sC_pGBP\right)^2\left(\omega^2+\left(\frac{R_2GBP}{R_2+R_3}\right)^2\right)\left(\omega^2+\left(\frac{GBP}{2\left(1+2R_sC_pGBP\right)}-\epsilon\right)^2\right)\left(\omega^2+\left(\frac{GBP}{2\left(1+2R_sC_pGBP\right)}+\epsilon\right)^2\right)} \tag{6.82}$$

Noting that the noise from each of the R_s resistors is uncorrelated, setting $R_{d2} = 2R_1R_3/R_2$ and integrating Equation 6.82 over infinite limits, yields the mean square voltage noise at V_{out} associated with both R_s resistors given by Equation 6.83.

$$\overline{\left|\sqrt{2}v_{OR_s}(t)\right|^2}_{R_{d2}=2R_1R_3/R_2} = \frac{2K\theta C_p^2R_sR_3^2GBP}{R_2C_f^2\left(2R_2\left(1+R_sC_pGBP\right)+R_3\right)} + \frac{2K\theta \hat{A}_vR_fR_sR_3^2}{R_p\left(\hat{A}_vR_p+2R_f\right)C_fR_2^2} \tag{6.83}$$

Johnson noise due to dielectric resistance R_p

The output noise PSD due to R_p is given by Equation 6.84, where in common with R_s the analysis has been simplified by noting that for the amplifier design, $C_p \ll C_f$, $1/C_fR_f \ll GBP$, $R_s \ll R_p$ and $R_s \ll R_f$ and where

$$\epsilon = \sqrt{\left(GBP/2\left(1+2R_sC_pGBP\right)\right)^2 - GBP\left(\hat{A}_vR_p+2R_f\right)/\left(\left(1+2R_sC_pGBP\right)\hat{A}_vR_pR_fC_f\right)}$$

and the open loop DC gain $\hat{A}_v$ of both OA1 and OA2 are assumed to be identical.

$$S_{OR_p}(\omega) = \frac{K\theta(GBP)^4\left(\frac{R_{d2}}{2R_1+R_{d2}}+\frac{R_3}{R_2+R_3}\right)^2}{2C_f^2\left(1+2R_sC_pGBP\right)^2\left(\omega^2+\left(\frac{R_2GBP}{R_2+R_3}\right)^2\right)\left(\omega^2+\left(\frac{GBP}{2\left(1+2R_sC_pGBP\right)}-\epsilon\right)^2\right)\left(\omega^2+\left(\frac{GBP}{2\left(1+2R_sC_pGBP\right)}+\epsilon\right)^2\right)} \quad (6.84)$$

Setting $R_{d2} = 2R_1R_3/R_2$ and Integrating Equation 6.84 over infinite limits yields the mean square Johnson voltage noise at V_{out} associated with R_p given by Equation 6.85. The mean square voltage noise at V_{out} associated with R_p is insensitive to R_s for $R_s \ll R_p$ and $R_s \ll R_f$.

$$\overline{\left|v_{OR_p}(t)\right|^2}_{R_{d2}=2R_1R_3/R_2} \cong \frac{K\theta\hat{A}_vR_fR_3^2}{C_f\left(\hat{A}_vR_p+2R_f\right)R_2^2} \quad (6.85)$$

It should be noted that R_p which is the insulation resistance of the PZT-5H temperature sensor is inversely proportional to temperature and therefore the mean square Johnson voltage noise at V_{out} is increased not only by a rise in temperature but also a reduction in R_p. The DC value of R_p is approximately $90G\Omega$ at 25℃ and represents the worst-case scenario and it is therefore this value that is used in the calculation of the Johnson noise.

Johnson noise due to feedback resistances R_f

The output noise PSD due to either the OA1 or OA2 feedback resistor R_f is given by Equation 6.86 where $R_{d2} = 2R_1R_3/R_2$ and for the amplifier design, $C_p \ll C_f$, $1/C_fR_f \ll GBP$, $R_s \ll R_p$ and $R_s \ll R_f$, and as before $\epsilon = \sqrt{\left(GBP/2\left(1+2R_sC_pGBP\right)\right)^2 - GBP\left(\hat{A}_vR_p+2R_f\right)/\left(\left(1+2R_sC_pGBP\right)\hat{A}_vR_pR_fC_f\right)}$.

$$S_{OR_f}(\omega) = \frac{8R_S^2C_p^2K\theta(GBP)^4\left(\omega^2+\left(\frac{1}{2R_SC_p}\right)^2\right)\left(\frac{R_3}{R_2+R_3}\right)^2}{R_fC_f^2\left(1+2R_SC_pGBP\right)^2\left(\omega^2+\left(\frac{R_2GBP}{R_2+R_3}\right)^2\right)\left(\omega^2+\left(\frac{GBP}{2\left(1+2R_SC_pGBP\right)}-\epsilon\right)^2\right)\left(\omega^2+\left(\frac{GBP}{2\left(1+2R_SC_pGBP\right)}+\epsilon\right)^2\right)} \tag{6.86}$$

Integrating Equation 6.86, the mean square voltage noise at V_{out} due to either the OA1 or OA2 feedback resistor R_f is given by Equation 6.87.

$$\overline{\left|v_{OR_f}(t)\right|^2}_{R_{d2}=2R_1R_3/R_2} = \frac{4K\theta R_S^2C_p^2R_3^2GBP}{C_f^2R_fR_2\left(2R_2(1+R_SC_pGBP)+R_3\right)} + \frac{K\theta\hat{A}_vR_pR_3^2}{C_f\left(\hat{A}_vR_p+2R_f\right)R_2^2} \tag{6.87}$$

Noting that the noise sources associated with the R_f resistances are uncorrelated with respect to each other, the total mean squared noise voltage at V_{out} due to both R_f resistances is therefore given by Equation 6.88.

$$\overline{\left|\sqrt{2}v_{OR_f}(t)\right|^2}_{R_{d2}=2R_1R_3/R_2} = \frac{8K\theta R_S^2C_p^2R_3^2GBP}{C_f^2R_fR_2\left(2R_2(1+R_SC_pGBP)+R_3\right)} + \frac{2K\theta\hat{A}_vR_pR_3^2}{C_f\left(\hat{A}_vR_p+2R_f\right)R_2^2} \tag{6.88}$$

Johnson noise due to difference stage resistance R_1

The output noise PSD due to R_1 is given by Equation 6.89, where the frequency dependent gain of OA3 is modelled as $A_v(j\omega) = \hat{A}_v/(1+j\omega/\omega_c)$ and $GBP = \omega_c\hat{A}_v$.

$$S_{OR_1}(\omega) = \frac{2K\theta R_1R_{d2}^2(GBP)^2}{(2R_1+R_{d2})^2\left(\omega^2+\left(\frac{R_2GBP}{R_2+R_3}\right)^2\right)} \tag{6.89}$$

Integrating Equation 6.89 yields the mean square voltage noise at V_{out} due to R_1 given by Equation 6.90.

$$\overline{\left|v_{OR_1}(t)\right|^2} \cong \frac{K\theta R_1R_{d2}^2(R_2+R_3)GBP}{R_2(2R_1+R_{d2})^2} \tag{6.90}$$

Setting $R_{d2} = 2R_1R_3/R_2$ yields Equation 6.91.

$$\overline{\left|v_{OR_1}(t)\right|^2}_{R_{d2}=2R_1R_3/R_2} = \frac{K\theta R_1R_3^2GBP}{R_2(R_2+R_3)} \tag{6.91}$$

Johnson noise due to difference stage resistance R_2

Equation 6.92 gives the output noise PSD due to R_2.

$$S_{OR_2}(\omega) = \frac{2K\theta R_2 R_3^2 (GBP)^2}{(R_2+R_3)^2\left(\omega^2+\left(\frac{R_2 GBP}{R_2+R_3}\right)^2\right)} \tag{6.92}$$

Integrating Equation 6.92 yields the mean square voltage noise at V_{out} due to R_2 given by Equation 6.93.

$$\overline{\left|v_{OR_2}(t)\right|^2} \cong \frac{K\theta R_3^2 GBP}{R_2+R_3} \tag{6.93}$$

Johnson noise due to difference stage resistance R_3

Equation 6.94 gives the output noise PSD due to R_3.

$$S_{OR_3}(\omega) = \frac{2K\theta R_3 R_2^2 (GBP)^2}{(R_2+R_3)^2\left(\omega^2+\left(\frac{R_2 GBP}{R_2+R_3}\right)^2\right)} \tag{6.94}$$

Integrating Equation 6.94 yields the mean square voltage noise at V_{out} due to R_3 given by Equation 6.95.

$$\overline{\left|v_{OR_3}(t)\right|^2} \cong \frac{K\theta R_2 R_3 GBP}{R_2+R_3} \tag{6.95}$$

Johnson noise due to difference stage resistances R_{d2}

Equation 6.96 gives the output noise PSD due to one R_{d2}.

$$S_{OR_{d2}}(\omega) = \frac{2K\theta R_{d2} R_1^2 (GBP)^2}{(2R_1+R_{d2})^2\left(\omega^2+\left(\frac{R_2 GBP}{R_2+R_3}\right)^2\right)} \tag{6.96}$$

Integrating Equation 6.96 yields the mean square voltage noise at V_{out} due to R_2 given by Equation 6.97.

$$\overline{\left|v_{OR_{d2}}(t)\right|^2} \cong \frac{K\theta R_{d2} R_1^2 (R_2+R_3) GBP}{R_2(2R_1+R_{d2})^2} \tag{6.97}$$

Equation 6.98 gives the mean square voltage noise at V_{out} due to the two uncorrelated R_{d2} voltage divider resistances.

$$\overline{\left|\sqrt{2}v_{OR_{d2}}(t)\right|^2} \cong \frac{2K\theta R_{d2}R_1^2(R_2+R_3)GBP}{R_2(2R_1+R_{d2})^2} \tag{6.98}$$

Setting $R_{d2} = 2R_1R_3/R_2$ yields Equation 6.99.

$$\overline{\left|\sqrt{2}v_{OR_{d2}}(t)\right|^2}_{R_{d2}=2R_1R_3/R_2} \cong \frac{K\theta R_1R_3GBP}{(R_2+R_3)} \tag{6.99}$$

6.5.4 Op-amps input referred noise sources

The op-amps also contribute to the total noise, which is modelled by an input referred voltage noise in series at the non-inverting input and two input-referred current noise sources between ground and both the inverting and non-inverting inputs. The LMC 6081 data sheet noise specification is given as a one sided PSD in units of RMS voltage and current per $\sqrt{Hz}$ respectively. The input referred voltage noise figure includes both AWGN Johnson noise and Gaussian $1/f$ noise, while the input referred current noise which is due to the input bias and power supply currents is modelled as AWGN shot noise. The input referred voltage noise specification for the LMC 6081 is shown in Figure 6.4, which has been adapted from the published figure in the Texas instruments LMC 6081 data sheet.

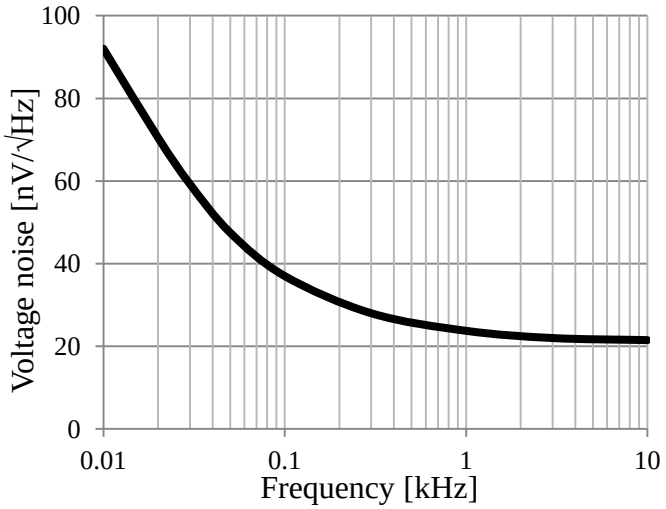

Figure 6.4 LMC 6081 op-amp input referred noise voltage

The input referred noise current is generally very low for CMOS amplifiers such as the LMC6081 and it is common practice to ignore it. However, in this application, the inverting input referred noise currents into OA1 and OA2 cannot be easily dismissed since they flow through the high impedance feedback network of the charge amplifier stages and must therefore be considered.

The published typical input referred noise current for the LMC6081 is $0.2fA/\sqrt{Hz}$ and therefore Equation 6.100 gives the two-sided input referred current noise PSD for the LMC6081, where I_b is the input bias current specified, and q_e is the charge on one electron.

$$S_s(\omega) = I_b q_e = 2 \times 10^{-32}(A^2/Hz) \tag{6.100}$$

The published typical input referred noise voltage for the LMC6081 is $22nV/\sqrt{Hz}$ @$1kHz$, which is made up of both Johnson noise and $1/f$ noise. The one-sided sum of the PSD's due to both noise types is therefore given by $S_{rv}(\omega) = S_{1/f}(\omega) + S_{Jv}(\omega)$ where $S_{rv}(\omega)$ is the PSD of the total input referred voltage noise, $S_{1/f}(\omega)$ is the PSD of the $1/f$ noise component and $S_{Jv}(\omega)$ is the PSD of the Johnson noise component. By squaring the published input referred noise voltage $\left(V/\sqrt{Hz}\right)$ vs frequency curve of the LMC6081 and using the published $1kHz$ specification given above yields an estimate for $S_{rv}(\omega)$ given by Equation 6.101, which assumes that the input referred noise voltage Johnson and $1/f$ noise components are uncorrelated.

$$S_{rv}(\omega) = S_{1/f}(\omega) + S_{Jv}(\omega) \cong \frac{16\pi \times 10^{-14}}{\omega} + 4.2 \times 10^{-16}\ (V^2/Hz) \tag{6.101}$$

The PSDs of the total input referred voltage noise and input referred current components, $S_{rv}(\omega)$ and $S_s(\omega)$ respectively are estimated from a one-sided spectra where only positive frequencies are considered and therefore when properly integrating over positive and negative frequency limits, both $S_{Jv}(\omega)$ and $S_s(\omega)$ must be halved. It is however convenient to evaluate $S_{1/f}(\omega)$ over positive frequencies only since a minimum frequency limit is specified and it is therefore the one-sided spectrum numerator constant that is used. As described above, the rule of thumb lower frequency limit is the reciprocal of the period of observation which is taken as

the required continuous period of sensor operation, $t_{op} = 8\,hours$, yielding a minimum noise frequency limit of $\omega_{min} = \pi/14400\ rads^{-1}$.

Input referred voltage $1/f$ noise due to OA1 and OA2

Both the OA1 and OA2 noise sources are assumed to be uncorrelated to each other and to produce the same noise amplitude. The input referred voltage noise from one op-amp gives rise to a noise current through the R_s resistances, the PZT sensor element and feedback networks of both charge amplifier stages which produces an associated voltage response at the outputs of OA1 and OA2 denoted by $V_{OA1\,1/f}$ and $V_{OA2\,1/f}$.

Applying $\left(V_{OA1\,1/f} - V_{OA2\,1/f}\right)$ to the difference amplifier stage and letting $R_{d2} = 2R_1R_3/R_2$ yields the output noise PSD due to the input referred $1/f$ voltage noise, $V_{1/f}$ from one op-amp which is given by Equation 6.102 where for the amplifier design, $C_p \ll C_f$, $1/R_fC_f \ll GBP$, $R_s \ll R_p$ and $R_s \ll R_f$, $\epsilon = \sqrt{\left(GBP/2\left(1 + 2R_sC_pGBP\right)\right)^2 - GBP\left(\hat{A}_vR_p + 2R_f\right)/\left(\left(1 + 2R_sC_pGBP\right)\hat{A}_vR_pR_fC_f\right)}$ and $\hat{A}_v$ is the open loop DC gain of the op-amps.

To ensure convergence and a valid result, the approximation $\left(\hat{A}_vR_p + 2R_f\right)/\hat{A}_vR_pR_fC_f \ll GBP$ cannot be applied to ϵ since to do so would introduce a pole at $\omega = 0$ leading to the divergence of Equation 6.102 when integrated.

$$S_{1/f}(\omega)_{OA1} = S_{1/f}(\omega)_{OA2} \cong \frac{16\pi\times10^{-14}(GBP)^4\left(\frac{R_3}{R_2+R_3}\right)^2\left(\omega^2+\left(\frac{2R_f+R_p}{R_fR_pC_f}\right)^2\right)}{\left(1+2R_sC_pGBP\right)^2\omega\left(\omega^2+\left(\frac{R_2GBP}{R_2+R_3}\right)^2\right)\left(\omega^2+\left(\frac{GBP}{2\left(1+2R_sC_pGBP\right)}-\epsilon\right)^2\right)\left(\omega^2+\left(\frac{GBP}{2\left(1+2R_sC_pGBP\right)}+\epsilon\right)^2\right)} \quad (6.102)$$

The influence of the pole associated with the difference amplifier stage can be considered negligible since the $1/f$ relationship has a much greater influence in attenuating the noise power than the GBP of OA3 and $S_{1/f}(\omega)$ can therefore be written as Equation 6.103.

$$S_{1/f}(\omega)_{OA1} = S_{1/f}(\omega)_{OA2} \cong$$

$$\frac{16\pi\times10^{-14}(GBP)^2\left(\omega^2+\left(\frac{2R_f+R_p}{R_fR_pC_f}\right)^2\right)R_3^2}{\left(1+2R_sC_pGBP\right)^2R_2^2\omega\left(\omega^2+\left(\frac{GBP}{2(1+2R_sC_pGBP)}-\epsilon\right)^2\right)\left(\omega^2+\left(\frac{GBP}{2(1+2R_sC_pGBP)}+\epsilon\right)^2\right)} \tag{6.103}$$

Integrating Equation 6.103 over $\omega_{min} = \pi/14400$ to ∞ yields the mean square voltage noise at V_{out} due to the $1/f$ noise produced by both OA1 and OA2, given by Equation 6.104 under the easily satisfied constraint that $GBP \gg \omega_{min}$.

$$\overline{\left|v_{out\ 1/f}(t)\right|^2}_{R_{d2}=2R_1R_3/R_2} \cong$$

$$\frac{1}{2\pi}\int_{\pi/14400}^{\infty}\frac{16\pi\times10^{-14}(GBP)^2\left(\omega^2+\left(\frac{2R_f+R_p}{R_fR_pC_f}\right)^2\right)R_3^2}{\left(1+2R_sC_pGBP\right)^2R_2^2\omega\left(\omega^2+\left(\frac{GBP}{2(1+2R_sC_pGBP)}-\epsilon\right)^2\right)\left(\omega^2+\left(\frac{GBP}{2(1+2R_sC_pGBP)}+\epsilon\right)^2\right)}d\omega$$

$$\cong \frac{4\times10^{-14}R_3^2}{R_2^2}ln\left(\left(\frac{14400GBP}{\pi(1+2R_sC_pGBP)}\right)^2+1\right) \cong \frac{8\times10^{-14}R_3^2}{R_2^2}ln\left(\frac{14400GBP}{\pi(1+2R_sC_pGBP)}\right) \tag{6.104}$$

Equation 6.105 gives the total mean square voltage noise at V_{out} due to the two uncorrelated $1/f$ noise sources of op-amps OA1 and OA2.

$$\overline{\left|\sqrt{2}v_{out\ 1/f}(t)\right|^2}_{R_{d2}=2R_1R_3/R_2} \cong \frac{16\times10^{-14}R_3^2}{R_2^2}ln\left(\frac{14400GBP}{\pi(1+2R_sC_pGBP)}\right) \tag{6.105}$$

Input referred voltage $1/f$ noise due to OA3

Equation 6.106 gives the output noise PSD due to the input referred $1/f$ noise voltage of OA3.

$$S_{1/f}(\omega)_{OA3} = \frac{16\pi\times10^{-14}(GBP)^2}{\omega\left(\omega^2+\left(\frac{R_2GBP}{R_2+R_3}\right)^2\right)} \tag{6.106}$$

Integrating Equation 6.106 yields the mean square voltage noise at V_{out} due to the $1/f$ noise produced by OA3 given by Equation 6.107 under the constraint $GBP \gg \omega_{min}$.

$$\overline{\left|v_{out\,1/f}(t)\right|^2}_{R_{d2}=2R_1R_3/R_2} = \frac{1}{2\pi}\int_{\pi/14400}^{\infty} \frac{16\pi\times10^{-14}(GBP)^2}{\omega\left(\omega^2+\left(\frac{R_2GBP}{R_2+R_3}\right)^2\right)}d\omega$$

$$\cong \frac{4\times10^{-14}(R_2+R_3)^2}{R_2^2} ln\left(\left(\frac{14400R_2GBP}{\pi(R_2+R_3)}\right)^2+1\right) \cong \frac{8\times10^{-14}(R_2+R_3)^2}{R_2^2} ln\left(\frac{14400R_2GBP}{\pi(R_2+R_3)}\right) \quad (6.107)$$

Input referred Johnson noise voltage due to OA1 and OA2

The output noise PSD at V_{out} due to the input referred Johnson noise voltage of OA1 and OA2 for $R_{d2} = 2R_1R_3/R_2$ is given by Equation 6.108 where for the amplifier design, $C_p \ll C_f$, $1/R_fC_f \ll GBP$, $R_s \ll R_p$ and $R_s \ll R_f$ and $\epsilon = \sqrt{\left(GBP/2\left(1+2R_sC_pGBP\right)\right)^2 - GBP\left(\hat{A}_vR_p+2R_f\right)/\left(\left(1+2R_sC_pGBP\right)\hat{A}_vR_pR_fC_f\right)}$

$$S_{jv}(\omega)_{OA1} = S_{jv}(\omega)_{OA2} \cong$$

$$\frac{2.1\times10^{-16}(GBP)^4\left(\frac{R_3}{R_2+R_3}\right)^2\left(\omega^2+\left(\frac{2R_f+R_p}{R_fR_pC_f}\right)^2\right)}{\left(1+2R_sC_pGBP\right)^2\left(\omega^2+\left(\frac{R_2GBP}{R_2+R_3}\right)^2\right)\left(\omega^2+\left(\frac{GBP}{2(1+2R_sC_pGBP)}-\epsilon\right)^2\right)\left(\omega^2+\left(\frac{GBP}{2(1+2R_sC_pGBP)}+\epsilon\right)^2\right)} \quad (6.108)$$

Integrating Equation 6.108 yields the mean square voltage noise at V_{out} due to the input referred Johnson noise voltage produced by OA1 and OA2 given by Equation 6.109.

$$\overline{\left|v_{out\,Jv}(t)\right|^2}_{R_{d2}=2R_1R_3/R_2} =$$

$$\frac{1}{2\pi}\int_{-\infty}^{\infty} \frac{2.1\times10^{-16}(GBP)^4\left(\frac{R_3}{R_2+R_3}\right)^2\left(\omega^2+\left(\frac{2R_f+R_p}{R_fR_pC_f}\right)^2\right)}{\left(1+2R_sC_pGBP\right)^2\left(\omega^2+\left(\frac{R_2GBP}{R_2+R_3}\right)^2\right)\left(\omega^2+\left(\frac{GBP}{2(1+2R_sC_pGBP)}-\epsilon\right)^2\right)\left(\omega^2+\left(\frac{GBP}{2(1+2R_sC_pGBP)}+\epsilon\right)^2\right)}d\omega$$

$$\cong \frac{1.05\times10^{-16}GBPR_3^2}{\left(2\left(1+R_sC_pGBP\right)+\frac{R_3}{R_2}\right)R_2^2} + \frac{1.05\times10^{-16}\hat{A}_v\left(2R_f+R_p\right)^2R_3^2}{R_pR_fC_f\left(\hat{A}_vR_p+2R_f\right)R_2^2} \quad (6.109)$$

The total mean square voltage noise at V_{out} due to the two uncorrelated input referred voltage Johnson noise sources of op-amps OA1 and OA2 is therefore given by Equation 6.110.

$$\overline{\left|\sqrt{2}v_{out\,Jv}(t)\right|^2}_{R_{d2}=2R_1R_3/R_2} \cong \frac{2.1\times10^{-16}GBPR_3^2}{R_2\left(R_2\left(1+R_sC_pGBP\right)+2R_3\right)} + \frac{2.1\times10^{-16}\hat{A}_v\left(2R_f+R_p\right)^2R_3^2}{R_pR_fC_f\left(\hat{A}_vR_p+2R_f\right)R_2^2}$$

(6.110)

Input referred voltage Johnson noise due to OA3

Equation 6.111 gives the output noise PSD due to the input referred Johnson noise voltage produced by OA3.

$$S_{Jv}(\omega)_{OA3} = \frac{2.1\times10^{-16}(GBP)^2}{\left(\omega^2+\left(\frac{R_2GBP}{R_2+R_3}\right)^2\right)} \tag{6.111}$$

Integrating Equation 6.111 yields the mean square voltage noise at V_{out} due to the Johnson noise voltage produced by OA3 given by Equation 6.112.

$$\overline{\left|v_{out\,Jv}(t)\right|^2}_{R_{d2}=2R_1R_3/R_2} = \frac{1}{2\pi}\int_{-\infty}^{\infty}\frac{2.1\times10^{-16}(GBP)^2}{\left(\omega^2+\left(\frac{R_2GBP}{R_2+R_3}\right)^2\right)}d\omega = 1.05\times10^{-16}GBP(1+\frac{R_3}{R_2})$$

(6.112)

Input referred current shot noise due to OA1 and OA2

The current through R_s due to the input referred shot noise at V^+ would be zero in the case that common voltage dividers are used for both OA1 and OA2 since the non-inverting voltage is common to and correlated at both the non-inverting inputs of OA1 and OA2. However, since separate voltage dividers may be necessary to mitigate the effects of the input offset voltage specification of OA1 and OA2, this assumption cannot be made since the noise voltages appearing at the non-inverting inputs of OA1 and OA2 are now uncorrelated.

In common with the Johnson noise calculation for R_{d1} described above, the influence of the pole associated with the difference amplifier stage can therefore be considered negligible since the first order pole formed by C_n and R_{d1} attenuates the noise at a cut-off frequency very much lower than the GBP of OA3 such that $2/C_n\,R_{d1} \ll R_3GBP/(R_2+R_3)$.

Setting $R_{d2} = 2R_1R_3/R_2$, the output noise PSD at V_{out} for one op-amp due to the input referred shot noise current $S_s(\omega)_{\ V^+OA1,OA2}$ at the non-inverting V^+ input produced by OA1 and OA2 is given by Equation 6.113 where for the amplifier design $C_p \ll C_f$, $1/R_fC_f \ll GBP$, $R_s \ll R_p$ and $R_s \ll R_f$, and $\epsilon = \sqrt{\left(GBP/2\left(1+2R_sC_pGBP\right)\right)^2 - GBP\left(\hat{A}_vR_p+2R_f\right)/\left(\left(1+2R_sC_pGBP\right)\hat{A}_vR_pR_fC_f\right)}$

$$S_s(\omega)_{\ V^+\ R_{d2}=2R_1R_3/R_2} \cong$$

$$\frac{2\times10^{-34}(GBP)^2R_3^2\left(\omega^2+\left(\frac{2R_f+R_p}{R_fR_pC_f}\right)^2\right)}{R_2^2C_n^2\left(1+2R_sC_pGBP\right)^2(\omega^2+(2/C_nR_{d1})^2)\left(\omega^2+\left(\frac{GBP}{2(1+2R_sC_pGBP)}-\epsilon\right)^2\right)\left(\omega^2+\left(\frac{GBP}{2(1+2R_sC_pGBP)}+\epsilon\right)^2\right)} \tag{6.113}$$

Integrating Equation 6.113 yields Equation 6.114 for the output mean squared noise voltage $\overline{|v_{out\,s}(t)|^2}_{V^+\ R_{d2}=2R_1R_3/R_2}$ at V_{out} associated with the V^+ input bias current of either OA1 or OA2.

$$\overline{|v_{out\,s}(t)|^2}_{V^+\ R_{d2}=2R_1R_3/R_2} \cong$$

$$\frac{1}{2\pi}\int_{-\infty}^{+\infty}\frac{2\times10^{-34}(GBP)^2R_3^2\left(\omega^2+\left(\frac{2R_f+R_p}{R_fR_pC_f}\right)^2\right)}{R_2^2C_n^2\left(1+2R_sC_pGBP\right)^2(\omega^2+(2/C_nR_{d1})^2)\left(\omega^2+\left(\frac{GBP}{2(1+2R_sC_pGBP)}-\epsilon\right)^2\right)\left(\omega^2+\left(\frac{GBP}{2(1+2R_sC_pGBP)}+\epsilon\right)^2\right)}d\,\omega$$

$$= \frac{10^{-34}R_{d1}R_3^2}{2C_nR_2^2} + \frac{10^{-34}\hat{A}_vR_{d1}^2\left(2R_f+R_p\right)^2R_3^2}{4R_pR_fC_f\left(\hat{A}_vR_p+2R_f\right)R_2^2} \tag{6.114}$$

Noting that the input referred current noise sources associated with the non-inverting inputs of OA1 and OA2 are uncorrelated with respect to each other, Equation 6.115 gives the total mean squared noise voltage at V_{out} due to both OA1 and OA2, where $\hat{A}_v$ is the open loop DC gain of OA1 and OA2.

$$\overline{\left|\sqrt{2}v_{out\,s}(t)\right|^2}_{V^+R_{d2}=2R_1R_3/R_2} = \frac{10^{-34}R_{d1}R_3^2}{C_nR_2^2} + \frac{10^{-34}\hat{A}_vR_{d1}^2\left(2R_f+R_p\right)^2R_3^2}{2R_pR_fC_f\left(2R_f+\hat{A}_vR_p\right)R_2^2} \tag{6.115}$$

Setting $R_{d2} = 2R_1R_3/R_2$, the output noise PSD due to the input referred shot noise current for one op-amp at the inverting V^- input produced by OA1 or OA2 is

given by Equation 6.116 under the design constraints of $C_p \ll C_f$, $1/R_f C_f \ll GBP$, $R_s \ll R_p$ and $R_s \ll R_f$, and where the denominator constant $\epsilon = \sqrt{\left(GBP/2\left(1+2R_sC_pGBP\right)\right)^2 - GBP\left(\hat{A}_v R_p + 2R_f\right)/\left(\left(1+2R_sC_pGBP\right)\hat{A}_v R_p R_f C_f\right)}$

$$S_s(\omega)_{V^- R_{d2}=2R_1R_3/R_2} = \frac{8\times10^{-34}R_s^2C_p^2(GBP)^4\left(\omega^2+\left(\frac{1}{2R_sC_p}\right)^2\right)\left(\frac{R_3}{R_2+R_3}\right)^2}{C_f^2\left(1+2R_sC_pGBP\right)^2\left(\omega^2+\left(\frac{R_2GBP}{R_2+R_3}\right)^2\right)\left(\omega^2+\left(\frac{GBP}{2(1+2R_sC_pGBP)}-\epsilon\right)^2\right)\left(\omega^2+\left(\frac{GBP}{2(1+2R_sC_pGBP)}+\epsilon\right)^2\right)} \quad (6.116)$$

Integrating Equation 6.116 yields Equation 6.117 for the mean square voltage noise at V_{out} due to the input referred shot noise current for one op-amp at the inverting V^- input produced by OA1 and OA2, where $\hat{A}_v$ is the open loop DC gain of OA1 and OA2.

$$\overline{|v_{out\,s}(t)|^2}_{V^- R_{d2}=2R_1R_3/R_2} = \frac{1}{2\pi}\int_{-\infty}^{\infty} \frac{8\times10^{-34}R_s^2C_p^2(GBP)^4\left(\omega^2+\left(\frac{1}{2R_sC_p}\right)^2\right)\left(\frac{R_3}{R_2+R_3}\right)^2}{C_f^2\left(1+2R_sC_pGBP\right)^2\left(\omega^2+\left(\frac{R_2GBP}{R_2+R_3}\right)^2\right)\left(\omega^2+\left(\frac{GBP}{2(1+2R_sC_pGBP)}-\epsilon\right)^2\right)\left(\omega^2+\left(\frac{GBP}{2(1+2R_sC_pGBP)}+\epsilon\right)^2\right)} d\omega$$

$$= \frac{4\times10^{-34}R_s^2C_p^2R_3^2GBP}{C_f^2R_2\left(2R_2(1+R_sC_pGBP)+R_3\right)} + \frac{10^{-34}\hat{A}_vR_fR_pR_3^2}{C_f\left(\hat{A}_vR_p+2R_f\right)R_2^2} \quad (6.117)$$

Equation 6.118 gives the total mean square voltage noise at V_{out} due to the two uncorrelated input referred shot noise current sources of op-amps OA1 and OA2.

$$\overline{\left|\sqrt{2}v_{out\,s}(t)\right|^2}_{V^- R_{d2}=2R_1R_3/R_2} = \frac{8\times10^{-34}R_s^2C_p^2R_3^2GBP}{C_f^2R_2\left(2R_2(1+R_sC_pGBP)+R_3\right)} + \frac{2\times10^{-34}\hat{A}_vR_fR_pR_3^2}{C_f\left(\hat{A}_vR_p+2R_f\right)R_2^2} \quad (6.118)$$

Input referred current shot noise due to OA3

Equation 6.118 gives the output noise PSD due to the input referred shot noise current at the non-inverting V^+ input produced by OA3.

$$S_s(\omega)_{V^+OA3} = \frac{2\times10^{-34}(GBP)^2R_1^2R_{d2}^2}{\left(\omega^2+\left(\frac{R_2GBP}{R_2+R_3}\right)^2\right)(R_{d2}+2R_1)^2} \tag{6.119}$$

Integrating Equation 6.119 yields Equation 6.120 for the mean square voltage noise at V_{out} due to the input referred shot noise current at the non-inverting V^+ input produced by OA3.

$$\overline{|v_{out\,s}(t)|^2}_{V^+OA3} = \frac{1}{2\pi}\int_{-\infty}^{\infty}\frac{2\times10^{-34}(GBP)^2R_1^2R_{d2}^2}{\left(\omega^2+\left(\frac{R_2GBP}{R_2+R_3}\right)^2\right)(R_{d2}+2R_1)^2}d\omega = \frac{10^{-34}GBP(R_2+R_3)R_1^2R_{d2}^2}{R_2(R_{d2}+2R_1)^2} \tag{6.120}$$

Setting $R_{d2} = 2R_1R_3/R_2$ yields Equation 6.121.

$$\overline{|v_{out\,s}(t)|^2}_{V^+} = \frac{10^{-34}R_1^2R_3^2GBP}{R_2(R_2+R_3)} \tag{6.121}$$

Equation 6.122 gives the output noise PSD due to the input referred shot noise current at the inverting V^- input produced by OA3.

$$S_s(\omega)_{V^-OA3} = \frac{2\times10^{-34}(GBP)^2R_2^2R_3^2}{\left(\omega^2+\left(\frac{R_2GBP}{R_2+R_3}\right)^2\right)(R_2+R_3)^2} \tag{6.122}$$

Integrating Equation 6.122 yields Equation 6.123 for the mean square voltage noise at V_{out} due to the input referred shot noise current at the inverting V^- input produced by OA3.

$$\overline{|v_{out\,s}(t)|^2}_{V^-} = \frac{1}{2\pi}\int_{-\infty}^{\infty}\frac{2\times10^{-34}(GBP)^2R_2^2R_3^2}{\left(\omega^2+\left(\frac{R_2GBP}{R_2+R_3}\right)^2\right)(R_2+R_3)^2}d\omega = \frac{10^{-34}GBPR_2R_3^2}{(R_2+R_3)} \tag{6.123}$$

6.5.5 Signal to noise ratio and resolution

A Matlab script was written to calculate the total mean squared amplifier output noise given by the sum of the mean squared noise models derived in Sections 6.5.3 and 6.5.4, denoted by $\overline{|v_o(t)|^2}$ and the associated SNR values due to both $1K$ and full-scale amplitude sinusoidal temperature signals. By far the greatest contributors to the total mean squared noise at the amplifier output were found to be due to R_1, R_2, R_3, R_{d2} and the input referred noise voltage of OA3. The SNR due to

a $1K$ amplitude sinusoidal temperature using the amplifier output sensitivity of $0.15\,V/K$ is calculated using Equation 6.124.

$$SNR = 10log_{10}\left(0.15^2/2\overline{|v_o(t)|^2}\right) = 61.3dB \tag{6.124}$$

Equation 6.125 gives the associated full-scale SNR for a $5V$ peak-to-peak sine wave.

$$SNR = 10log_{10}\left(2.5^2/2\overline{|v_o(t)|^2}\right) = 85.8dB \tag{6.125}$$

The e-health platform uses an $8\,bit$ analogue to digital converter (ADC) to digitize the sensor signal for transmission to a smartphone and storage. The full-scale SNR of the recorded signal due to quantization at the ADC stage, denoted by SNR_q is given by the well-known relationship of Equation 6.126 for a full-scale sinusoidal signal where it is assumed that the quantisation noise can be considered additive.

$$SNR_q = 6.02B + 1.76 \tag{6.126}$$

An associated SNR, which is denoted by SNR_{q+sn}, that includes both the quantisation noise and signal noise is given by Equation 6.127 where B is the ADC native number of bits and it is assumed that the quantisation noise is not only additive but also uncorrelated to the signal and signal noise.

$$SNR_{q+sn} = 10log_{10}\left(\frac{2.5^2}{2\overline{|v_o(t)|^2} + 2.5^2 \times 10^{-(0.602B+0.176)}}\right) \tag{6.127}$$

For an $8\,bit$, $12\,bit$ and $16\,bit$ DAC, the approximate values of SNR_q are given by $49.2dB$, $74dB$ and $98.1dB$ respectively while the associated approximate values of SNR_{q+sn} are given by $49.2dB$, $73.7dB$ and $85.5dB$ respectively. It can therefore be seen that for an $8\,bit$ or $12\,bit$ ADC, the SNR is mainly limited by the quantization noise while for a $16\,bit$ ADC the SNR is mainly limited by the signal noise.

In the absence of signal noise, and other noise sources and distortion that originate within the ADC, the minimum signal voltage that can be measured for a $16\,bit$, $12\,bit$ and $8\,bit$ ADC are given by $5/2^{16}V \approx 7.63 \times 10^{-5}V$, $0.00122V$ and $0.0195V$ respectively. At an amplifier output sensitivity of $0.15\,V/K$, the associated

minimum temperatures that can be measured are therefore $(7.63 \times 10^{-5}/0.15)K \approx 0.00051K$, $0.00813K$ and $0.13K$ respectively.

The SNR_{q+sn} can also be written as Equation 6.128 where B_{eq} is the equivalent number of bits that would produce a quantisation signal to noise ratio SNR_q equal to SNR_{q+sn} in the absence of other noise sources and distortion that originate within the ADC.

$$SNR_{q+sn} = 6.02B_{eq} + 1.76 \tag{6.128}$$

Equation 6.129 therefore gives the equivalent number of bits.

$$B_{eq} = \frac{SNR_{q+sn} - 1.76}{6.02} \tag{6.129}$$

Substituting the values of SNR_{q+sn} given above for a $16\,bit$, $12\,bit$ and $8\,bit$ ADC yields $B_{eq} = ((85.5 - 1.76)/6.02)bits = 13.9\,bits$, $11.95\,bits$, and $8\,bits$ respectively. The minimum signal voltages that can be measured using a $16\,bit$, $12\,bit$ and $8\,bit$ ADC are therefore given by $5/2^{13.9}V \approx 0.00033V$, $0.00126V$ and $0.0195V$, and the associated minimum temperatures that can be measured are therefore $(0.00033/0.15)K \approx 0.0022K$, $0.0084K$ and $0.13K$ respectively. In the absence of other noise sources and distortion that originate within the ADC, it can be stated that when the signal is digitized using an $8\,bit$ ADC, the noise floor of the analogue input signal is very much smaller than the quantisation noise and the resolution remains unchanged. However, the use of a $12\,bit$ ADC increases the minimum temperature that can be measured due to the signal noise $v_o(t)$ by approximately 3.3% corresponding to a reduction in the native resolution of approximately 3.17%. The use of a $16\,bit$ ADC increases the minimum temperature that can be measured by 332% corresponding to a reduction in the native resolution of approximately 76.9%. Resolution is defined here as the reciprocal of the minimum temperature that can be measured.

6.6 e-Health platform

Figure 6.5 shows the e-Health platform schematic that was used in parallel with the Agilent DSO7052A oscilloscope and Benchvue PC interface to record the charge-conditioning amplifier response measurements. The platform is constructed using an Arduino Uno based platform equipped with a $16MHz$ Atmega 328 microcontroller, $8\ bit$ ADC and an HC-05 Bluetooth module.

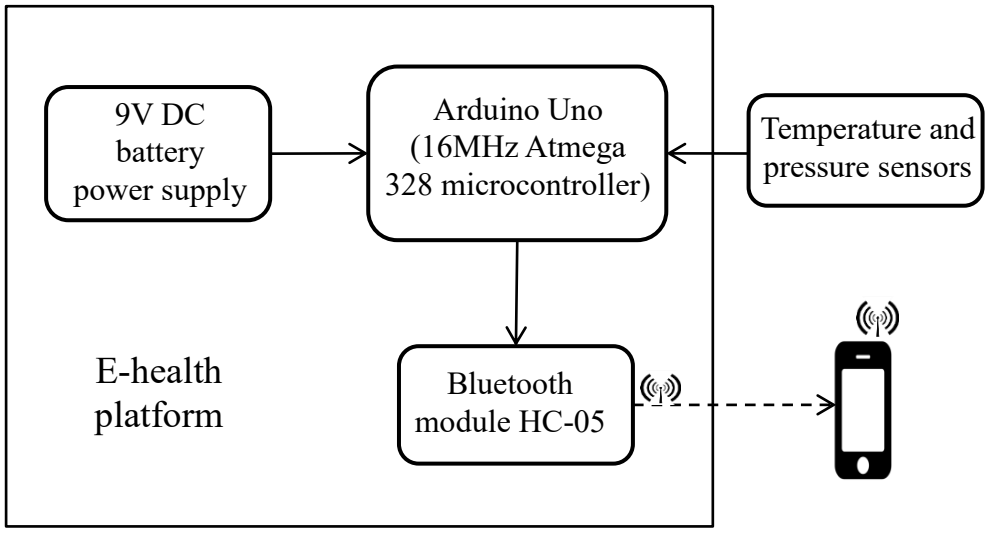

Figure 6.5 Schematic of the e-Health platform

The Bluetooth module pushes the measured data to a mobile smartphone that, in turn pushes the measured data over Wi-Fi to an SQLite database on a remote server via a smartphone app. When Wi-Fi is not available, the smartphone stores the data and automatically uploads the measured data to the server when Wi-Fi becomes available. Subsequent retrieval of the measurement data is via a PC using a DB browser application. The $9V$ battery that supplies the Arduino platform also supplies the unipolar charge-mode signal-conditioning amplifier via an on-board $5V$ regulated power supply. The amplifier design is such that its power consumption is significantly less than the maximum rated power specification of the on-board power supply.

6.7 Conclusions

For a native piezoelectric leakage resistance, $R_p = 90G\Omega$, the desired charge-mode signal conditioning output response given by Equation 6.7 is realised using the unipolar and bipolar signal-conditioning designs presented in Section 6.3.2 and Section 6.3.3 respectively regardless of the value of R_f. The desired response is also realised for $R_f = 1G\Omega$ when R_p is reduced to $R_p = 100M\Omega$ due to moisture or crack formation as described in Section 6.3.2. However, when $R_p = 100M\Omega$ and $R_f = 1T\Omega$, as required for field use, the decay time constant is reduced and the specified signal decay, which is limited to 98% after an $8\,hour$ period, is no longer met. Under these circumstances, the effect of a reduced R_p on the decay time constant can be mitigated using the enhanced open loop gain design described in Section 6.3.4 with the gain factor set to $G_g = 10$.

The contribution of the bias and bias offset currents to the overall drift voltage that can be expected after an operating period of $8\,hours$ using the unipolar and bipolar signal-conditioning designs presented in Section 6.3.2 and Section 6.3.3 respectively can be neglected for all values of R_p and for both $R_f = 1G\Omega$ and $R_f = 1T\Omega$. The contribution of voltage offset to the overall drift voltage after the $8\,hour$ operating period using the unipolar and bipolar signal-conditioning designs presented in Section 6.3.2 and Section 6.3.3 respectively can be neglected when $R_p = 90G\Omega$ for both $R_f = 1G\Omega$ and $R_f = 1T\Omega$, and when $R_p = 100M\Omega$ for $R_f = 1G\Omega$. However, when $R_p = 100M\Omega$ and $R_f = 1T\Omega$, a drift voltage of approximately $40mV$, which is equivalent to a measurement error of approximately $0.25K$, will develop over an $8\,hour$ measurement period. In this case, replacement of the piezoelectric sensor element is required. Alternatively, the use of the voltage compensation method described in Section 6.4.5 will mitigate the increasing drift voltage over the measurement period. Lower values of R_p will result in a greater drift with the drift following an approximately inversely proportional relationship to R_p.

Similarly, the contribution of maximum bias voltage drift after an $8\,hour$ operating period can be neglected when $R_p = 90G\Omega$ for both $R_f = 1G\Omega$ and $R_f = 1T\Omega$, and when $R_p = 100M\Omega$ for $R_f = 1G\Omega$. However, when $R_p = 100M\Omega$

and $R_f = 1T\Omega$, a drift voltage of approximately $1V$, which is equivalent to a large measurement error of approximately $6K$, will develop over an $8\,hour$ measurement period. Replacement of the piezoelectric sensor element is also required in this case. Alternatively, the use of the voltage compensation method described in Section 6.4.5 will mitigate the increasing drift voltage over the measurement period. In common with the input offset voltage case, the magnitude of the bias voltage drift follows an approximately inversely proportional relationship to R_p.

The use of the enhanced open loop gain signal-conditioning design described in Section 6.3.4 may help to mitigate output voltage drift due to input bias currents, input offset voltages and differences in the bias voltages. However, application of this method rather than using the voltage compensation method is for the present treated with caution since the input bias currents and offset voltages of OA4 and OA5, and the differences in the bias voltages seen at the non-inverting inputs of OA4 and OA5 have not been taken into account in the analysis. A full analysis and construction of the enhanced open loop gain design is the subject of future work.

The analysis makes the assumption that feedback resistances of $R_f = 1T\Omega$ are achievable. The dielectric resistance of the polypropylene feedback capacitors is extremely high, however in practice it may not be large enough to realise an overall feedback resistance as high as $R_f = 1T\Omega$. An alternative solution to achieving the required specification is the use of a real-time decay compensation scheme based on the discussion in Section 7.2.3 in tandem with a slightly reduced and more easily realisable overall value of R_f to reduce low frequency signal decay. A disadvantage of this solution is that the output offsets and the output noise will increase monotonically with time, reducing the output SNR such that there is a trade-off between the SNR at the end of the $8\,hour$ measurement period and the value of R_f used. By selecting a suitable value of R_f, a minimum acceptable SNR at the end of the measurement period can therefore be realised. The use of decay compensation with a reduced requirement for large R_f will be the subject of future work. By far the greatest contributors to the total mean squared noise at the amplifier output are due to R_1, R_2, R_3, R_{d2} and the input referred noise voltage of OA3. The noise contribution of the difference amplifier stage is therefore a focus for noise reduction in future work.

Chapter 7

Sensor pyroelectric response

7.1 Introduction

This chapter describes the steady state and transient pyroelectric response of the sensor element and signal-conditioning system. Section 7.2 and Section 7.3 describe the methodology and transient response results respectively to a transient temperature change applied by a Peltier tile affixed to the PZT-5H sensor element substrate surface, and yields an experimental estimate of the temperature to voltage conversion factor. Section 7.4 and Section 7.5 describe the methodology and steady state response results respectively for a temperature change applied at the PZT-5H element substrate surface. The steady state response results yields a confirmation of the temperature to voltage conversion factor and system linearity, and provides an experimental value for the effective pyroelectric coefficient. Section 7.6 describes the background of the simulated time-frequency response models and Section 7.7 describes the simulated time-frequency response results in terms of the amplitude, phase and phase delay for different elastomer liner thicknesses.

7.2 Methodology – transient pyroelectric response

7.2.1 Experimental set-up

A block diagram of the experimental set-up is shown in Figure 7.1. The experimental set-up is similar to that described in Section 5.3.1 but with the Agilent parameter analyser replaced with the bipolar charge amplifier discussed in Section 6.3.3 and the e-Health platform discussed in Section 6.6.

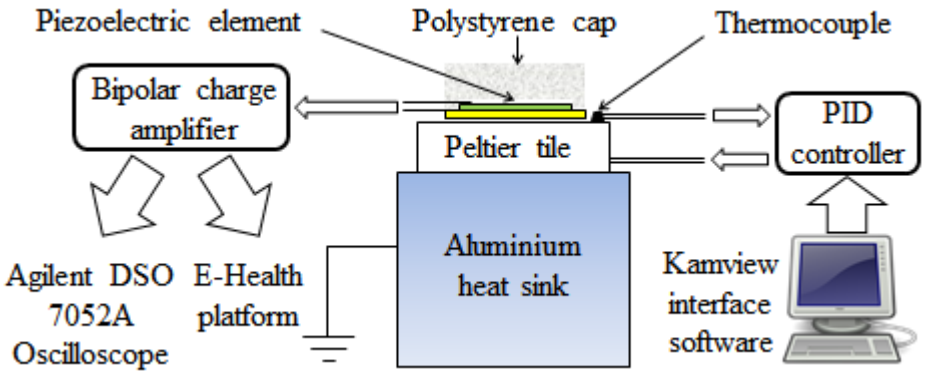

Figure 7.1 Sensor transient pyrooelectric response measurement set-up

The terminations of the sensor element flying leads were fixed to a glass slide using Agar electrically conducting silver paste to form electrodes near the edge of the slide. The sensor was attached to the bipolar differential input charge amplifier design discussed in Section 6.3.3 via a cable terminated with crocodile clips suitable for connection to the silver paste electrodes. The sensor element was placed substrate down on a European Thermodynamics Peltier tile and aluminium heat sink assembly, and affixed using RS Heat Sink Compound Plus paste to limit mechanical loading and ensure good thermal conduction over the entire brass substrate surface. The paste also served to suppress the large $4.6kHz$ flexure resonance mode, ensuring uncorrupted low frequency immittance measurements.

Room convection currents that can give rise to a non-uniform temperature distribution in the sensor element during impedance measurements will result in the measurement of an additional pyroelectric charge by the charge amplifier. To minimise this error, the sensor was shielded by placing the entire experimental set-up inside the Signatone probe station described in Section 5.3.1 and covering the sensor

element with a cap fashioned from expanded polystyrene. Care was taken to ensure the polystyrene cap was close to but did not touch the surface of the PZT sensor element. The very low thermal conductivity of expanded polystyrene reduces the occurrence of steady state temperature gradients and axial heat flows within the piezoelectric and substrate materials that would otherwise exist due to a temperature difference between the Peltier tile / substrate interface and sensor element top electrode.

7.2.2 Experiment procedure

Initial considerations on the experimental set-up are as described in Section 5.3.1. The $\pm 18V$ rail voltage bipolar charge amplifier described in Section 6.3.3 was used, rather than the unipolar single rail $5V$ amplifier described in Section 6.3.2, to avoid clipping of the voltages at the outputs V_{OA1} and V_{OA2} of the charge amplification stages. The signal-conditioning amplifier described in Section 6.2.3 is designed for use as a battery operated stand-alone device and is not suitable due to the LMC 6081 opamp specified maximum permitted supply voltage of $5.5V$. Since the output voltage is biased to half the supply voltage, the peak output of around $2.75V$ is too low to allow recording of the transient temperature peaks produced by the Peltier tile in response to the initial hunting period of the PID controller, resulting in clipping of the response. The forward gain of the bipolar charge amplifier was set to $G = 1$ at the difference amplifier stage. Two cases are considered: 1) The bipolar signal-conditioning amplifier fitted with $1\mu F$ polypropylene feedback capacitors and $1G\Omega$ thick film on alumina feedback resistors; and 2) Fitted with $1.5\mu F$ polypropylene feedback capacitors and $1G\Omega$ thick film on alumina feedback resistors. The two cases realise nominal time constants of $\tau = 1000s$ and $\tau = 1500s$ respectively.

The temperature of the Peltier tile was controlled using the KamView proportional-integrator-differentiator (PID) controller, with the target temperature being selected using the KamView user interface. The Peltier tile temperature feedback signal was implemented by the use of a K-type thermocouple attached at a

corner of the Peltier tile surface. The transient pyroelectric response of the sensor was measured for a $10°C$ step target input to the PID controller.

The experimental procedure is as follows:

1) Set the feedback capacitors at OA1 and OA2 to $C_f = 1\mu F$.
2) Apply a $10°C$ temperature step at the Kamview user interface.
3) Record output voltage response of the amplifier using the Agilent DSO7052A oscilloscope and Benchvue PC interface, and simultaneously record the thermocouple temperature data via the Kamview user interface for a duration of $150\ seconds$ settling time.
4) Repeat steps 2) and 3), replacing the $1\mu F$ feedback capacitors with $C_f = 1.5\mu F$.

The response was measured for a duration of $150\ seconds$ to allow the PID controller to settle at the steady state Peltier temperature of $10°C$ above ambient to allow the amplifier response voltage temperature conversion factor to be calculated. The voltage temperature conversion factor is discussed further in Section 7.5.1. The response decay during the measurement duration due to the time constant of the signal-conditioning charge amplifier stages is significant and therefore a decay compensation scheme was devised, and which is described in Section 7.2.3.

7.2.3 Response decay compensation

The measured response $V_o(t)$ to a voltage applied at the input of the PID controller is dependent on the overall transfer function of the system. The system comprises the PID controller, Peltier tile, PZT-5H sensing element, and the signal conditioning amplifier such that $V_o(t) = -{C_f}^{-1}\mathcal{L}^{-1}\{G(s)A(s)\}$ where $G(s)$ is the Laplace transfer function of the system, $-{C_f}^{-1}A(s)$ is the transfer function of the amplifier and as before C_f is the feedback capacitance of a single charge amplifier stage. The overall system response can therefore also be described in terms of the continuous time convolution of the respective impulse responses of the system $g(t)$

and charge amplifier $a(t)$ such that $V_o(t) = -{C_f}^{-1} g(t) * a(t)$. Further convolving $V_o(t)$ with the impulse response $\mathcal{L}^{-1}\{1/A(s)\}$ such that $a(t) * \mathcal{L}^{-1}\{1/A(s)\} = \delta(t)$ yields $V_o'(t) = -{C_f}^{-1} g(t) * a(t) * \mathcal{L}^{-1}\{1/A(s)\} = -{C_f}^{-1} s(t) * \delta(t) = -{C_f}^{-1} s(t)$ where $V_o'(t)$ is the decay compensated $V_o(t)$ and $\mathcal{L}^{-1}$ denotes inverse Laplace transformation. The decay due to the charge amplifier is effectively negated and the signal is therefore decay compensated.

The continuous-time transfer function of the charge amplifier is $A(s) = s/\left(s + {\tau_f}^{-1}\right)$ where $\tau_f = C_f R_f$ and R_f is the feedback resistance of a single charge amplifier stage. Since the amplifier response has been discretised, such that $V_o(t)$ is recorded as $V_o(n)$ where n is the discrete time index, it is necessary to write $A(s)$ in an equivalent discrete form as a z-transform $A(z)$. For discrete signals, $z \triangleq e^{sT_s}$ and therefore $s = T_s^{-1} ln(z)$. Writing as a MacLaurin series, s may be expanded to yield Equation 7.1.

$$s = \frac{2}{T_s} \sum_{m=0}^{\infty} \left[\frac{1}{2m+1} \left(\frac{z-1}{z+1} \right)^{2m+1} \right] \tag{7.1}$$

The bilinear transform [109] approximates s by using only the term in $m = 0$ to yield Equation 7.2.

$$s \cong \frac{2}{T_s} \left(\frac{z-1}{z+1} \right) \tag{7.2}$$

The effect of truncation is to introduce frequency warping such that increasing frequency on the $j\omega$ axis in the s plane to ∞ is mapped onto one rotation on the unit circle in the z plane rather than aliasing infinitely in the exact case. The effect of frequency warping therefore increases with frequency, resulting in ever-increasing compression on the unit circle in the z-domain. However, at frequencies much lower than half the sampling rate the approximation is accurate. Writing s and z complex variables as the sum of their real and imaginary parts yields Equation 7.3. The approximately equal sign is replaced with an equal sign since the real and imaginary parts of s denoted by δ and ω are no longer considered to be equivalent on both sides and are distinguished on the right hand side by being denoted as δ' and ω' respectively.

$$s = \delta + j\omega = \frac{2}{T_s}\left(\frac{e^{(\delta'+j\omega')T_s}-1}{e^{(\delta'+j\omega')T_s}+1}\right) = \frac{2}{T_s}\left(\frac{e^{(\delta'+j\omega')\frac{T_s}{2}}-e^{-(\delta'+j\omega')\frac{T_s}{2}}}{e^{(\delta'+j\omega')\frac{T_s}{2}}+e^{-(\delta'+j\omega')\frac{T_s}{2}}}\right) = \frac{2}{T_s}tanh(\delta'+j\omega')\frac{T_s}{2} \quad (7.3)$$

For small $\delta' + j\omega'$, then $tanh(\delta' + j\omega')T_s/2 \cong (\delta' + j\omega')T_s/2$ and therefore $\delta + j\omega \cong \delta' + j\omega'$. Since the bilinear transform is applied to an impulse response for which the Laplace transform region of convergence includes the $j\omega$ axis, then a small positive, negative (within the region of convergence such that all poles lie to the left of the negative value) or zero value of δ is valid. Also since $T_s = 0.1s$ and the maximum frequency present in the signal is approximately $0.2\,rad/s = 0.1/\pi\,Hz$, then the maximum frequency is very much less than $2f_s$ where $f_s = 1/T_s$ is the sampling frequency and therefore the effect of frequency warping is likely to be negligible. It can therefore be stated that $\omega' \cong \omega = (2/T_s)tan(\omega' T_s/2)$. In situations where frequency warp compensation is required then for the case of warp compensation at the cut-on frequency, the $(2/T_s)$ factor in Equation 7.3 can be replaced by the factor $\tau_f{}^{-1}/tan(T_s/2\tau_f)$ before substitution into $A(s)$. This compensation factor forces the phase and gain of both $A(s)$ and its bilinear transformed transfer function $A(z)$ to be equal at the $-3dB$ cut-on frequency given by $\tau_f{}^{-1} rad/s$ of the amplifier. Substituting $T_s = 0.1s$ and $\tau_f = 1500s$ it is evident that $\tau_f{}^{-1}/tan(T_s/2\tau_f)$ is an insignificant 3.7×10^{-8} % less than $2/T_s$ and therefore warp compensation is considered unnecessary.

Substituting Equation 7.3 for s into $A(s) = s/(s + \tau_f^{-1})$ and rearranging yields Equation 7.4.

$$A(z) = \frac{z-1}{z-1+\frac{T_s}{2\tau_f}(z+1)} \quad (7.4)$$

The reciprocal of $A(z)$ is therefore given by Equation 7.5.

$$\frac{1}{A(z)} = 1 + \frac{T_s}{2\tau_f}\frac{(z+1)}{(z-1)} \quad (7.5)$$

Inverse Z transforming Equation 7.5 yields Equation 7.6 for the discrete impulse response $c(n)$ of $1/A(z)$ where n is the time index, $u(n)$ is the discrete Heaviside step function and $\delta(n)$ is the Kronecker delta function.

$$c(n) = \frac{T_s}{\tau_f}u(n) + \left(1 - \frac{T_s}{2\tau_f}\right)\delta(n) \tag{7.6}$$

The influence of signal decay in the sampled version of $V_o(t)$ given by $V_o(n)$ may therefore be negated by discrete convolution of $c(n)$ with $V_o(n)$ to yield Equation 7.7.

$$V_o'(n) = V_o(n) * c(n) = \left(1 - \frac{T_s}{2\tau_f}\right)V_o(n) + \frac{T_s}{\tau_f}u(n) * V_o(n) \tag{7.7}$$

The vector $c(n)$ was simple to construct in Excel using Equation 7.6 and basic column operator tools, and discrete convolution was performed in Matlab using the xlsread and xlswrite functionality to import vectors $V_o(n)$ and $c(n)$ from their native Excel spreadsheet for manipulation and to export the resultant decay compensated $V_o(n)$ vector back to the Excel spreadsheet. A comparison of the compensated and uncompensated plots of $V_o(t)$ for a $10°C$ step PID transient with $C_f = 1\mu F$ is shown in Figure 7.2.

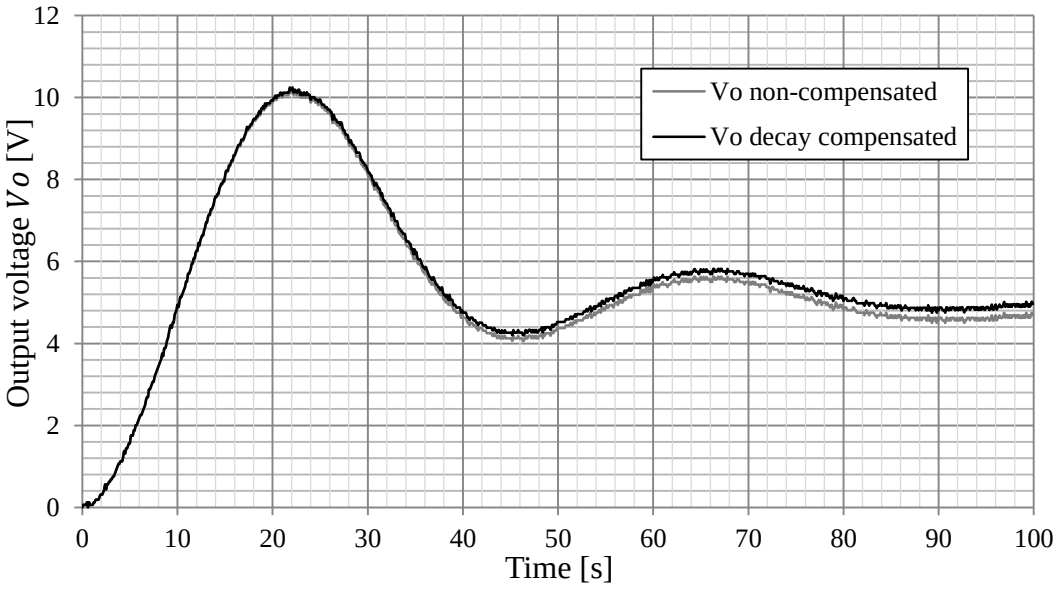

Figure 7.2 Compensated and uncompensated responses to a $10°C$ step PID transient from $20°C$, $C_f = 1\mu F$, $G = 1$, $T_s = 0.1s$

The application of this method of decay compensation to the raw non-compensated $V_o(n)$ data, recorded at a sampling period $T_s = 0.1s$, for the cases of $C_f = 1\mu F$ and $C_f = 1.5\mu F$ is described in Section 7.3.

7.3 Measurement – transient pyroelectric response

7.3.1 Results

The pyroelectric response of the sensor element and charge amplifier system to a $10°C$ temperature step PID transient applied by a Peltier tile to the sensor substrate surface using a PID controller with thermocouple temperature feedback is shown in Figure 7.3 for feedback capacitances set to $C_f = 1\mu F$ and Figure 7.4 for feedback capacitances set to $C_f = 1.5\mu F$. In both cases a feedback resistance of $R_f = 1G\Omega$ was used. Shown are the thermocouple measured Peltier temperature and decay compensated PZT sensor voltage responses to the applied temperature transient and the $\Delta\theta$ equivalent sensor response calculated using the measured sensor conversion factor in the steady state (sensitivity) given by $CF = V_o(150s)/10\ (VK^{-1})$. The voltage to temperature conversion factors for $C_f = 1\mu F$ and $C_f = 1.5\mu F$ were calculated as 0.47 and 0.32 respectively.

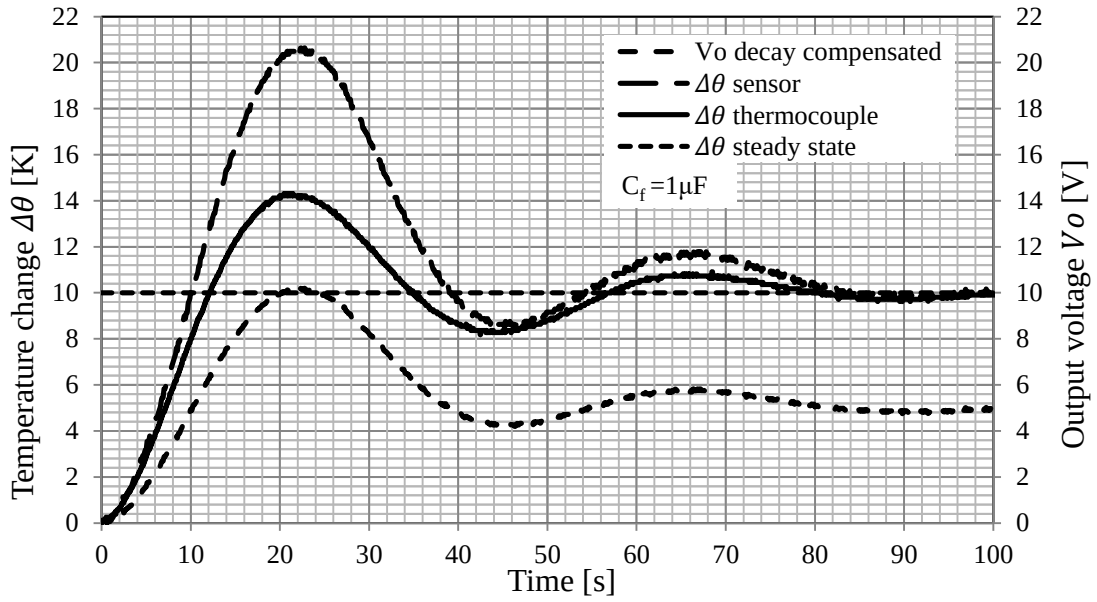

Figure 7.3 Decay compensated response of the sensor to a $10°C$ step PID transient from $20°C$, $C_f = 1\mu F$, $G = 1$, $T_s = 0.1s$

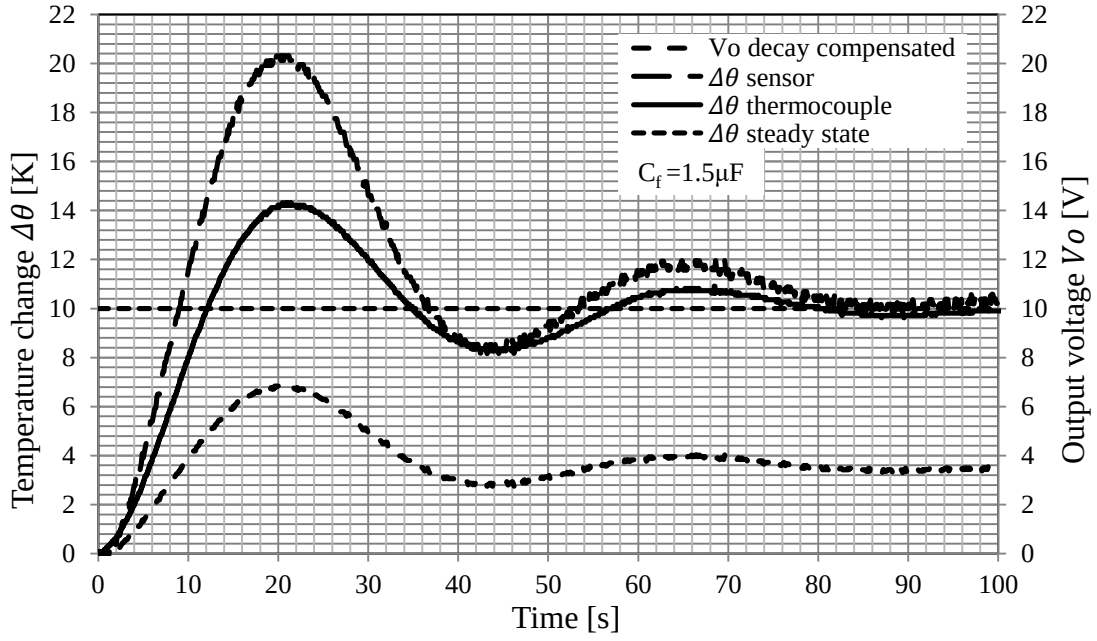

Figure 7.4 Decay compensated response of the sensor to a $10°C$ step PID transient from $20°C$, $C_f = 1.5\mu F$, $G = 1$, $T_s = 0.1s$

Voltage decay compensation, which was discussed in Section 7.2.3, was applied to the charge amplifier responses by convolving the oscilloscope sampled output voltage vector with the inverse z-transform of the reciprocal of the bilinear transform of the continuous time-domain transfer function of the charge amplifier stage. Voltage decay compensation allows the transient decay part of the response of the sensor to be 'removed', allowing the true sensitivity of the sensor to be estimated at the steady state temperature of the Peltier and sensing element.

7.3.2 Discussion

During the PID controller hunting-period, it can be seen from Figure 7.3 and Figure 7.4 that at the first peak the temperature recorded by the thermocouple is approximately 30% lower than those recorded using the respective pyroelectric sensor conversion factors. The type K thermocouple used as the temperature reference is required only to measure the steady state temperature of the Peltier tile, and it is likely that this difference is due to the slower response of the thermocouple to the PID induced temperature 'hunting' transient compared to the pyroelectric

response of the sensor element. Since the output voltage gain of the signal-conditioning amplifier is inversely proportional to C_f, it is expected that the ratio of the conversion factors using $1\mu F$ and $1.5\mu F$ capacitances would be $1\mu F\ /1.5\mu F = 1.5$. With conversion factors for $C_f = 1\mu F$ and $C_f = 1.5\mu F$ of 0.47 and 0.32 respectively, the ratio of $0.47/0.32 = 1.47$ agrees well with expectation, and the small discrepancy is easily explained by nominal C_f value tolerances of $\pm 5\%$ and measurement reading error due to signal noise.

The output voltage-temperature conversion factor (sensitivity) of the sensor and signal conditioning system for $C_f = 1.5\mu F$ is given by $sens = G \times 0.32\ [V/K]$. For $G = 1$, the sensitivity is therefore given by $sens(G = 1) = 0.32\ V/K$. To provide an adequate temperature range when the sensor element is used with the $5V$ unipolar amplifier, setting $G = 0.5$ yields a sensitivity of $sens(G = 0.5) \approx 0.16\ V/K$.

7.4 Methodology – accumulative pyroelectric response

7.4.1 Experimental set-up

A block diagram of the experimental set-up is shown in Figure 7.5. The experimental set-up is similar to that described in Section 7.2.1 but with the bipolar charge amplifier replaced with the unipolar charge amplifier discussed in Section 6.3.2.

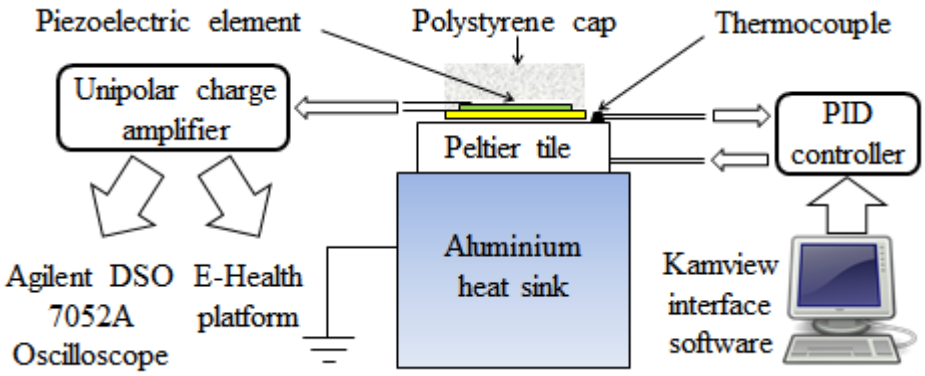

Figure 7.5 Sensor accumulative pyroelectric response measurement set-up

The terminations of the sensor element flying leads were fixed to a glass slide using Agar electrically conducting silver paste to form electrodes. The sensor was attached to the unipolar differential input charge amplifier design discussed in Section 6.3.2 via a cable terminated with crocodile clips suitable for connection to the silver paste electrodes. The sensor element was placed substrate down on a European Thermodynamics Peltier tile and aluminium heat sink assembly, and affixed using RS Heat Sink Compound Plus paste to limit mechanical loading and ensure good thermal conduction over the entire brass substrate surface.

Room convection currents that can give rise to a non-uniform temperature distribution in the sensor element during impedance measurements will result in the measurement of an additional pyroelectric charge by the charge amplifier. To minimise this error, the sensor was shielded by placing the entire experimental set-up inside the Signatone probe station used for the experimental set-up described in Section 5.3.1, and the sensor element was covered with a cap fashioned from expanded polystyrene. Care was taken to ensure the polystyrene cap was close to but did not touch the surface of the PZT sensor element. The very low thermal conductivity of expanded polystyrene reduces the occurrence of steady state temperature gradients and axial heat flows within the piezoelectric and substrate materials that would otherwise exist due to a temperature difference between the Peltier tile / substrate interface and sensor element top electrode.

7.4.2 Experiment procedure

The steady state pyroelectric response of the sensor was measured in $2°C$ increments for a round trip over the temperature range $20°C \rightarrow 42°C \rightarrow 20°C$. The unipolar differential input signal conditioning charge amplifier design discussed in Section 6.3.2 was used to measure the output voltage response to the charge produced by the PZT sensor element that is proportional to the charge generated by each incremental step in temperature. The voltage response was measured using an Agilent DSO7052A oscilloscope and the measured data was also pushed to a remote server using the e-Health platform described in Section 6.6. The feedback networks of the charge amplifier are fitted with $C_f = 1.5\mu F \pm 5\%$ polypropylene capacitors

and $R_f = 1G\Omega \pm 1\%$ thick film on alumina resistors yielding an amplifier time constant, τ of approximately $\tau = 1500s$. The voltage response of the charge amplifier therefore gradually decays with a time constant of approximately $25\ minutes$. Since the duration of the measurement period was around $40\ minutes$, a continuous measurement of the temperature response was not possible due to a significant amplifier response decay over the course of the measurement period. It was therefore necessary to measure the response between each temperature increment separately.

The experimental procedure is as follows:

1) Apply a $2°C$ temperature increase from $20°C - 22°C$ allowing precisely a $2\ minute$ settling time to ensure the sensor is at a uniform temperature.
2) Record the amplifier output voltage response using the Agilent DSO7052A oscilloscope.
3) While maintaining a uniform $22°C$, reset the signal conditioning amplifier feedback networks by discharging the feedback capacitors via a series combination of $1k\Omega$ resistor and short-circuit switch in parallel with each C_f to yield zero voltage at both amplifier outputs.
4) Apply a $2°C$ temperature increase from $22°C - 24°C$ allowing precisely a $120\ second$ settling time.
5) Repeat steps 2) to 4), incrementing the temperature by $2°C$ up to a temperature of $42°C$.

The response was measured at precisely the same interval of $120\ seconds$ after initiation of each temperature increment to allow the PID controller time to settle at each temperature. The time taken between the initiation of each temperature increment and measurement of the response was maintained at precisely $3\ minute$s including the $2\ minute$ settling time. An accumulative voltage is defined as the sum of the individual temperature increments up to the desired temperature. The response for a temperature change from $22°C - 26°C$ was therefore obtained by adding the individual responses for each of the increments $20°C - 22°C$, $22°C - 24°C$ and

$24°C - 26°C$ giving the true temperature response characteristic. This procedure results in a measurement error due to the $120\ second$ response decay periods at each incremental temperature measurement, however this error is predictable and constant at each increment allowing remedial adjustment of the results by the decay compensation method described in Section 7.2.3 which is applied to the PID transient response data of the first $2°C$ temperature increment. A decay compensation factor is calculated from the ratio of the calculated amplifier decay compensated response voltage at a settling time of $120\ seconds$ and the measured non-compensated amplifier response at the settling time of $120\ seconds$. The PID hunting behaviour is the same at each $2°C$ temperature interval and therefore the decay compensated response at the $120\ second$ settling time of each temperature increment was found by multiplying the decay compensation factor by the non-compensated response voltage.

7.5 Measurement – accumulative pyroelectric response

7.5.1 Results

The decay compensated accumulative voltage response to $5°C$ temperature increments is shown in Figure 7.6.

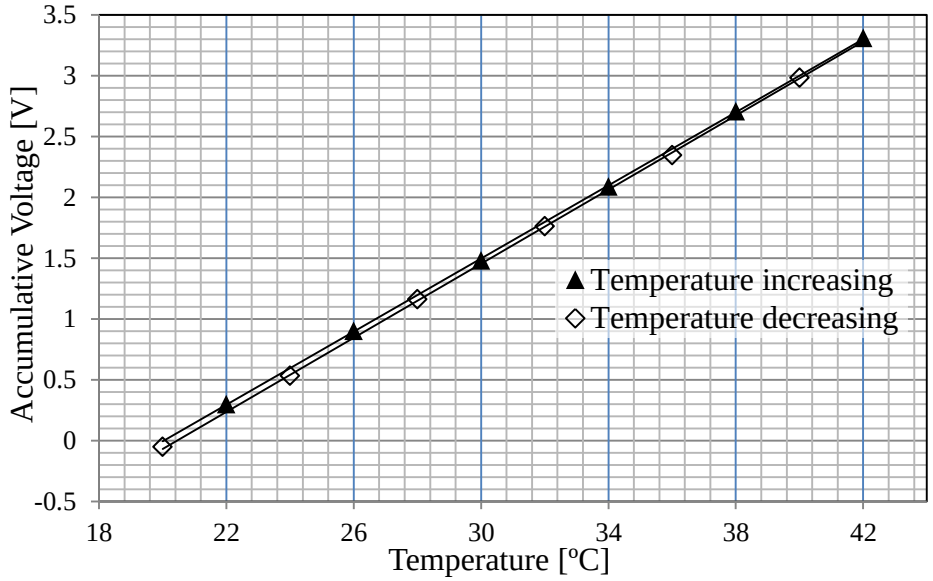

Figure 7.6 Decay compensated accumulative voltage versus temperature: linear trend-line fit, feedback $C_f = 1.5\mu F$, forward gain $G = 0.5$

The unipolar charge amplifier feedback capacitors and forward gain were set to $C_f = 1.5\mu F$ and $G = 0.5$. The expected sensitivity of the sensor at the steady state, which is determined in Section 7.3.1 for $G = 1$ as $sens = 0.32\ V/K$ is therefore given by $sens(G = 0.5) \approx 0.16\ V/K$.

Using a linear trend line fit for both temperature increasing and temperature decreasing data sets using the Excel curve fitting tool yields decay compensated sensitivities of $sens = 0.1503\,V/K$ and $sens = 0.1523\,V/K$ respectively. These values are approximately $0.01\,V/K$ and $0.0075\,V/K$ lower than the sensitivity value obtained from the transient analysis of Section 7.2.

7.5.2 Effective pyroelectric coefficient P_{eff}

Using signal-conditioning amplifier feedback capacitors of $C_f = 1.5\mu F$ nominal, the signal-conditioning amplifier provides an averaged measured response sensitivity of $0.1513V/K$. With the gain of the forward difference amplification stage set to $G = 0.5$, an amplifier response temperature to voltage conversion factor of $0.1513(V/K)$ requires a charge of $-0.1513C_f\ (C/K)$ and therefore the total measured pyroelectric coefficient P_{eff} is approximately $-0.1513C_f/A_s\ (C/m^2K)$ where A_s is the area of the sensor element silver electrodes. Since the electrode radius is $9.1mm$, the measured total pyroelectric response P_{eff} is therefore approximately $-865\,\mu C/m^2K$. This value agrees well with the total estimated response of $P_{eff} \approx -800$ to $-900\,\mu Cm^{-2}K^{-1}$ given in Section 4.6 and confirms the anticipated pyroelectric response enhancement due to substrate clamping.

7.5.3 Sensor accuracy estimate

The accuracy of the sensor is estimated by taking the mean of the amplifier response to each $2°C$ increment from $20°C$ to $40°C$ and taking the greatest positive and negative deviations from this mean as a percentage of the mean. These were found to be $+2.75\%$ and -3.25%. A prudent estimate of accuracy can therefore be stated as $\pm 3.5\%$. However, since the temperature reference is obtained using a

thermocouple integrated with the Peltier tile and PID controller, the validity of the estimate is therefore dependent on the accuracy of the thermocouple. With a typical accuracy of $\pm 2.2°C$ at low temperatures for the type K thermocouple used, ($\pm 10.5\%$ at $20°C$ and $\pm 5.5\%$ at $40°C$) over the temperature range of interest, this estimate of sensor accuracy is treated with caution.

7.5.4 Discussion

From Figure 7.6 it is demonstrated that the sensor response under short-circuit conditions is linear over the temperature range $20°C$ and $42°C$. It is considered that the small $0.05V$ deviation at $20°C$ which is equivalent to approximately $0.33°C$ in the round trip $20°C \rightarrow 42°C \rightarrow 20°C$ measurement is due to measurement error rather than any underlying rate-independent hysteretic or other physical process. However, this observation requires further investigation to confirm measurement error and this will be the subject of future work. Furthermore, the sensitivity values obtained from the accumulative response results of Section 7.5 are approximately $0.01\,V/K$ and $0.0075\,V/K$ lower than the sensitivity value obtained from the transient analysis of Section 7.3. This discrepancy is believed to be most probably due to the use of different signal-conditioning amplifiers with the unipolar design being used for the transient response analysis, and the bipolar design being used for the accumulative response analysis. While the feedback capacitors used in both signal-conditioning designs are nominally identical, the $\pm 5\%$ tolerance can explain the discrepancy since the signal-conditioning response is sensitive to variations in feedback capacitance values. The discrepancy may alternatively be due to the accuracy of the thermocouple as discussed in Section 7.5.3.

From the theoretical calculation of P_{eff} given in Section 4.6, and assuming that $p^s = -350\,\mu C m^{-2} K^{-1}$ such that $P_{eff} = -850\,\mu C m^{-2} K^{-1}$, the theoretical value of the temperature to voltage conversion factor is given by $CF = sens(G = 0.5) = -P_{eff} A_s / C_f = 0.1476\,V/K$. This value agrees well with the conversion factor measured in Section 7.5.1.

7.6 Sensor response: time – frequency analysis

7.6.1 Sensor charge-mode output voltage model

The Fourier domain charge-mode signal conditioning amplifier output voltage, $V_{out}(j\omega)$, which was derived in Chapter 6, Section 6.3.2, is repeated below for clarity.

$$V_{out}(j\omega) = \frac{j\omega \mathrm{Q}(j\omega) GBP\left(\frac{R_3}{R_2+R_3}\right)}{R_s C_p C_f \left(j\omega + GBP\left(\frac{R_2}{R_2+R_3}\right)\right)\left(j\omega + \frac{1}{R_f C_f}\right)\left(j\omega + \frac{1}{2R_s C_p}\right)} + \frac{V_{cc}}{2}$$

$$\cong \frac{R_3 j\omega \mathrm{Q}(j\omega)}{R_2 R_s C_p C_f \left(j\omega + \frac{1}{R_f C_f}\right)\left(j\omega + \frac{1}{2R_s C_p}\right)} + \frac{V_{cc}}{2} \quad (6.7)$$

Equation 7.8 gives the equivalent Laplace domain output voltage, $V_{out}(s)$.

$$V_{out}(s) = \frac{s\mathrm{Q}(s) GBP\left(\frac{R_3}{R_2+R_3}\right)}{R_s C_p C_f \left(s + GBP\left(\frac{R_2}{R_2+R_3}\right)\right)\left(s + \frac{1}{R_f C_f}\right)\left(s + \frac{1}{2R_s C_p}\right)} + \frac{V_{cc}}{2}$$

$$\cong \frac{R_3 s\mathrm{Q}(s)}{R_2 R_s C_p C_f \left(s + \frac{1}{R_f C_f}\right)\left(s + \frac{1}{2R_s C_p}\right)} + \frac{V_{cc}}{2} \quad (7.8)$$

Omitting the $V_{cc}/2$ DC bias and setting the forward difference amplifier stage to $G = 0.5$ yields Equation 7.9 and Equation 7.10 for the Fourier and Laplace domain output voltages respectively.

$$V_{out}(j\omega) = \frac{j\omega \mathrm{Q}(j\omega)}{2R_s C_p C_f \left(j\omega + \frac{1}{R_f C_f}\right)\left(j\omega + \frac{1}{2R_s C_p}\right)} \quad (7.9)$$

$$V_{out}(s) = \frac{s\mathrm{Q}(s)}{2R_s C_p C_f \left(s + \frac{1}{R_f C_f}\right)\left(s + \frac{1}{2R_s C_p}\right)} \quad (7.10)$$

The terms $\mathrm{Q}(s)$ and $\mathrm{Q}(j\omega)$, R_p and C_p are the negative surface bound charge, equivalent dielectric resistance and capacitance of the PZT-5H low frequency equivalent circuit model given by Equation 4.33 to Equation 4.35 in Chapter 4, Section 4.7. These are repeated below for clarity with $\mathrm{Q}(s)$ given by Equation 7.11 quoted in the Laplace domain. Equation 7.12 and Equation 7.13 give the negative

bound charge due to a temperature change only with the subscript θ indicating temperature only.

$$C_p = \frac{A_s}{l_p}\left(\frac{(1-\mu_b)\beta^2 A_p}{2\left(E_b A_b+\alpha(1-\mu_b)A_p\right)} + \frac{e_{33}^2}{c_{33}^E} + \varepsilon_{33}^S\right) \tag{4.33}$$

$$R_p = \frac{l_p}{\delta_{33} A_s} \tag{4.34}$$

$$\mathrm{Q}(j\omega) = A_s\left[\begin{array}{c}\left(2e_{31}\varphi_{p1}^E + e_{33}\varphi_{p3}^E + p^s - \frac{\beta E_b A_b \varphi_{p1}^E}{E_b A_b+\alpha(1-\mu_b)A_p}\right)\Delta\bar{\theta}(j\omega) + \\ \frac{\beta E_b A_b \varphi_b \Delta\bar{\theta}_b(j\omega) - \beta\left((1-\mu_b)A_p\frac{c_{31}^E}{c_{33}^E} + \mu_b A_b\frac{A_{ps}}{A_{bs}}\right)T_3(j\omega)}{E_b A_b+\alpha(1-\mu_b)A_p} + \frac{e_{33}}{c_{33}^E}T_3(j\omega)\end{array}\right] \tag{4.35}$$

$$\mathrm{Q}(s) = A_s\left[\begin{array}{c}\left(2e_{31}\varphi_{p1}^E + e_{33}\varphi_{p3}^E + p^s - \frac{\beta E_b A_b \varphi_{p1}^E}{E_b A_b+\alpha(1-\mu_b)A_p}\right)\Delta\bar{\theta}(s) + \\ \frac{\beta E_b A_b \varphi_b \Delta\bar{\theta}_b(s) - \beta\left((1-\mu_b)A_p\frac{c_{31}^E}{c_{33}^E} + \mu_b A_b\frac{A_{ps}}{A_{bs}}\right)T_3(s)}{E_b A_b+\alpha(1-\mu_b)A_p} + \frac{e_{33}}{c_{33}^E}T_3(s)\end{array}\right] \tag{7.11}$$

$$\mathrm{Q}_\theta(j\omega) = A_s\left[\begin{array}{c}\left(2e_{31}\varphi_{p1}^E + e_{33}\varphi_{p3}^E + p^s - \frac{\beta E_b A_b \varphi_{p1}^E}{E_b A_b+\alpha(1-\mu_b)A_p}\right)\Delta\bar{\theta}(j\omega) \\ + \frac{\beta E_b A_b \varphi_b}{E_b A_b+\alpha(1-\mu_b)A_p}\Delta\bar{\theta}_b(j\omega)\end{array}\right] \tag{7.12}$$

$$\mathrm{Q}_\theta(s) = A_s\left[\begin{array}{c}\left(2e_{31}\varphi_{p1}^E + e_{33}\varphi_{p3}^E + p^s - \frac{\beta E_b A_b \varphi_{p1}^E}{E_b A_b+\alpha(1-\mu_b)A_p}\right)\Delta\bar{\theta}(s) \\ + \frac{\beta E_b A_b \varphi_b}{E_b A_b+\alpha(1-\mu_b)A_p}\Delta\bar{\theta}_b(s)\end{array}\right] \tag{7.13}$$

The sensor output voltage response, V_{out} to a surface temperature change is therefore modelled by substituting the Fourier and Laplace domain expressions for $\Delta\bar{\theta}$ and $\Delta\bar{\theta}_b$ derived in Section 4.9 and 4.10 into Equation 7.12 and 7.13 respectively with further substitution of Equation 7.12 and 7.13 into the appropriate Fourier or Laplace output voltage response models given by Equation 7.9 or Equation 7.10.

7.6.2 Signal conditioning response decay effects

Measurements using charge-mode type signal conditioning are made during a decaying transient that occurs due to the necessity of using finite resistances R_f in the feedback network. As discussed in Chapter 6, these feedback resistors are required to adequately limit the influence of drift due to operational amplifier bias current, bias current offset and voltage offset mechanisms. These mechanisms produce a continuous current that flows onto the feedback capacitances, increasing the output voltage to saturation linearly with time. It is therefore desirable to investigate the effect of a finite R_f on the amplitude and phase of the measured temperature change during the slow decay present during measurement. It is required that during the measurement period the frequency and time dependent phase and amplitude do not depart significantly from that of the thermal signal to ensure that measurements adequately represent the temperature being measured to a specified accuracy.

Using the charge-mode amplifier response model given by Equation 7.10, the amplifier output voltage can be written in Laplace form as given by Equation 7.14 where $\mathrm{Q}_\theta(s)$ is the Laplace domain negative bound surface charge due to a spatial mean temperature change in the piezoelectric medium as discussed in Section 4.8. The forward difference stage gain is set to $G = R_3/R_3 = 0.5$ and R_s is set to zero since its effect on the low frequencies of interest is small. This is a reasonable assumption since R_s, which is approximately 100Ω, introduces a high frequency $-3db$ roll-off at $f_c = 1/4\pi R_s C_p \approx 40kHz$.

$$V_{out}(s) = \frac{s\mathrm{Q}_\theta(s)}{C_f\left(s+\frac{1}{R_f C_f}\right)} \tag{7.14}$$

By considering that $\mathrm{Q}_\theta(t)$ is sinusoidal and in the steady state at a frequency of ω_o, then $\mathrm{Q}_\theta(t)$ can be represented by $\mathrm{Q}_\theta(t) = \widehat{\mathrm{Q}}_\theta(\omega_o)e^{j(\omega_o t - \nu(\omega_o))}$, where $\widehat{\mathrm{Q}}_\theta(\omega_o)$ and $\nu(\omega_o)$ are the frequency dependent amplitude and frequency dependent phase relative to $\Delta\theta_{skin}(j\omega)$. $\widehat{\mathrm{Q}}_\theta(\omega_o)$ and $\nu(\omega_o)$ are determined by the thermal properties of the PZT sensor element and liner. $V_{out}(s)$ is therefore given by

Equation 7.15 where the standard Laplace transform $\mathcal{L}\{e^{\omega_o t}\} = 1/(s - j\omega_o)$ has been used.

$$V_{out}(s) = \frac{s\widehat{\mathrm{Q}}_\theta(\omega_o)e^{-j(\nu(\omega_o))}}{C_f(s-j\omega_o)\left(s+\frac{1}{R_f C_f}\right)} \tag{7.15}$$

Inverse Laplace transforming Equation 7.15 yields Equation 7.16.

$$V_{out}(t) = \widehat{\mathrm{Q}}_\theta(\omega_o)\frac{\left(j\omega_o+\frac{1}{R_f C_f}e^{-\left(\frac{1}{R_f C_f}+j\omega_o\right)t}\right)}{C_f\left(j\omega_o+\frac{1}{R_f C_f}\right)}e^{j(\omega_o t-\nu(\omega_o))} \tag{7.16}$$

The angle and absolute values of $V_{out}(t)e^{-j\omega_o t}$ yields the time and frequency dependent phase and amplitude at the amplifier output relative to the measurand $\Delta\theta_{skin}(t)$ respectively. By writing Equation 7.16 fully in polar form, it can be seen that for a particular ω_o, $V_{out}(t)$ is a phase and amplitude modulated version of the ideal constant amplitude and phase output voltage, $V_{out}(t)_{ideal}$ given by Equation 7.17.

$$V_{out}(t)_{ideal} = \frac{\widehat{\mathrm{Q}}_\theta(\omega_o)}{C_f}e^{j(\omega_o t-\nu(\omega_o))} \tag{7.17}$$

The steady state response can be found by letting $t \to \infty$ in Equation 7.16, or equivalently by letting $s = j\omega$ in Equation 7.14 and substituting the Fourier transform of $\mathrm{Q}_\theta(t)$ which is given by $\mathrm{Q}_\theta(j\omega) = 2\pi\widehat{\mathrm{Q}}_\theta\delta(\omega - \omega_o)e^{-j\nu(\omega_o)}$ followed by taking the inverse Fourier transform to yield the same result. It can also be seen from Equation 7.16 that letting R_f get very large, such that the decay time constant $\tau_d = R_f C_f \to \infty$, that the output voltage response approaches the ideal response given by $V_{out}(t)_{ideal}$. The ideal response is also obtained at $t = 0$ irrespective of the value of R_f. At $\omega_o = 0$, it can be seen that as $t \to \infty$, the amplifier response decays to zero with the decay time constant of $\tau_d = R_f C_f$.

A time frequency analysis that includes the effect of the thermal transient nature of the combined sensor element, charge-mode conditioning amplifier and liner and that describes the time dependent phase and amplitude response at V_{out} to an applied temperature change $\Delta\theta_{skin}(t)$ is described in Section 7.7. The analysis,

which is based on the mathematical models described in Section 7.6.1, uses a Padé approximant method to obtain the time frequency responses for the cases of temperature measurement with the sensor element placed directly on the measurement surface, and with an elastomer liner placed between the sensor and measurement surface.

7.6.3 The Padé approximant method

The time-domain response of the sensor and signal conditioning can be found by taking inverse Laplace transforms of the Laplace domain mathematical models derived and described in Chapter 4. As discussed in Section 4.9.1, finding the precise inverse Laplace transform is an intractable task for all but the simplest cases. If required, the exact inverse Laplace transform can be obtained by using tables of standard fractional inverse Laplace transforms together with the well-known sum to infinite relationship for geometric expansions or using a Maclaurin expansion. The resulting solution is in terms of infinite sums of complementary error functions and a convergent solution will require the summation of a large number of error functions with the required number increasing as the required time period increases. In addition, the calculation is extremely tedious for all but the simplest transfer functions, produces an unintuitive result and renders no more useful information than can be found using the Padé approximant approach.

The Padé approximant method involves equating a ratio of polynomials of unknown coefficients to a suitably truncated Taylor series of the function to be approximated. The procedure is to first select the orders of the numerator and denominator polynomials and normalise the denominator polynomial such that the zero order term is equal to one. This is followed by multiplying both sides by the denominator polynomial and equating the powers of both sides to yield a set of equations in the polynomial coefficients. The final step is to solve the set of equations simultaneously to evaluate the polynomial coefficients and therefore the approximant. The order of both denominator and numerator polynomials required to adequately approximate a function is determined by trial and error, with the initial requirements that the resulting Laplace domain approximant must have no right hand

Laplace plane poles and that the numerator order must be less than or equal to the denominator order. The approximation is improved at the cost of computing time by using as high an order as possible for both numerator and denominator polynomials such that the difference in denominator and numerator orders is constant.

7.6.4 Verification of the Padé approximant method

To obtain the required time-frequency models, the inverse Laplace transforms of the mathematical models described in Section 7.6.1 are required. However, determining an exact solution is an extremely tedious if not intractable problem. To circumvent this problem, a response was computed symbolically in Matlab using the Padé and ilaplace functionality to allow an approximate time domain response function with variables of liner thickness, frequency and time. To verify the application of the Padé approximant method, the time domain response of the approximant was compared to the exact solution of the temperature at the insulated surface of a silicone elastomer liner, which is relatively easy to calculate, in response to an applied temperature on the outside surface. The transient response to a temperature step of $1°C$ using the exact solution and the Padé approximant are compared, while the steady state amplitude and phase frequency responses are compared using the Padé approximant solution with a 'steady state' time set to $t = 10^{10}\ seconds$ in Matlab, and directly using the absolute and angle values of the associated Fourier transfer function.

Equation 4.134 for the limiting case $l_b, l_p \ll l_e$ such that the thermal effects of the sensor are considered negligible, and as before $\Delta\theta_s(s)$ is the temperature at the sensor surface and is repeated below for ease of reference.

$$\Delta\theta_s(s) = \frac{\Delta\theta_{skin}(s)}{\cosh\sqrt{\frac{s}{K_e}}l_e} \tag{4.134}$$

Expanding the denominator of Equation 4.134, followed by multiplication of the numerator and denominator by $exp\left(-l_e\sqrt{s/K_e}\right)$, yields Equation 7.18 for the temperature on the surface.

$$\Delta\theta_s(s) = \frac{2\, e^{-\sqrt{\frac{s}{K_e}}l_e}}{1+e^{-2\sqrt{\frac{s}{K_e}}l_e}}\Delta\theta_{skin}(s) \tag{7.18}$$

Using the relationship for the sum to infinite of a geometric series, the reciprocal of the denominator can be written as Equation 7.19 where the series always converges such that $re\{\sqrt{s/K_e}\} > 0$ and re denotes the real part.

$$\frac{1}{1+e^{-2\sqrt{\frac{s}{K_e}}l_e}} = \sum_{n=0}^{\infty}(-1)^n e^{-2n\sqrt{\frac{s}{K_e}}l_e} \tag{7.19}$$

Equation 7.19 can be also be obtained by computing a Maclaurin expansion of $1/(1+x^2)$, where $x = e^{-l_e\sqrt{s/K_e}}$.

Substituting Equation 7.19 into Equation 7.18 yields Equation 7.20.

$$\Delta\theta_s(s) = 2\sum_{n=0}^{\infty}(-1)^n e^{-(2n+1)\sqrt{\frac{s}{K_e}}l_e}\,\Delta\theta_{skin}(s) \tag{7.20}$$

Representing the applied temperature by a complex exponential at frequency ω_o such that $\Delta\theta_{skin}(s) = \Delta\hat{\theta}_{skin}/(s - j\omega_o)$ and substituting into Equation 7.20 yields Equation 7.21 for the temperature at the sensor surface $x = -l_b$.

$$\Delta\theta_s(s) = \frac{\Delta\hat{\theta}_{skin}}{\sqrt{j\omega_o}}\left(\frac{1}{\sqrt{s}+\sqrt{j\omega_o}} + \frac{1}{\sqrt{s}-\sqrt{j\omega_o}}\right)\sum_{0}^{\infty}(-1)^n e^{-(2n+1)\sqrt{\frac{s}{K_e}}l_e} \tag{7.21}$$

Using the standard fractional calculus inverse Laplace transforms $\mathcal{L}^{-1}\{e^{-\vartheta\sqrt{s}}/\sqrt{s}\} = (1/\sqrt{\pi t})exp(-\vartheta^2/4t)$ and $\mathcal{L}^{-1}\{e^{-\vartheta\sqrt{s}}/\sqrt{s}(\sqrt{s}+\sqrt{j\omega_o})\} = e^{j\omega_o t}e^{\vartheta\sqrt{j\omega_o}}erfc(\sqrt{j\omega_o t} + \vartheta/2\sqrt{t})$, where ϑ is a constant, together with a partial fraction expansion where $erfc(x)$ is the complimentary error function given by $erfc(x) = 1 - (2/\pi)\int_0^x e^{-t^2}dt$ and noting that $erfc(\infty) = (2/\pi)\int_0^\infty e^{-t^2}dt = 1$ to yield $erfc(x) = (2/\pi)\int_x^\infty e^{-t^2}dt$, and applying to Equation 7.21, the sinusoidal temperature step response is given by Equation 7.22.

$$\Delta\theta_s(t) = \Delta\hat{\theta}_{skin} e^{j\omega_o t} \sum_{n=0}^{\infty} (-1)^n \left\{ \begin{array}{l} \left(e^{-\frac{(2n+1)l_e}{2\sqrt{K_e t}}\sqrt{j\omega_o}} \right) erfc\left(\frac{(2n+1)l_e}{2\sqrt{K_e t}} - \sqrt{j\omega_o t} \right) + \\ \left(e^{\frac{(2n+1)l_e}{2\sqrt{K_e t}}\sqrt{j\omega_o}} \right) erfc\left(\frac{(2n+1)l_e}{2\sqrt{K_e t}} + \sqrt{j\omega_o t} \right) \end{array} \right\}$$

(7.22)

Setting $\omega_o = 0$ to represent a $1°C$ Heaviside $\Delta\hat{\theta}_{skin}$ temperature step yields the response given by Equation 7.23.

$$\Delta\theta_s(t) = 2\Delta\hat{\theta}_{skin} \sum_{n=0}^{\infty} (-1)^n erfc\left(\frac{(2n+1)l_e}{2\sqrt{K_e t}} \right) \tag{7.23}$$

Using Matlab, it is found that $\lim_{t\to\infty} \sum_{n=0}^{\infty} (-1)^n erfc\left((2n+1)l_e/2\sqrt{K_e t}\right)$ is equal to 0.5 and therefore in the limit as $t \to \infty$, Equation 7.23 reduces to Equation 7.24 as expected for the boundary condition of zero heat flow at the sensor external surface such that $\Delta\theta_s(t) \to \Delta\hat{\theta}_{skin}$.

$$\lim_{t\to\infty} \Delta\theta_s(t) = 2\Delta\hat{\theta}_{skin} \lim_{t\to\infty} \sum_{n=0}^{\infty} (-1)^n erfc\left(\frac{(2n+1)l_e}{2\sqrt{K_e t}} \right) = \Delta\hat{\theta}_{skin} \tag{7.24}$$

The result of Equation 7.24 can also be found by using the Fourier form of Equation 4.134 given by Equation 4.135.

$$\Delta\theta_s(j\omega) = \frac{\Delta\hat{\theta}_{skin}(j\omega)}{\cosh(1+j)\sqrt{\frac{\omega}{2K_e}} l_e} \tag{4.135}$$

Considering a sinusoidal excitation $\Delta\hat{\theta}_{skin} e^{j\omega_o t}$ to have existed for all time such that the Fourier transform is given by $\Delta\theta_{skin}(j\omega) = 2\pi\Delta\hat{\theta}_{skin}\delta(\omega - \omega_o)$, then substitution into Equation 4.135 yields Equation 7.25 where δ is the Dirac impulse function.

$$\Delta\theta_s(j\omega) = \frac{2\pi\Delta\hat{\theta}_{skin}\delta(\omega-\omega_o)}{\cosh(1+j)\sqrt{\frac{\omega_o}{2K_e}} l_e} \tag{7.25}$$

Taking the inverse Fourier transform of Equation 7.25 and rearranging yields Equation 7.26.

$$\Delta\theta_s(t) = \frac{\Delta\hat{\theta}_{skin}\, e^{j\omega_o t}}{\cosh(1+j)\sqrt{\frac{\omega_o}{2K_e}}l_e} = \frac{\Delta\hat{\theta}_{skin}\, e^{j\left(\omega_o t - arctan\left(tanh\sqrt{\frac{\omega_o}{2K_e}}l_e\, tan\sqrt{\frac{\omega_o}{2K_e}}l_e\right)\right)}}{\sqrt{\cos^2\sqrt{\frac{\omega_o}{2K_e}}l_e + \sinh^2\sqrt{\frac{\omega_o}{2K_e}}l_e}} \tag{7.26}$$

Setting $\omega_o = 0$ in Equation 7.26 gives the desired result of the steady state $\Delta\theta_s(t) = \Delta\hat{\theta}_{skin}$. The phase and amplitude response are given by the $arctan$ term in the exponent and the reciprocal of the denominator term respectively.

Using Equation 7.23, the temperature transient response $\Delta\theta_s(t)$ to a $\Delta\hat{\theta}_{skin} = 1°C$ Heaviside step for different typical elastomer liner thicknesses, denoted by l_e, was calculated using Matlab and is shown in Figure 7.7 where the summation was truncated at $n = 90$. The choice of $n = 90$ ensured the sufficient convergence of $\Delta\theta_s(t)$ up to $t = 10{,}000\ seconds$. However, for longer observation times, a greater value of n is required to avoid a divergent result. The complimentary error function $erfc$ terms in Equation 7.22 were replaced by imaginary error function $erfi$ terms to allow the evaluation of complex error function arguments in Matlab, where the relationship between the $erfc$ and $erfi$ functions is given by $erfc(x) = 1 - j \times erfi(-jx)$.

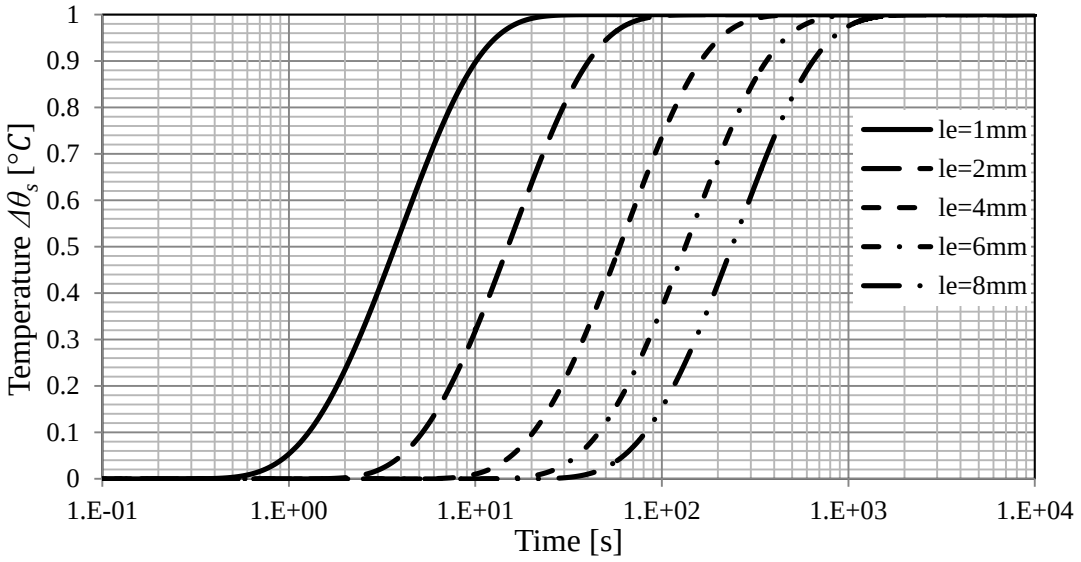

Figure 7.7 Liner surface temperature response to a $1°C$ step, $n = 90$, $0Hz$

The liner surface temperature response for the same $\Delta\hat{\theta}_{skin} = 1°C$ $0Hz$ Heaviside step was also obtained by applying a Padé approximant of order of zero in

the numerator and six in the denominator (one zero and six poles), which is denoted by [0,6], to Equation 4.134 and is shown in Figure 7.8.

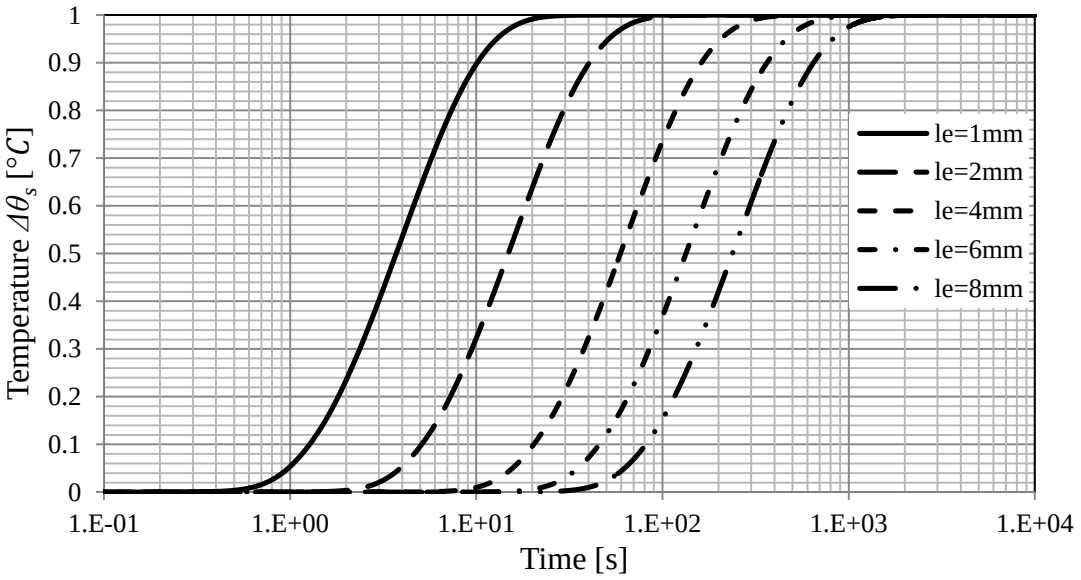

Figure 7.8 Liner surface temperature response to a $1°C$ step, Padé [0,6], $0Hz$

It can be seen from Figure 7.8 that the Padé approximant response very closely matches the 'exact' error function response given by Figure 7.7 for $n = 90$ and a duration of $10^4\,seconds$. The steady state Padé approximant frequency response and the steady state frequency response for both amplitude and phase were obtained from the absolute and angle values of the Padé approximant time domain response at a time of $10^{10}s$ to approximate the steady state, and Equation 4.135 for a frequency range of $1\,nrads^{-1}$ to $1\,rads^{-1}$ for different liner thicknesses. Figure 7.9 and Figure 7.10 show the amplitude response using the Fourier transfer function of Equation 4.135 and the Padé approximant respectively, while Figure 7.11 and Figure 7.12 show the phase response using Equation 4.135 and the steady state Padé approximant response respectively.

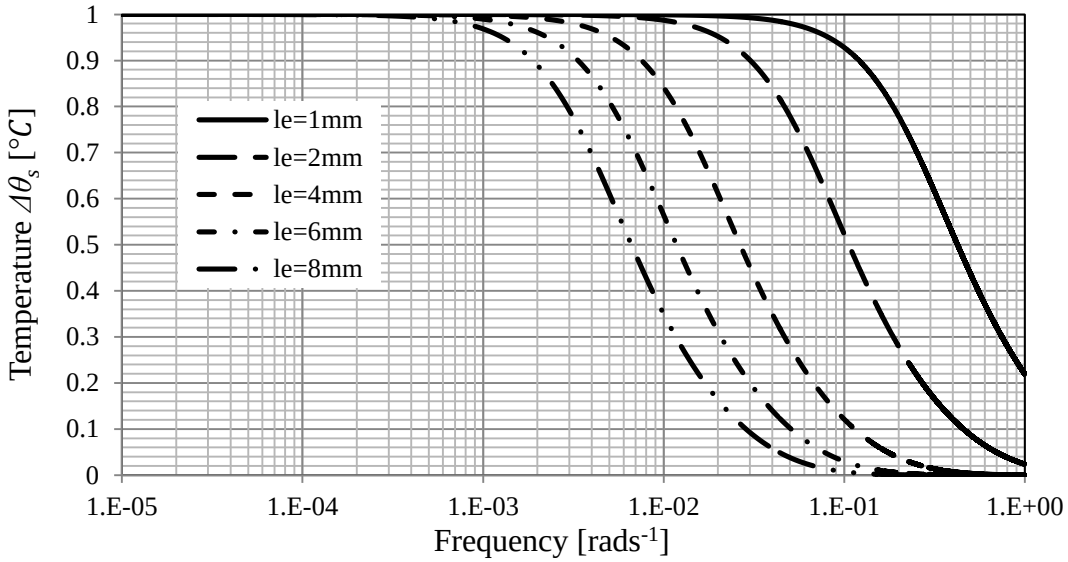

Figure 7.9 Liner $\Delta\theta_s$ steady state amplitude response vs frequency - Fourier

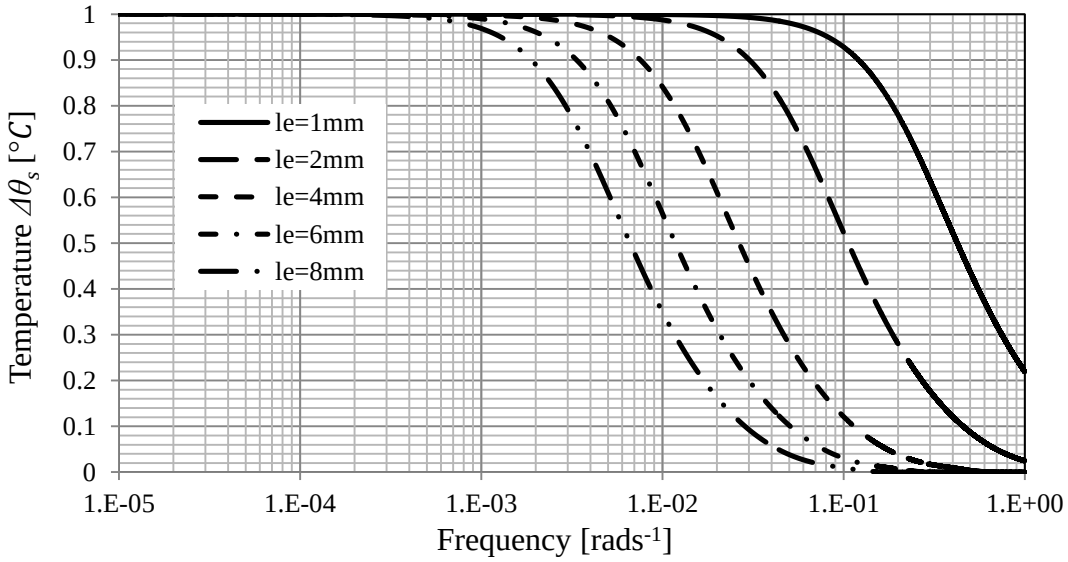

Figure 7.10 Liner $\Delta\theta_s$ steady state amplitude response vs frequency - Padé [0,6]

It can be seen from Figure 7.10 that the Padé approximant amplitude response very closely matches the Fourier transfer function response given by Figure 7.9 over the frequency range $10\mu rads^{-1}$ to $1rads^{-1}$. Both responses were calculated down to $1nrads^{-1}$, however since the calculated amplitude values below $10\mu rads^{-1}$ are almost equal, these values are omitted for clarity.

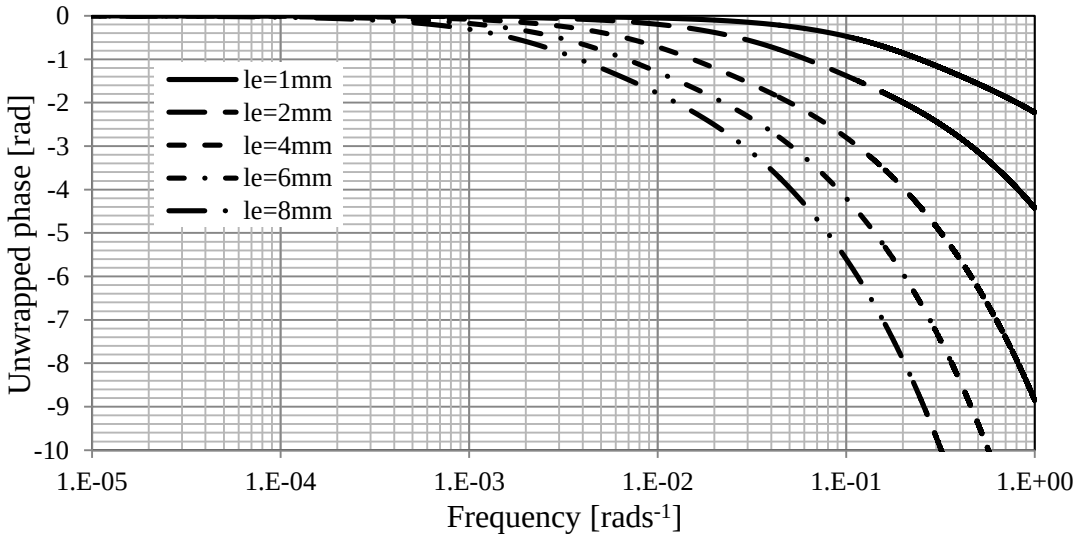

Figure 7.11 Liner $\Delta\theta_s$ steady state phase response vs frequency - Fourier

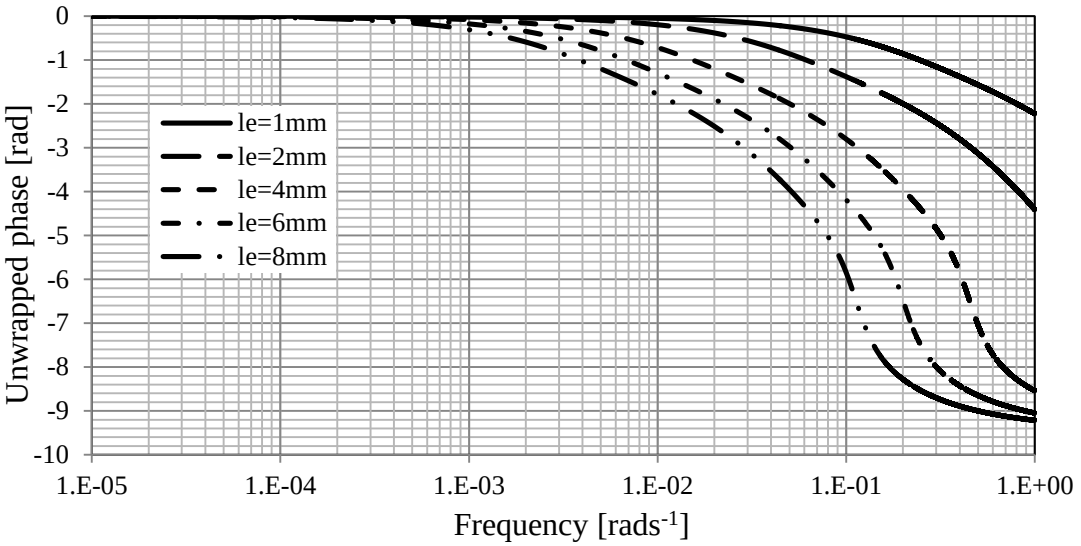

Figure 7.12 Liner $\Delta\theta_s$ temperature steady state phase vs frequency, Padé [0,6]

It can be seen from Figure 7.12 that for the $l_e = 1mm$ and $l_e = 2mm$ thicknesses, the Padé approximant phase response very closely matches the exact Fourier transfer function phase response given by Figure 7.11 over the frequency range $10\mu rads^{-1}$ to $1rads^{-1}$. However when $l_e = 4mm$, $6mm$ and $8mm$ the Padé approximant departs from the exact phase response of Figure 7.11 at frequencies of approximately $0.3rads^{-1}$, $0.15rads^{-1}$ and $0.1rads^{-1}$ respectively.

Notwithstanding the departure in phase response predicted by the Padé approximant method at higher frequencies, the very close match in the transient and steady state amplitude responses up to a frequency of $1rads^{-1}$ confirms the Padé

approximant method as a sufficiently robust solution to obtain the required inverse Laplace transforms of the hyperbolic mathematical models described in Chapter 4.

7.7 Sensor temperature response – time-frequency analysis

7.7.1 Methodology

The Padé approximant method was applied using Matlab to identify the appropriate Padé numerator and denominator polynomial orders, which is denoted by [Numerator, Denominator], for the cases of with and without the presence of an elastomer liner between the sensor element and measurement surface. The Padé approximant orders that yield intuitively reasonable results within an acceptable computing time are [3,4] and [0,6] respectively. The Padé [3,4] approximant was applied to the spatial mean substrate and spatial mean piezoelectric temperature transfer function models given by $\Delta\bar{\theta}(s)/\Delta\theta_s(s)$ and $\Delta\bar{\theta}_b(s)/\Delta\theta_s(s)$ respectively using Equation 4.117 and Equation 4.118 for a temperature change applied at the substrate surface such that $l_e = 0mm$ and $\Delta\theta_s(s) = \Delta\theta_{skin}(s)$. Similarly, a Padé [0,6] approximant was applied to the spatial mean substrate and piezoelectric temperature transfer function models using Equation 4.128 and Equation 4.129 for a temperature change $\Delta\theta_{skin}(s)$ applied to the surface of an elastomer liner for typical thicknesses of $l_e = 1mm$ to $8mm$.

The thermal responses of the liner and piezoelectric element introduce significant transient effects to the signal presented at the signal conditioning amplifier input. In addition, the thermal signal low frequency components continuously decay at the amplifier output during the measurement period as discussed in Section 7.6.2. It is therefore important to investigate the effect of the whole sensor system on the signal conditioning output frequency response over the measurement period to determine how faithfully the response represents the measured interface temperature signal. To investigate the time-frequency behaviour of the sensor element and charge amplifier in terms of the transient and frequency responses to a general applied surface skin temperature signal, $\Delta\theta_{skin}(s)$, the skin temperature was modelled by a unit amplitude complex exponential test function,

such that $\Delta\theta_{skin}(s) = 1/(s - j\omega_o)$, to represent a $1°C$ peak amplitude sinusoidal skin temperature at a frequency of ω_o. The use of a complex exponential model function provides the generality required to analyse the effects of the sensor and signal-conditioning amplifier on the phase and amplitude of the frequencies contained in the input temperature signal. Similar to the principle used in the derivation of the discrete Fourier transform (DFT), the reasoning here is that any real world time-limited signal such as the temperature signal measured by the sensor can, in mathematical terms be made periodic with a period equal to the signal duration, denoted by T_d, which is in this case 8 $hours$. The associated fundamental frequency is therefore given by $\omega_d = 2\pi/T_d$. The resulting periodic signal can therefore be written as a Fourier series sum of discrete complex exponentials at harmonics of ω_d such that $\omega_d = 2\pi d/T_d$ to yield Equation 7.27 and Equation 7.28 where $\Delta\theta_{skin}(j\omega_d)$ is the Fourier transform of the temperature signal over the period $t = 0 \rightarrow T_d$.

$$\Delta\theta_{skin}(t)_{periodic} = \sum_{d=-\infty}^{\infty} C_d e^{j\omega_d t} \tag{7.27}$$

$$C_d = \frac{1}{T_d}\int_0^{T_d} \Delta\theta_{skin}(t) e^{-j\omega_d t}\, dt = \frac{\Delta\theta_{skin}(j\omega_d)}{T_d} \tag{7.28}$$

Taking the Laplace transform over one period $t = 0 \rightarrow T_d$ of the Fourier series representation given by Equation 7.27 yields Equation 7.29 for the Laplace transform of the time-limited signal.

$$\Delta\theta_{skin}(s) = \mathcal{L}\{\Delta\theta_{skin}(t)\} = \frac{1}{T_d}\sum_{d=-\infty}^{\infty} \Delta\theta_{skin}(j\omega_d)\frac{(1-e^{-sT_d})}{(s-j\omega_d)} \tag{7.29}$$

A complete description of the Laplace transform of the real-world time-limited temperature signal is therefore given by the Laplace transform of an infinite summation of complex exponentials. Each complex exponential is at a discrete multiple of the fundamental frequency and weighted by the value of the product of the reciprocal of the period and the Fourier transform evaluated at each harmonic of the fundamental frequency. The time delay term e^{-sT_d} in the numerator of Equation 7.29 ensures that the signal is zero beyond time T_d as required. The use of a complex exponential model test function, such that $\Delta\theta_{skin}(s) = 1/(s - j\omega_o)$, therefore provides the generality required to allow the effect of the sensor and signal-

conditioning amplifier on the phase and amplitude of the frequencies contained in the input temperature signal to be analysed.

The Padé approximant models were substituted into Equation 7.30 for the $\Delta\theta_{skin}(s)$ to charge transfer function given by $\mathrm{Q}_{tf}(s)$, with $\mathrm{Q}_{tf}(s)$ and $\Delta\theta_{skin}(s) = 1/(s - j\omega_o)$ substituted into the charge amplifier Laplace domain output voltage given by Equation 7.31. The forward difference gain was set to $G = R_3/R_2 = 0.5$.

$$\mathrm{Q}_{tf}(s) = \frac{\mathrm{Q}(s)}{\Delta\theta_{skin}(s)} = A_s \left[\begin{array}{c} \left(2e_{31}\varphi_{p1}^{E} + e_{33}\varphi_{p3}^{E} + p^{s} - \frac{\beta E_b A_b \varphi_{p1}^{E}}{E_b A_b + \alpha(1-\mu_b)A_p}\right)\frac{\Delta\bar{\theta}(s)}{\Delta\theta_{skin}(s)} \\ + \frac{\beta E_b A_b \varphi_b}{E_b A_b + \alpha(1-\mu_b)A_p}\frac{\Delta\bar{\theta}_b(s)}{\Delta\theta_{skin}(s)} \end{array} \right] \tag{7.30}$$

$$V_{out}(s) = \frac{R_3 s \ \text{Padé}\{\mathrm{Q}_{tf}(s)\}}{R_2 R_s C_p C_f (s - j\omega_o)\left(s + \frac{1}{R_f C_f}\right)\left(s + \frac{1}{2R_s C_p}\right)} = \left[\frac{s \ \text{Padé}\{\mathrm{Q}_{tf}(s)\}}{2R_s C_p C_f (s - j\omega_o)\left(s + \frac{1}{R_f C_f}\right)\left(s + \frac{1}{2R_s C_p}\right)}\right]_{G=0.5} \tag{7.31}$$

The inverse Laplace transform of Equation 7.31 was evaluated using the Matlab symbolic ilaplace functionality for liner thicknesses of $l_e = 0mm, 1mm, 2mm, 4mm, 6mm$ and $8mm$ to yield the time domain transient responses for each l_e in terms of both time and the applied frequency ω_o. By choosing a particular time, t_o and setting $\omega_o = \omega$ to signify that the frequency is now treated as a variable, the instantaneous frequency response of the combined charge amplifier and thermal charge transfer function can then be plotted in terms of the amplitude, phase and phase delay as a function of frequency using the Matlab abs and $angle$ functionality $abs\left(V_{out}(t_o, \omega)\right)$, $angle\left(e^{-j\omega_o t} V_{out}(t_o, \omega)\right)$ and $-angle\left(e^{-j\omega t_o} V_{out}(t_o, \omega)\right)/\omega$ respectively.

Similarly, by choosing a particular $\omega = \omega_o$, the transient response of the combined charge amplifier and charge transfer function can then be plotted in terms of the amplitude, phase and phase delay as a function of time from $abs\left(V_{out}(t, \omega_o)\right)$, $angle\left(e^{-j\omega_o t} V_{out}(t, \omega_o)\right)$ and $-angle\left(e^{-j\omega_o t} V_{out}(t, \omega_o)\right)/\omega_o$ respectively. In

the following sections the amplitude, phase and phase delay are plotted as functions of both time and frequency for liner thicknesses of $l_e = 0mm$, $1mm$ and $8mm$ using 3-d surface plots to provide a clearer analysis of the time-frequency response behaviours. The 3-d plots were obtained using the Matlab 'surfl' surface plotting functionality that provides surface lighting tools.

7.7.2 Transient response: $l_e = 0mm$

The amplifier $V_{out}(t)$ transient response to a $1°C$ step temperature change at $\omega_o = 0\, rads^{-1}$ is given in Figure 7.13. The maximum temperature to voltage conversion factor is $CF = 0.1476\, V/K$, which is calculated using the Matlab scripts and the relevant brass substrate and PZT-5H material constants listed in Appendix A.1. It can be seen that this value of CF agrees well with that determined experimentally in Sections 7.3 and 7.5.

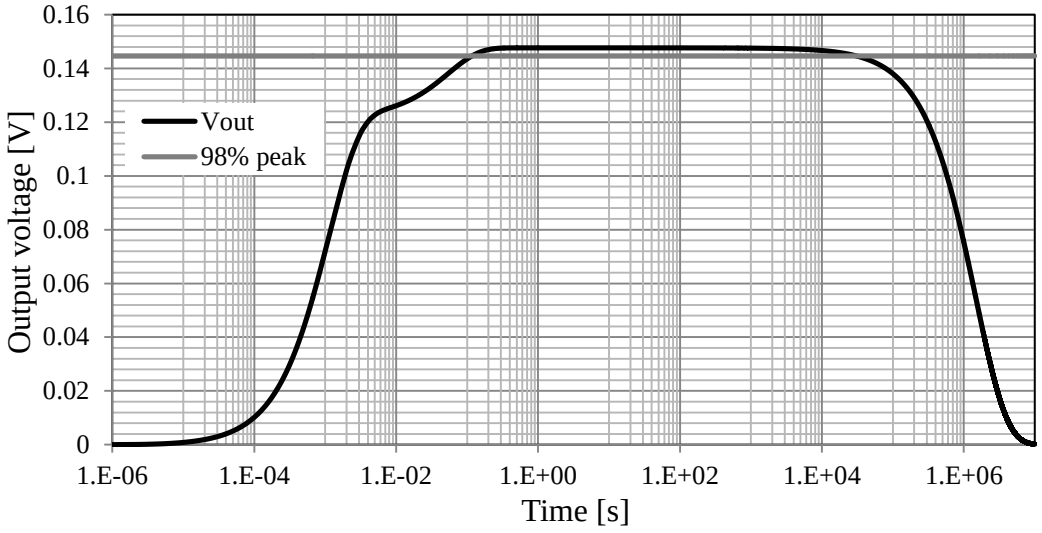

Figure 7.13 Amplifier V_{out} temperature response to a $1°C$ step, Padé [3,4], $0Hz$

It can be seen from Figure 7.13 that the response rises to a peak of $0.1476V$ at approximately $0.9s$ after application of the $1°C$ step. The first part of the response from $t = 1\mu s$ to $5ms$ is due to thermal expansion in the brass substrate and, to a much lesser extent the rise time of the charge-conditioning amplifier, which is approximately $\tau_r = 4\mu s$. The second increase in response from $t = 5ms$ to the peak output at $0.9s$ is due to subsequent heating in the piezoelectric medium as heat

diffuses through the substrate, and is due mainly to a change in the polarisation of the piezoelectric medium via the primary pyroelectric coefficient. The subsequent response decay is due to the time constant of the amplifier charge stage feedback networks such that $\tau_f = R_f C_f = 1.5 \times 10^6 s$. The permitted 2% reduction in the peak output voltage, which is indicated by the 98% output voltage line, limits the operating time from approximately $0.12s$ to $29000s$ between the thermal rise time and the permitted amplifier response decay. The upper time limit therefore corresponds to the required operating time of $8\ hours$ $(28800s)$.

7.7.3 Time-frequency response: $l_e = 0mm$

The amplitude time-frequency response of the sensor to an applied temperature change at the substrate interface such that $l_e = 0mm$ is shown in Figure 7.14. The applied interface temperature is modelled by complex exponentials at different frequencies of amplitude $1K$ at the substrate surface as discussed in Section 7.7.1. By considering sequential time 'slices' parallel to the frequency axis, it can be seen that the amplitude frequency response at the signal-conditioning output evolves in time toward the steady state frequency response. Similarly by considering sequential frequency 'slices' parallel to the time axis, the transient amplitude behaviour of the sensor can be examined at different frequencies. Initially, the transient response is dominated by the thermal transient response of the piezoelectric medium and substrate; and the rise time of the signal-conditioning amplifier, while towards the steady state it is dominated by the signal conditioning amplifier decay time constant.

After periods of $0.12s$ and $0.18s$, the amplitude reaches the required 98% of peak value at frequencies of $10^{-10} rads^{-1}$ and $6.8 rads^{-1}$ respectively. As discussed in Section 7.7.2, the initial transient is due to heat transfer, first in the substrate, followed by the piezoelectric medium. After an operating period of $8\ hours$ corresponding to the data-tips at $2.9 \times 10^4 s$, the amplitude remains at approximately 98% of the peak value with a maximum amplitude of $0.1482V$ corresponding to 100.4% of the peak value at a frequency of $150 \mu rads^{-1}$.

It can therefore be stated that when the sensor is configured to measure the interface temperature at the substrate surface such that $l_e = 0mm$, that the amplitude frequency response is approximately constant and within the required specification such that it faithfully represents the interface temperature amplitude over the frequency range of DC to $6.8rads^{-1}$ for a measurement period of $0.18s$ to $2.9 \times 10^4 s$. At time periods greater than $2.9 \times 10^4 s$, it can be seen that the amplitude frequency response approaches a steady state that is dominated by the first order high pass response of the charge-conditioning amplifier at low frequencies, and by the thermal response of the sensor element at high frequencies. It can also be seen that in the steady state, closely approximated by the data-tips at $10^8 s$, the amplitude frequency response that satisfies the required specification is now limited to a frequency range of $3.3\mu rads^{-1}$ to $6.8rads^{-1}$. While this minimum frequency is extremely low, a real world temperature signal will contain significant DC and very low frequency components that will decay toward zero in the steady state. It cannot therefore be assumed that the sensor will faithfully represent the interface temperature amplitude at time periods greater than $2.9 \times 10^4 s$.

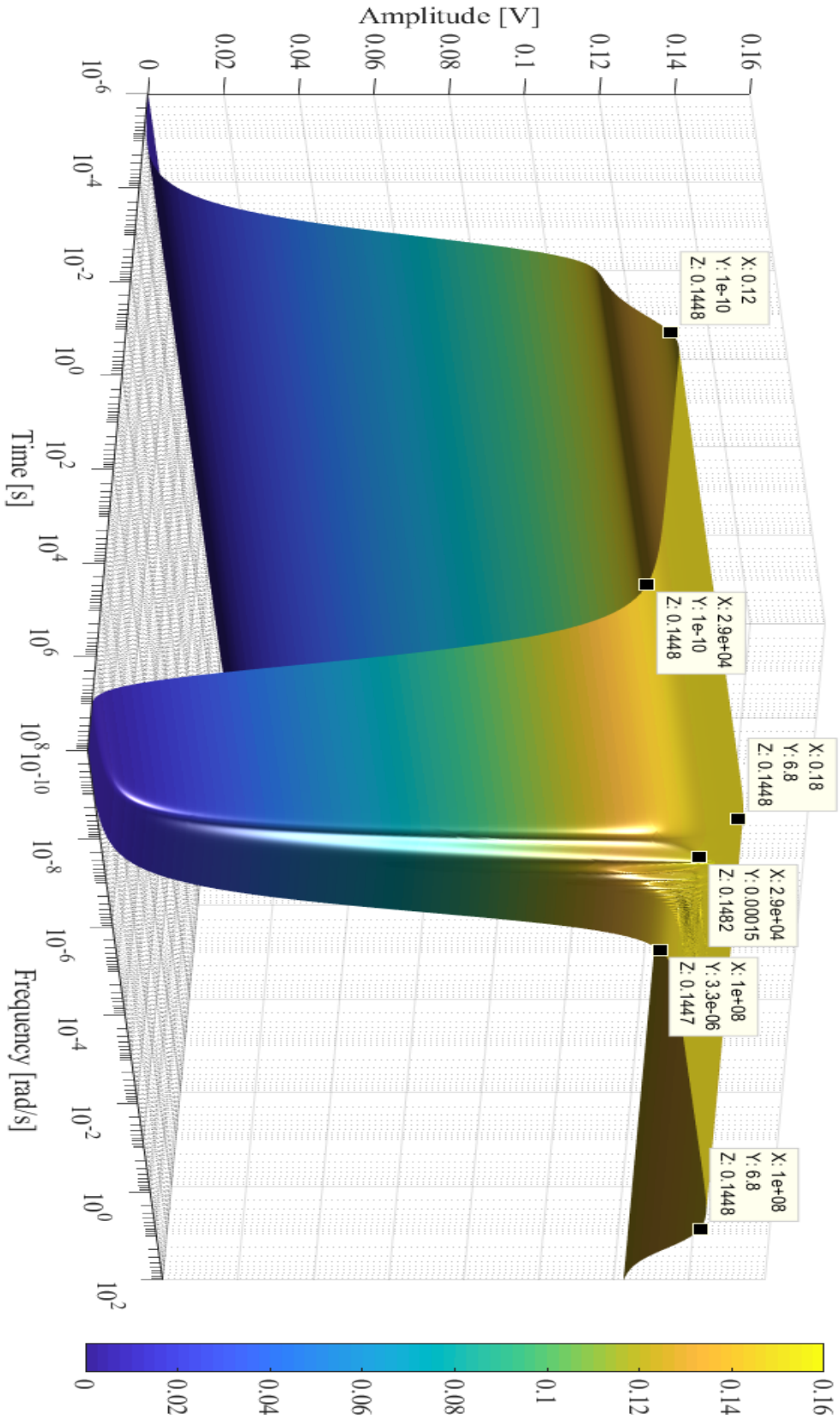

Figure 7.14 Amplitude time frequency plot at $l_e = 0mm$

The phase time-frequency response of the sensor at $l_e = 0mm$ is shown in Figure 7.15. By considering sequential time 'slices' parallel to the frequency axis, it can be seen that the phase frequency response at the signal-conditioning output evolves in time toward the steady state frequency response. Similarly by considering sequential frequency 'slices' parallel to the time axis, the transient phase behaviour of the sensor can be examined at different frequencies.

It can be seen from Figure 7.15 that after a period of $1\mu s$ the phase is $2.85 \times 10^{-8} rads$ and increases to $-4.45 \times 10^{-6} rads$ over the sensor operating frequency range of $10^{-10} rads^{-1}$ to $6.8 rads^{-1}$. After an operating period of $8\ hours$ corresponding to the data-tips at $2.9 \times 10^{4} s$, the phase remains at $2.85 \times 10^{-8} rads$ for a frequency of $10^{-10} rads^{-1}$, and reduces to $-0.065 rads$ at a frequency of $6.8 rads^{-1}$. The maximum phase over the sensor operating frequency range of $10^{-10} rads^{-1}$ to $6.8 rads^{-1}$ throughout an operating period of $8\ hours$ is $0.014 rads$ at a frequency of $8 \times 10^{-4} rads^{-1}$, which is equivalent to approximately 0.8°. It can therefore be stated that when the sensor is configured to measure the interface temperature at the substrate surface with $l_e = 0mm$, that the phase response is low over the frequency range of DC to $6.8 rads^{-1}$. The effect of the phase response on the input temperature signal is negligible and the sensor response will faithfully represent the interface temperature phase over this frequency range and over a measurement period of $10^{-6} s$ to $2.9 \times 10^{4} s$. At time periods greater than $2.9 \times 10^{4} s$, it can be seen that the phase frequency response approaches a steady state that is dominated by the first order high pass response of the charge-conditioning amplifier at low frequencies, and by the thermal response of the sensor element at high frequencies. It can also be seen that in the steady state, represented by the data-tips at $10^{8} s$, the phase increases from a minimum of $-0.065 rads$ at a frequency of $6.8 rads^{-1}$ to $\pi/2\ rads$ at $10^{-10} rads^{-1}$. Allowing a maximum phase shift of $0.2 rads$, the frequency is now limited to a range of $3.3\mu rads^{-1}$ to $6.8 rads^{-1}$. While this minimum frequency is extremely low, a real world temperature signal will contain significant DC and very low frequency components that exhibit large phase shifts and it cannot therefore be assumed that the sensor will faithfully represent the interface temperature phase at time periods greater than $2.9 \times 10^{4} s$.

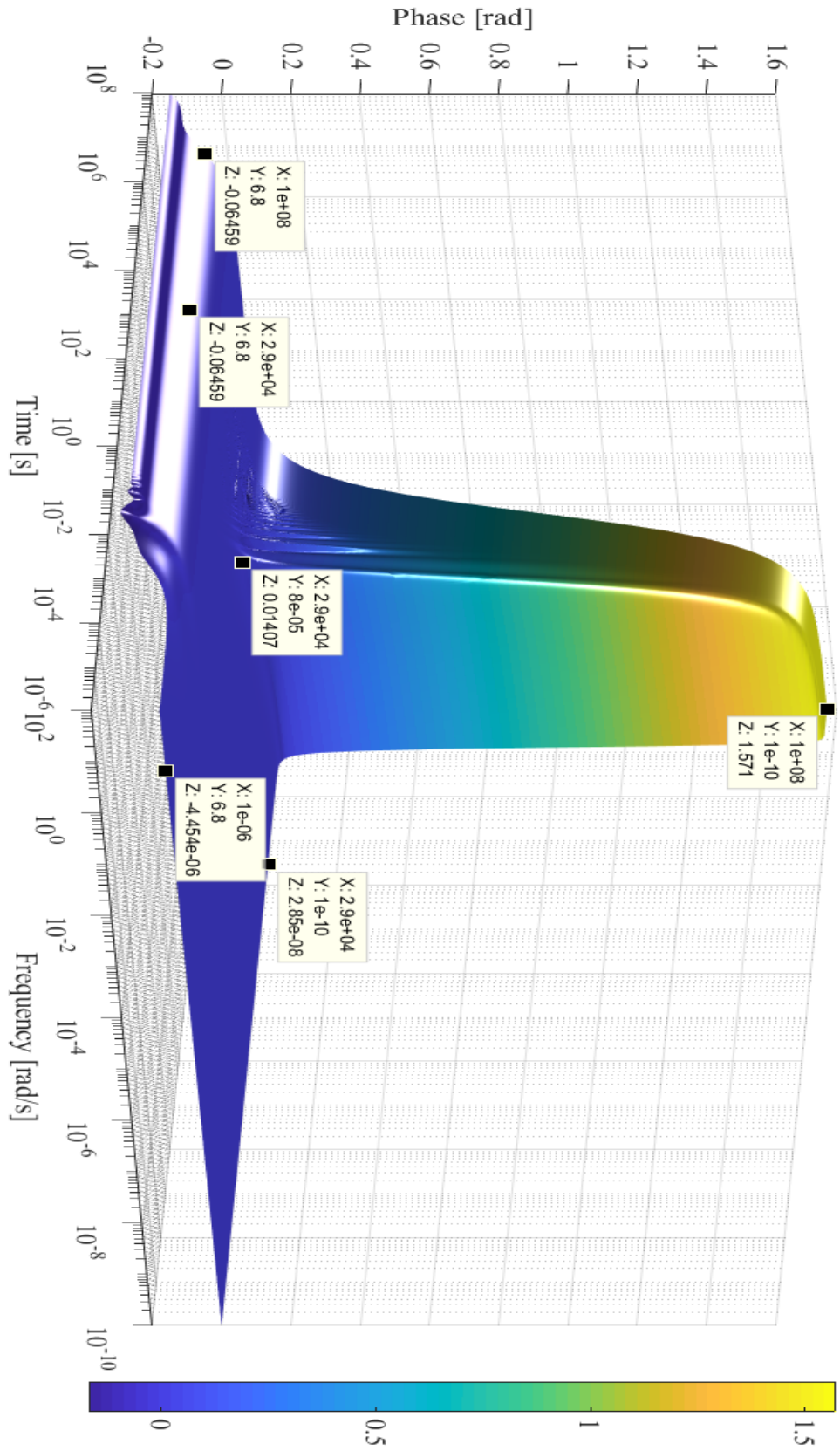

Figure 7.15 Phase time frequency plot at $l_e = 0mm$

The phase delay time-frequency response of the sensor at $l_e = 0mm$ is shown in Figure 7.16. By considering sequential time 'slices' parallel to the frequency axis, it can be seen that the phase delay frequency response at the signal-conditioning output evolves in time toward the steady state frequency response. Similarly by considering sequential frequency 'slices' parallel to the time axis, the transient phase delay behaviour of the sensor can be examined at different frequencies.

It can be seen from Figure 7.16 that after periods of $0.12s$ and $0.18s$ at frequencies of $10^{-10}rads^{-1}$ and $6.8rads^{-1}$ respectively, the phase delay is approximately constant at $0.008s$, inferring that the phase is approximately linear for all frequencies between $10^{-10}rads^{-1}$ and $6.8rads^{-1}$. The periods of $0.12s$ and $0.18s$ refer to the minimum time required for the amplitude response at all frequencies to reach the required 98% of peak value. After an operating period of $8\,hours$, corresponding to the data-tips at $2.9 \times 10^4 s$, the phase delay is approximately $0.009s$ at $6.8rads^{-1}$ and therefore remains very close to the corresponding value at $0.18s$. However, at a frequency of $10^{-10}rads^{-1}$ the phase delay increases to $285s$, while at an intermediate frequency of $10^{-4}rads^{-1}$, the phase delay is $131.5s$.

When compared to the period corresponding to each frequency, these phase delays are small and it can therefore be stated that when the sensor is configured to measure the interface temperature at the substrate surface with $l_e = 0mm$, that the phase delay can be considered low over the frequency range of DC to $6.8rads^{-1}$. Furthermore, the effect of the phase delay on the input temperature signal is negligible and the sensor response will faithfully represent the interface temperature for this frequency range over a measurement period of $0.18s$ to $2.9 \times 10^4 s$. At time periods greater than $2.9 \times 10^4 s$, the phase delay approaches a steady state that is dominated by the first order high pass response of the charge conditioning amplifier at low frequencies, and the phase delay increases steeply at frequencies below $3.3\mu rads^{-1}$. It cannot therefore be assumed that the sensor will faithfully represent the interface temperature signal at time periods greater than $2.9 \times 10^4 s$.

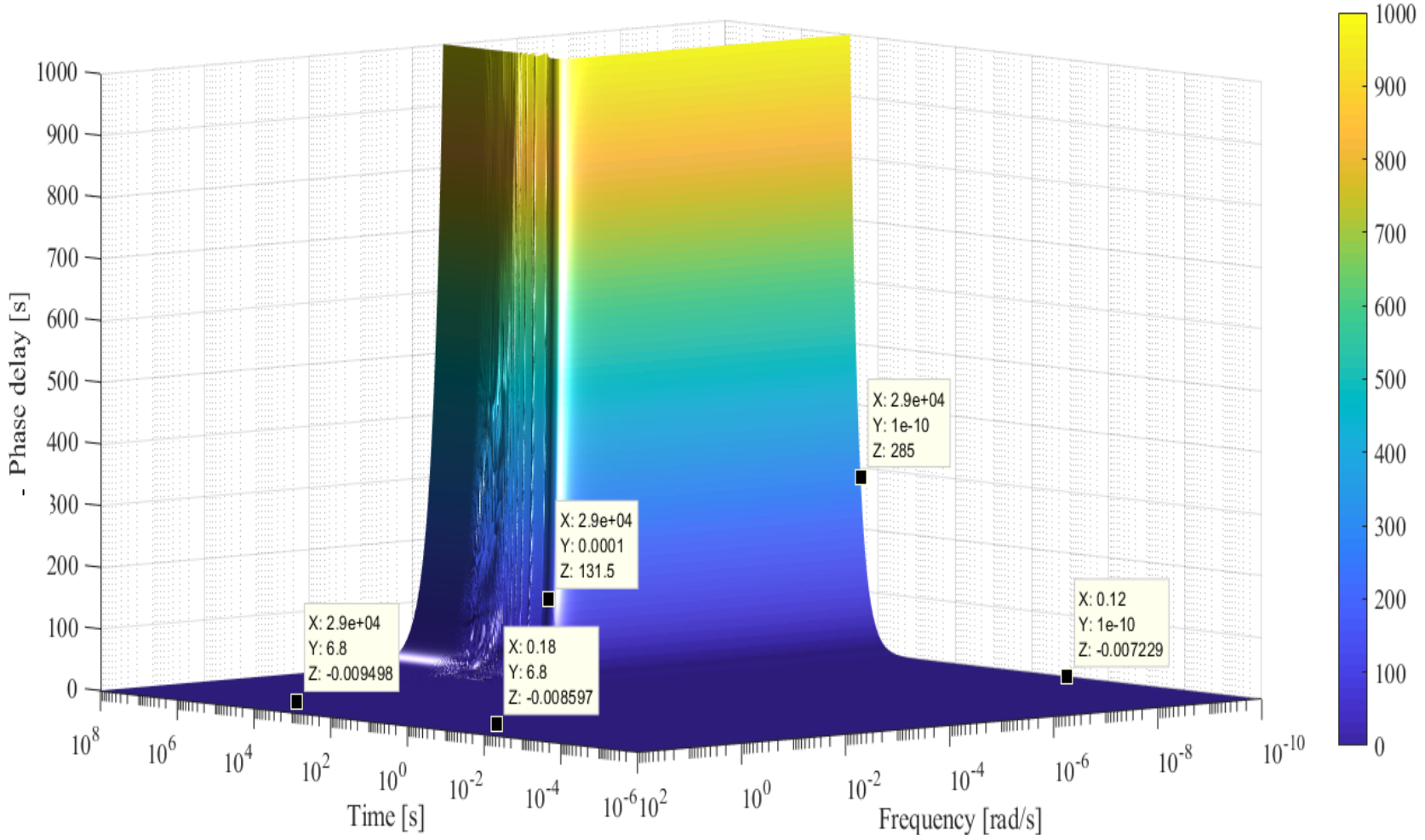

Figure 7.16 Negative phase delay time frequency plot at $l_e = 0mm$

7.7.4 Time-frequency response: $l_e = 1mm$

The amplitude time-frequency response of the sensor to an applied temperature change at the external liner interface with $l_e = 1mm$ is shown in Figure 7.17. The applied interface temperature is modelled by complex exponentials at different frequencies of amplitude $1K$ at the external liner surface as discussed in Section 7.7.1. Initially, the transient response is dominated by the thermal transient response of the elastomer liner, piezoelectric medium and substrate; and the rise time of the signal-conditioning amplifier, while towards the steady state it is dominated by the signal conditioning amplifier decay time constant.

After periods of $48s$ and $80s$, the amplitude reaches the required 98% of peak value at frequencies of $10^{-10}rads^{-1}$ and $17mrads^{-1}$ respectively. This initial transient is due to heat transfer, first in the liner followed by the substrate and piezoelectric medium. After an operating period of $8\,hours$ corresponding to the data-tips at $2.9 \times 10^4 s$, the amplitude remains at approximately 98% of the peak value.

It can therefore be stated that when the sensor is configured to measure the interface temperature at the external liner surface with $l_e = 1mm$, that the amplitude frequency response is approximately constant and within the required specification. However, this amplitude response now faithfully represents the interface temperature amplitude only over a restricted frequency range of DC to $17mrads^{-1}$ and measurement period of $80s$ to $2.9 \times 10^4 s$. At time periods greater than $2.9 \times 10^4 s$, it can be seen that the amplitude frequency response approaches a steady state that is dominated by the first order high pass response of the charge-conditioning amplifier at low frequencies, and by the thermal response of the sensor element at high frequencies. It can also be seen that in the steady state, which is closely approximated by the data-tips at $10^8 s$, the amplitude frequency response that satisfies the required specification is now further restricted to a frequency range of $3.3\mu rads^{-1}$ to $17mrads^{-1}$. While this minimum frequency is extremely low, a real world temperature signal will contain significant DC and very low frequency components that will decay toward zero in the steady state. Furthermore, at $17mrads^{-1}$, which corresponds to a period of approximately $6\,minutes$, this

maximum frequency restricts the use of the sensor if faster temperature changes occur due to exertion for example. It cannot therefore be assumed that the sensor will faithfully represent the interface temperature amplitude where fast temperature changes occur at any time during the operating period of $2.9 \times 10^4 s$ and at times greater than the operating period.

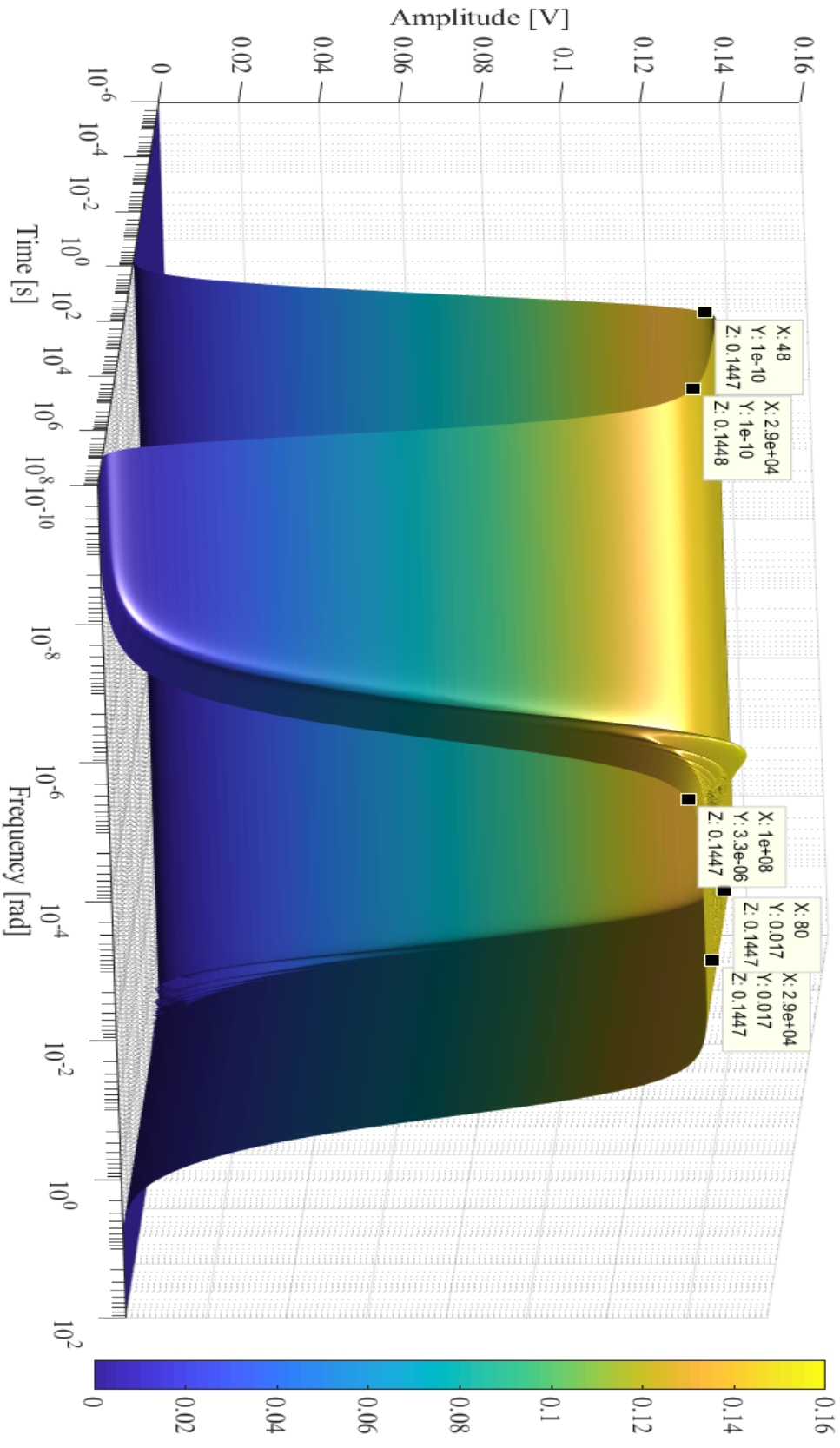

Figure 7.17 Amplitude time frequency plot at $l_e = 1mm$

The phase time-frequency response of the sensor at $l_e = 1mm$ is shown in Figure 7.18. By considering sequential time 'slices' parallel to the frequency axis, it can be seen that the phase frequency response at the signal-conditioning output evolves in time toward the steady state frequency response. Similarly by considering sequential frequency 'slices' parallel to the time axis, the transient phase behaviour of the sensor can be examined at different frequencies.

It can be seen from Figure 7.18 that after a period of $10ms$ the phase is $2.714 \times 10^{-8} rads$ and increases to $-0.17 \times 10^{-3} rads$ over the now restricted sensor operating frequency range of $10^{-10} rads^{-1}$ to $17mrads^{-1}$. After an operating period of $8\,hours$ corresponding to the data-tips at $2.9 \times 10^4 s$, the phase remains at $2.714 \times 10^{-8} rads$ for a frequency of $10^{-10} rads^{-1}$, and reduces to $-0.224 rads$ at a frequency of $17mrads^{-1}$. The maximum phase over the restricted sensor operating frequency range of $10^{-10} rads^{-1}$ to $17mrads^{-1}$ throughout an operating period of $8\,hours$ is $0.013 rads$ at a frequency of $7.7 \times 10^{-5} rads^{-1}$, which is equivalent to approximately $0.75°$. It can therefore be stated that when the sensor is configured to measure the interface temperature at the external liner surface with $l_e = 1mm$, that the phase response is low over the frequency range of DC to to $17mrads^{-1}$. The effect of the phase response on the input temperature signal is negligible and the sensor response will faithfully represent the interface temperature phase over this restricted frequency range and over a measurement period of $10ms$ to $2.9 \times 10^4 s$. At time periods greater than $2.9 \times 10^4 s$, it can be seen that the phase frequency response approaches a steady state that is dominated by the first order high pass response of the charge-conditioning amplifier at low frequencies, and by the thermal response of the sensor element at high frequencies. It can also be seen that in the steady state, represented by the data-tips at $10^8 s$, the phase increases from a minimum of $-0.224 rads$ at a frequency of $17mrads^{-1}$ to $\pi/2\, rads$ at $10^{-10} rads^{-1}$. Allowing a maximum phase shift of approximately $0.2 rads$, the frequency is now limited to a range of $3.3\mu rads^{-1}$ to less than $17mrads^{-1}$. While this minimum frequency is extremely low, a real world temperature signal will contain significant DC and very low frequency components that exhibit large phase shifts and it cannot therefore be assumed that the sensor will faithfully represent the interface temperature phase at time periods greater than $2.9 \times 10^4 s$.

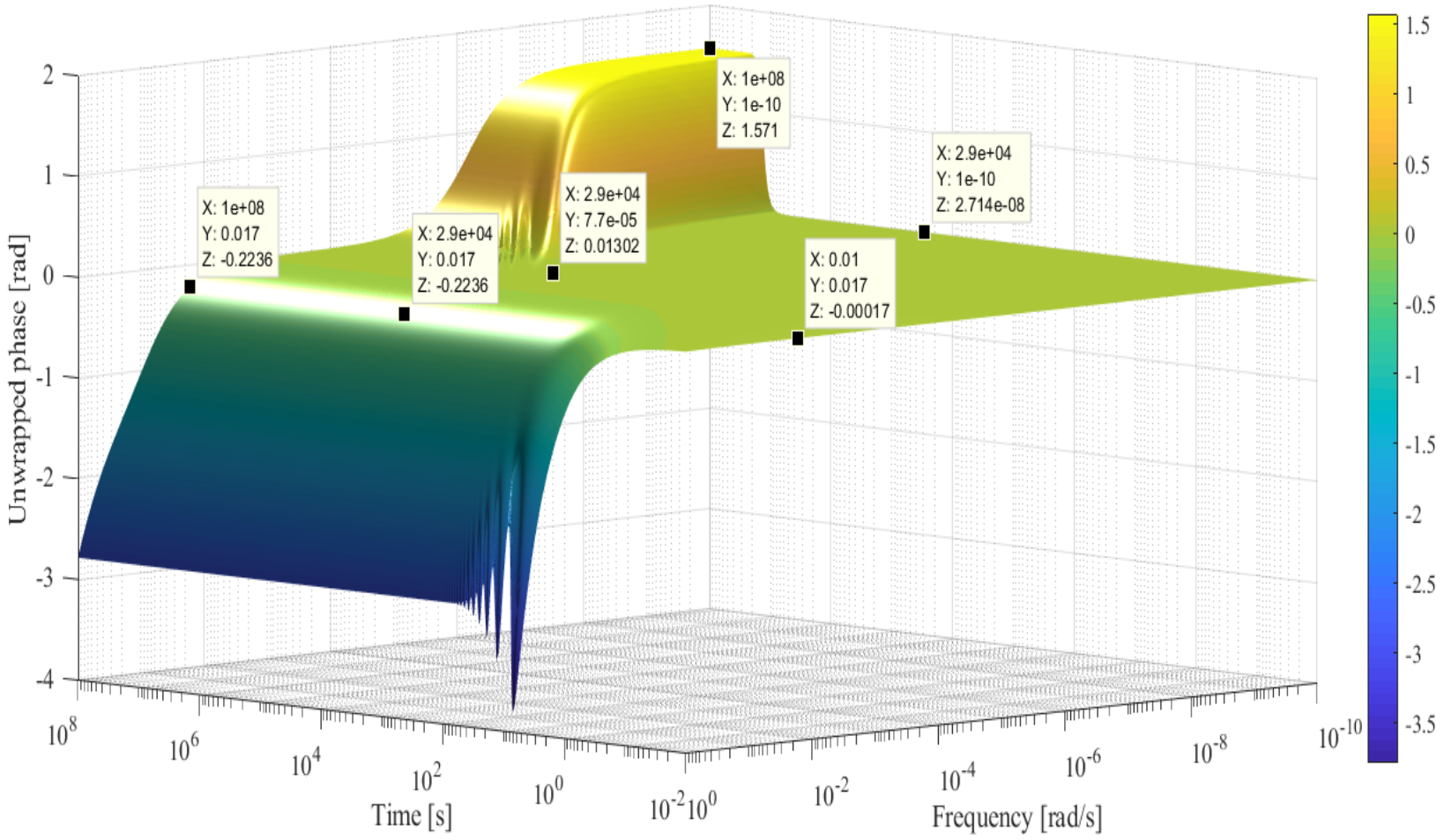

Figure 7.18 Phase time frequency plot at $l_e = 1mm$

The phase delay time-frequency response of the sensor at $l_e = 1mm$ is shown in Figure 7.19. By considering sequential time 'slices' parallel to the frequency axis, it can be seen that the phase delay frequency response at the signal-conditioning output evolves in time toward the steady state frequency response. Similarly by considering sequential frequency 'slices' parallel to the time axis, the transient phase delay behaviour of the sensor can be examined at different frequencies.

It can be seen from Figure 7.19 that after periods of $48s$ and $80s$ at frequencies of $10^{-10}rads^{-1}$ and $17mrads^{-1}$ respectively, the phase delay is $12.37s$ and $13.08s$ respectively, inferring that the phase is approximately linear for all frequencies between $10^{-10}rads^{-1}$ and $17mrads^{-1}$. The periods of $48s$ and $80s$ refer to the minimum time required for the amplitude response at all frequencies to reach the required 98% of peak value. After an operating period of $8\,hours$, corresponding to the data-tips at $2.9 \times 10^4 s$, the phase delay is $13.15s$ at $17mrads^{-1}$ and therefore remains very close to the corresponding value at $80s$. However, at a frequency of $10^{-10}rads^{-1}$ the phase delay reduces to $-271.4s$, while at an intermediate frequency of $10^{-4}rads^{-1}$, the phase delay is $-118.4s$.

When compared to the period corresponding to each frequency, these phase delays are small and it can therefore be stated that when the sensor is configured to measure the interface temperature at the external liner surface with $l_e = 1mm$, that the phase delay can be considered low over the frequency range of DC to to $17mrads^{-1}$. The effect of the phase delay on the input temperature signal is therefore negligible and the sensor response will faithfully represent the interface temperature for this restricted frequency range over a measurement period of $80s$ to $2.9 \times 10^4 s$. At time periods greater than $2.9 \times 10^4 s$, the phase delay approaches a steady state that is dominated by the first order high pass response of the charge conditioning amplifier at low frequencies, and the phase delay increases steeply at frequencies below $3.3\mu rads^{-1}$. It cannot therefore be assumed that the sensor will faithfully represent the interface temperature signal at time periods greater than $2.9 \times 10^4 s$.

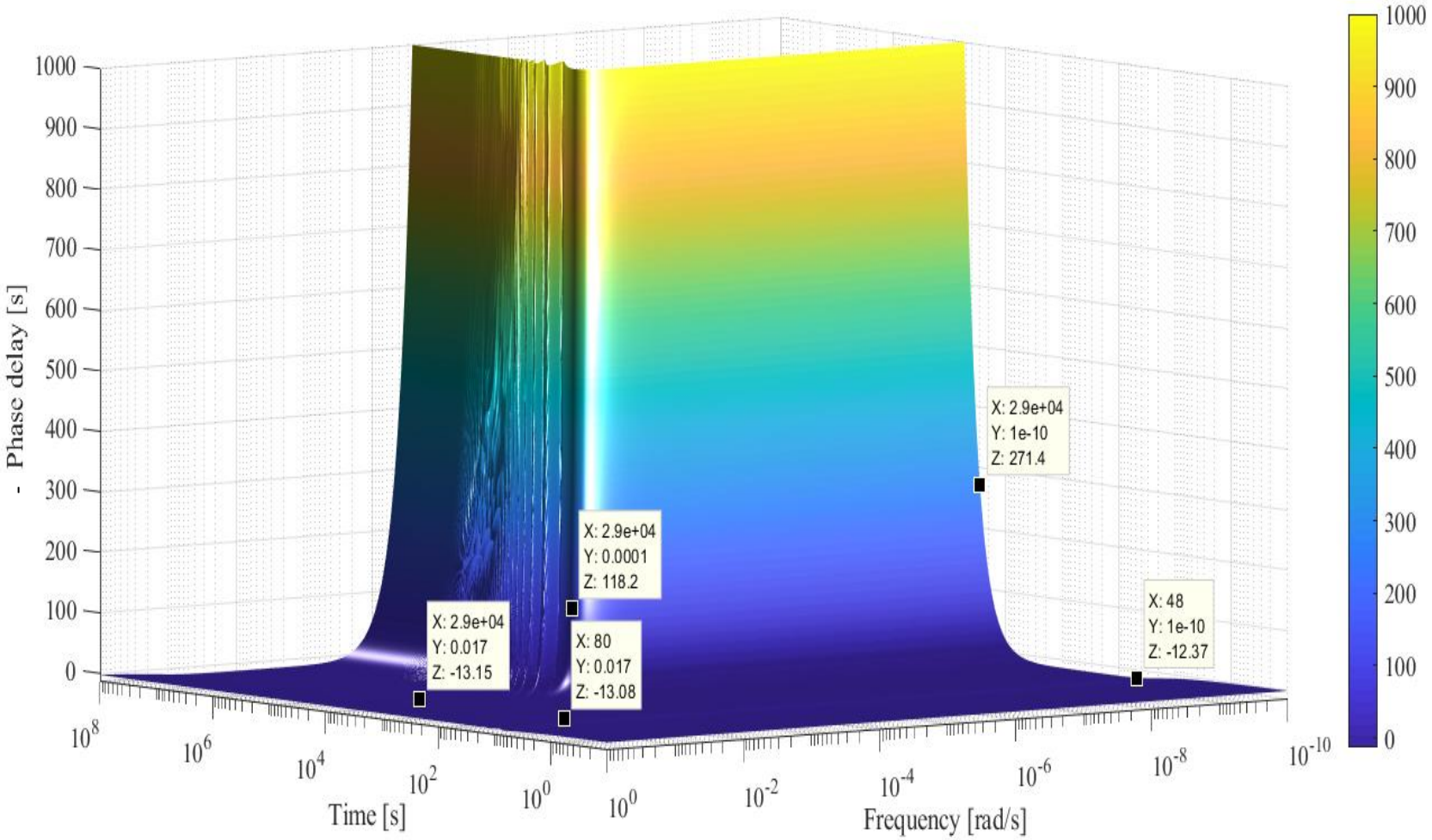

Figure 7.19 Negative phase delay time frequency plot at $l_e = 1mm$

7.7.5 Time-frequency response: $l_e = 8mm$

The amplitude time-frequency response of the sensor to an applied temperature change at the external liner interface with $l_e = 8mm$ is shown in Figure 7.20. The applied interface temperature is modelled by complex exponentials at different frequencies of amplitude $1K$ at the external liner surface as discussed in Section 7.7.1. Initially, the transient response is dominated by the thermal transient response of the elastomer liner, piezoelectric medium and substrate; and the rise time of the signal-conditioning amplifier, while towards the steady state it is dominated by the signal conditioning amplifier decay time constant.

After periods of $1300s$ and $2200s$, the amplitude reaches the required 98% of peak value at frequencies of $10^{-10}rads^{-1}$ and $0.63mrads^{-1}$ respectively. This initial transient is due to heat transfer, first in the liner followed by the substrate and piezoelectric medium. After an operating period of $8\,hours$ corresponding to the data-tips at $2.9 \times 10^4 s$, the amplitude remains at approximately 98% of the peak value.

It can therefore be stated that when the sensor is configured to measure the interface temperature at the external liner surface with $l_e = 8mm$, that the amplitude frequency response is approximately constant and within the required specification. However, this amplitude response now faithfully represents the interface temperature amplitude only over a severely restricted frequency range of DC to $0.63mrads^{-1}$ and measurement period of $2200s$ to $2.9 \times 10^4 s$. At time periods greater than $2.9 \times 10^4 s$, it can be seen that the amplitude frequency response approaches a steady state that is dominated by the first order high pass response of the charge-conditioning amplifier at low frequencies, and by the thermal response of the sensor element at high frequencies. It can also be seen that in the steady state, which is closely approximated by the data-tips at $10^8 s$, the amplitude frequency response that satisfies the required specification is now further restricted to a frequency range of $3.3\mu rads^{-1}$ to $0.63mrads^{-1}$. While this minimum frequency is extremely low, a real world temperature signal will contain significant DC and very low frequency components that will decay toward zero in the steady state. Furthermore, at $0.63mrads^{-1}$, which corresponds to a period of approximately $166\,minutes$, this

maximum frequency severely restricts the use of the sensor in the likely event that faster temperature changes will occur. It cannot therefore be assumed that the sensor will faithfully represent the interface temperature at any time during or at times greater than the operating period of $2.9 \times 10^4 s$.

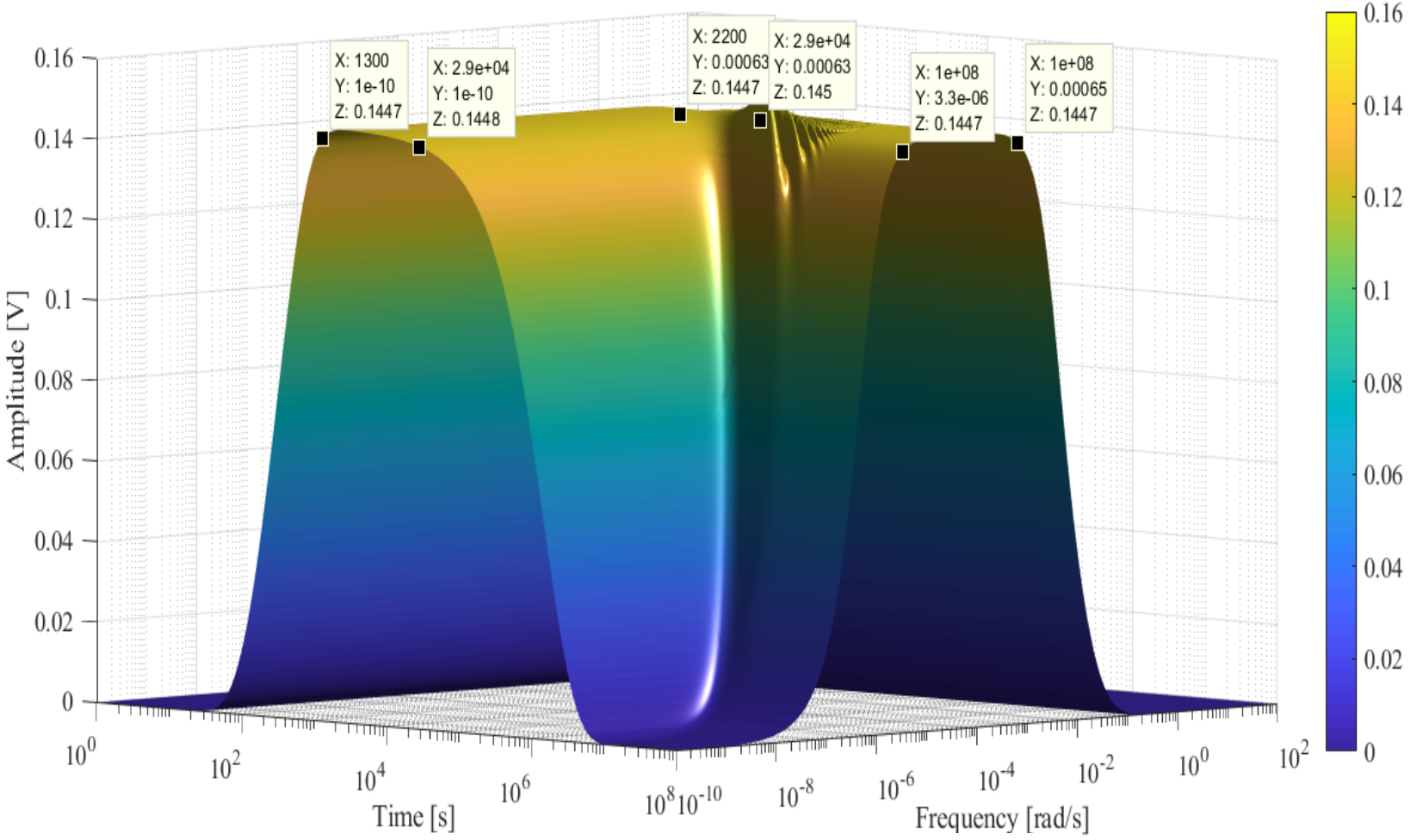

Figure 7.20 Amplitude time frequency plot at $l_e = 8mm$

The phase time-frequency response of the sensor at $l_e = 8mm$ is shown in Figure 7.21. By considering sequential time 'slices' parallel to the frequency axis, it can be seen that the phase frequency response at the signal-conditioning output evolves in time toward the steady state frequency response. Similarly by considering sequential frequency 'slices' parallel to the time axis, the transient phase behaviour of the sensor can be examined at different frequencies.

It can be seen from Figure 7.21 that after a period of $1s$ the phase is $-1.03 \times 10^{-8} rads$ and increases to $-0.55 \times 10^{-3} rads$ over the now severely restricted sensor operating frequency range of $10^{-10} rads^{-1}$ to $0.63 mrads^{-1}$. After an operating period of 8 $hours$ corresponding to the data-tips at $2.9 \times 10^4 s$, the phase remains at $-1.03 \times 10^{-8} rads$ for a frequency of $10^{-10} rads^{-1}$, and reduces to $-0.237 rads$ at a frequency of $0.63 mrads^{-1}$. The phase reduces monotonically over the restricted sensor operating frequency range of $10^{-10} rads^{-1}$ to $0.63 mrads^{-1}$ throughout the operating period of 8 $hours$.

It can therefore be stated that when the sensor is configured to measure the interface temperature at the external liner surface with $l_e = 1mm$, that the phase response is low over the frequency range of DC to $0.63 mrads^{-1}$. The effect of this phase response on the input temperature signal is negligible and the sensor response will faithfully represent the interface temperature phase over this severely restricted frequency range and over a measurement period of $1s$ to $2.9 \times 10^4 s$. At time periods greater than $2.9 \times 10^4 s$, it can be seen that the phase frequency response approaches a steady state that is dominated by the first order high pass response of the charge-conditioning amplifier at low frequencies, and by the thermal response of the sensor element at high frequencies. It can also be seen that in the steady state, represented by the data-tips at $10^8 s$, the phase increases from a minimum of $-0.236 rads$ at a frequency of $0.63 mrads^{-1}$ to $\pi/2\, rads$ at $10^{-10} rads^{-1}$. Allowing a maximum phase shift of approximately $0.2 rads$, the frequency is now limited to a range of $3.3 \mu rads^{-1}$ to less than $0.63 mrads^{-1}$. While this minimum frequency is extremely low, a real world temperature signal will contain significant DC and very low frequency components that exhibit large phase shifts and it cannot therefore be assumed that the sensor will faithfully represent the interface temperature phase at time periods greater than $2.9 \times 10^4 s$.

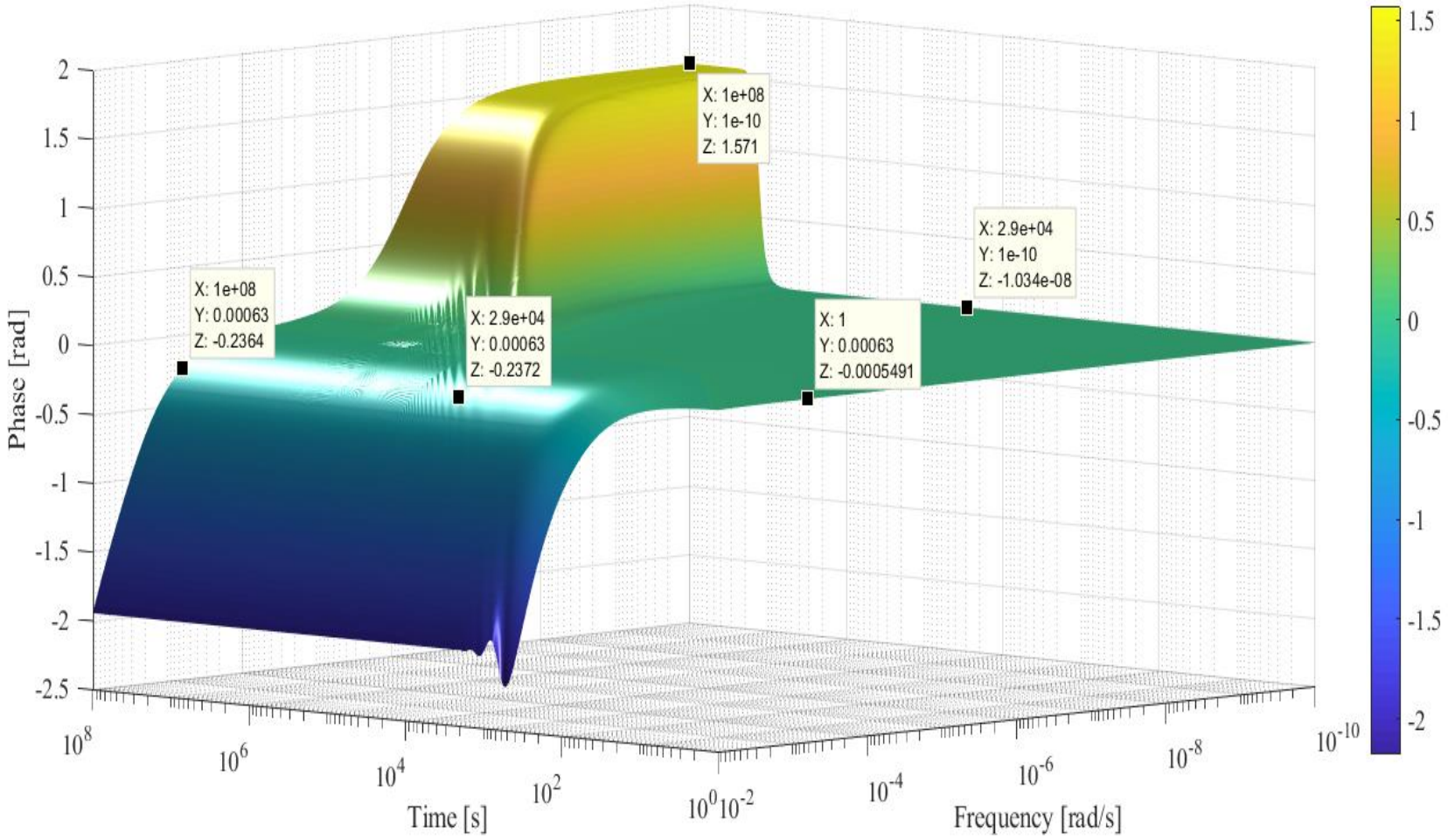

Figure 7.21 Phase time frequency plot at $l_e = 8mm$

The phase delay time-frequency response of the sensor at $l_e = 8mm$ is shown in Figure 7.22. By considering sequential time 'slices' parallel to the frequency axis, it can be seen that the phase delay frequency response at the signal-conditioning output evolves in time toward the steady state frequency response. Similarly by considering sequential frequency 'slices' parallel to the time axis, the transient phase delay behaviour of the sensor can be examined at different frequencies.

It can be seen from Figure 7.22 that after periods of $1300s$ and $2200s$ at frequencies of $10^{-10}rads^{-1}$ and $0.63mrads^{-1}$ respectively, the phase delay is $356.4s$ and $374.3s$ respectively, inferring that the phase is approximately linear for all frequencies between $10^{-10}rads^{-1}$ and $0.63mrads^{-1}$. The periods of $1300s$ and $2200s$ refer to the minimum time required for the amplitude response at all frequencies to reach the required 98% of peak value. After an operating period of $8\ hours$, corresponding to the data-tips at $2.9 \times 10^4 s$, the phase delay is $376.4s$ at $0.63mrads^{-1}$ and therefore remains very close to the corresponding value at $2200s$. However, at a frequency of $10^{-10}rads^{-1}$ the phase delay reduces to $103.4s$, while at an intermediate frequency of $10^{-4}rads^{-1}$, the phase delay is $249.8s$.

When compared to the period corresponding to each frequency, these phase delays are small and it can therefore be stated that when the sensor is configured to measure the interface temperature at the external liner surface with $l_e = 8mm$, that the phase delay can be considered low over the frequency range of DC to to $0.63mrads^{-1}$. The effect of the phase delay on the input temperature signal is therefore negligible and the sensor response will faithfully represent the interface temperature for this severely restricted frequency range over a measurement period of $2200s$ to $2.9 \times 10^4 s$. At time periods greater than $2.9 \times 10^4 s$, the phase delay approaches a steady state that is dominated by the first order high pass response of the charge conditioning amplifier at low frequencies, and the phase delay increases steeply at frequencies below $3.3\mu rads^{-1}$. It cannot therefore be assumed that the sensor will faithfully represent the interface temperature signal at time periods greater than $2.9 \times 10^4 s$.

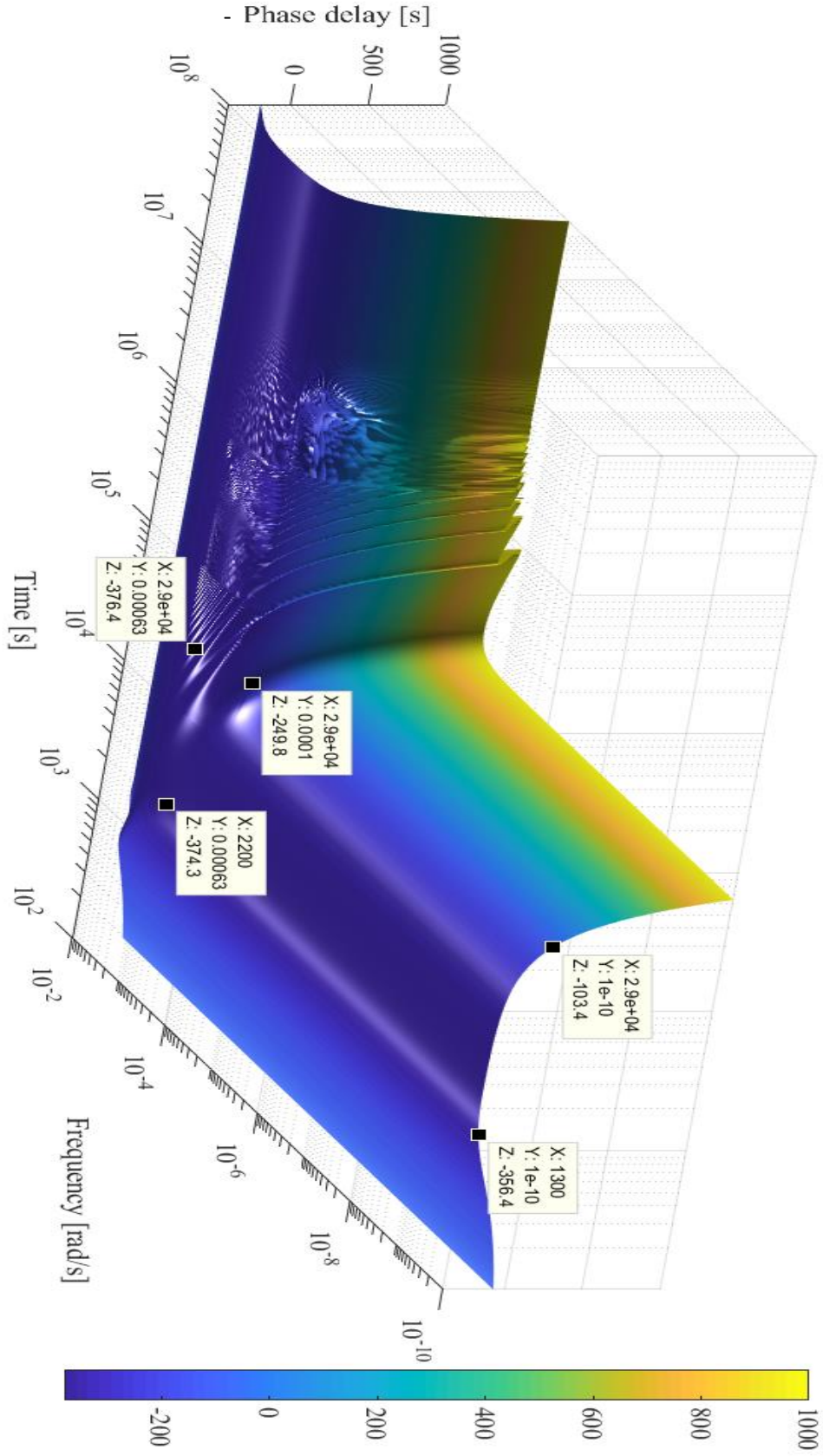

Figure 7.22 Negative phase delay time frequency plot at $l_e = 8mm$

7.7.6 Verification of the Padé steady-state responses at V_{out}

The steady state responses given by the Padé approximant in the time-frequency plots given in Section 7.7.3 to Section 7.7.5 can be investigated for steady state accuracy by writing the Laplace response at the amplifier output $V_{out}(s)$ in Fourier form $V_{out}(j\omega)$ and applying a steady state sinusoidal surface temperature such that $\Delta\theta_{skin}(j\omega) = 2\pi\Delta\hat{\theta}_{skin}\delta(\omega - \omega_o)$. $V_{out}(j\omega)$ is therefore given by Equation 7.32 where the Fourier form of $\mathrm{Q}_{tf}(s)$ given by Equation 7.30 is given by Equation 7.33 and $\Delta\bar{\theta}(j\omega)$ and $\Delta\bar{\theta}_b(j\omega)$ are given by Equation 4.130 and Equation 4.131 respectively.

$$V_{out}(j\omega) = \frac{R_3 j\omega\, \mathrm{Q}(j\omega)}{R_2 R_s C_p C_f\left(j\omega+\frac{1}{R_f C_f}\right)\left(j\omega+\frac{1}{2R_s C_p}\right)} = \left[\frac{j\omega 2\pi\Delta\hat{\theta}_{skin}\delta(\omega-\omega_o)\,\mathrm{Q}_{tf}(j\omega)}{2R_s C_p C_f\left(j\omega+\frac{1}{R_f C_f}\right)\left(j\omega+\frac{1}{2R_s C_p}\right)}\right]_{G=0.5} \tag{7.32}$$

$$\mathrm{Q}_{tf}(j\omega) = \frac{\mathrm{Q}(j\omega)}{\Delta\theta_{skin}(j\omega)} = A_s\left[\left(2e_{31}\varphi_{p1}^E + e_{33}\varphi_{p3}^E + p^s - \frac{\beta E_b A_b \varphi_{p1}^E}{E_b A_b + \alpha(1-\mu_b)A_p}\right)\frac{\Delta\bar{\theta}(j\omega)}{\Delta\theta_{skin}(j\omega)} + \frac{\beta E_b A_b \varphi_b}{E_b A_b + \alpha(1-\mu_b)A_p}\frac{\Delta\bar{\theta}_b(j\omega)}{\Delta\theta_{skin}(j\omega)}\right] \tag{7.33}$$

The inverse Fourier transform of Equation 7.32 yields Equation 7.34.

$$V_{out}(t) = e^{j\omega_o t}\left[\frac{j\omega_o\,\mathrm{Q}_{tf}(j\omega_o)}{2R_s C_p C_f\left(j\omega_o+\frac{1}{R_f C_f}\right)\left(j\omega_o+\frac{1}{2R_s C_p}\right)}\right]_{G=0.5} \tag{7.34}$$

In a similar way to that described in Section 7.7.1 for the transient response, the steady state frequency response of the combined charge amplifier and charge transfer function, $\mathrm{Q}_{tf}(j\omega_o)$ can be plotted in terms of the amplitude and phase as a function of frequency using the Matlab plotting functionality $abs\left(V_{out}(t,\omega_o)\right)$ and $angle\left(e^{-j\omega_o t}V_{out}(t,\omega_o)\right)$. As a check that the Padé approximant results described above are reasonable, the steady state amplitude and phase response plots for

$l_e = 0mm$ and $l_e = 8mm$ are compared with the respective Padé approximant plots at $t = 10^8$ to represent the steady state. The steady state amplitude response plots for $l_e = 0mm$ and $l_e = 8mm$ are given by Figure 7.23 and Figure 7.24 respectively.

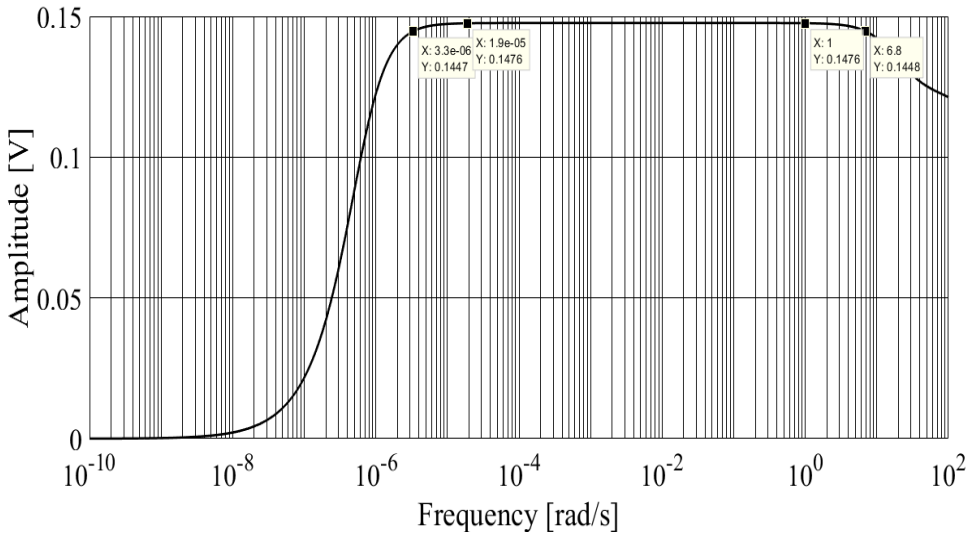

Figure 7.23 Steady state amplitude frequency response at $l_e = 0mm$

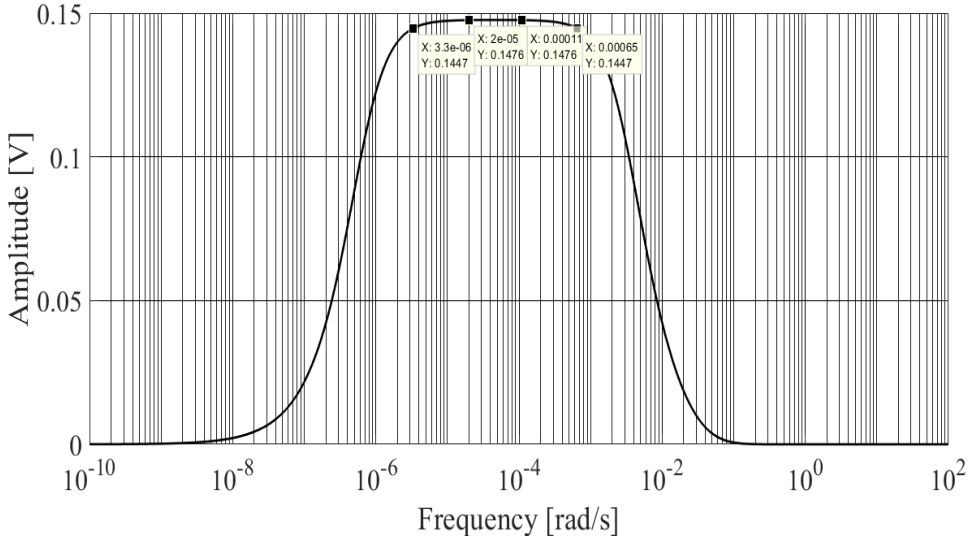

Figure 7.24 Steady-state amplitude frequency response at $l_e = 8mm$

By comparing the 98% of peak amplitude values given by $3.3\mu rads^{-1}$ and $6.8rads^{-1}$ in Figure 7.23 for $l_e = 0mm$, and $3.3\mu rads^{-1}$ and $0.65mrads^{-1}$ in Figure 7.24 for $l_e = 8mm$ with the corresponding amplitude values at $t = 10^8 s$ in Figure 7.14 and Figure 7.20 respectively, it can be seen that these are identical. The

corresponding steady state phase response plots for $l_e = 0mm$ and $l_e = 8mm$ are given in Figure 7.25 and Figure 7.26 respectively.

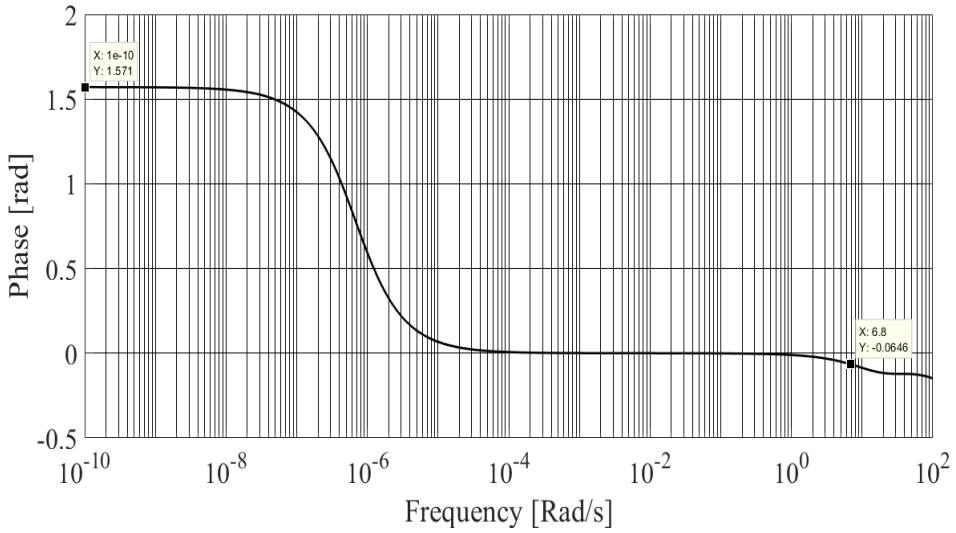

Figure 7.25 Steady-state phase frequency response at $l_e = 0mm$

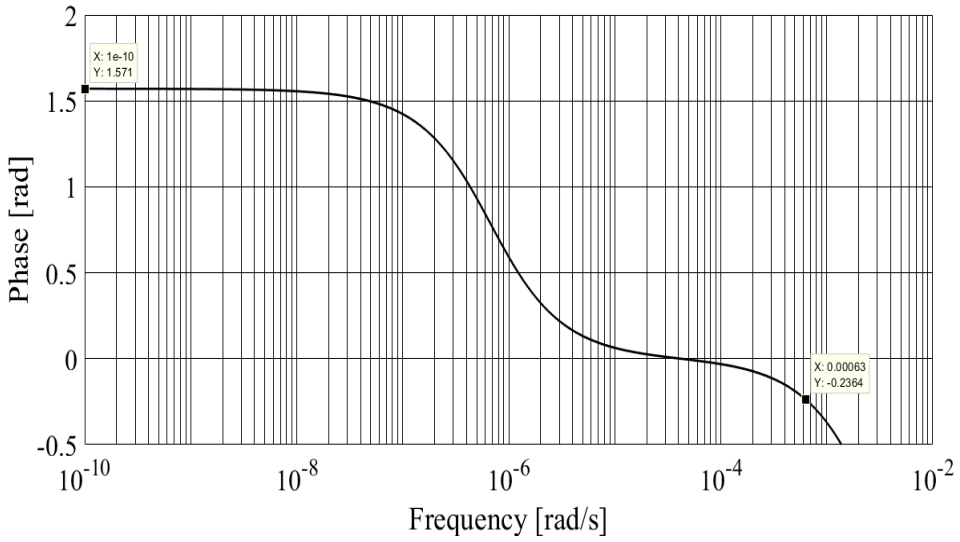

Figure 7.26 Steady-state phase frequency response at $l_e = 8mm$

By comparing the 98% peak amplitude phase given by the datatips at $6.8rads^{-1}$ for $l_e = 0mm$ in Figure 7.25, and $0.63mrads^{-1}$ for $l_e = 8mm$ in Figure 7.26 with the corresponding phase values at $t = 10^8 s$ in Figure 7.17 and Figure 7.21 respectively, it can be seen that these are also identical. Furthermore, the values of the phase at $\omega = 10^{-10} rads^{-1}$ in the Padé approximant plots and steady state plots

for both liner thicknesses is $\pi/2\,rads$ as expected due to the first order high-pass characteristic of the signal conditioning amplifier.

While the agreement in the values obtained by the steady-state and Padé approximant methods do not prove that the Padé approximants are accurate at all times and frequencies, the comparison does however provide a useful additional check that improves confidence in the validity and application of the Padé approximant method.

7.8 Conclusions

A signal decay compensation scheme that was applied to the measurement data of Section 7.3 and Section 7.5 is presented in Section 7.2.3. It is shown that signal decay compensation is an effective tool in compensating for the signal-conditioning decay observed in the raw measurement data. The application of a similar scheme to provide real-time decay compensation to mitigate the need for very large feedback resistances in a practical measurement system is the subject of future work. In Section 7.3 it is shown that the sensor and signal conditioning system produces a faster response demonstrated by an approximately 50% greater amplitude at the first transient hunting peak than the commonly used type K thermocouple, which is attached to the Peltier tile to provide the surface temperature reference. In Section 7.3 and Section 7.5, the experimentally observed temperature to voltage conversion factors (CF) for the transient response and accumulative responses for $C_f = 1.5\mu F$ are given by $CF = sens(G = 0.5) = 0.16\,V/K$ and $CF = sens(G = 0.5) = 0.1503\,V/K$ respectively and agree reasonably well with the theoretical value of 0.1476. The transient response conversion factors with $G = 1$ for $C_f = 1\mu F$ and $C_f = 1.5\mu F$ of 0.47 and 0.32 respectively yield a ratio of $0.47/0.32 = 1.47$ that agrees well with the expectation of an inverse proportional relationship between charge amplifier gain and C_f. The small discrepancy is easily explained by nominal C_f value tolerances of $\pm 5\%$ and measurement reading error due to signal noise.

It Section 7.5 it is demonstrated that the sensor response under short-circuit conditions is linear over the temperature range $20°C$ and $42°C$. It is considered that the small $0.05V$ deviation at $20°C$ which is equivalent to approximately $0.33°C$ in

the round trip $20°C \rightarrow 42°C \rightarrow 20°C$ measurement is due to measurement error rather than any underlying rate-independent hysteretic or other physical process. However, this observation requires further investigation to confirm measurement error and this will be the subject of future work.

In Section 7.5.2, the measured total pyroelectric response P_{eff} is demonstrated to be approximately $-870\ \mu C/m^2K$. This value agrees well with the calculated response of $P_{eff} \approx -800$ to $-900\ \mu Cm^{-2}K^{-1}$ given in Section 4.6 and confirms the anticipated pyroelectric response enhancement due to substrate clamping.

A prudent estimate of the sensor element and charge amplifier accuracy is given as $\pm 3.5\%$ in Section 7.5.3. However, since the temperature reference is obtained using a thermocouple integrated with the Peltier tile and PID controller, the validity of the estimate is dependent on the accuracy of the thermocouple. With a typical accuracy of $\pm 2.2°C$ at low temperatures for the type K thermocouple used, ($\pm 10.5\%$ at $20°C$ and $\pm 5.5\%$ at $40°C$) over the temperature range of interest, this estimate of sensor accuracy is treated with caution and improving this estimate of accuracy will be the subject of future work.

From the results of Section 7.7.2 and Section 7.7.3, the sensor is capable of a fast response when used directly against the measurement surface with a rise time to 98% peak and peak output of $0.12s$ and $0.9s$ respectively for a DC step of $1K$. The sensor is capable of measuring frequencies up to $6.8rads^{-1}$ ($\approx 1.1Hz$) with a rise time to the 98% peak of $0.18s$ for a sinusoidal step of amplitude $1K$. However, from the results of Section 7.7.4 and Section 7.7.5 that the use of a polymer liner between the sensor element and measurement surface severely limits the usable frequency response of the sensor due to severe amplitude and phase distortion, precluding the direct use of the sensor to measure the skin surface temperature. This result is no surprise and confirms intuition that this would be the case. Application of the method described in [88] that describes a Gaussian-learning algorithm presents a possible solution to providing a meaningful indirect measure of the skin temperature from the heavily amplitude- and phase-distorted sensor signal measured. The ability to reliably measure skin surface temperature within a prosthetic socket without direct

sensor element to skin contact is a desirable aim and this is the subject of future work.

An additional consideration when using a liner is that when compressed, the liner thickness, specific heat capacity and the density may change significantly. This in turn will cause a change in the diffusion coefficient (diffusivity) of the liner elastomer material, which is specific heat capacity and density dependent. A change in the thickness, specific heat capacity and density may therefore significantly influence the response at the output of the signal-conditioning amplifier. Further work is required to investigate possible effects on the sensor response.

Chapter 8

ICT limitations to e-Health

8.1 Introduction

As advancing technology allows e-health devices increasingly to become smaller, lighter and smarter, they become more attractive for use in the permanent and continuous monitoring of patients [110]. Of particular interest in this thesis is their use in monitoring people who are prone to developing health problems such as those who regularly wear prosthetic limbs or those living with diabetes. As discussed in Chapter 1, people with diabetes are particularly prone to the development of pressure sores due to, for example, an ill-fitting prosthesis or a significant change in the residual limb volume. Continuous monitoring of relevant biometrics and knowledge of the magnitude and distribution of direct forces at the interface between the residual limb and prosthetic socket may be useful in providing an early warning of the development of tissue damage. Ultimately, the application of an early warning e-health monitoring system on vulnerable patients will provide the patient and/or health authorities with health related data that may be critical in avoiding injury and indicate medical intervention if necessary.

E-health has grown rapidly in recent years [111]. However, in the case of critical m-health (mobile health) monitoring systems where a patient may require to be monitored continuously or emergency alerts may be critical to patient welfare, it is vital that patient data is not lost and in some cases that patient data reach the relevant authority with minimal delay to avoid life threatening complications. However, issues with mobile communications channel availability and issues with latency and limited bandwidth in data networks and data network equipment may threaten the transmission of this data to the health authority.

This rapid growth in e-health applications is putting stress onto already stretched data networks and is threatening their ability to provide the quality of service (QoS) required [112]. If the realisation of a robust and reliable wearable monitoring system is to be achieved these issues must be addressed. It is suggested that one of the most fundamental threats to providing the necessary QoS demanded by critical e-health services is the technological limitations of electronic based data networks. In this light, these limitations were investigated, in terms of the issues of sustainable growth in bandwidth and power consumption, and are described below.

Recent years have seen a rapid growth in demand for high-speed data transmission and high bandwidth. With this rapid growth in demand, data centres are under pressure to provide ever-increasing data rates through their networks and at the same time improve the quality of data handling in terms of reduced latency, increased scalability and improved channel speed for users. However, as data rates increase, present technology based on well-established CMOS technology is becoming increasingly difficult to scale and consequently data networks are struggling to satisfy current network demand. In this chapter the interrelated issues of growing demand for data, electronic scalability, power consumption, limited copper interconnect bandwidth and the limited speed of CMOS electronics will be discussed from the perspective of speed and latency in data networks.

Section 8.2 discusses the globally increasing demand for data in terms of IP data centre and mobile data traffic, while Section 8.3 describes latency in data transmission and its causes. The causes of latency are expanded upon in Section 8.4 where the speed limitations of CMOS electronics are discussed, and possible solutions in the form of all-optical data processing are discussed in Section 8.5.

8.2 Global demand for data

Global demand for data has been increasing year on year at an exponentially increasing rate. ICT equipment manufacturer Cisco predicts that global data centre IP traffic (which includes traffic between data centres) will pass $20\ Zetabytes/year$ mark by the end of 2021 as shown in Figure 8.1 ($1\ Zetabyte = 10^{21}\ bytes$). This is more than three times its 2016 level and represents a compound annual growth rate (CAGR) of 25% from 2016 to 2021 [113]. Between 2019 and 2021, the volume of data passing through communication networks is forecast to increase by 50%.

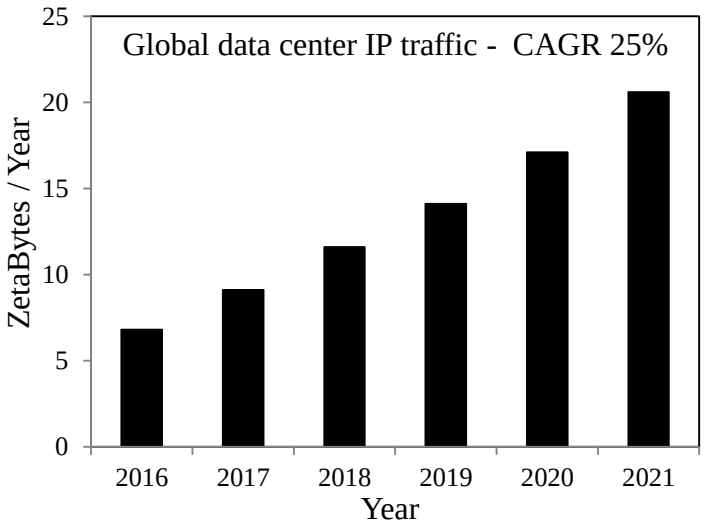

Figure 8.1 Global data centre IP demand forecast 2016-2021

Global mobile data traffic demand is showing the most rapid increase and is forecast to increase exponentially more than 6-fold between 2017 and 2022 at a CAGR of 46% as shown in Figure 8.2. In addition, mobile data traffic is forecast to represent 20% of total IP data by 2022 reaching $77.3\ Exabytes/month$ with 79% of this data being video [114] ($1\ Exabyte = 10^{18}\ bytes$). The largest share of this rise is attributable to growth in smart phone and machine-to-machine (M2M) devices. Smart phones alone generate between 10 and 20 times more data traffic than conventional mobile phones [115].

These current trends have resulted in electronic bottlenecks in data networks and new developments in cloud computing may compound this problem further. The growing demand for high speed, low latency data transmission has generated a need

for substantially increased capacity and improved connectivity within data centres. However it is suggested in [116] that current data centres performing all data processing based on CMOS based electronic switching are incapable of sustaining these demands into the future.

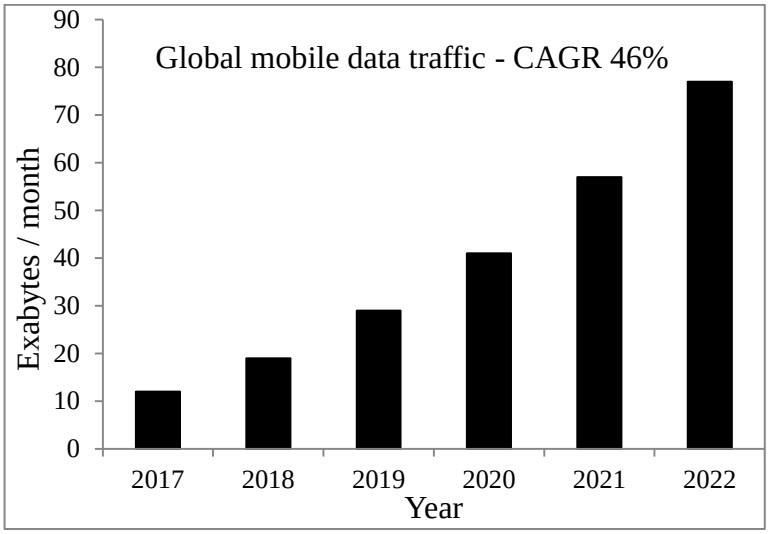

Figure 8.2 Global mobile data traffic forecast 2017-2022

A further threat comes from potentially unsustainable power consumption with Global ICT (information and communications technology) energy consumption being estimated in [117] to rise from approximately $1700TWh$ per year to an estimated $5900\,TWh$ per year with a best case scenario of $2800\,TWh$ per year by 2025. This amounts to 10.5% of global electricity production and includes energy consumption due to consumer device use, fixed access Wi-Fi use, wireless networks access use, data centre use including cooling and hardware production. In particular, data centre energy consumption alone is forecast to account for 4.5% of global electricity production by 2025, which is a five-fold increase from 0.9% of global electricity production in 2015.

8.3 Latency

The growing demand for high speed, low latency data transmission has generated a need for substantially increased capacity and improved connectivity within data centres. However, current data centres performing all data processing

based on electronic switching and routing use copper interconnects limited to a capacity of around $1Gb/s$ to $10Gb/s$. Issues of electronic bottlenecks that lead to increased latency and reduced bandwidth to the user are therefore becoming apparent. In fact, Google have reported that an additional latency of $400ms$ costs 0.44% in lost search sessions; while Amazon have reported that an additional latency of $100ms$ costs 1% in lost sales. The reason for this latency is two-fold. Firstly, the scaling of copper interconnects has resulted in increasing switching delays and an increased additional contribution to chip power density. Secondly, the scaling of CMOS electronics, specifically the threshold voltage has resulted in significant transistor junction leakage currents that incur an increase in static on-chip power consumption. While the increase in static power consumption his has in part been mitigated by the end of threshold voltage scaling, the dynamic switching power continues to present a problem since it is proportional to the square of the supply voltage. This relationship forces the maximum switching speed to be restricted to maintain total power dissipation at a sustainable level. If device power density is not controlled, providing adequate cooling will present an intractable problem and result in an increased risk of thermal runaway and reduced system reliability.

8.4 Limitations of CMOS technology

8.4.1 Dennard scaling and Moore's law

The mobility of silicon imposes a fundamental maximum speed on the silicon transistor of around $100GHz$ [118]. However, while this speed has been demonstrated for simple CMOS devices, microprocessor speed has plateaued at around the $4GHz$ mark. The limiting factor is power dissipation and it would be impossible for the millions of transistors in a processor to operate at much faster than $4GHz$ without overheating and thermal runaway that would result in the destruction of the chip. This problem has its root in CMOS transistor scaling.

The well-known CMOS transistor scaling rules first described by Robert Dennard in 1974 describes how transistor size can be reduced while at the same time increasing switching speed and reducing power consumption [119]. Dennard scaling

states that as transistor size reduces, power consumption will reduce while maximum clock speed can be increased. An important observation of Dennard scaling is that power density (Watts per unit chip area) has remained approximately constant as transistor density has increased. In addition, the density of transistors has been increasing by a factor of about two every 18 months for over 40 years. Gordon Moore first suggested such an exponential improvement in transistor density in 1965 with an estimated doubling of transistor density every two years [120]. Despite the increasing technical challenges of integration and fabrication, Moore's foresight has, until today been validated, leading to what is known as 'Moore's law'. However, as of 2019, Intel's latest $10nm$ technology has encountered many technical difficulties and its latest generation of processors, which is the first new generation in 3 years, may signal the end of Moore's law. Intel has forecast that Moore's law is ending, and increasing attention is now on the improvement of processor architectures, rather than scaling, to achieve increased processing speed.

8.4.2 Electronic interconnect scaling

With the advancement of Moore's Law, both chip speed and chip power consumption are increasingly being affected by on-chip copper interconnect limitations. There are two main types of interconnect at chip level. Local interconnects are very short connections at the device level; and global interconnects are long connections between blocks, carrying for example power and clock signal. The resistance, R of local interconnects that connect individual MOS transistors increases while the capacitance, C reduces by the scaling factor. This serves to maintain the RC delay of local interconnects approximately constant with scaling. Since chip size and complexity has been increasing, global on-chip interconnects have actually increased in length and in number resulting in increased R and C with scaling, resulting in increased RC delay. Compounding this situation in both local and global interconnects is increasing parasitic capacitance and copper resistivity at very small scales. The consequence of increasing R and C is not limited to increased delay and limits on chip speed. The power consumption of interconnects is directly proportional to capacitance. It therefore follows that power consumption particularly

in global interconnects will rise with scaling, and therefore that the interconnect contribution to overall chip power density will increase. While progress has been made to reduce the capacitance of interconnects by using low dielectric constant interconnect separating layers, this approach has not fully mitigated the rise in capacitance and the issue persists [121].

As data centres scale to meet demand, rack and switching/routing copper interconnects must get longer to connect server racks to each other and to routers and switches. The number and total length of interconnects will therefore increase exponentially with scaling. Power consumption will increase as a consequence since the capacitance of each interconnect rises with the length of interconnect, and the bandwidth of the copper interconnects will reduce as the delay increases as a result of increased resistance and capacitance. Thus copper interconnects and electronic switches in data centres are limited to $10Gb/s$ serial data rates per channel with a maximum range in the $10's$ of metres with a length of $100m$ only possible at very high power consumption.

To circumvent this problem, data centres have widely employed optical fibre interconnects. While these have solved the issues of space and reach, they use CMOS based optical/electronic/optical (OEO) transceivers which until recently have been limited to $10Gb/s$. However, Intel have announced a new MXC type optical interconnect which is designed to connect top of the rack (ToR) switches to each other and to the core switches, or to connect servers to extra storage or graphic processing units (GPU's). This interconnect is capable of $800Gb/s$ in total each way with a maximum of $25Gb/s$ serial data rate per fibre (64 fibres with 32 each way) [122]. This interconnect can operate up to $300m$ at reduced power consumption compared with copper cables. While this technology can overcome the attenuation and bandwidth limits of copper cables, it still requires bandwidth-limited and power hungry OEO transceivers.

8.4.3 CMOS speed

Despite the continuing validity of Moore's law, Dennard scaling came to an end in 2005 with the development of $90nm$ lithography. At this level, transistor

gates become too thin to prevent current from leaking into the substrate. In addition, threshold voltage scaling resulted in an increase in junction leakage currents. The relationship $P_d = CV^2F$, where C is the CMOS switch lumped capacitance (sum of junction and gate capacitances) and V is the supply voltage, relates the dynamic switching power consumption P_d to the frequency, F in the basic CMOS inverter building block and illustrates the past success of CMOS scaling. The expression for P_d can be justified as follows. Here a $1-0$ transition charges the equivalent capacitance through the source-drain of the PMOS type transistor, dissipating half the energy, and in the $0-1$ transition, the capacitor discharges the stored charge through the source-drain of the NMOS transistor resulting in an approximate total energy dissipation of $2 * \frac{1}{2} C\, V^2$ over one cycle. There is also a brief short-circuit dynamic power consumption due to both transistors conducting simultaneously for a short time. This is due to the finite rise and fall time during a state transition that results in an input gate voltage range for which both NMOS and PMOS transistors are open simultaneously.

With Dennard scaling, as transistor dimensions scale smaller, C reduces and the supply voltage can be reduced (since CMOS threshold voltage scales with the gate oxide layer thickness). Power consumption per inverter is therefore reduced and therefore overall chip power density can be maintained at a sustainable level. However, in 2005 leakage current became a problem at the $90nm$ technology node due to the scaling of the gate oxide thickness, which increases gate oxide tunnelling. Furthermore, subthreshold currents also increase due to the scaling of the threshold voltage. Leakage currents have resulted in a rise in chip static power density, P_s and, in the case of junction leakage currents, present the risk of spontaneous transistor state switching and corruption of data. Supply voltage scaling ended at around $1V$, ending the scaling of the threshold voltage and helping mitigate the rise in junction leakage currents. However, this has been at the expense of the dynamic power consumption, which is proportional to V^2, and chip power density has therefore been increasing overall as a result. It therefore became necessary to limit the overall chip power consumption, $P_d + P_s$ by reducing the clock frequency F to avoid excessive power density. High power density runs the risk of causing thermal runaway and destruction of the chip in addition to creating cooling challenges and power

consumption cost issues when scaled to the size of a data centre. In the short term, it is clear that increasing clock speeds to satisfy demand is not a realistic option. In effect, device thermal density has become a limiting design criterion that is threatening to bring Moore's law of scaling to an end [123].

In the short term, while effective cooling can be achieved, Moore's law will hold. However, power density is no longer approximately constant as previously predicted by Dennard's Law but will increase with transistor density. The maximum power density that can be sustained together with the limitations of parallelism and copper interconnect bandwidth lead to a fundamental limit on the processing power of present electronic data centres. Research into reducing CMOS leakage currents has demonstrated improvements in data handling capacity and power efficiency [124]. However, these improvements have been slow with only modest gains in reduced leakage current achieved. Graphene [125] and nanowire [126] technologies are being investigated as a replacement for current CMOS based devices. However, research in these areas is in its infancy and operational devices are many years from market.

8.4.4 Computing speed and Amdahl's law

As discussed in Section 8.4.2 and Section 8.4.3, leakage current and global interconnect problems have made it necessary to limit power consumption by reducing the clock frequency and therefore also the processing speed. Consequently, since 2005 chip manufacturers Intel and AMD have concentrated on introducing parallel processing CPUs using multicore processors to increase processing power with the latest high performance server processors capable of supporting up to $10Gb/s$ data rates. While parallelism can do nothing to reduce power consumption or help overcome interconnect bandwidth limitations, it can contribute to reducing latency by speeding up the processing of requests. Parallel processing can compensate to a degree for limited clock frequencies but clearly results in increased power consumption since an effective doubling in performance requires at least two processors.

While parallel processing can, to a degree compensate for limited clock frequencies by providing a speed-up in computing, it clearly results in increased power consumption since an effective doubling in performance requires at least two processors. In addition, Amdahl's parallelism law states that 'If a computation has a serial component, s % and a parallel component, f % such that $s + f = 1$, then the speedup denoted by S_e is given by Equation 8.1 where n is the number of processors.

$$S_e = \frac{1}{1-f+\frac{f}{n}} \tag{8.1}$$

The maximum speed-up given an infinite number of processors is therefore $1/(1-f)$. The relationship between S_e and n for different parallel portions f is shown by Figure 8.3.

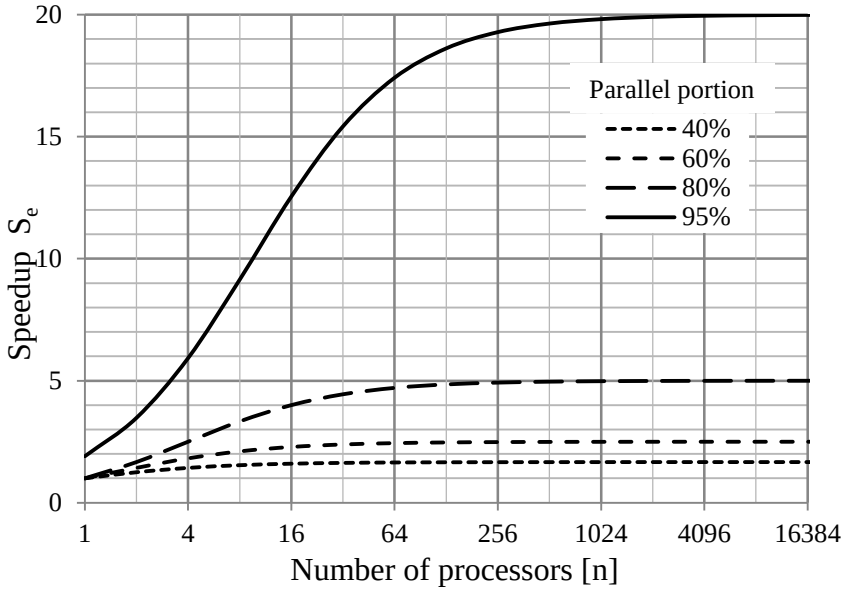

Figure 8.3 The effect of Amdahl's Law

The greater the parallel portion f, the higher the speed-up [127]. However, it can be seen from Figure 8.3 that there is a fundamental maximum improvement in computational speed that is dependent upon the proportion of serial computation, beyond which further additional parallel processors will contribute a rapidly diminishing improvement in processing speed. Therefore, the performance per watt that is initially constant will eventually decrease rapidly as the number of processors is increased beyond the optimum number. As the number of parallel processors *n*

increases the maximum speed-up value is achieved, beyond which adding more processors returns diminishing additional computational advantage and increases power consumption. The performance per watt, which is initially constant, will eventually decrease rapidly as the number of processors is increased beyond the optimum number. When a *request* is implemented in a parallel computing system, the overall response time is dictated by the distribution of parallel operations and therefore by the slowest operation. Latency in any of the parallel operations will therefore reduce the ideal speed-up discussed above.

8.5 Toward all-optical data processing

In today's networks the use of state of the art optical technologies has vastly improved single wavelength channel data rates. Serial data rates per a single optical wavelength channel have grown from the adoption of $OC-1$ in 1980 with $OC-768$ equivalent to $40Gb/s$ in common use today. $OC-n$ refers to the serial data capacity $n*51.84\,\mathrm{Mb/s}$ of each optical carrier in a DWDM (dense wave division multiplex) configuration. As an example of the current state of the art, DWDM systems are commercially available that use $OC-678$ across 80 channels with a $50GHz$ ITU grid. The total bit rate achieved is $80*678*51.48\,\mathrm{Mb/s}$ or approximately $1.4\mathrm{Tb/s}$. These serial data rates have been predominantly governed and limited by the bandwidth limited electronics available at fibre ends used for the data processing where OEO (optical electronic optical) CMOS based transceivers are required for further processing by electronic means.

From the discussion in Section 8.4, it is suggested that the fundamental limits on electronic switching speeds, power consumption and parallel processing may, in the near future, severely affect the ability of data networks to satisfy both quantitatively and qualitatively, the exponentially increasing demand for data. Disruptive technologies are therefore required to greatly improve available bandwidth, serial processing speed while at the same time reducing power consumption. Perhaps the greatest challenge is in the realisation of an all-optical CPU.

However, a fundamental problem in developing the all-optical CPU is the difficulty in developing a photonic analogue to replace the CMOS transistor technology necessary to carry out logic operations and provide buffering. To perform as a logic element, an optical transistor must especially satisfy the conditions of gain for fan-out and be able to be cascaded. Research in this area is in its infancy however, some progress in the development of the optical transistor has been reported and research groups have been successful in demonstrating what may become possible future solutions to this problem.

In [128] an optical transistor has been demonstrated where a single stored gate photon can control the transmission of applied source photons. The gate photon is effectively the analogue of the gate voltage in a CMOS transistor. Here, a weak light gate pulse is stopped and stored inside an optical resonator. A single stored gate photon controls the transmission of applied source photons resulting in an 80% source attenuation. One stored gate photon was shown to switch many hundreds of source photons. In fact more gate photons can be stored resulting in an improved efficiency in source attenuation. The construction consists of an optical resonator formed by two mirrors at either side of a high finesse sealed optical cavity containing super-cooled caesium gas. The mirror separation is precisely calibrated for the wavelength of light to allow resonance while preserving phase. The source photons pass through the first mirror, entering the resonator and reflecting back and forth. This process allows the creation of a large electromagnetic field overcoming the confinement of the resonator and allows the light to pass through. When a single gate photon is fired into the resonator, it is absorbed and re-emitted many times as it reflects back and forth between the mirrors. Eventually the entire cloud of Caesium gas behaves like it is in an excited state, blocking the resonator transmission and effectively switching the transistor to the off state. The transistor is switched back on again by applying another gate pulse to the caesium gas.

This result has demonstrated a key requirement of the ability to turn a strong signal on and off using a weak one thereby allowing fan out where a single output could be used to control hundreds of other transistors. Also, since the source requires only one photon to control the source output, the potential exists for extremely low switching power consumption. In addition, since photons are effectively stored, this

principle may be applicable to the development of the much sought after optical memory necessary for buffering data in data networks. However, the transistor is clearly not compatible with CMOS fabrication and since it requires three lasers for the gate and source; and lasers to allow super-cooling of the caesium gas, it is unlikely to provide a practical solution in the foreseeable future.

Another approach presented in [129] is the development of a silicon optical transistor which uses an asymmetric coupled add/drop filter consisting of a micro-ring resonator next to an optical waveguide representing the source. Normally light will pass through the source waveguide and exit unaffected since weak source coupling with the micro-ring ensures that nonlinear effects are negligible. Its resonance will therefore remain unaffected. However, at a specific resonant frequency the light will interact with the micro-ring resonator greatly reducing the output and changing the state to off. This change in resonant frequency is achieved using another optical waveguide representing the gate. The input of the required light power to the gate waveguide couples in enough power to cause non-linear effects (e.g. the Kerr effect) in the micro-ring introducing an appreciable red-shift through the thermo-optic effect. This has the effect of changing the resonant frequency to that required to switch the source state from on to off. Since the source frequency is identical to the gate frequency, the cascadability requirement is satisfied. The ratio of the gate to source signals is reported to be nearly $6dB$ which allows fan-out to at least two other optical transistors. In addition, the device is reported to operate at $10GHz$. A notable advantage of this technology is compatibility with current state of the art CMOS fabrication techniques allowing scalability and avoiding the need to develop new fabrication techniques from the ground up.

8.6 Conclusions

The challenges ICT networks must face today have been discussed and it has been shown that an increasing amount of traffic, increasing power consumption and electronic bottlenecks are three main challenges that need to be addressed today. The ability of the information and communication sector ICT networks to satisfy the growing global demand for data is under threat due to the speed limitations of current

CMOS based electronic technologies, leading to electronic bottlenecks. The CMOS speed limitations are a result of the ending of Dennard scaling and the inability to provide sufficient cooling for CMOS based data-centre servers. Attempts to scale the speed up using the parallel signal processing in part helps to overcome this bottleneck, but is fundamentally limited by Amdahl's law due to a continued requirement for a serial data processing portion. The increase in demand for data coupled with ICT scaling and increased CMOS data speed has also resulted in a near exponential rise in power consumption. This growth is due to not only scaling to meet demand but also the power hungry cooling systems necessary to maintain CMOS based ICT equipment at temperature low enough to avoid thermal runaway and maintain the legally required ICT system reliability.

While optical fibre networks have a vast potential data handling capacity with relatively low power consumption, and current all-optical wavelength routing can help improve data network throughput, ultimately, at network endpoints, any such improvement will be constrained by fundamentally limited CMOS electronic signal processing capabilities. The growth in power consumption coupled in the absence of mature disruptive technologies will therefore soon hinder the ability of data networks to further scale to satisfy future demand for data. The solution to satisfying the rapid increase in demand for processing power in data centres is, in the medium to long term unlikely to be found using present CMOS technology. However, developments in optical routing show promise in reducing the need for CMOS based OEO transeivers, while progress in the development of the optical analogue of the CMOS transistor shows promise in the future realisation of all-optical data processing.

Chapter 9

Conclusions and future work

9.1 Conclusions

There are currently no commercially available wearable sensor technologies designed for the real time monitoring of temperature and pressure within the environment of a prosthetic socket despite the desirability of such a system for monitoring amputee patients during daily activity, and despite ongoing prosthetic socket mounted sensors research since the 1960's.

Commercially available PZT elements are identified as promising candidates for use as wearable prosthetic socket mounted sensors. PZT devices exhibit both piezoelectric and pyroelectric effects and are therefore interesting candidates for both temperature and pressure sensing applications. They also fulfil the requirements of robustness, a low thickness profile and low cost. A major disadvantage not exhibited by other sensor technologies is response voltage decay due to the finite input impedance of the necessary signal conditioning amplifier and dielectric leakage. However, in Chapter 6 it is shown that it is possible to mitigate these problems by the application of an appropriate signal conditioning design.

The piezoelectric and substrate constitutive state equations and associated low frequency diffusion equations required to find an LTI model of the sensor response to external thermal and elastic stimuli have been derived. These state equations were used to develop the mathematical models that describe the electric field response due to a surface temperature and/or applied axial stress and include the effect of substrate clamping and both internal equivalent resistance that represents dielectric leakage and an externally connected resistance that represents the input resistance of a follow-on signal-conditioning amplifier. While response models for both applied axial stress and temperature have been derived, the research presented in this thesis has concentrated on the use of the temperature response models of the PZT-5H sensor element to investigate the signal conditioning output voltage response.

The effect of the adhesive used to bond the substrate and electroded piezoelectric media has a negligible effect on the sensor element response when the adhesive temperature is kept below the glass transition temperature allowing the assumption that the piezoelectric medium is rigidly bonded to the substrate. While this assumption holds, the observed effective pyroelectric response is approximately 180% greater than the constant stress pyroelectric coefficient that is observed in the absence of substrate clamping. At temperatures above the glass transition temperature, it can be expected that the observed pyroelectric response will be significantly reduced and it is therefore important that the sensor element is not exposed to temperatures above approximately $80°C$. The effect of substrate clamping on the low frequency sensor element capacitance is to decrease it by approximately 30% compared to the constant stress capacitance value that is observed in the absence of the substrate.

At low frequency, the piezoelectric element is adequately modelled as a shunt-connected capacitor, C_p and resistor, R_p in parallel with a current source, which represents the rate of change of the negative piezoelectric medium bound surface charge due to a temperature change or applied axial stress. It has been demonstrated that C_p , C_o and C_m exhibit an approximately linear relationship with temperature and that all capacitances show a significant increase with increasing temperature over the range $20°C - 40°C$. The observed increases in capacitance are

not only be related to the temperature dependence of the dielectric constant, but also temperature dependence of the stiffness coefficients of the substrate and piezoelectric media and possibly the stress-charge piezoelectric coefficients. C_o exhibits the largest absolute increase of $2nF$ while C_m exhibits the greatest percentage increase at 25.2% over the temperature range $20°C - 40°C$ suggesting that the constant strain permittivity increases approximately linearly with temperature while the stiffnesses of the piezoelectric and substrate media reduce with temperature over the temperature range $20°C - 40°C$. These temperature dependencies indicate an undesirable temperature dependent gain and cut-on frequency that will lead to a non-linear sensor element voltage response, V_o over the temperature range $20°C - 40°C$. The effective pyroelectric coefficient, P_{eff} was also identified as being dependent on the stiffness coefficients of the substrate and piezoelectric media, and the stress-charge piezoelectric coefficients. However, the measured accumulative voltage response discussed in Chapter 7, Section 7.5 was found to exhibit linearity over the required operating temperature range of $20°C - 40°C$.

For the native piezoelectric leakage resistance, $R_p = 90G\Omega$ of the PZT-5H Murata Type 7BB-27-4 diaphragm element used, the desired charge-mode signal conditioning output response was realised using both the unipolar and bipolar signal-conditioning designs presented in Section 6.3.2 and Section 6.3.3 respectively regardless of the value of the feedback resistances R_f. The desired response is also realised for $R_f = 1G\Omega$ when R_p is reduced to $R_p = 100M\Omega$ due to moisture or crack formation as described in Section 6.3.2. However, when $R_p = 100M\Omega$ and $R_f = 1T\Omega$, as required for field use, the decay time constant is reduced and the specified signal decay, which is limited to 98% after an $8\,hour$ period, is no longer met. It was found that under these circumstances, the effect of a reduced R_p on the decay time constant could be mitigated using an enhanced open loop gain design, which was developed and is presented in Section 6.3.4. Future work to investigate the effect of prolonged cyclic stress and aging on the resistivity of the sensor element and to build and test the enhanced open loop gain design is required.

The contribution of the bias and bias offset currents to the overall drift voltage that can be expected after an operating period of $8\,hours$ using both of the unipolar and bipolar signal-conditioning designs was found to be can be negligible

for all values of R_p and for feedback resistances of both $R_f = 1G\Omega$ and $R_f = 1T\Omega$. It was also found that the contribution of voltage offset to the overall drift voltage after the $8\,hour$ operating period using the unipolar and bipolar signal-conditioning designs can be neglected when $R_p = 90G\Omega$ for both $R_f = 1G\Omega$ and $R_f = 1T\Omega$, and when $R_p = 100M\Omega$ for $R_f = 1G\Omega$. However, when $R_p = 100M\Omega$ and $R_f = 1T\Omega$, a drift voltage of approximately $40mV$, which is equivalent to a measurement error of approximately $0.25K$, will develop over an $8\,hour$ measurement period. In this case, replacement of the piezoelectric sensor element is required. Alternatively, the use of the voltage compensation method described in Section 6.4.5 will mitigate the increasing drift voltage over the measurement period. Lower values of R_p will result in a greater drift with the drift following an approximately inversely proportional relationship to R_p. Similarly, the contribution of maximum bias voltage drift after an $8\,hour$ operating period can be neglected when $R_p = 90G\Omega$ for both $R_f = 1G\Omega$ and $R_f = 1T\Omega$, and when $R_p = 100M\Omega$ for $R_f = 1G\Omega$. However, when $R_p = 100M\Omega$ and $R_f = 1T\Omega$, a drift voltage of approximately $1V$, which is equivalent to a measurement error of approximately $6K$, will develop over an $8\,hour$ measurement period. Replacement of the piezoelectric sensor element is also required in this case. Alternatively, as above, the use of the voltage compensation method described in Section 6.4.5 will mitigate the increasing drift voltage over the measurement period. In common with the input offset voltage case, the magnitude of the bias voltage drift follows an approximately inversely proportional relationship to R_p.

The use of the enhanced open loop gain signal-conditioning design described in Section 6.3.4 may help to mitigate output voltage drift due to input bias currents, input offset voltages and differences in the bias voltages. However, application of this method rather than the voltage compensation method is for the present treated with caution since the input bias currents and offset voltages of OA4 and OA5, and the differences in the bias voltages seen at the non-inverting inputs of OA4 and OA5 have not been taken into account in the analysis. A full analysis and construction of the enhanced open loop gain design is the subject of future work.

By far the greatest contributors to the total mean squared noise at the amplifier output are due to R_1, R_2, R_3, R_{d2} and the input referred noise voltage of

OA3. The noise contribution of the difference amplifier stage is therefore a focus for noise reduction in future work.

The analysis of Chapter 6 makes the assumption that feedback resistances of $R_f = 1T\Omega$ are achievable. The dielectric resistance of the polypropylene feedback capacitors is extremely large, however in practice it may not be large enough to realise an overall feedback resistance as high as $R_f = 1T\Omega$. An alternative solution to achieving the required maximum 98% signal decay after an $8\,hour$ period specification is the use of a real-time decay compensation scheme based on the discussion in Section 7.2.3. Decay compensation can be applied in tandem with a slightly reduced and more easily realisable overall value of R_f to reduce low frequency signal decay and mitigate the requirement for very large feedback resistances in a practical measurement system. A disadvantage identified with this method is that the output offsets and the output noise will increase with time. As the signal is decay compensated, the offset voltages at the end of the $8\,hour$ measurement period will be greater and the output SNR will be lower such that there is a trade-off between the SNR at the end of the measurement period and the value of R_f used. By selecting a suitable value of R_f, a maximum acceptable overall drift and minimum acceptable SNR at the end of the measurement period can be realised. It was demonstrated in Section 7.3 and Section 7.5 that signal decay compensation is an effective method of compensating for the signal-conditioning decay observed in the raw measurement data of the transient and accumulative voltage response measurements. The use of decay compensation with a reduced requirement for large R_f will be the subject of future work.

In Section 7.3 it is shown that the sensor and signal conditioning system produces a faster response demonstrated by an approximately 50% greater amplitude at the first transient hunting peak than the commonly used type K thermocouple, which is attached to the Peltier tile to provide the surface temperature reference. In Section 7.3 and Section 7.5, the experimentally observed temperature to voltage conversion factors (CF) for the transient response and accumulative responses for $C_f = 1.5\mu F$ are given by $CF = sens(G = 0.5) = 0.16\,V/K$ and $CF = sens(G = 0.5) = 0.1503\,V/K$ respectively. These values agree reasonably well with the theoretical value of 0.1476. The transient response conversion factors with $G = 1$

for $C_f = 1\mu F$ and $C_f = 1.5\mu F$ of 0.47 and 0.32 respectively yield a ratio of $0.47/0.32 = 1.47$ that agrees well with the expectation of an inverse proportional relationship between charge amplifier gain and C_f. The small discrepancy is easily explained by nominal C_f value tolerances of $\pm 5\%$ and measurement reading error due to signal noise.

It Section 7.5 it is demonstrated that the sensor response under short-circuit conditions is linear over the temperature range $20°C$ and $42°C$. It is considered that the small $0.05V$ deviation at $20°C$ which is equivalent to approximately $0.33°C$ in the round trip $20°C \rightarrow 42°C \rightarrow 20°C$ measurement is due to measurement error rather than any underlying rate-independent hysteretic or other physical process. However, this observation requires further investigation to confirm measurement error and this will be the subject of future work.

In Section 7.5.2, the measured total pyroelectric response P_{eff} is demonstrated to be approximately $-870\ \mu C/m^2K$. This value agrees well with the calculated response of $P_{eff} \approx -800$ to $-900\ \mu C m^{-2}K^{-1}$ given in Section 4.6 and confirms the anticipated pyroelectric response enhancement due to substrate clamping.

A prudent estimate of the sensor element and charge amplifier accuracy is given as $\pm 3.5\%$ in Section 7.5.3. However, since the temperature reference is obtained using a thermocouple integrated with the Peltier tile and PID controller, the validity of the estimate is dependent on the accuracy of the thermocouple. With a typical accuracy of $\pm 2.2°C$ at low temperatures for the type K thermocouple used, ($\pm 10.5\%$ at $20°C$ and $\pm 5.5\%$ at $40°C$) over the temperature range of interest, this estimate of sensor accuracy is treated with caution and improving this estimate of accuracy will be the subject of future work.

From the results of Section 7.7.2 and Section 7.7.3, it can be seen that the sensor is capable of a fast response when used directly against the measurement surface. For a DC step of $1K$, the rise time to 98% peak output, and to peak output is $0.12s$ and $0.9s$ respectively. The sensor is capable of measuring frequencies up to $6.8rads^{-1}$ ($\approx 1.1Hz$) with a rise time to the 98% peak of $0.18s$ for a sinusoidal step of amplitude $1K$. This performance is promising for the application of the sensor as a medical diagnostic tool in the detection of high frequency temperature

oscillations at the skin surface that are symptomatic of some vascular and other diseases.

However, from the results of Section 7.7.4 and Section 7.7.5, the use of a polymer liner between the sensor element and measurement surface severely limits the usable frequency response of the sensor due to severe amplitude and phase distortion, precluding the direct use of the sensor to measure the skin surface temperature. This result is no surprise and confirms intuition that this would be the case. Achieving a reliable measure of skin surface temperature within a prosthetic socket without direct sensor element to skin contact is a desirable aim and this will be the subject of future work.

An additional consideration when using a liner is that when compressed, the liner thickness, specific heat capacity and the density may change significantly. This in turn will cause a change in the diffusion coefficient (diffusivity) of the liner elastomer material, which is specific heat capacity and density dependent. A change in the thickness, specific heat capacity and density may therefore significantly influence the response at the output of the signal-conditioning amplifier. Further work is required to investigate possible effects on the sensor response.

The challenges ICT networks must face today have been discussed and it has been shown that an increasing amount of traffic, increasing power consumption and electronic bottlenecks are three main challenges that need to be addressed today. The ability of the information and communication sector ICT networks to satisfy the growing global demand for data is under threat due to the speed limitations of current CMOS based electronic technologies, leading to electronic bottlenecks. The CMOS speed limitations are a result of the ending of Dennard scaling and the inability to provide sufficient cooling for CMOS based data-centre servers. Attempts to scale the speed up using the parallel signal processing in part helps to overcome this bottleneck, but is fundamentally limited by Amdahl's law due to a continued requirement for a serial data processing portion. The increase in demand for data coupled with ICT scaling and increased CMOS data speed has also resulted in a near exponential rise in power consumption. This growth is due to not only scaling to meet demand but also the power hungry cooling systems necessary to maintain

CMOS based ICT equipment at temperature low enough to avoid thermal runaway and maintain the legally required ICT system reliability.

While optical fibre networks have a vast potential data handling capacity with relatively low power consumption, and current all-optical wavelength routing can help improve data network throughput and reduce the need for OEO tranceivers, ultimately, at network endpoints, any such improvement will be constrained by fundamentally limited CMOS electronic signal processing capabilities. The growth in power consumption coupled with the absence of new and disruptive technologies may soon hinder the ability of data networks to further scale to satisfy future demand. The solution to satisfying the rapid increase in demand for processing power in data centres is, in the long term unlikely to be found using current CMOS based technology. The solution to satisfying the rapid increase in demand for processing power in data centres is, in the medium to long term unlikely to be found using present CMOS technology. However, progress in the development of the optical analogue of the CMOS transistor shows promise in the future realisation of all-optical data processing.

9.2 Future work

In Section 6.3.4 it was shown that the use of the enhanced open loop gain signal-conditioning design may help to mitigate output voltage drift due to input bias currents, input offset voltages and differences in the bias voltages. Further work will include a full theoretical analysis, construction and test of the enhanced open loop gain design.

The charge amplifier designs described in Section 6.3 require very large feedback resistances to realise the required specification. An alternative solution to reducing low frequency signal decay and achieving the charge amplifier specification is the use of a real-time decay compensation scheme based on the discussion in Section 7.2.3 in tandem with slightly reduced and more easily realisable overall values of feedback resistances. Further research is required to investigate the use of decay compensation with reduced feedback resistance values. The signal decay compensation scheme was applied to the measurement data of Section 7.3 and

Section 7.5 where it was demonstrated to be an effective tool in compensating for the signal-conditioning decay observed in the raw measurement data.

In Section 6.5 it was identified that by far the greatest contributors to the total mean squared noise at the amplifier output are due to the charge amplifier forward difference gain stage. While the output noise SNR demonstrated is acceptable, further research is desirable to investigate an alternative or modified forward difference stage design to realise an improved SNR at the charge amplifier output.

In Section 7.5.1 it was demonstrated that the sensor response under short-circuit conditions is linear over the temperature range $20°C$ and $42°C$ with a small $0.05V$ deviation at $20°C$ equivalent to approximately $0.33°C$ in the round trip $20°C \rightarrow 42°C \rightarrow 20°C$ measurement. Future research will investigate the cause of this deviation to determine whether it is due to measurement error or an underlying rate-independent hysteretic or other physical process.

In Section 7.5.3 an estimate of the sensor element and charge amplifier accuracy was given as $\pm 3.5\%$ with the temperature reference being obtained using a type K thermocouple. The validity of this estimate is thereofore dependent on the accuracy of the thermocouple. With a typical accuracy of $\pm 2.2°C$ at low temperatures for the type K thermocouple used, ($\pm 10.5\%$ at $20°C$ and $\pm 5.5\%$ at $40°C$) over the temperature range of interest, this estimate of sensor accuracy must be treated with caution. Further research is therefore required to devise an improved temperature reference method, allowing an improved estimate of sensor accuracy.

Section 7.7.4 and Section 7.7.5 demonstrate that the use of a polymer liner between the sensor element and measurement surface severely limits the usable frequency response of the sensor due to severe amplitude and phase distortion, precluding the direct use of the sensor to measure the skin surface temperature. Since the ability to reliably measure skin surface temperature within a prosthetic socket without direct sensor element to skin contact is a desirable aim, future research will investigate the application of the Gaussian-learning algorithm described in [98] as a possible solution to providing a meaningful indirect measure of skin temperature from a heavily amplitude and phase distorted sensor signal.

Appendices

A.1 Table of material constants

$c_{11}^E = 126\ GPa$	$c_{12}^E = 79.5\ GPa$	$c_{31}^E = 84.1\ GPa$	$c_{33}^E = 117\ GPa$
$e_{31} = -6.55\ Cm^{-2}$	$e_{33} = 23.3\ Cm^{-2}$	$\varphi_{p1} \approx \varphi_{p3} = 4\ \mu mm^{-1}K^{-1}$	$\varphi_b = 19\ \mu mm^{-1}K^{-1}$
$\alpha = 84.6\ GPa$	$\beta = -46.6\ Cm^{-2}$	$P^S \approx -350\ \mu Cm^{-2}K^{-1}$	$\varepsilon_{33}^S = 13\ nFm^{-1}$
$\mu_b = 0.34$	$E_b = 110\ GPa$	$\frac{A_p}{A_b} = 0.568$	$\frac{A_b}{A_p} = 1.761$
$l_p = 0.23\ mm$	$l_b = 0.3\ mm$	$C_{sp}^{S,E} = 350\ Jkg^{-1}K^{-1}$	$C_{spb}^S = 380 Jkg^{-1}K^{-1}$
$C_e = 1800\ Jkg^{-1}K^{-1}$	$k_p = 1.1 Wm^{-1}K^{-1}$	$k_b = 109 Wm^{-1}K^{-1}$	$k_e = 0.2 Wm^{-1}K^{-1}$
$\rho_p = 7800\ kgm^{-3}$	$\rho_e = 1100\ kgm^{-3}$	$\rho_b = 8500\ kgm^{-3}$	$A_s = 2.6 \times 10^{-4} m^2$

All constants relating to the piezoelectric medium are for PZT-5H. The constants α and β are defined as:

$$\alpha = c_{11}^E + c_{12}^E - 2\frac{\left(c_{31}^E\right)^2}{c_{33}^E} = \frac{E_{p1}^E}{1-\mu_{p1}^E}$$

$$\beta = 2\left(e_{31} - e_{33}\frac{c_{31}^E}{c_{33}^E}\right)$$

A.2 Thermodynamic potentials

Equations A.2.1 to A.2.4 give the well-known scalar thermodynamic potentials as the Electric Gibbs free energy, Elastic Gibbs free energy, Gibbs free energy and Helmholtz free energy in matrix form, where the internal energy of the system is given by U.

$$G_e = U - \theta\Sigma - \boldsymbol{E}^t\boldsymbol{D} \qquad \text{Electric Gibbs free energy} \qquad (A.2.1)$$

$$G_p = U - \theta\Sigma - \boldsymbol{T}^t\boldsymbol{S} \qquad \text{Elastic Gibbs free energy} \qquad (A.2.2)$$

$$G = U - \theta\Sigma - \boldsymbol{E}^t\boldsymbol{D} - \boldsymbol{T}^t\boldsymbol{S} \qquad \text{Gibbs free energy} \qquad (A.2.3)$$

$$A = U - \theta\Sigma \qquad \text{Helmholtz free energy} \qquad (A.2.4)$$

Equation 3.2 gives the differential form of the internal energy.

$$dU = \theta d\Sigma + \boldsymbol{T}^t d\boldsymbol{S} + \boldsymbol{E}^t d\boldsymbol{D} \qquad (3.2)$$

Total differentiation of Equations A.2.1 to A.2.4 followed by substitution of dU given by Equation 3.2 yields the differential form of the scalar thermodynamic potentials given by Equation 3.5 and Equation A.2.5 to Equation A.2.7.

$$dG_e = \boldsymbol{T}^t d\boldsymbol{S} - \boldsymbol{D}^t d\boldsymbol{E} - \Sigma d\theta \qquad (\boldsymbol{S}, \boldsymbol{E}, \Delta\theta \text{ IV form}) \qquad (3.5)$$

$$dG_p = -\boldsymbol{S}^t d\boldsymbol{T} + \boldsymbol{E}^t d\boldsymbol{D} - \Sigma d\theta \qquad (\boldsymbol{T}, \boldsymbol{D}, \Delta\theta \text{ IV form}) \qquad (A.2.5)$$

$$dG = -\boldsymbol{S}^t d\boldsymbol{T} - \boldsymbol{D}^t d\boldsymbol{E} - \Sigma d\theta \qquad (\boldsymbol{T}, \boldsymbol{E}, \Delta\theta \text{ IV form}) \qquad (A.2.6)$$

$$dA = \boldsymbol{T}^t d\boldsymbol{S} + \boldsymbol{E}^t d\boldsymbol{D} - \Sigma d\theta \qquad (\boldsymbol{S}, \boldsymbol{D}, \Delta\theta \text{ IV form}) \qquad (A.2.7)$$

Using a similar analysis to that given in Section 3.3.1, the piezoelectric constitutive state Equations are derivable in four equivalent forms by suitable choice of thermodynamic potential, given by Equation 3.5 and Equation A.2.5 to Equation A.2.7, each with the set of independent variables (IV) shown in brackets.

A.3 Ferroelectric hysteresis and losses

A.3.1 Ferroelectric hysteresis

The existence of hysteresis in any system results in non-linearity of response and energy losses due to for example finite dielectric resistivity, rate dependence of the piezoelectric constants and viscous damping effects. Piezoelectric materials that have large piezoelectric coefficients such as PZT and in particular the so-called soft PZT-5H, also tend to exhibit the most pronounced electro-mechanical hysteresis effects [130]. Hysteresis is a departure in the behaviour of piezoelectric materials from the linear theory, which is valid for small signal static and quasi-static operation; and at small electric fields and stresses well below those required for 180° ferroelectric domain switching. In the unrealisable 'ideal' poled piezoelectric material, the application of an increasing electric field in the same direction as the remanent polarisation of the piezoelectric material would exhibit a behaviour that exactly follows the linear piezoelectric constitutive equations up to the coercive electric field required for 180° domain reversal. When the electric field reaches the coercive field, $-E_c$, an instantaneous and simultaneous 180° domain reversal throughout the ferroelectric material will occur resulting in a change in remanent $(E = 0)$ polarisation from $+P_r \; to \; - \; P_r$. Beyond E_c, the ferroelectric material, which is now poled in the opposite direction will continue to follow behaviour predicted by the linear constitutive equations. Likewise, on reducing the applied electric field, the piezoelectric would continue to behave as the linear constitutive equations predict until the electric field reaches E_c where a further instantaneous 180° domain reversal occurs returning the piezoelectric material to its initial remanent polarisation state when E is reduced to zero. In addition to the remanent polarisation, an instantaneous 180° domain reversal will also result in an instantaneous reversal of the strain of the ferroelectric material parallel to the direction of the applied electric field at $-E_c$, however the remanent strain $(E = 0)$ remains unchanged. The constitutive equations would therefore accurately predict the behaviour of the 'ideal' piezoelectric material everywhere except at the two values of electric field $(\pm E_c)$ where instantaneous 180° domain reversal takes place. For the case of the $P - E$ measurement, cycling the electric field to $\pm E_c$ will produce a counter-clockwise asymmetric oblique

trapezoidal shaped hysteresis loop in the range $\pm E_c$ with two instantaneous polarisation reversals at $\pm E_c$. This 'ideal' material hysteresis is therefore non-linear having two values at both $+E_c$ and $-E_c$, and is independent of frequency (is rate independent). With the exception of $\pm E_c$ the 'ideal' piezoelectric material will everywhere exhibit behaviour described by the linear constitutive equations in either polarisation state. However real piezoelectric materials exhibit a multitude of both linear and non-linear hysteretic processes, many for which the causes are not fully understood [131].

The nature of ferroelectric hysteresis can be categorised into two main areas - non-linear rate-independent and linear rate-dependent types, the latter for which the hysteresis is dependent on the frequency of the excitation field. Hysteresis involving mixed electrical and mechanical variables produces a 'clockwise' loop, where the measured response to a driving field reduces in time as the driving field is cycled. Examples of this type are the so-called piezoelectric hysteresis electric field (E) – strain (S) (with E as the x-axis) measurement used to characterise the performance of piezoelectric actuators; and the stress (T) - electric displacement (D) hysteresis measurement used to characterise the performance of piezoelectric force sensors and accelerometers under short-circuit conditions. Conversely, the well-known Polarisation (P) – electric field (E) (with E as the x-axis) measurement produces a counter-clockwise hysteresis curve.

Hysteresis effects prevalent in ferroelectric materials may be further described as either 'switching' or 'non-switching'. A main contribution to the hysteresis characterised by $P-E$ and $S-E$ measurements are of the non-linear rate-independent switching type. In piezo ceramics such as PZT and polymers such as PVDF, at excitation fields high enough to reverse or 'switch' the ferroelectric domains, ferroelectric domain switching unlike the 'ideal' ferroelectric material is not instantaneous and begins to occur at excitation fields below E_c. Individual ferroelectric domains switch at different coercive fields both above and below E_c and some do not switch at all. A further 'switching' contribution to the hysteresis observed is a rate-dependent type due to delays in domain switching.

The contributions of 'Non-switching' hysteretic behaviour is predominantly due to linear rate-dependent processes due to for example, mechanical damping

caused by internal friction; dielectric losses (at low frequency dominated by dielectric leakage), and crystalline defects exhibiting a Debye type relaxation [132]. Crystalline defects that contribute both a polarisation and elastic dipole such as those evident in ferroelectric materials simultaneously create a relaxation in the piezoelectric coefficients and a contribution to the relaxation in both the elastic and dielectric constants [133].

Under short-circuit $E = 0$ conditions and at electric fields well below that required for the onset of domain switching, the main contributions to hysteresis are linear and rate-dependent. For constant sinusoidal excitation, these may be described by the inclusion of a rate-dependent imaginary term in the elastic, dielectric and piezoelectric constants. At low frequencies, the elastic and dielectric terms are given by $j\omega\eta$ and $-j\,\delta/\omega$ respectively, where η is the damping constant matrix and δ is the conductivity matrix. The imaginary parts of the piezoelectric constants are low in comparison to those of the elastic and dielectric constants and are generally ignored [134]. The imaginary parts of the elastic and dielectric constants account for material losses mainly in the form of heat dissipation due to viscous damping and the finite resistivity of the dielectric.

A.3.2 Joule heating and viscous friction

The state equations developed in Chapter 3 do not include the effect of rate-dependent heat generation due to internal viscous friction or Joule heating due to dielectric leakage. Heating can generally be neglected in low frequency applications, however if necessary, these effects can be taken into account by returning to Equation 3.2 that describes the combined first and second laws of thermodynamics in the piezoelectric material, and considering an additional change in the internal energy due to these effects.

The internal energy can be written in terms of the electro-mechanical pairs $\boldsymbol{E-S}$, $\boldsymbol{D-S}$ or $\boldsymbol{D-T}$ as the independent variables. The $\boldsymbol{E-S}$ independent variable form of the internal energy allows the mechanical and electrical components of the loss power to be delineated more easily in the final expression of internal energy. The alternative forms discussed above produce coupled mechanical and

electrical terms that contain both electrical and mechanical loss components that are not so intuitive. To include losses, Equation 3.32 is written in time differential form as Equation A.3.1.

$$\frac{\partial U}{\partial t} = \theta_o \boldsymbol{\gamma}^{E,t} \frac{\partial \boldsymbol{S}}{\partial t} + \theta \boldsymbol{p}^{S,t} \frac{\partial \boldsymbol{E}}{\partial t} + \boldsymbol{E}^t \boldsymbol{p}^S \frac{\partial \theta}{\partial t} + \rho C_{sp}^{S,E} \frac{\partial \theta}{\partial t} + \boldsymbol{S}^t \boldsymbol{c}^E \frac{\partial \boldsymbol{S}}{\partial t} + \boldsymbol{E}^t \boldsymbol{\varepsilon}^S \frac{\partial \boldsymbol{E}}{\partial t} \qquad \text{(A.3.1)}$$

To include mechanical losses and assuming that the piezoelectric material can be described by the Kelvin-Voigt viscous damping model, then the stiffness matrix, $\boldsymbol{c}^E$ can be replaced with a Kelvin-Voigt operator such that $\boldsymbol{c}^E \rightarrow \left(\boldsymbol{c}^E + \boldsymbol{\eta}^E \frac{\partial}{\partial t}\right)$ [135] where $\boldsymbol{\eta}^E$ is introduced as a matrix of viscous friction coefficients. In a similar way the thermal stress coefficient matrix, $\boldsymbol{\gamma}^{E,t}$ can be replaced with the operator such that $\boldsymbol{\gamma}^{E,t} \rightarrow \left(\boldsymbol{\gamma}^{E,t} + \boldsymbol{\varphi}^{E,t} \boldsymbol{\eta}^{E,t} \frac{\partial}{\partial t}\right)$. The inclusion of electrical Joule losses due to dielectric leakage can be included by replacing the permittivity $\boldsymbol{\varepsilon}^S$ by $\left(\boldsymbol{\varepsilon}^S + \boldsymbol{\delta} \int_0^t \{\} dt\right)$ with the assumption that the electric field is zero before time $t = 0$ where $\boldsymbol{\delta}$ is the conductivity matrix of the piezoelectric medium. Substituting the mechanical and electrical operators yields Equation A.3.2.

$$\frac{\partial U_{total}}{\partial t} = \theta_o \boldsymbol{\gamma}^{E,t} \frac{\partial \boldsymbol{S}}{\partial t} + \theta \boldsymbol{p}^{S,t} \frac{\partial \boldsymbol{E}}{\partial t} + \boldsymbol{E}^t \boldsymbol{p}^S \frac{\partial \theta}{\partial t} + \rho C_{sp}^{S,E} \frac{\partial \theta}{\partial t} + \boldsymbol{S}^t \boldsymbol{c}^E \frac{\partial \boldsymbol{S}}{\partial t} + \boldsymbol{E}^t \boldsymbol{\varepsilon}^S \frac{\partial \boldsymbol{E}}{\partial t}$$
$$+ \frac{\partial \boldsymbol{S}^t}{\partial t} \boldsymbol{\eta}^E \frac{\partial \boldsymbol{S}}{\partial t} + \boldsymbol{E}^t \boldsymbol{\delta} \int_0^t \frac{\partial \boldsymbol{E}}{\partial t} dt \qquad \text{(A.3.2)}$$

Separating the internal energy loss terms and denoting these by U_{loss} yields Equation A.3.3.

$$\frac{\partial U_{loss}}{\partial t} = \frac{\partial \boldsymbol{S}^t}{\partial t} \boldsymbol{\eta}^E \frac{\partial \boldsymbol{S}}{\partial t} + \boldsymbol{E}^t \boldsymbol{\delta} \int_0^t \frac{\partial \boldsymbol{E}}{\partial t} dt = \frac{\partial \boldsymbol{S}^t}{\partial t} \boldsymbol{\eta}^E \frac{\partial \boldsymbol{S}}{\partial t} + \boldsymbol{E}^t \boldsymbol{\delta} \boldsymbol{E} \qquad \text{(A.3.3)}$$

Equation A.3.3 is valid for the looser assumption of a small temperature change such that the piezoelectric state equations remain valid. $\partial U_{loss}/\partial t$ is the rate of heat generated per unit volume within the piezoelectric medium due to Joule heating and viscous friction. It can be seen that when $\boldsymbol{E}$ is independent of the spatial dimensions, the dielectric loss term $\boldsymbol{E}^t \boldsymbol{\delta} \boldsymbol{E}$ is equivalent to the Ohm's law power relationship $P = V^2/R$ divided by the volume of the piezoelectric medium, which is independent of frequency and where $R = R_p$ is the equivalent electrical resistance

between the electrodes. In general, the electric field will vary with position along the poling axis, for example when there is a temperature gradient or in a piezoelectric thickness mode resonator under high frequency excitation and therefore, in general the power loss density is also spatially dependent, varying in both time and position.

Assuming that $\partial U_{loss}/\partial t$ is completely converted to heat and denoting the total entropy of the system as Σ_T, then the rate of change of the total entropy of the system $\partial \Sigma_T/\partial t$ is given by Equation A.3.4.

$$\frac{\partial \Sigma_T}{\partial t} = \boldsymbol{\gamma}^{E,t}\frac{\partial \boldsymbol{S}}{\partial t} + \boldsymbol{p}^{S,t}\frac{\partial \boldsymbol{E}}{\partial t} + \frac{\rho C_{sp}^{S,E}\frac{\partial \theta}{\partial t} + \frac{\partial \boldsymbol{S}^t}{\partial t}\boldsymbol{\eta}^E\frac{\partial \boldsymbol{S}}{\partial t} + \boldsymbol{E}^t\boldsymbol{\delta}\boldsymbol{E}}{\theta} \tag{A.3.4}$$

Equation A.3.5 therefore gives the total entropy.

$$\Sigma_T = \boldsymbol{\gamma}^{E,t}\boldsymbol{S} + \boldsymbol{p}^{S,t}\boldsymbol{E} + \int_0^t \left(\frac{\rho C_{sp}^{S,E}\frac{\partial \theta}{\partial t} + \frac{\partial \boldsymbol{S}^t}{\partial t}\boldsymbol{\eta}^E\frac{\partial \boldsymbol{S}}{\partial t} + \boldsymbol{E}^t\boldsymbol{\delta}\boldsymbol{E}}{\theta}\right) dt \tag{A.3.5}$$

In an adiabatically isolated piezoelectric medium, work done on the medium produces zero net entropy change since heat can neither enter nor leave. However, where Joule heating or viscous damping is present, the internal entropy and the temperature will rise monotonically with time due to the last term of Equation A.3.5.

Where the boundary conditions of the problem under consideration produces temperature changes within the piezoelectric medium that can be considered small such that $\theta \cong \theta_o$, then Equation A.3.5 can be written as Equation A.3.6. There is therefore an additional net outflow or dissipation of heat from the piezoelectric medium with an associated reduction in entropy equal to the integral term in Equation A.3.6. Since this heat must be removed to an external reservoir at a lower temperature, there will be a monotonic increase in the entropy of the whole system (constituting the entropy, Σ_T of the piezoelectric medium and the entropy of the external heat reservoir) with time.

$$\Sigma_T \cong \boldsymbol{\gamma}^{E,t}\boldsymbol{S} + \boldsymbol{p}^{S,t}\boldsymbol{E} + \frac{\rho C_{sp}^{S,E}\Delta\theta}{\theta_o} + \frac{1}{\theta_o}\int_0^t \left(\frac{\partial \boldsymbol{S}^t}{\partial t}\boldsymbol{\eta}^E\frac{\partial \boldsymbol{S}}{\partial t} + \boldsymbol{E}^t\boldsymbol{\delta}\boldsymbol{E}\right) dt \tag{A.3.6}$$

In the derivation of the sensor models discussed in Chapter 4, the rate dependent nature of the piezoelectric constant and viscous friction losses are considered negligible since the frequencies under consideration are very low. Joule

heat generation, unlike viscous friction is not dependent on frequency and since the conductivity of piezo-ceramics is very low, the effect on heating can also be safely neglected. However, since the dielectric loss is inversely proportional to frequency, significant effects on the low frequency phase and amplitude of the sensor response cannot be neglected.

For application as temperature or pressure sensor where the device is adiabatically isolated on all but the measuring surface, it is essential that the body measurement surface can adequately absorb the resulting flow of Joule heat without significantly affecting its temperature. However, it is intuitive that a temperature or applied axial stress excitation would result in only a small net heat flow of the piezoelectric medium that will limit the increase of temperature due to heating. The approximation of $\theta \cong \theta_o$ is therefore considered to be valid in the development of the mathematical models.

Power loss can also be described by assuming sinusoidal excitation and applying the concept of complex power to Equation 3.2 to yield the RMS power given by Equation A.3.7. The elastic-dielectric and thermal variables are the peak values and the superscript $*$ indicates the complex conjugate.

$$j\omega U_{loss} = P_{loss} = \frac{1}{2} \times Re\{\theta(j\omega\Sigma)^* + \boldsymbol{T}^t(j\omega\boldsymbol{S})^* + \boldsymbol{E}^t(j\omega\boldsymbol{D})^*\} \tag{A.3.7}$$

By substituting the constitutive equations given by Equations 3.22 to 3.24 into Equation A.3.7, the power loss is given by Equation A.3.8.

$$P_{loss} = \frac{1}{2} \times Re\left\{\begin{array}{c} -\theta j\omega\left(\boldsymbol{\gamma}^{E,t}\boldsymbol{S} + \boldsymbol{p}^{S,t}\boldsymbol{E} + \frac{\rho C_{sp}^{S,E}\Delta\theta}{\theta}\right)^* - (\boldsymbol{S}^t\boldsymbol{c}^E - \boldsymbol{E}^t\boldsymbol{e} - \boldsymbol{\gamma}^{E,t}\Delta\theta)j\omega\boldsymbol{S}^* \\ -\boldsymbol{E}^t j\omega(\boldsymbol{e}\boldsymbol{S} + \boldsymbol{\varepsilon}^S\boldsymbol{E} + \boldsymbol{p}^S\Delta\theta)^* \end{array}\right\} \tag{A.3.8}$$

Rewriting Equation A.3.8 yields Equation A.3.9.

$$P_{loss} = \frac{1}{2}\omega \times Im\left\{\begin{array}{c} \theta\left(\boldsymbol{\gamma}^{E,t}\boldsymbol{S} + \boldsymbol{p}^{S,t}\boldsymbol{E} + \frac{\rho C_{sp}^{S,E}\Delta\theta}{\theta}\right)^* + (\boldsymbol{S}^t\boldsymbol{c}^E - \boldsymbol{E}^t\boldsymbol{e} - \boldsymbol{\gamma}^{E,t}\Delta\theta)\boldsymbol{S}^* \\ +\boldsymbol{E}^t(\boldsymbol{e}\boldsymbol{S} + \boldsymbol{\varepsilon}^S\boldsymbol{E} + \boldsymbol{p}^S\Delta\theta)^* \end{array}\right\} \tag{A.3.9}$$

Rationalising Equation A.3.9 and removing the terms for which the imaginary part is zero yields Equation A.3.10 that represents the dissipative part of the complex power.

$$P_{loss} = \frac{1}{2}\omega * Im\{\boldsymbol{S}^t\boldsymbol{c}^E\boldsymbol{S}^* + \boldsymbol{E}^t(\boldsymbol{\varepsilon}^S\boldsymbol{E})^*\} \tag{A.3.10}$$

Substituting the complex operator forms of $\boldsymbol{c}^E$ and $\boldsymbol{\varepsilon}^S$ such that $\boldsymbol{c}^E \rightarrow (\boldsymbol{c}^E + j\omega\boldsymbol{\eta}^E)$ and $\boldsymbol{\varepsilon}^S \rightarrow (\boldsymbol{\varepsilon}^S - j\,\boldsymbol{\delta}/\omega)$ into Equation A.3.10 yields Equation A.3.11.

$$P_{loss} = \frac{1}{2}\omega * Im\{\boldsymbol{S}^t(\boldsymbol{c}^E + j\omega\boldsymbol{\eta}^E)\boldsymbol{S}^* + \boldsymbol{E}^t(\boldsymbol{\varepsilon}^S + j\,\boldsymbol{\delta}/\omega)\boldsymbol{E}^*\} \tag{A.3.11}$$

Rationalising Equation A.3.11 yields Equation A.3.12.

$$P_{loss} = \frac{1}{2} * \{\omega^2\boldsymbol{S}^t\boldsymbol{\eta}^E\boldsymbol{S}^* + \boldsymbol{E}^t\boldsymbol{\delta}\boldsymbol{E}^*\} \tag{A.3.12}$$

If steady state sinusoidal excitation is assumed for Equation 5.77), then both Equations A.3.3 and (A.3.12) are equivalent when averaged over time. Equation A.3.3 includes an additional term representing the 2ω power ripple for which the time average and therefore the RMS value is zero.

While the effect of Joule heating and viscous heating in piezoelectric devices when used as a low frequency sensor is negligible, heating may however become a problem in resonator and ultrasound applications where high frequency excitation is used and where the effect of viscous damping, which is frequency dependent, can become significant. In Chapter 5, impedance measurements at excitation frequencies up to $200kHz$ over a range of temperatures are undertaken to investigate the effect of temperature on the sensor susceptances. However, the use of a Peltier device with temperature feedback coupled to a PID controller to vary the temperature ensures that the effect of heating due mainly to viscous friction is continuously compensated maintaining the sensor temperature approximately constant.

A.4 Internal energy in $\boldsymbol{T-E}$ form

An expression for the internal energy U in $T-E$ form is found by substituting Equations 3.22, 3.23 and 3.34, in their differential form, into Equation 3.2 to give Equation A4.1. The approximation $\theta \cong \boldsymbol{\theta_o}$ for small $\boldsymbol{\Delta\theta}$ used in Equation 3.21b cannot be introduced until the end of the following analysis and $\boldsymbol{\theta_o}$ is therefore properly replaced by θ in Equation 3.34.

$$dU = \theta(\boldsymbol{\gamma}^{E,t}\boldsymbol{s}^{E}(d\boldsymbol{T} + \boldsymbol{e}^{t}d\boldsymbol{E} + \boldsymbol{\gamma}^{E}d\theta) + \boldsymbol{p}^{S,t}d\boldsymbol{E}) + \rho C_{sp}^{S,E}d\theta + \boldsymbol{T}^{t}\boldsymbol{s}^{E}(d\boldsymbol{T} + \boldsymbol{e}^{t}d\boldsymbol{E} + \boldsymbol{\gamma}^{E}d\theta) + \boldsymbol{E}^{t}(\boldsymbol{e}\boldsymbol{s}^{E}(d\boldsymbol{T} + \boldsymbol{e}^{t}d\boldsymbol{E} + \boldsymbol{\gamma}^{E}d\theta) + \boldsymbol{\varepsilon}^{S}d\boldsymbol{E} + \boldsymbol{p}^{S}d\theta) \quad \text{(A4.1)}$$

Noting that the specific heat capacities are related by $C_{sp}^{T,E} = C_{sp}^{S,E} + \theta_o\boldsymbol{\gamma}^{E,t}\boldsymbol{\varphi}^{E,t}/\rho$ for a small temperature change $\Delta\theta$ such that $\theta \cong \theta_o$, rationalising and rearranging Equation A4.1 using the relationships between the matrix constants discussed in Appendix A.6 yields Equation A4.2.

$$dU = \theta(\boldsymbol{\varphi}^{E,t}d\boldsymbol{T} + \boldsymbol{p}^{T,t}d\boldsymbol{E}) + (\boldsymbol{E}^{t}\boldsymbol{p}^{T} + \boldsymbol{T}^{t}\boldsymbol{\varphi}^{E})d\theta + \rho C_{sp}^{T,E}d\theta + \boldsymbol{T}^{t}\boldsymbol{s}^{E}d\boldsymbol{T} + \boldsymbol{E}^{t}\boldsymbol{\varepsilon}^{T}d\boldsymbol{E} + \boldsymbol{T}^{t}\boldsymbol{s}^{E}\boldsymbol{e}^{t}d\boldsymbol{E} + \boldsymbol{E}^{t}\boldsymbol{e}\boldsymbol{s}^{E}d\boldsymbol{T} \quad \text{(A4.2)}$$

Integrating Equation A4.2 yields Equation A4.3.

$$U = \theta(\boldsymbol{\varphi}^{E,t}\boldsymbol{T} + \boldsymbol{p}^{T,t}\boldsymbol{E}) + \rho C_{sp}^{T,E}\Delta\theta + \tfrac{1}{2}(\boldsymbol{T}^{t}\boldsymbol{s}^{E}\boldsymbol{T} + \boldsymbol{E}^{t}\boldsymbol{\varepsilon}^{T}\boldsymbol{E}) + \boldsymbol{E}^{t}\boldsymbol{e}\boldsymbol{s}^{E}\boldsymbol{T} \quad \text{(A4.3)}$$

For small $\boldsymbol{\Delta\theta}$, $\theta \cong \boldsymbol{\theta_o}$ and Equation A4.3 becomes Equation A4.4 as follows.

$$U \cong \theta_{\boldsymbol{o}}(\boldsymbol{\varphi}^{E,t}\boldsymbol{T} + \boldsymbol{p}^{T,t}\boldsymbol{E}) + \rho C_{sp}^{T,E}\Delta\theta + \tfrac{1}{2}(\boldsymbol{T}^{t}\boldsymbol{s}^{E}\boldsymbol{T} + \boldsymbol{E}^{t}\boldsymbol{\varepsilon}^{T}\boldsymbol{E}) + \boldsymbol{E}^{t}\boldsymbol{e}\boldsymbol{s}^{E}\boldsymbol{T} \quad \text{(A4.4)}$$

From Equation A4.4 for a small temperature change and thermodynamically reversible process, the work density is therefore given by $W = \frac{1}{2}(\boldsymbol{T}^{t}\boldsymbol{s}^{E}\boldsymbol{T} + \boldsymbol{E}^{t}\boldsymbol{\varepsilon}^{T}\boldsymbol{E}) + \boldsymbol{E}^{t}\boldsymbol{e}\boldsymbol{s}^{E}\boldsymbol{T}$ while the heat density is given by $Q = \theta_o(\boldsymbol{\varphi}^{E,t}\boldsymbol{T} + \boldsymbol{p}^{T,t}\boldsymbol{E}) + \rho C_{sp}^{T,E}\Delta\theta$. It is important to state that these relationships are for a small temperature change since $Q \neq \theta\Sigma = \theta(\boldsymbol{\varphi}^{E,t}\boldsymbol{T} + \boldsymbol{p}^{T,t}\boldsymbol{E}) + \rho C_{sp}^{T,E}\Delta\theta$. However, when a small temperature change is assumed, then $Q \cong \theta_o\Sigma$ is valid.

A.5 Transverse isotropy and isotropy

Piezoelectric materials of the $\mathrm{Pb\,Zr_x(Ti_{(1-x)})O_3}$ PZT family are transverse isotropic in nature and the stiffness matrix of PZT is therefore symmetrical about the main diagonal such that the stiffness matrix is equal to its transpose. Equation A5.1 shows the relationship between stress $\boldsymbol{T}$ and strain $\boldsymbol{S}$ given by Hooke's law in terms of the stiffness matrix $\boldsymbol{c}^E$ where $\boldsymbol{T} = \boldsymbol{c}^E\boldsymbol{S}$ with $c_{11}^E = c_{22}^E$, $c_{12}^E = c_{21}^E$ and $c_{31}^E = c_{13}^E = c_{21}^E = c_{23}^E = c_{32}^E$ producing a symmetrical stiffness matrix as a consequence of the transverse isotropic nature of the material.

$$\begin{pmatrix} T_1 \\ T_2 \\ T_3 \end{pmatrix} = \begin{pmatrix} c_{11}^E & c_{12}^E & c_{13}^E \\ c_{21}^E & c_{22}^E & c_{23}^E \\ c_{31}^E & c_{32}^E & c_{33}^E \end{pmatrix} \begin{pmatrix} S_1 \\ S_2 \\ S_3 \end{pmatrix} \rightarrow \begin{pmatrix} T_1 \\ T_2 \\ T_3 \end{pmatrix} = \begin{pmatrix} c_{11}^E & c_{12}^E & c_{31}^E \\ c_{12}^E & c_{11}^E & c_{31}^E \\ c_{31}^E & c_{31}^E & c_{33}^E \end{pmatrix} \begin{pmatrix} S_1 \\ S_2 \\ S_3 \end{pmatrix} \tag{A5.1}$$

In a similar way, Equation A5.2 gives the relationship between stress T and strain S in terms of the compliance matrix $\boldsymbol{s}^E$ with $s_{11}^E = s_{22}^E$, $s_{12}^E = s_{21}^E$ and $s_{31}^E = s_{13}^E = s_{21}^E = s_{23}^E = s_{32}^E$ producing a symmetrical stiffness matrix as a consequence of the transverse isotropic nature of the material.

$$\begin{pmatrix} S_1 \\ S_2 \\ S_3 \end{pmatrix} = \begin{pmatrix} s_{11}^E & s_{12}^E & s_{13}^E \\ s_{21}^E & s_{22}^E & s_{23}^E \\ s_{31}^E & s_{32}^E & s_{33}^E \end{pmatrix} \begin{pmatrix} T_1 \\ T_2 \\ T_3 \end{pmatrix} \rightarrow \begin{pmatrix} S_1 \\ S_2 \\ S_3 \end{pmatrix} = \begin{pmatrix} s_{11}^E & s_{12}^E & s_{31}^E \\ s_{12}^E & s_{11}^E & s_{31}^E \\ s_{31}^E & s_{31}^E & s_{33}^E \end{pmatrix} \begin{pmatrix} T_1 \\ T_2 \\ T_3 \end{pmatrix} \tag{A5.2}$$

The superscript E indicates that the quantity is measured at constant electric field. The mechanical behaviour of the material is therefore identical in all directions parallel to the $1-2$ $plane$, but is in general different perpendicular to the $1-3$ and $2-3$ $planes$ perpendicular to the poled $3-axis$.

Hooke's law for a transverse isotropic material can also be written in either stiffness or compliance form as Equation A5.3 and Equation A5.4, where E_{p1}^E and E_{p3}^E are the constant electric field (short-circuit) Young's moduli relative to the $1-$, $2-$ axes and $3-$ axis respectively. The terms μ_{p1}^E and μ_{p3}^E are the constant electric field Poisson's ratios relative to the $1-, 2-$ axes and $3-$ axis respectively. μ_{p1}^E is the negative ratio of the strain in the $2-$ axis to the strain in the $1-$ $axis$ for an applied strain in the 1- axis and vice-versa, and μ_{p3}^E is the negative ratio of the strain

in the $2-$ or $1-$ axis to the strain the $3-$ axis for an applied strain in the $3-$ axis. The subscript px is used to indicate quantities that apply to the piezoelectric material under consideration with x indicating the axis. The subscript 1 refers to both the $1-\ axis$ and $2-\ axis$ since these have identical properties in transverse isotropic materials such as the PZT family.

$$\begin{pmatrix} T_1 \\ T_2 \\ T_3 \end{pmatrix} =$$

$$\frac{E_{p1}^E E_{p3}^E}{(1+\mu_{p1}^E)\left(1-\mu_{p1}^E-2(\mu_{p3}^E)^2\frac{E_{p3}^E}{E_{p1}^E}\right)} \begin{pmatrix} \frac{\left(1-(\mu_{p3}^E)^2\frac{E_{p3}^E}{E_{p1}^E}\right)}{E_{p3}^E} & \frac{\left(\mu_{p1}^E+(\mu_{p3}^E)^2\frac{E_{p3}^E}{E_{p1}^E}\right)}{E_{p3}^E} & \frac{\mu_{p3}^E(1+\mu_{p1}^E)}{E_{p1}^E} \\ \frac{\left(\mu_{p1}^E+(\mu_{p3}^E)^2\frac{E_{p3}^E}{E_{p1}^E}\right)}{E_{p3}^E} & \frac{\left(1-(\mu_{p3}^E)^2\frac{E_{p3}^E}{E_{p1}^E}\right)}{E_{p3}^E} & \frac{\mu_{p3}^E(1+\mu_{p1}^E)}{E_{p1}^E} \\ \frac{\mu_{p3}^E(1+\mu_{p1}^E)}{E_{p1}^E} & \frac{\mu_{p3}^E(1+\mu_{p1}^E)}{E_{p1}^E} & \frac{\left(1-(\mu_{p1}^E)^2\right)}{E_{p1}^E} \end{pmatrix} \begin{pmatrix} S_1 \\ S_2 \\ S_3 \end{pmatrix}$$

(A5.3)

$$\begin{pmatrix} S_1 \\ S_2 \\ S_3 \end{pmatrix} = \begin{pmatrix} \frac{1}{E_{p1}^E} & -\frac{\mu_{p1}^E}{E_{p1}^E} & -\frac{\mu_{p3}^E}{E_{p1}^E} \\ -\frac{\mu_{p1}^E}{E_{p1}^E} & \frac{1}{E_{p1}^E} & -\frac{\mu_{p3}^E}{E_{p1}^E} \\ -\frac{\mu_{p3}^E}{E_{p1}^E} & -\frac{\mu_{p3}^E}{E_{p1}^E} & \frac{1}{E_{p3}^E} \end{pmatrix} \begin{pmatrix} T_1 \\ T_2 \\ T_3 \end{pmatrix} \tag{A5.4}$$

For an isotropic material, the Young's modulus and Poisson's ratio are equal in all axes and Hooke's law reduces to Equations A5.5 and A5.6 giving the stiffness and compliance matrix forms respectively, where E_b and μ_b are the Young's modulus and Poisson's ratio for all three axes. The subscript b is used to indicate quantities that apply to the isotropic brass substrate of the piezoelectric device under consideration and the stiffness matrix is denoted by c_b.

$$\begin{pmatrix} T_{b1} \\ T_{b2} \\ T_{b3} \end{pmatrix} = \frac{E_b}{(1+\mu_b)(1-2\mu_b)} \begin{pmatrix} 1-\mu_b & \mu_b & \mu_b \\ \mu_b & 1-\mu_b & \mu_b \\ \mu_b & \mu_b & 1-\mu_b \end{pmatrix} \begin{pmatrix} S_{b1} \\ S_{b2} \\ S_{b3} \end{pmatrix} = c_b S_b \tag{A5.5}$$

$$\begin{pmatrix} S_{b1} \\ S_{b2} \\ S_{b3} \end{pmatrix} = \frac{1}{E_b} \begin{pmatrix} 1 & -\mu_b & -\mu_b \\ -\mu_b & 1 & -\mu_b \\ -\mu_b & -\mu_b & 1 \end{pmatrix} \begin{pmatrix} T_{b1} \\ T_{b2} \\ T_{b3} \end{pmatrix} \tag{A5.6}$$

A.6 Alternative forms of the diffusion equation

It may sometimes be advantageous to use the diffusion equation in an alternative form to minimise the analysis required in the development of specific solutions. The three alternative forms of the diffusion equation are presented in this section starting with a derivation of the relationship between the constant strain - constant stress and constant electric field - constant electric displacement material constant matrices.

Rewriting Equation 3.23 in terms of $\boldsymbol{E}$ and substituting into Equation 3.22 and rearranging gives Equation A6.1 where $\boldsymbol{\beta}^S$ is the inverse constant strain permittivity matrix.

$$\boldsymbol{T} = (\boldsymbol{c}^E + \boldsymbol{e}^t\boldsymbol{\beta}^S\boldsymbol{e})\boldsymbol{S} - \boldsymbol{e}^t\boldsymbol{\beta}^S\boldsymbol{D} - (\boldsymbol{\gamma}^E - \boldsymbol{e}^t\boldsymbol{\beta}^S\boldsymbol{p}^S)\Delta\theta \tag{A6.1}$$

The matrix product $\boldsymbol{e}^t\boldsymbol{\beta}^S$ is the transpose of the stress-voltage form of the piezoelectric constant $\boldsymbol{h}$ such that $\boldsymbol{h}^t = \boldsymbol{e}^t\boldsymbol{\beta}^S$**.** Similarly, rewriting Equation 3.22 in terms of $\boldsymbol{S}$, substituting into Equation 3.23 and rearranging gives Equation A6.2 where $\boldsymbol{s}^E$ is the compliance at constant electric field and is the matrix inverse of $\boldsymbol{c}^E$.

$$\boldsymbol{D} = \boldsymbol{e}\boldsymbol{s}^E\boldsymbol{T} + (\boldsymbol{\varepsilon}^S + \boldsymbol{e}\boldsymbol{s}^E\boldsymbol{e}^t)\boldsymbol{E} + \left(\boldsymbol{p}^S + \boldsymbol{e}\boldsymbol{\varphi}_p^E\right)\Delta\theta \tag{A6.2}$$

A term $\boldsymbol{e}\boldsymbol{s}^E\boldsymbol{\gamma}^E$ resulting from the above substitution is equal to $\boldsymbol{e}\boldsymbol{s}^E\boldsymbol{c}^E\boldsymbol{\varphi}_p^E = \boldsymbol{e}\boldsymbol{\varphi}_p^E$. It can therefore be stated that $\boldsymbol{c}^D = (\boldsymbol{c}^E + \boldsymbol{e}^t\boldsymbol{\beta}^S\boldsymbol{e})$, $\boldsymbol{\gamma}^D = (\boldsymbol{\gamma}^E - \boldsymbol{e}^t\boldsymbol{\beta}^S\boldsymbol{p}^S)$, $\boldsymbol{\varepsilon}^T = (\boldsymbol{\varepsilon}^S + \boldsymbol{e}\boldsymbol{s}^E\boldsymbol{e}^t)$ and $\boldsymbol{p}^T = \left(\boldsymbol{p}^S + \boldsymbol{e}\boldsymbol{\varphi}_p^E\right)$ where $\boldsymbol{c}^D$and $\boldsymbol{\gamma}^D$ are the stiffness and thermal stress (or piezo-caloric) coefficients respectively at constant electric displacement (or open-circuit) while $\boldsymbol{\varepsilon}^T$and $\boldsymbol{p}^T$ are the permittivity and pyroelectric (or electro-caloric) coefficients respectively at constant stress (or mechanical short-circuit). Defining the thermal expansion coefficient at constant electric displacement as $\boldsymbol{\varphi}_p^D$ such that $\boldsymbol{\gamma}^D = \boldsymbol{c}^D\boldsymbol{\varphi}_p^D$ it can be stated that $(\boldsymbol{\gamma}^E - \boldsymbol{e}^t\boldsymbol{\beta}^S\boldsymbol{p}^S) = \boldsymbol{c}^D\boldsymbol{\varphi}_p^D$. Substituting for $\boldsymbol{\gamma}^E = \boldsymbol{c}^E\boldsymbol{\varphi}_p^E$ and $\boldsymbol{p}^S = \left(\boldsymbol{p}^T - \boldsymbol{e}\boldsymbol{\varphi}_p^E\right)$, using $\boldsymbol{c}^E = (\boldsymbol{c}^D - \boldsymbol{e}^t\boldsymbol{\beta}^S\boldsymbol{e})$ and noting that the compliance matrix at constant electric displacement $\boldsymbol{s}^D = [\boldsymbol{c}^D]^{-\mathbf{1}}$, the relationship between the open-circuit and short-circuit thermal expansion vectors, $\boldsymbol{\varphi}_p^D$ and $\boldsymbol{\varphi}_p^E$ respectively can be stated as Equation A6.3.

$$\boldsymbol{\varphi}_p^D = \boldsymbol{\varphi}_p^E - \boldsymbol{s}^D \boldsymbol{e}^t \boldsymbol{\beta}^S \boldsymbol{p}^T \tag{A6.3}$$

By a similar process, the relationships between the constant stress and constant strain inverse permittivity matrices, and the constant electric displacement and constant electric field compliance matrices can be deduced as Equation A6.4 and Equation A6.5 respectively.

$$\boldsymbol{s}^D = \boldsymbol{s}^E - \boldsymbol{s}^E \boldsymbol{e}^t \boldsymbol{\beta}^S \boldsymbol{e}\boldsymbol{s}^D = \boldsymbol{s}^E - \boldsymbol{s}^E \boldsymbol{e}^t \boldsymbol{\beta}^T \boldsymbol{e}\boldsymbol{s}^E \tag{A6.4}$$

$$\boldsymbol{\beta}^T = \boldsymbol{\beta}^S - \boldsymbol{\beta}^S \boldsymbol{e}\boldsymbol{s}^E \boldsymbol{e}^t \boldsymbol{\beta}^T = \boldsymbol{\beta}^S - \boldsymbol{\beta}^S \boldsymbol{e}\boldsymbol{s}^D \boldsymbol{e}^t \boldsymbol{\beta}^S \tag{A6.5}$$

Using the above relationships, the one-dimensional heat diffusion equation in stress-charge, strain-charge and stress-voltage forms given by Equations A6.6 to A6.8 respectively can be deduced by substitution and matrix manipulation. Equation 3.42 is repeated below to complete the set.

$$\frac{\partial \Delta\theta}{\partial t} = K^{T,D} \frac{\partial^2 \Delta\theta}{\partial x_3^2} - \frac{\theta_o}{\rho C_{sp}^{T,D}} \left(\boldsymbol{\varphi}_p^{D,t} \frac{\partial \boldsymbol{T}}{\partial t} + \boldsymbol{p}^{T,t} \boldsymbol{\beta}^T \frac{\partial \boldsymbol{D}}{\partial t} \right) \tag{A6.6}$$

$$\frac{\partial \Delta\theta}{\partial t} = K^{S,D} \frac{\partial^2 \Delta\theta}{\partial x_3^2} - \frac{\theta_o}{\rho C_{sp}^{S,D}} \left(\boldsymbol{\gamma}^{D,t} \frac{\partial \boldsymbol{S}}{\partial t} + \boldsymbol{p}^{S,t} \boldsymbol{\beta}^S \frac{\partial \boldsymbol{D}}{\partial t} \right) \tag{A6.7}$$

$$\frac{\partial \Delta\theta}{\partial t} = K^{T,E} \frac{\partial^2 \Delta\theta}{\partial x_3^2} - \frac{\theta_o}{\rho C_{sp}^{T,E}} \left(\boldsymbol{\varphi}_p^{E,t} \frac{\partial \boldsymbol{T}}{\partial t} + \boldsymbol{p}^{T,t} \frac{\partial \boldsymbol{E}}{\partial t} \right) \tag{A6.8}$$

$$\frac{\partial \Delta\theta}{\partial t} = K^{S,E} \frac{\partial^2 \Delta\theta}{\partial x_3^2} - \frac{\theta_o}{\rho C_{sp}^{S,E}} \left(\boldsymbol{\gamma}^{E,t} \frac{\partial \boldsymbol{S}}{\partial t} + \boldsymbol{p}^{S,t} \frac{\partial \boldsymbol{E}}{\partial t} \right) \tag{3.42}$$

The specific heat capacities are also related to each other through the material constants. For example, the relationship between the specific heat capacity at constant strain and electric displacement in Equation A6.7 is related to the specific heat capacity at constant strain and electric field in Equation 3.42 by the relationship $C_{sp}^{S,D} = C_{sp}^{S,E} - \theta_o \boldsymbol{p}^{S,t} \boldsymbol{\beta}^S \boldsymbol{p}^S / \rho = C_{sp}^{S,E} - \theta_o (p^S)^2 / \rho \varepsilon_{33}^S$ for a small temperature change. In practice the difference between $C_{sp}^{S,D}$ and $C_{sp}^{S,E}$ is generally small since the term $\theta_o (p^S)^2 / \rho \varepsilon_{33}^S$ (magnitude of the order $10^{-1} JKg^{-1}K^{-1}$) is much less than the specific heat capacities (magnitude of the order $10^2 JKg^{-1}K^{-1}$). The same is true for $C_{sp}^{T,D}$ and $C_{sp}^{T,E}$ and therefore for practical purposes the specific heat capacities are usually assumed to be approximately equal for a small temperature change.

Equations A.6.6 to A6.8 and Equation 3.42 are entirely equivalent and careful choice of the form used in an analysis can reduce the effort required to find a solution. For the development of the model, it is advantageous to use the stress-charge form of the diffusion Equation 3.42 with the strain $\boldsymbol{S}$ and the electric displacement $\boldsymbol{D}$ as the independent variables. Using this approach, the electric displacement can be set to zero without loss of generality and can be re-introduced later by considering a complex $\boldsymbol{\varepsilon}^S$ for steady state sinusoidal thermal and applied stress excitation or for the introduction of the Laplace variable to ε^S for consideration of general low frequency thermal and applied stress signal excitation. The application of the Laplace transform to a low frequency approximation is valid after a sufficient time such that the transient response features due to damped ringing of the sensor and substrate is negligible or as $t \to \infty$. In practice, the effect of ringing is negligible particularly for temperature excitation where rate of change of temperature is generally low.

A.7 Diffusion equations coupling constants

The approximate values of the constants listed below are for PZT-5H with a brass substrate and $\theta_o = 300K$. The dash superscript in the permittivity $\varepsilon_{33}^{S\,\prime}$ term in coefficients c_4 to c_7 and c_{10} to c_{13} indicates that an external equivalent conductivity due to for example the addition of a resistance connected across the piezoelectric electrodes may simply be added to the internal conductivity of the dielectric in the complex part of $\varepsilon_{33}^{S\,\prime}$ since these are obtained under spatially averaged conditions. Conversely, an external equivalent conductivity may not be added to the internal conductivity in the complex part of ε_{33}^{S} in coefficients c_1 to c_3 since these are obtained under spatially dependent conditions. The coefficient c_2 and therefore $K_{eff}^{S,E}$ is independent of an electric displacement due to an external equivalent conductivity. The coefficients c_4 to c_7 and c_{10} to c_{13} are calculated for $\delta_s \to 0$ and $\delta_s \to \infty$ and are listed below. All coefficients that are dependent on ε_{33}^{S} are evaluated by assuming an ideal dielectric for which the electrical conductivity δ_{33}^{S} is zero.

$$K_{eff}^{S,E} = \frac{k_p}{\theta_o C_2 + \rho c_{sp}^{S,E}} \approx 4.18 \times 10^{-7} \left(\frac{m^2}{s}\right) \tag{A.7.1a}$$

$$K^{S,E} = \frac{k_p}{\rho c_{sp}^{S,E}} \approx 4.19 \times 10^{-7} \left(\frac{m^2}{s}\right) \tag{A.7.1b}$$

$$K_{effb}^{S} = \frac{k_b(1-\mu_b)(1-2\mu_b)}{\rho_b c_{spb}^{S}(1-\mu_b)(1-2\mu_b) + \theta_o \varphi_b^2 E_b(1+\mu_b)} \approx 334 \times 10^{-7} \left(\frac{m^2}{s}\right) \tag{A.7.2a}$$

$$K_{b}^{S} = \frac{k_b}{\rho_b c_{spb}^{S}} \approx 342 \times 10^{-7} \left(\frac{m^2}{s}\right) \tag{A.7.2b}$$

$$C_1 = 2\alpha\varphi_{p1}^{E} - \frac{\beta\left(c_{33}^{E} P^{S} + e_{33}\left(2c_{31}^{E}\varphi_{p1}^{E} + c_{33}^{E}\varphi_{p3}^{E}\right)\right)}{c_{33}^{E}\varepsilon_{33}^{S} + e_{33}^{2}} \approx 35.25 \times 10^{4} \quad \left(\frac{N}{m^2 K}\right) \tag{A.7.3}$$

$$C_2 = \frac{\varepsilon_{33}^{S}\left(2c_{31}^{E}\varphi_{p1}^{E} + c_{33}^{E}\varphi_{p3}^{E}\right)^2 - 2e_{33}p^{S}\left(2c_{31}^{E}\varphi_{p1}^{E} + c_{33}^{E}\varphi_{p3}^{E}\right) - c_{33}^{E}\left(p^{S}\right)^2}{c_{33}^{E}\varepsilon_{33}^{S} + e_{33}^{2}} \approx 10.3 \left(\frac{N}{m^2 K^2}\right) \tag{A.7.4}$$

$$C_3 = \frac{\varepsilon_{33}^S\left(2c_{31}^E\varphi_{p1}^E + c_{33}^E\varphi_{p3}^E\right) - e_{33}p^S}{c_{33}^E\varepsilon_{33}^S + e_{33}^2} \approx 111.4 \times 10^{-7}\left(\frac{1}{K}\right) \quad \text{(A.7.5)}$$

$$C_4 = \frac{\left(\alpha\left(c_{33}^E\varepsilon_{33}^{S\,\prime} + e_{33}^2\right) - \beta e_{33}c_{31}^E\right)\varphi_{p1}^E - c_{33}^E\frac{\beta}{2}\left(p^S + e_{33}\varphi_{p3}^E\right)}{c_{33}^E\frac{\beta^2}{2} + \left(c_{33}^E\varepsilon_{33}^{S\,\prime} + e_{33}^2\right)\left(\frac{\alpha A_p(1-\mu_b) + E_bA_b}{A_p(1-\mu_b)}\right)}\left(\frac{1}{K}\right) \quad \text{(A.7.6a)}$$

$$\lim_{\delta_s \to 0} C_4 = \frac{\left(\alpha\left(c_{33}^E\varepsilon_{33}^S + e_{33}^2\right) - \beta e_{33}c_{31}^E\right)\varphi_{p1}^E - c_{33}^E\frac{\beta}{2}\left(p^S + e_{33}\varphi_{p3}^E\right)}{c_{33}^E\frac{\beta^2}{2} + \left(c_{33}^E\varepsilon_{33}^S + e_{33}^2\right)\left(\frac{\alpha A_p(1-\mu_b) + E_bA_b}{A_p(1-\mu_b)}\right)} \approx 4.1 \times 10^{-7} \quad \text{(A.7.6b)}$$

$$\lim_{\delta_s \to \infty} C_4 = \frac{\alpha\varphi_{p1}^E}{\left(\frac{\alpha A_p(1-\mu_b) + E_bA_b}{A_p(1-\mu_b)}\right)} \approx 8.95 \times 10^{-7} \quad \text{(A.7.6c)}$$

$$C_5 = \frac{\left(c_{33}^E\varepsilon_{33}^{S\,\prime} + e_{33}^2\right)E_bA_b\varphi_b}{c_{33}^E\frac{\beta^2}{2}A_p(1-\mu_b) + \left(c_{33}^E\varepsilon_{33}^{S\,\prime} + e_{33}^2\right)\left(\alpha A_p(1-\mu_b) + E_bA_b\right)}\left(\frac{1}{K}\right) \quad \text{(A.7.7a)}$$

$$\lim_{\delta_s \to 0} C_5 = \frac{\left(c_{33}^E\varepsilon_{33}^S + e_{33}^2\right)E_bA_b\varphi_b}{c_{33}^E\frac{\beta^2}{2}A_p(1-\mu_b) + \left(c_{33}^E\varepsilon_{33}^S + e_{33}^2\right)\left(\alpha A_p(1-\mu_b) + E_bA_b\right)} \approx 129.6 \times 10^{-7} \quad \text{(A.7.7a)}$$

$$\lim_{\delta_s \to \infty} C_5 = \frac{E_bA_b\varphi_b\ (s/c)}{\alpha A_p(1-\mu_b) + E_bA_b} \approx 147.5 \times 10^{-7} \quad \text{(A.7.7b)}$$

$$C_6 = -\frac{\left(c_{33}^E\varepsilon_{33}^{S\,\prime} + e_{33}^2\right)\mu_bA_b}{c_{33}^E\frac{\beta^2}{2}A_p(1-\mu_b) + \left(c_{33}^E\varepsilon_{33}^{S\,\prime} + e_{33}^2\right)\left(\alpha A_p(1-\mu_b) + E_bA_b\right)}\left(\frac{m^2}{N}\right) \quad \text{(A.7.8a)}$$

$$\lim_{\delta_s \to 0} C_6 = -\frac{\left(c_{33}^E\varepsilon_{33}^S + e_{33}^2\right)\mu_bA_b}{c_{33}^E\frac{\beta^2}{2}A_p(1-\mu_b) + \left(c_{33}^E\varepsilon_{33}^S + e_{33}^2\right)\left(\alpha A_p(1-\mu_b) + E_bA_b\right)} \approx -2.11 \times 10^{-12} \quad \text{(A.7.8b)}$$

$$\lim_{\delta_s \to \infty} C_6 = -\frac{\mu_bA_b}{\alpha A_p(1-\mu_b) + E_bA_b} \approx -2.4 \times 10^{-12} \quad \text{(A.7.8c)}$$

$$C_7 = -\frac{\left(c_{31}^E\varepsilon_{33}^{S\,\prime} + e_{31}e_{33}\right)A_p(1-\mu_b)}{c_{33}^E\frac{\beta^2}{2}A_p(1-\mu_b) + \left(c_{33}^E\varepsilon_{33}^{S\,\prime} + e_{33}^2\right)\left(\alpha A_p(1-\mu_b) + E_bA_b\right)}\left(\frac{m^2}{N}\right) \quad \text{(A.7.9a)}$$

$$\lim_{\delta_s \to 0} C_7 = -\frac{\left(c_{31}^E\varepsilon_{33}^S + e_{31}e_{33}\right)\mu_bA_b}{c_{33}^E\frac{\beta^2}{2}A_p(1-\mu_b) + \left(c_{33}^E\varepsilon_{33}^S + e_{33}^2\right)\left(\alpha A_p(1-\mu_b) + E_bA_b\right)} \approx -1.07 \times 10^{-12} \quad \text{(A.7.9b)}$$

$$\lim_{\delta_s \to \infty} C_7 = -\frac{c_{31}^E\mu_bA_b}{c_{33}^E\left(\alpha A_p(1-\mu_b) + E_bA_b\right)} \approx -1.90 \times 10^{-12} \quad \text{(A.7.9c)}$$

$$C_8 = \frac{\theta_o}{\rho_p C_{sp}^{S,E} + \theta_o c_2} \approx 114 \times 10^{-6} \ \left(\frac{m^2 K^2}{N}\right) \tag{A.7.11}$$

$$C_9 = \frac{2\theta_o \varphi_b E_b (1-2\mu_b)}{\rho_b C_{spb}^{S}(1-\mu_b)(1-2\mu_b) + \theta_o \varphi_b^2 E_b (1+\mu_b)} \approx 58.2 \times 10^{-6} \ (K) \tag{A.7.12}$$

$$C_{10} = \frac{\beta c_{33}^E E_b A_b \varphi_{p1}^E - c_{33}^E (\alpha A_p (1-\mu_b) + E_b A_b)(2e_{31}\varphi_{p1}^E + e_{33}\varphi_{p3}^E + p^s)}{c_{33}^E \frac{\beta^2}{2} A_p (1-\mu_b) + (\alpha A_p (1-\mu_b) + E_b A_b)\left(e_{33}^2 + c_{33}^E \varepsilon_{33}^{S\,\prime}\right)} \left(\frac{N}{CK}\right) \tag{A.7.13a}$$

$$\lim_{\delta_s \to 0} C_{10}\delta_s = 0 \tag{A.7.13b}$$

$$\lim_{\delta_s \to \infty} C_{10}\frac{\delta_s}{s} = \frac{\beta E_b A_b \varphi_{p1}^E - (\alpha A_p (1-\mu_b) + E_b A_b)(2e_{31}\varphi_{p1}^E + e_{33}\varphi_{p3}^E + p^s)}{(\alpha A_p (1-\mu_b) + E_b A_b)} \approx 3.5 \times 10^{-4} \tag{A.7.13c}$$

$$C_{11} = \frac{-\beta c_{33}^E E_b A_b \varphi_b}{c_{33}^E \frac{\beta^2}{2} A_p (1-\mu_b) + (\alpha A_p (1-\mu_b) + E_b A_b)\left(e_{33}^2 + c_{33}^E \varepsilon_{33}^{S\,\prime}\right)} \left(\frac{N}{CK}\right) \tag{A.7.14a}$$

$$\lim_{\delta_s \to 0} C_{11}\delta_s = 0 \tag{A.7.14b}$$

$$\lim_{\delta_s \to \infty} C_{11}\frac{\delta_s}{s} = \frac{-\beta E_b A_b \varphi_b}{\alpha A_p (1-\mu_b) + E_b A_b} \approx 6.87 \times 10^{-4} \tag{A.7.14c}$$

$$C_{12} = \frac{c_{33}^E \beta \mu_b A_b}{c_{33}^E \frac{\beta^2}{2} A_p (1-\mu_b) + (\alpha A_p (1-\mu_b) + E_b A_b)\left(e_{33}^2 + c_{33}^E \varepsilon_{33}^{S\,\prime}\right)} \quad \left(\frac{m^2}{C}\right) \tag{A.7.15a}$$

$$\lim_{\delta_s \to 0} C_{12}\delta_s = 0 \tag{A.7.15b}$$

$$\lim_{\delta_s \to \infty} C_{12}\frac{\delta_s}{s} = \frac{\beta \mu_b A_b}{\alpha A_p (1-\mu_b) + E_b A_b} \approx -6.35 \times 10^{-11} \tag{A.7.15c}$$

$$C_{13} = \frac{A_p (1-\mu_b)(\beta c_{31}^E - \alpha e_{33}) - e_{33} E_b A_b}{c_{33}^E \frac{\beta^2}{2} A_p (1-\mu_b) + (\alpha A_p (1-\mu_b) + E_b A_b)\left(e_{33}^2 + c_{33}^E \varepsilon_{33}^{S\,\prime}\right)} \left(\frac{m^2}{C}\right) \tag{A.7.16a}$$

$$\lim_{\delta_s \to 0} C_{13}\delta_s = 0 \tag{A.7.16b}$$

$$\lim_{\delta_s \to \infty} C_{13}\frac{\delta_s}{s} = \frac{A_p (1-\mu_b)(\beta c_{31}^E - \alpha e_{33}) - e_{33} E_b A_b}{c_{33}^E (\alpha A_p (1-\mu_b) + E_b A_b)} \approx -2.88 \times 10^{-10} \tag{A.7.16c}$$

$$C_{14} = \frac{e_{33}\left(2c_{31}^{E}\varphi_{p1}^{E} + c_{33}^{E}\varphi_{p3}^{E}\right) + c_{33}^{E}P^{S}}{c_{33}^{E}\varepsilon_{33}^{S} + e_{33}^{2}} \approx -6.96 \times 10^{3}\left(\frac{N}{CK}\right) \tag{A.7.17}$$

$$E_3 = \frac{-\frac{e_{33}}{c_{33}^{E}}T_3 - \beta\left(C_4\Delta\bar{\theta} + C_5\Delta\bar{\theta}_b + C_6T_{b3} + C_7T_3\right) - \left((2e_{31} - \beta)\varphi_{p1} + e_{33}\varphi_{p3} + P^{S}\right)\Delta\theta + D_3}{\varepsilon_{33}^{S} + \frac{e_{33}^{2}}{c_{33}^{E}}} \tag{A.7.18}$$

References

[1] Lirk, P., Stadlbauer, K.H. and Hollmann, M.W., 2013. ESA Clinical Trials Network 2012: PLATA–Prevention of Phantom Limb Pain After Transtibial Amputation. Randomised, double blind, controlled, multicentre trial comparing optimised intravenous pain control versus optimised intravenous pain control plus regional anaesthesia.

[2] Centers for Disease Control and Prevention (CDC, 2012). Increasing prevalence of diagnosed diabetes--United States and Puerto Rico, 1995-2010. *MMWR. Morbidity and mortality weekly report*, *61*(45), p.918.

[3] Centers for Disease Control and Prevention, 2011. National diabetes fact sheet: national estimates and general information on diabetes and prediabetes in the United States, 2011. *Atlanta, GA: US department of health and human services, centers for disease control and prevention*, *201*(1), pp.2568-2569.

[4] Stekelenburg, A., Gawlitta, D., Bader, D.L. and Oomens, C.W., 2008. Deep tissue injury: how deep is our understanding? *Archives of physical medicine and rehabilitation*, *89*(7), pp.1410-1413.

[5] Van Gilder, C., MacFarlane, G.D., Harrison, P., Lachenbruch, C. and Meyer, S., 2010. The demographics of suspected deep tissue injury in the United States: an analysis of the International Pressure Ulcer Prevalence Survey 2006-2009. *Advances in skin & wound care*, *23*(6), pp.254-261.

[6] Schindler, C.A., Mikhailov, T.A., Kuhn, E.M., Christopher, J., Conway, P., Ridling, D., Scott, A.M. and Simpson, V.S., 2011. Protecting fragile skin: nursing interventions to decrease development of pressure ulcers in pediatric intensive care. *American Journal of Critical Care*, *20*(1), pp.26-35.

[7] Lipsky, B.A., Tabak, Y.P., Johannes, R.S., Vo, L., Hyde, L. and Weigelt, J.A., 2010. Skin and soft tissue infections in hospitalised patients with diabetes: culture isolates and risk factors associated with mortality, length of stay and cost. *Diabetologia*, *53*(5), pp.914-923.

[8] Zhang, Y., Sun, J.W. and Rolfe, P., 2010, December. Tissue oxygenation and haemodynamics measurement with spatially resolved NIRS. In *Sixth International Symposium on Precision Engineering Measurements and Instrumentation* (Vol. 7544, p. 75443Q). International Society for Optics and Photonics.

[9] Ghoseiri, K. and Safari, M.R., 2014. Prevalence of heat and perspiration discomfort inside prostheses: literature review.

[10] Webber, C.M. and Davis, B.L., 2015. Design of a novel prosthetic socket: Assessment of the thermal performance. *Journal of biomechanics*, *48*(7), pp.1294-1299.

[11] Peery, J.T., Ledoux, W.R. and Klute, G.K., 2005. Residual-limb skin temperature in transtibial sockets. *Journal of Rehabilitation Research & Development*, *42*(2).

[12] Klute, G.K., Kallfelz, C.F. and Czerniecki, J.M., 2001. Mechanical properties of prosthetic limbs: Adapting to the patient. *Journal of Rehabilitation Research & Development*, *38*(3).

[13] Lake, C. and Supan, T.J., 1997. The incidence of dermatological problems in the silicone suspension sleeve user. *JPO: Journal of Prosthetics and Orthotics*, *9*(3), pp.97-106.

[14] Hagberg, K. and Brånemark, R., 2001. Consequences of non-vascular trans-femoral amputation: A survey of quality of life, prosthetic use and problems. *Prosthetics and orthotics international*, *25*(3), pp.186-194.

[15] Wright, C.I., Kroner, C.I. and Draijer, R., 2006. Non-invasive methods and stimuli for evaluating the skin's microcirculation. *Journal of pharmacological and toxicological methods*, *54*(1), pp.1-25.

[16] Podtaev, S., Morozov, M. and Frick, P., 2008. Wavelet-based correlations of skin temperature and blood flow oscillations. *Cardiovascular Engineering*, *8*(3), pp.185-189.

[17] Dias, D. and Paulo Silva Cunha, J., 2018. Wearable health devices—vital sign monitoring, systems and technologies. *Sensors*, *18*(8), p.2414.

[18] Ahrens, T., 2008. The most important vital signs are not being measured. *Australian Critical Care*, *21*(1), pp.3-5.

[19] Aarts, V., Dellimore, K.H., Wijshoff, R., Derkx, R., van de Laar, J. and Muehlsteff, J., 2017, May. Performance of an accelerometer-based pulse presence detection approach compared to a reference sensor. In *2017 IEEE 14th International Conference on Wearable and Implantable Body Sensor Networks (BSN)* (pp. 165-168). IEEE.

[20] Chan, M., EstèVe, D., Fourniols, J.Y., Escriba, C. and Campo, E., 2012. Smart wearable systems: Current status and future challenges. *Artificial intelligence in medicine*, *56*(3), pp.137-156.

[21] Shaltis, P.A., Reisner, A. and Asada, H.H., 2006, August. Wearable, cuff-less PPG-based blood pressure monitor with novel height sensor. In *2006 International Conference of the IEEE Engineering in Medicine and Biology Society* (pp. 908-911). IEEE.

[22] Langewouters, G.J., Zwart, A., Busse, R. and Wesseling, K.H., 1986. Pressure-diameter relationships of segments of human finger arteries. *Clinical physics and physiological measurement*, *7*(1), p.43.

[23] Cretikos, M.A., Bellomo, R., Hillman, K., Chen, J., Finfer, S. and Flabouris, A., 2008. Respiratory rate: the neglected vital sign. *Medical Journal of Australia*, *188*(11), pp.657-659.

[24] Lovett, P.B., Buchwald, J.M., Stürmann, K. and Bijur, P., 2005. The vexatious vital: neither clinical measurements by nurses nor an electronic monitor provides accurate measurements of respiratory rate in triage. *Annals of emergency medicine*, *45*(1), pp.68-76.

[25] Fieselmann, J.F., Hendryx, M.S., Helms, C.M. and Wakefield, D.S., 1993. Respiratory rate predicts cardiopulmonary arrest for internal medicine inpatients. *Journal of general internal medicine*, *8*(7), pp.354-360.

[26] Guo, L., Berglin, L., Wiklund, U. and Mattila, H., 2013. Design of a garment-based sensing system for breathing monitoring. *Textile research journal*, *83*(5), pp.499-509.

[27] Seoane, F., Mohino-Herranz, I., Ferreira, J., Alvarez, L., Buendia, R., Ayllón, D., Llerena, C. and Gil-Pita, R., 2014. Wearable biomedical measurement systems for assessment of mental stress of combatants in real time. *Sensors*, *14*(4), pp.7120-7141.

[28] Zhang, Y., Sun, J.W. and Rolfe, P., 2010, December. Tissue oxygenation and haemodynamics measurement with spatially resolved NIRS. In *Sixth International Symposium on Precision Engineering Measurements and Instrumentation* (Vol. 7544, p. 75443Q). International Society for Optics and Photonics.

[29] Huang, C.Y., Chan, M.C., Chen, C.Y. and Lin, B.S., 2014. Novel wearable and wireless ring-type pulse oximeter with multi-detectors. *Sensors*, *14*(9), pp.17586-17599.

[30] Mendelson, Y., Dao, D.K. and Chon, K.H., 2013, May. Multi-channel pulse oximetry for wearable physiological monitoring. In 2013 IEEE International Conference on Body Sensor Networks (pp. 1-6). IEEE.

[31] Chen, C.-M.; Kwasnicki, R.; Lo, B.; Yang, G.Z. Wearable Tissue Oxygenation Monitoring Sensor and a Forearm Vascular Phantom Design for Data Validation. In Proceedings of the 11th International Conference on Wearable and Implantable Body Sensor Networks, Zurich, Switzerland, 16–19 June 2014; pp. 64–68.

[32] Webb, R.C., Bonifas, A.P., Behnaz, A., Zhang, Y., Yu, K.J., Cheng, H., Shi, M., Bian, Z., Liu, Z., Kim, Y.S. and Yeo, W.H., 2013. Ultrathin conformal devices for precise and continuous thermal characterization of human skin. Nature materials, 12(10), p.938.

[33] Holowatz, L.A., Thompson-Torgerson, C.S. and Kenney, W.L., 2008. The human cutaneous circulation as a model of generalized microvascular function. *Journal of applied physiology*, *105*(1), pp.370-372.

[34] Miozzi, C., Amendola, S., Bergamini, A. and Marrocco, G., 2017, May. Reliability of a re-usable wireless epidermal temperature sensor in real conditions. In 2017 IEEE 14th International Conference on Wearable and Implantable Body Sensor Networks (BSN) (pp. 95-98). IEEE.

[35] Lee, Y.D. and Chung, W.Y., 2009. Wireless sensor network based wearable smart shirt for ubiquitous health and activity monitoring. *Sensors and Actuators B: Chemical*, *140*(2), pp.390-395.

[36] Bianchi, A.M., Mendez, M.O. and Cerutti, S., 2010. Processing of signals recorded through smart devices: sleep-quality assessment. *IEEE Transactions on Information Technology in Biomedicine*, *14*(3), pp.741-747.

[37] Jourand, P., De Clercq, H., Corthout, R. and Puers, R., 2009. Textile integrated breathing and ECG monitoring system. *Procedia Chemistry*, *1*(1), pp.722-725.

[38] Syduzzaman, M., Patwary, S.U., Farhana, K. and Ahmed, S., 2015. Smart textiles and nano-technology: A general overview. *J. Text. Sci. Eng*, *5*, p.1000181.

[39] Nemati, E., Deen, M.J. and Mondal, T., 2012. A wireless wearable ECG sensor for long-term applications. *IEEE Communications Magazine*, *50*(1), pp.36-43.

[40] Internet: https://www.forbes.com/sites/ptc/2014/02/12/google-contacts-will-help-diabetics-monitor-blood-sugar-via-tears/#61ac52437881 (accessed January 2020).

[41] Müller, A.J., Knuth, M., Nikolaus, K.S., Krivánek, R., Küster, F. and Hasslacher, C., 2013. First clinical evaluation of a new percutaneous optical fiber glucose sensor for continuous glucose monitoring in diabetes.

[42] Internet: https://nemauramedical.com/sugarbeat/ (accessed January 2020).

[43] Schrock Jr, R.D., Zettl, J.H., Burgess, E.M. and Romano, R.L., 1968. A preliminary report of basic studies from Prosthetics Research Study. *Bull Prosthet Res*, *10*, pp.90-105.

[44] Appoldt, F., Bennett, L. and Contini, R., 1968. Stump-socket pressure in lower extremity prostheses. *Journal of biomechanics*, *1*(4), pp.247-257.

[45] Huff, E.A., Ledoux, W.R., Berge, J.S. and Klute, G.K., 2008. Measuring residual limb skin temperatures at the skin-prosthesis interface. *JPO: Journal of Prosthetics and Orthotics*, *20*(4), pp.170-173.

[46] Dumbleton, T., Buis, A.W., McFadyen, A., McHugh, B.F., McKay, G., Murray, K.D. and Sexton, S., 2009. Dynamic interface pressure distributions of two transtibial prosthetic socket concepts. *Journal of Rehabilitation Research & Development*, *46*(3).

[47] Beil, T.L., Street, G.M. and Covey, S.J., 2002. Interface pressures during ambulation using suction and vacuum-assisted prosthetic sockets. *Journal of rehabilitation research and development*, *39*(6), pp.693-700.

[48] Mathur, N., Glesk, I. and Buis, A., 2014. Skin temperature prediction in lower limb prostheses. *IEEE Journal of Biomedical and Health informatics*, *20*(1), pp.158-165.

[49] Ghoseiri, K., Zheng, Y.P., Hing, L.L.T., Safari, M.R. and Leung, A.K., 2016. The prototype of a thermoregulatory system for measurement and control of temperature inside prosthetic socket. *Prosthetics and orthotics international*, *40*(6), pp.751-755.

[50] Al-Fakih, E., Abu Osman, N. and Mahmad Adikan, F., 2016. Techniques for interface stress measurements within prosthetic sockets of transtibial amputees: A review of the past 50 years of research. *Sensors*, *16*(7), p.1119.

[51] Polliack, A.A., Sieh, R.C., Craig, D.D., Landsberger, S., McNeil, D.R. and Ayyappa, E., 2000. Scientific validation of two commercial pressure sensor systems for prosthetic socket fit. *Prosthetics and orthotics international*, *24*(1), pp.63-73.

[52] Buis, A.W.P. and Convery, P., 1997. Calibration problems encountered while monitoring stump/socket interface pressures with force sensing resistors: techniques adopted to minimise inaccuracies. *Prosthetics and orthotics international*, *21*(3), pp.179-182.

[53] Al-Fakih, E.A., Osman, N.A.A., Adikan, F.R.M., Eshraghi, A. and Jahanshahi, P., 2015. Development and validation of fiber Bragg grating sensing pad for interface pressure measurements within prosthetic sockets. *IEEE Sensors Journal*, *16*(4), pp.965-974.

[54] Wheeler, J.W., Dabling, J.G., Chinn, D., Turner, T., Filatov, A., Anderson, L. and Rohrer, B., 2011. MEMS-based bubble pressure sensor for prosthetic socket interface pressure measurement. In *2011 Annual International Conference of the IEEE Engineering in Medicine and Biology Society* (pp. 2925-2928). IEEE.

[55] Dabling, J.G., Filatov, A. and Wheeler, J.W., 2012, August. Static and cyclic performance evaluation of sensors for human interface pressure measurement. In *2012 Annual International Conference of the IEEE Engineering in Medicine and Biology Society* (pp. 162-165). IEEE.

[56] Liu, Y., Yu, P., Wang, Y., Dong, Z. and Xi, N., 2008, January. The modelling and experiments of a PVDF micro-force sensor. In *2008 3rd IEEE International Conference on Nano/Micro Engineered and Molecular Systems* (pp. 60-64). IEEE.

[57] Afanas'ev, A.V., Lebedev, V.S., Orlov, I.Y. and Khrulev, A.E., 2001. An infrared pyrometer for monitoring the temperature of materials in vacuum systems. *Instruments and Experimental Techniques*, *44*(2), pp.275-278.

[58] Chang, C.C. and Tang, C.S., 1998. An integrated pyroelectric infrared sensor with a PZT thin film. *Sensors and Actuators A: Physical*, *65*(2-3), pp.171-174.

[59] Köhler, R., Suchaneck, G., Padmini, P., Sandner, T., Gerlach, G. and Hofmann, G., 1999. RF-sputtered PZT thin films for infrared sensor arrays. *Ferroelectrics*, *225*(1), pp.57-66.

[60] Kamel, T.M., 2007. Pyroelectricity versus conductivity in soft lead zirconate titanate (PZT) ceramics. *Journal of Materials Research*, *22*(12), pp.3448-3454.

[61] Silver-Thorn, B., Steege, J.W. and Childress, D.S., 1996. A review of prosthetic interface stress investigations. *Journal of rehabilitation research and development*.

[62] IEEE Standard on Piezoelectricity, 1987. ANSI/IEEE Std 176–1987

[63] Baoyuan, S., Jiantong, W., Jun, Z. and Min, Q., 2003. A new model describing physical effects in crystals: the diagrammatic and analytic methods for macro-phenomenological theory. *Journal of Materials Processing Tech.*, *1*(139), pp.444-447.

[64] Berlincourt, D.A., Cmolik, C. and Jaffe, H., 1960. Piezoelectric properties of polycrystalline lead titanate zirconate compositions. *Proceedings of the IRE*, *48*(2), pp.220-229.

[65] Kugel, V.D. and Cross, L.E., 1998. Behavior of soft piezoelectric ceramics under high sinusoidal electric fields. *Journal of applied physics*, *84*(5), pp.2815-2830.

[66] Noheda, B., Gonzalo, J.A., Cross, L.E., Guo, R., Park, S.E., Cox, D.E. and Shirane, G., 2000. Tetragonal-to-monoclinic phase transition in a ferroelectric perovskite: The structure of PbZr 0.52 Ti 0.48 O 3. *Physical Review B*, *61*(13), p.8687.

[67] Jaffe, B., 2012. *Piezoelectric ceramics* (Vol. 3). Elsevier.

[68] Wang, D., Fotinich, Y. and Carman, G.P., 1998. Influence of temperature on the electromechanical and fatigue behavior of piezoelectric ceramics. *Journal of applied physics*, *83*(10), pp.5342-5350.

[69] Dih, J.J. and Fulrath, R.M., 1978. Electrical Conductivity in Lead Zirconate Titanate Ceramics. *Journal of the American Ceramic Society*, *61*(9-10), pp.448-451.

[70] Gerson, R. and Jaffe, H., 1963. Electrical conductivity in lead titanate zirconate ceramics. *Journal of Physics and Chemistry of Solids*, *24*(8), pp.979-984.

[71] De Jong, M., Chen, W., Geerlings, H., Asta, M. and Persson, K.A., 2015. A database to enable discovery and design of piezoelectric materials. *Scientific data*, *2*(1), pp.1-13.

[72] Hearmon, R.F.S., 1957. Equations for transforming elastic and piezoelectric constants of crystals. *Acta Crystallographica*, *10*(2), pp.121-124.

[73] Catti, M., Noel, Y. and Dovesi, R., 2003. Full piezoelectric tensors of wurtzite and zinc blende ZnO and ZnS by first-principles calculations. *Journal of Physics and Chemistry of Solids*, *64*(11), pp.2183-2190.

[74] Jordan, T.L. and Ounaies, Z., 2001. *Piezoelectric ceramics characterization* (No. ICASE-2001-28). INSTITUTE FOR COMPUTER APPLICATIONS IN SCIENCE AND ENGINEERING HAMPTON VA.

[75] Smits, J.G., 1976. Iterative method for accurate determination of the real and imaginary parts of the materials coefficients of piezoelectric ceramics. *IEEE Transactions on Sonics and Ultrasonics*, *23*(6), pp.393-401.

[76] Jaffe, H. and Berlincourt, D.A., 1965. Piezoelectric transducer materials. *Proceedings of the IEEE*, *53*(10), pp.1372-1386.

[77] Thomsen, J.S., 1960. Thermodynamics of an irreversible quasi-static process. *American Journal of Physics*, *28*(2), pp.119-122.

[78] Heywang, W., Lubitz, K. and Wersing, W. eds., 2008. *Piezoelectricity: evolution and future of a technology* (Vol. 114). Springer Science & Business Media.

[79] Davidson, A., Buis, A. and Glesk, I., 2017. Toward novel wearable pyroelectric temperature sensor for medical applications. *IEEE Sensors Journal*, *17*(20), pp.6682-6689.

[80] Demirel, Y., 2007. *Nonequilibrium thermodynamics: transport and rate processes in physical, chemical and biological systems*. Elsevier.

[81] Ekoue, F., d'Halloy, A.F., Gigon, D., Plantamp, G. and Zajdman, E., 2013. Maxwell-Cattaneo regularization of heat equation. *World Academy of Science, Engineering and Technology*, *7*, pp.05-23.

[82] Krasnyuk, I.B. and Riskiev, T.T., 1994. Determination of the relaxation time of a heat flux. *Journal of engineering physics and thermophysics*, *67*(3-4), pp.975-984.

[83] Kirsanov, Y.A., Kirsanov, A.Y., Gil'fanov, K.K. and Yudakhin, A.E., 2015. On measurement of the thermal relaxation time in transient thermal processes of solids. *Russian Aeronautics (Iz VUZ)*, *58*(3), pp.251-257.

[84] Davidson, A., Buis, A. and Glesk, I., 2017. Toward novel wearable pyroelectric temperature sensor for medical applications. *IEEE Sensors Journal*, *17*(20), pp.6682-6689.

[85] Internet: http://www.aerogel.org/ (accessed January 2020).

[86] Choonee, K., Syms, R.R.A., Ahmad, M.M. and Zou, H., 2009. Post processing of microstructures by PDMS spray deposition. *Sensors and Actuators A: Physical*, *155*(2), pp.253-262.

[87] IEEE Standard on Piezoelectricity, 1987. ANSI/IEEE Std 176–1987.

[88] Internet: http://www.engineeringtoolbox.com/ (accessed January 2020).

[89] Internet: https://www.bostonpiezooptics.com/ceramic-materials-pzt (accessed January 2020).

[90] Internet: http://www.matweb.com/search/datasheettext.aspx?matguid= c8282346458040f5b92209678ad01e3e (accessed January 2020).

[91] Internet: https://www.epotek.com/site/files/Techtips/pdfs/tip19.pdf/ (accessed January 2020).

[92] Internet: https://www.scribd.com/doc/34864965/PZT-Material-Properties (accessed January 2020).

[93] Internet: http://www.piezo.com/prodmaterialprop.html/ (accessed January 2020).

[94] Internet: https://ntrs.nasa.gov/archive/nasa/casi.ntrs.nasa.gov/19980236888.pdf Hooker, M.W., 1998. Properties of PZT-based piezoelectric ceramics between 150°C and 250 °C (accessed January 2020).

[95] Debnath, L., 2016. The double Laplace transforms and their properties with applications to functional, integral and partial differential equations. *International Journal of Applied and Computational Mathematics*, *2*(2), pp.223-241.

[96] Klute, G.K., Rowe, G.I., Mamishev, A.V. and Ledoux, W.R., 2007. The thermal conductivity of prosthetic sockets and liners. *Prosthetics and orthotics international*, *31*(3), pp.292-299.

[97] Webber, C.M., Klittich, M.R., Dhinojwala, A. and Davis, B.L., 2014. Thermal conductivities of commercially available prosthetic materials. *JPO: Journal of Prosthetics and Orthotics*, *26*(4), pp.212-215.

[98] Mathur, N., Glesk, I. and Buis, A., 2016. Thermal time constant: optimising the skin temperature predictive modelling in lower limb prostheses using Gaussian processes. *Healthcare technology letters*, *3*(2), pp.98-104.

[99] Ghoseiri, K., Zheng, Y.P., Leung, A.K., Rahgozar, M., Aminian, G., Lee, T.H. and Safari, M.R., 2018. Temperature measurement and control system for transtibial prostheses: Functional evaluation. *Assistive Technology*, *30*(1), pp.16-23.

[100] Jin, H., Dong, S.R., Luo, J.K. and Milne, W.I., 2011. Generalised Butterworth-Van Dyke equivalent circuit for thin-film bulk acoustic resonator. *Electronics Letters*, *47*(7), pp.424-426.

[101] Ferrari, V., Marioli, D. and Taroni, A., 2001. Theory, modeling and characterization of PZT-on-alumina resonant piezo-layers as acoustic-wave mass sensors. *Sensors and Actuators A: Physical*, *92*(1-3), pp.182-190.

[102] Sherrit, S. and Mukherjee, B.K., 2007. Characterization of piezoelectric materials for transducers. *arXiv preprint arXiv:0711.2657*.

[103] Berlincourt D, Krueger HA, Near C. Properties of Morgan electro ceramic ceramics. Technical Publication TP-226, Morgan Electro Ceramics. 2000.

[104] Chen, W.P., Chan, H.L., Yiu, F.C.H., Ng, K.M.W. and Liu, P.C.K., 2002. Water-induced degradation in lead zirconate titanate piezoelectric ceramics. *Applied physics letters*, *80*(19), pp.3587-3589.

[105] Van Den Ende, D.A., Bos, B., Groen, W.A. and Dortmans, L.M.J.G., 2009. Lifetime of piezoceramic multilayer actuators: Interplay of material properties and actuator design. *Journal of electroceramics*, *22*(1-3), pp.163-170.

[106] Takahashi, M., 1971. Electrical resistivity of lead zirconate titanate ceramics containing impurities. *Japanese Journal of Applied Physics*, *10*(5), p.643.

[107] Kealhofer, C., Lahme, S., Urban, T. and Baum, P., 2015. Signal-to-noise in femtosecond electron diffraction. *Ultramicroscopy*, *159*, pp.19-25.

[108] Ross, D.A., 1979. *Optoelectronic devices and optical imaging techniques*. Macmillan International Higher Education.

[109] Matsuno, Y., 1984. *Bilinear Transformation Method (Mathematics in Science and Engineering; V. 174)*. Elsevier.

[110] Jung, J., Ha, K., Lee, J., Kim, Y. and Kim, D., 2008. Wireless body area network in a ubiquitous healthcare system for physiological signal monitoring and health consulting. *International Journal of Signal Processing, Image Processing and Pattern Recognition*, *1*(1), pp.47-54.

[111] Rajasekaran, M.P., Radhakrishnan, S. and Subbaraj, P., 2009. Elderly patient monitoring system using a wireless sensor network. *Telemedicine and e-Health*, *15*(1), pp.73-79.

[112] Liu, W., Park, E.K. and Krieger, U., 2012, October. eHealth interconnection infrastructure challenges and solutions overview. In *2012 IEEE 14th International Conference on e-Health Networking, Applications and Services (Healthcom)* (pp. 255-260). IEEE.

[113] Internet: https://www.cisco.com/c/en/us/solutions/collateral/service-provider/global-cloud-index-gci/white-paper-c11-738085.html (accessed January 2020).

[114] Internet: https://www.cisco.com/c/en/us/solutions/collateral/service-provider/visual-networking-index-vni/white-paper-c11-738429.html (accessed January 2020).

[115] Internet: “Explosive Growth in Data Traffic and the future of Global Communications Infrastructure,” Ntt, https://www.ntt.com/en/resources/articles/global-watch-vol2.html (accessed January 2020).

[116] Internet: Barney D. The great cloud bottleneck: How capacity issues can kill your cloud project. http://redmondmag.com/articles/2011/12/01/ cloud-bottleneck-issues. aspx, 2014 (accessed January 2020).

[117] Internet: Andrae A. Total Consumer Power Consumption Forecast. 2017. https://www. researchgate. net/publication/320225452 (accessed January 2020).

[118] Heydari, B., Bohsali, M., Adabi, E. and Niknejad, A.M., 2007. Millimeter-wave devices and circuit blocks up to 104 GHz in 90 nm CMOS. *IEEE Journal of Solid-State Circuits*, *42*(12), pp.2893-2903.

[119] Dennard, R.H., Gaensslen, F.H., Rideout, V.L., Bassous, E. and LeBlanc, A.R., 1974. Design of ion-implanted MOSFET's with very small physical dimensions. *IEEE Journal of Solid-State Circuits*, *9*(5), pp.256-268.

[120] Moore, G.E., 2006. Cramming more components onto integrated circuits, Reprinted from Electronics, volume 38, number 8, April 19, 1965, pp. 114 ff. *IEEE solid-state circuits society newsletter*, *11*(3), pp.33-35.

[121] Havemann, R.H. and Hutchby, J.A., 2001. High-performance interconnects: An integration overview. *Proceedings of the IEEE*, *89*(5), pp.586-601.

[122] Internet: Brodkin, J., 2014. Intel's 800 Gbps cables headed to cloud data centers and supercomputers. *Arstechnica*. https://arstechnica.com/ information-technology/2014/03/intels-800gbps-cables-headed-to-cloud-data-centers-and-supercomputers/ (accessed January 2020).

[123] Internet: Hruska, J., 2013. Intel's former chief architect: Moore's law will be dead within a decade. http//www.extremetech.com/computing/165331-intels-chief-architect-moores-law-will-be-dead-within-adecade/ *Aug*, *30*. (accessed January 2020).

[124] Singh, S.K., Kaushik, B.K., Chauhan, D.S. and Kum, S., 2013. Reduction of subthreshold leakage current in MOS transistors. *World Applied Sciences Journal*, *25*(3), pp.446-450.

[125] Graham-Rowe, D., 2008. Better Graphene Transistors. *Technology Review*, *3*, p.17.

[126] Gu, J.J., Wang, X.W., Shao, J., Neal, A.T., Manfra, M.J., Gordon, R.G. and Ye, P.D., 2012, December. III-V gate-all-around nanowire MOSFET process technology: From 3D to 4D. *2012 International Electron Devices Meeting* pp. 23-7. IEEE.

[127] Internet: Brian, T., 2006. Putting multicore processing in context: Part One. *Embedded*. https://www.embedded.com/putting-multicore-processing-in-context-part-one/ (accessed January 2020).

[128] Chen, W., Beck, K.M., Bücker, R., Gullans, M., Lukin, M.D., Tanji-Suzuki, H. and Vuletić, V., 2013. All-optical switch and transistor gated by one stored photon. *Science*, *341*(6147), pp.768-770.

[129] Varghese, L.T., Fan, L., Wang, J., Gan, F., Wang, X., Wirth, J.C., Niu, B., Tansarawiput, C., Xuan, Y., Weiner, A.M. and Qi, M., 2012, October. A silicon optical transistor. In *Frontiers in Optics* (pp. FW6C-6). Optical Society of America.

[130] Zhou, D. and Kamlah, M., 2005. Dielectric and piezoelectric performance of soft PZT piezoceramics under simultaneous alternating electromechanical loading. *Journal of the European Ceramic Society*, *25*(12), pp.2415-2420.

[131] Bertotti, G. and Mayergoyz, I.D., 2006. *The science of hysteresis: Hysteresis in materials* (Vol. 3). Gulf Professional Publishing, pp.431-433.

[132] Elissalde, B. and Ravez, J., 2001. Ferroelectric ceramics: defects and dielectric relaxations. *Journal of Materials Chemistry*, *11*(8), pp.1957-1967.

[133] Arlt, G., 1982. Piezoelectric relaxation. *Ferroelectrics*, *40*(1), pp.149-157.

[134] Tran-Huu-Hue, L.P., Levassort, F., Felix, N., Damjanovic, D., Wolny, W. and Lethiecq, M., 2000. Comparison of several methods to characterise the high frequency behaviour of piezoelectric ceramics for transducer applications. *Ultrasonics*, *38*(1-8), pp.219-223.

[135] Malkin, A.Y. and Isayev, A.I., 2017. *Rheology: concepts, methods, and applications*. Elsevier.